Novel Mesoporous Catalysts for Vacuum Residue Hydrocracking

Holda M. Purón Zepeda

Imperial College London

Chemical Engineering Department

Thesis submitted for the degree of Doctor of Philosophy (PhD) to Imperial College London

Supervised by Dr. Marcos Millán Agorio

August 2013

Double, double, toil and trouble;

Fire burn, and cauldron bubble.

Macbeth 4.1.10-11.

William Shakespeare

For Manuel

Declaration of Originality

This is to certify that this thesis was carried out by the author. The contents stated in this work are the original effort of the author and all else is appropriately referenced.

Holda Purón

Copyright Declaration

Abstract

Crude oil will continue to be an essential primary energy source during this century. The decline in light crude oil has increased the share of heavy oils in the crude slate fed to refineries. The development of new catalysts that can withstand deactivation by heavy feeds can be readily applied in industry. The aims of this work centred in the development and characterisation of novel NiMo mesoporous catalysts along the testing of such materials in hydrocracking reactions using a heavy hydrocarbon feed, Maya vacuum residue (VR). Four categories of catalytic supports were synthesised: mesoporous alumina (Al_2O_3), mesoporous alumina doped with Cr (Al_2O_3-Cr), mesoporous silica alumina (MSA) and carbon nanofibres (CNF). An experimental method was developed for one hour hydrocracking reactions between 400 and 450 °C in a batch reactor using VR. Selected catalysts were utilised in a second reaction with fresh feed. The catalysts short term deactivation was investigated and related to the product distribution and reaction conditions.

It was found that reaction temperature had an important impact on conversions and product distributions. The conversion of materials with a boiling point above 450 °C was mainly thermally driven. NiMo catalysts supported on Al_2O_3, Al_2O_3-Cr and CNF led to high asphaltene conversions without suffering significant deactivation. On the other hand, the MSA supported catalyst was active mainly due to thermal reactions and its pores were blocked by coke deposits by the first hour of reaction. The Al_2O_3-Cr support allowed not only higher NiMo dispersion than Al_2O_3, but also better dispersion of the coke deposits after reaction. NiMo catalysts supported on CNF showed they could be very active in VR hydroprocessing, depending on their synthesis conditions.

Acknowledgements

I want to thank my supervisor, Dr Marcos Millán, for giving me the opportunity to pursue a PhD and for his constant support during these years. I am grateful to him for sending me to Mexico and Spain to establish research collaborations as well as for the timely correction of this thesis. Also I also want to thank him for his confidence in my work, which allowed me to explore different interesting research paths.

My PhD was a very special and rewarding experience because I had the opportunity to work with great people. My sincere appreciation goes to Dr José Luis Pinilla for his invaluable advice, help, discussions, constant work suggestions, as well as his revision of this document. I also want to thank him for inviting me to participate in a research collaboration with ICB-CSIC. I really enjoyed the time I spent working with him in the lab. Above all, I thank him for his constant friendship and encouragement which really helped me with the challenges of this work.

Special thanks also go to Dr Beatriz Fidalgo and Pedro Arcelus, with whom I had the opportunity to work in different settings, from lab (re)construction to kinetics discussions to coffee, dinner and poker sessions. Their help and advice with my experimental work and thesis writing are duly noted. The most important thing I will treasure is their friendship.

I want to express my gratitude to Drs César Berrueco and Esther Lorente. Even though they left Imperial College some time ago, their constant support and friendship has been an important part of my PhD. I also want to thank Khairul Rostani for his help and friendship. I had the opportunity to work with Kee Kee Chin in her MSc project and I want to thank her for her efforts and for the energy she had in the lab.

The support team at Imperial College was very helpful and collaborative. I want to expressly thank Susi Underwood, Sarah Payne, Patricia Carry, Chin Lang, Jesús Gómez, Tony Meredith, Paul Mayer and Paul Crudge.

I want to thank CONACYT Mexico for giving me funds to pursue this PhD.

The people I worked with at CSIC-ICB were wonderful and helped me not only learn about graphenes, but also have a very good time. I want to give special thanks to Saúl de Llobet and Daniel Torres for collaborating in experimental work, as well as thank Drs

Isabel Suelves, Rafael Moliner and María de Jesús Lázaro for allowing me to participate in the joint research project.

I want to thank Dr Ascención Montoya at IMP for his teachings and for letting me work in his labs. Rosa Granados and Sixto Hernández were very helpful with my research at IMP as well.

I want to mention the people in Shell who encouraged me to pursue a PhD. I am grateful to Steve Emig and Wendy Miller for their support. Additionally, Drs José Bravo, Rafael Herrera, Carol Triebel, Stan Milam, Scott Wellington and, specially, Dr Mike Reynolds helped me realise I wanted to pursue a career in research.

I want to thank my great friends Gaby and Chango for helping me disconnect from work. I have really enjoyed our times spent during dinners, concerts, movies and trips.

My sincere gratitude goes to my family who has been extremely supportive during these long distance years. I want to thank Sergio and Güera, Vicky, Fina, Sofía and Loli for their encouragement. Special thanks go to my sister María and even more so to my parents. Their constant help has kept me going.

Finally, I want to express my greatest appreciation to my dear husband, Manuel, my source of inspiration. I know I could not have chosen a better partner to go through this. I admire his tenacity and passion, which were catching. It was an amazing opportunity to live through our PhDs simultaneously; I really thank him for his patience and commitment to both our projects throughout. We never thought we would grow so much together! I think we are ready for our next adventure!

Table of contents

List of tables

List of figures

List of abbreviations

ALKY	alkylation
APD	average pore diameter
API	American Petroleum Institute
AR	atmospheric residue
ATM	ammonium tetrathiomolybdate
BET	Brunauer, Emmet and Teller
BJH	Barret, Joyner and Halenda
BPR	back pressure regulator
$C_{>450°C}$	Conversion of the fraction boiling above 450 °C
$C_{ASPHALTENES}$	Asphaltene conversion
CCC	central composite circuscribed
CCU	catalytic cracker unit
CNF	carbon nanofibres
CNT	carbon nanotubes
CRU	catalytic reformer unit
CSIC	Consejo Superior de Investigación Científica
CUS	coordinated unsaturated sites
CVD	chemical vapour decomposition
DBT	dibenzothiophene
DETA	diethylenetriamine
DMDS	dimethyldisulfide
EDX	energy dispersive X-ray spectroscopy
FID	flame ionisation detector
FTIR	Fourier transmission infrared spectroscopy
GC	gas chromatographer
HCR	hydrocracker
HDM	hydrodemetallisation
HDN	hydrodenitrogenation
HDS	hydrodesulfurisation
HGO	heavy gas oil
HRTEM	high resolution transmission electron microscopy
HT	hydrotreater
HYD	hydrogenation
ICB-CSIC	Carbochemistry Institute
ICP	inductively coupled plasma
IFP	French Petroleum Institute
IMP	Mexican Petroleum Institute
ISOM	isomerisation

LGO	light gas oil
MALDI	matrix assisted laser desorption ionisation
MFC	mass flow controller
MSA	mesoporous silica alumina
n_A	number of acid sites
NH_3-TPD	ammonia temperature programmed desorption
n_M	number of metal sites
NMP	N-methyl-2-pyrrolidone
NMR	nuclear magnetic resonance
OES	emission spectrometer
OMA	organised mesoporous alumina
PAH	polyaromatic hydrocarbons
PILC	pillared clays
PS	polystyrene
PSD	pore size distribution
PSV	process safety valve
PT	pressure transducer
S_{BET}	BET surface area
SD	standard deviation
SE	standard error
SEC	size exclusion chromatography
SGO	standard gas oil
TCD	thermal conductivity detector
TEM	transmission electron microscopy
TGA	thermogravimetric analysis
TI	temperature indicator
TOS	time on stream
TPD	temperature programmed desorption
TPO	temperature programmed oxidation
TPR	temperature programmed reduction
UV-F	ultraviolet-fluorescence
VGO	vacuum gas oil
VR	vacuum residue
X_{AT}	ageing temperature
X_{CHR}	calcination heating rate
$X_{H2O:Al}$	H_2O:Al ratio
XPS	X-ray photoelectron spectroscopy
XRD	X-ray diffraction
XRF	X-ray fluorescence

Chapter 1: Introduction

In this chapter, an overview of the research questions this thesis aims to answer is provided. The aim and objectives of this thesis and its structure are included.

1.1. BACKGROUND

Crude oil derivatives provide more than 40% of the world's current energy fuel consumption (1). Nowadays, light and medium oils account for 85% of the crude production but the exploitation of these reserves is becoming technically complex (2). The decline in light crude oil has increased the share of heavy oils in the crude slate fed to refineries.

Heavy oils, with API gravity below 22°, have a larger content of heteroatoms, such as S and N, as well as polyaromatic hydrocarbons (PAH) which make them challenging to upgrade. This fact, combined with more stringent environmental regulations and increasing oil prices, has influenced advances in upgrading technologies that can process heavy feeds. Thermal or catalytic refining processes such as coking, visbreaking, catalytic cracking, hydrotreating and hydrocracking are employed to convert heavy oil fractions into valuable products. The process conditions and feedstock conversions of the technologies are shown in Figure 1.1. Among these technologies, hydrocracking employs higher pressures than the others while obtaining higher yields. Given their process similarities, hydrotreating and hydrocracking are categorised as hydroprocessing technologies.

Hydrocrackers are integral units of the refinery because they operate according to seasonal demand of different liquid fuels. They can process hydrogen deficient and heavy hydrocarbons and obtain higher yields of valuable products. During hydrocracking reactions a catalyst is used in a high H_2 partial pressure system to crack large hydrocarbons into smaller ones and simultaneously hydrogenate the products.

Hydrocrackers are costly to operate and maintain because of the severity of the process, thus the selection of an adequate catalyst plays a crucial role in obtaining desired product yields and ultimately in refinery economics. Advances in catalyst technology can be applied immediately in the industry capacity base without modification of the process units.

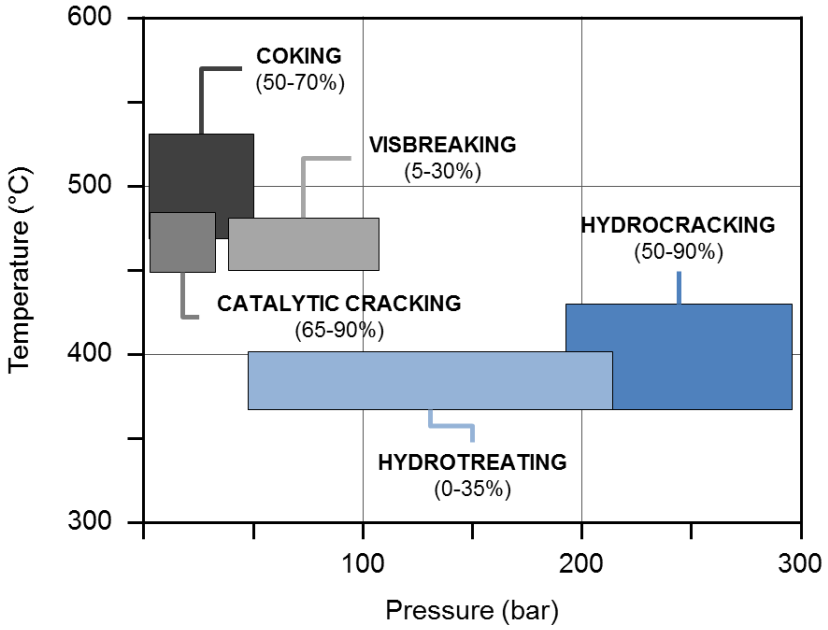

Figure 1.1. Operating conditions and conversion for heavy hydrocarbon conversion processes (3).

Hydrocracking was developed to obtain products with higher quality than the ones from the existing catalytic cracking units. Since the 1920s oil and coal products have been used as feedstock, although the process was not economical until late 1950s. The combination of hydrogen addition and thermal processes made this technology very important in refining since heavier feedstocks could be converted into middle distillates. The complexity of the process increases with increasing boiling point of the feed. When heavy feeds are hydrocracked, PAH polymerise and high yields of carbonaceous deposits, or coke, are formed on the catalyst.

Catalyst design plays an important role in allowing longer reaction cycles which in turn reduce operation costs. The choice of catalyst depends on the feed as well as the desired products. When heavier feeds are processed, catalysts with larger pores are used to allow molecules to diffuse into the pores to reach catalytic active sites. During operation, pores are blocked with coke deposits. Thus the development of catalysts that have large pores and are less susceptible to deactivation is a promising area of research.

The novelty of this work lies in the design and subsequent testing of materials for hydrocracking of vacuum residue (VR), for which limited information has been published. In summary, four classes of supports were studied: mesoporous alumina, mesoporous alumina doped with chromium, mesoporous silica alumina and carbon nanofibres.

1.2. AIM OF THE THESIS

The aim of this work is twofold: (1) to develop and characterise novel mesoporous catalysts and (2) test them in hydrocracking reactions using a heavy hydrocarbon feed. The objectives listed below were set out to achieve the above aim:

i) To study procedures to synthesise different types of supports and NiMo catalysts by:
   a. Understanding how synthesis conditions affect textural properties such as pore size and surface area of mesoporous aluminas.
   b. Testing different metal loadings in catalysts supported on mesoporous alumina.
   c. Evaluating the effect of adding a Cr dopant in mesoporous alumina.
   d. Synthesising mesoporous silica alumina.
   e. Developing carbon nanofibres and understanding how their preparation conditions influenced catalyst properties.

ii) To develop an experimental methodology to test the in-house developed catalysts for VR hydrocracking at short reaction times in a microbomb batch reactor, including reaction conditions and product analysis.

iii) To investigate the relationship between product distribution, reaction conditions and catalyst deactivation for each type of catalyst.

iv) To evaluate the catalysts characteristics by comparing between the different types of catalysts in their activity and short term deactivation.

Collaboration with two institutions was established during this project. Part of the catalyst development was carried out at the Enhanced Experimentation facilities in the Mexican Petroleum Institute (IMP) in Mexico City, Mexico. The synthesis of carbon nanofibres and characterisation of selected materials took place as part of a joint project, “I-LINK-0439: Nanostructured Carbon-Supported Catalysts for Hydroprocessing of Heavy Oils”, with the Carbochemistry Institute (ICB-CSIC) in Zaragoza, Spain.

1.3. STRUCTURE OF THIS THESIS

This thesis is divided into nine chapters. This chapter presents an introduction to the research questions it aims to answer. Chapter 2 provides a review of the state of the art in heavy oil hydrocracking and catalyst design. Chapter 3 details the experimental methodology, equipment and the procedures that were developed for product analysis.

Results are presented in Chapters 4 to 8. In each chapter the synthesis procedure and characterisation of the utilised materials is included.

The synthesis of mesoporous aluminas and the tailoring of their textural properties are presented in Chapter 4. The synthesis and characterisation of NiMo catalysts supported on these aluminas are also described.

Chapters 5 to 8 include results from testing NiMo catalysts supported on different materials in VR hydrocracking reactions. These chapters include characterisation of VR hydrocracking reaction products and of spent catalysts.

Chapter 5 contains an analysis on the variation of Ni and Mo metal loading on catalysts supported on an alumina selected from Chapter 4. Reaction product results are correlated to the metal content of the catalysts. The NiMo loading of the better performing catalyst was chosen as a benchmark for other supports.

In Chapter 6 a NiMo catalyst supported on a chromium-doped alumina is used for hydrocracking reactions. Product distribution and spent catalysts are analysed. The effect of Cr as a dopant is evaluated by comparing with results of a NiMo/alumina catalyst with the same metal content from Chapter 5.

Results from the hydrocracking activity of a NiMo catalyst supported on mesoporous silica alumina (MSA) are available in Chapter 7. The deactivation of NiMo/MSA materials is compared to the NiMo/alumina catalyst with the same metal loading from Chapter 5.

Chapter 8 includes results from the hydroprocessing activity of NiMo catalysts supported on carbon nanofibres. The effects of the support and catalyst synthesis on the activity of the materials are included. Also a comparison to a NiMo catalyst supported on mesoporous alumina, from Chapter 5, is covered.

The conclusions of this work are summarised in Chapter 9 together with recommendations for future work.

Chapter 2: Background

In this chapter, the background for current research in hydrocracking of heavy oils is discussed. Properties of heavy oil are first provided. Afterwards a description of a refinery and the technologies of heavy oil upgrading are available, emphasising on the industrial hydrocracking process. A description of the composition of hydrocracking catalysts and their synthesis follows. The reaction mechanisms for paraffins and heavy oils are included. The methods of catalyst deactivation, focusing on coke deposits, are described. Information on catalyst regeneration is provided. Finally, brief descriptions of catalyst and hydrocarbon characterisation techniques are included.

2.1. RESEARCH IN HYDROCRACKING OF HEAVY OILS

Interest in hydroprocessing research, which includes hydrotreating and hydrocracking, exists in the scientific community present in industry and academia (4). This research is essential to meet the challenge of producing low sulfur and high quality fuels from heavier feeds. Most of the industrial hydrocracking capacity is installed thus catalyst design optimisation is an important task to increase refinery margins. The development of catalytic supports and materials can yield novel results. An interesting report on the publication trends for sulfidic catalysts (5) found, unsurprisingly, that academia publishes in open literature whereas industry in patents. This topic is broader than hydrocracking of heavy oils because it includes hydrotreatment of lighter feeds and model compounds as well. Nevertheless, it showed that it is still an active field of research.

Figure 2.1 shows that publications on the topic of “heavy oil” and “hydrocracking” have increased in the past 30 years[1]. Within those publications, reports on vacuum residue, the heavy oil used in this work, were found as well. Fewer publications were found on the supports used for this thesis, such as alumina, mesoporous materials and carbon.

[1] Performed with SciVerse Scopus on 02/05/2013.

In regards to open literature publications[2] the most prolific group was that of J. Ancheyta at the Mexican Petroleum Institute. Their research dealt with topics covering catalyst design, catalyst deactivation, influence of support, process kinetics and conditions, among others. Several reviews were published by them on the aforementioned topics. Given their access to Maya crude oil and its fractions, it was the commonly used feed in their studies. Other academic groups dedicated to research in heavy oil processing include M. Gray at the University of Alberta, focusing on oil sands, and A. Marafi, A. Stanislaus and others at the Kuwait Institute for Scientific Research using Kuwait oil residua. The aforementioned research groups focused on analyses of the hydrocarbon feed and products, although some publications on catalyst characterisation were also found. Researchers, including E. Furimsky, J. A. Moulijn, C. Song and H. Fukuyama, among others, focus on the development and characterisation of hydroprocessing catalysts. Publications from the French Petroleum Institute (IFP) and industrial groups such as Syncrude Canada, Albemarle Catalysts and Haldor Topsøe centred on catalyst design and deactivation coupled with advanced characterisation techniques. A majority of references cited in this chapter are from the mentioned institutions and researchers.

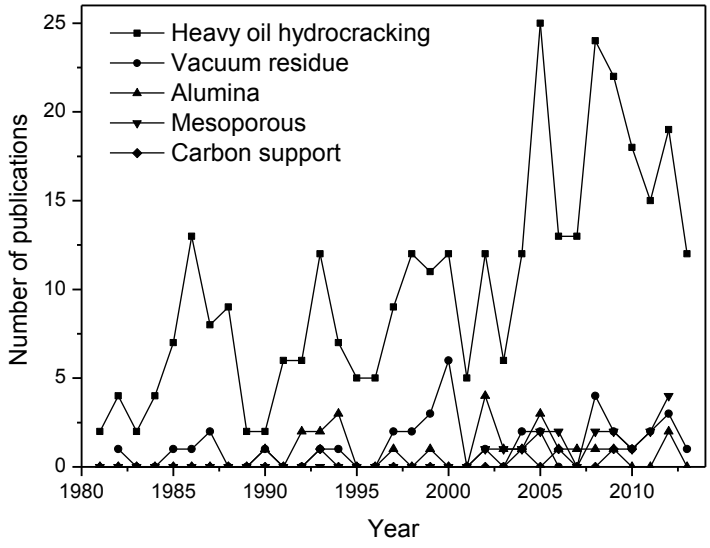

Figure 2.1. Number of publications by research theme.

[2] Verified by SciVerse Scopus on 02/05/2013.

2.2. HEAVY OIL

Crude oils consist of a varying mixture of hydrocarbons, which may contain other heteroatoms such as sulfur, nitrogen, oxygen and metals. Given the high complexity of the mixture of compounds found in oil, they are classified by their density. Heavy oils are defined as an oil with less than 22° API and sulfur content higher than 2% weight (3). Properties of a light and a heavy crude oil are listed in Table 2.1. It can be observed that the density of the heavy oil is higher than the one of the light oil.

Table 2.1. Main properties of crude oils (6,7).

Sample	Units	Light oil (Isthmus)	Heavy oil (Maya)
Density	API/sg	33/0.86	21/0.93
Asphaltene content	wt %	3	13
N	wt %	0.14	0.32
S	wt %	1.8	3.52
Ni + V	ppm	100	325
Atmospheric residue	vol %	40	31
Vacuum residue	vol %	11	59

Oils are fractioned into four main solubility components: asphaltenes, resin, aromatics, and saturates. These fractions are defined by their solubility and adsorption characteristics that group species of similar molecular size and type. Asphaltenes are considered the n-heptane insoluble fraction. The rest of the sample are the maltene constituents, or deasphalted oil, which are further fractionated with a polar solvent to separate the soluble resins. Finally, an adsorbent such as silica gel or alumina can be used to separate aromatics (benzene soluble) from saturates (n-pentane soluble). The methods ASTM D2006, ASTM D2007 and ASTM D4124 are used for this purpose. Depending on the nature of the oil one method might be better suited than another, particularly for heavy oils. The analysis of each fraction allows for better comparison in between different oils. An accepted hypothesis, which is still matter of research and debate, describes oil as a colloidal solution of the four fractions. Figure 2.2 describes how asphaltenes and resins form micelles, which are dispersed in aromatics and saturates.

Importantly, in heavy oil asphaltene content increases fourfold than in light oil and the content of heteroatoms increases as well, as observed in Table 2.1. Thus, lighter oils are easier to process than heavier oils. Asphaltene upgrading and heteroatom removal makes heavy oil processing complex.

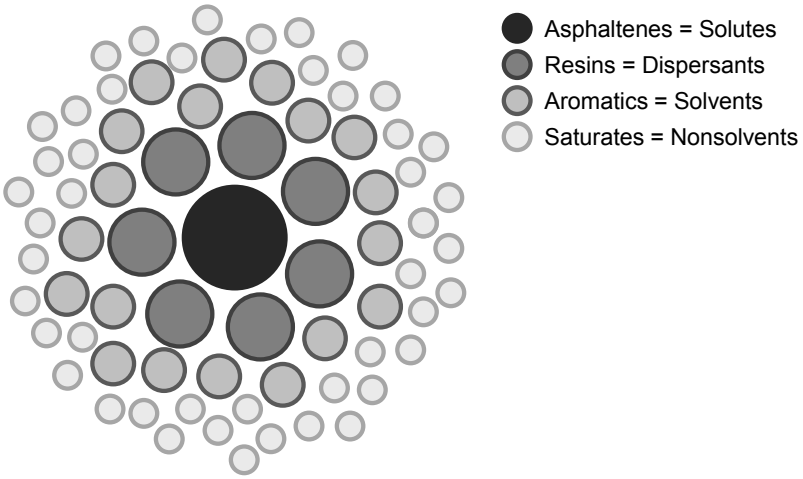

Figure 2.2. Representation of the colloidal nature of oil (8).

The atmospheric residue (AR) and vacuum residue (VR) fractions of oil are defined by boiling point, related to a refinery flow stream. AR is the heavier boiling point stream from the atmospheric distillation unit with a boiling range above 345 °C and VR is the heavier boiling point stream from the vacuum distillation unit, with a boiling range above 540 °C (9). The reactivity of VR is low when compared to AR; Maya VR is specially unreactive even when compared to other vacuum residua (10). Asphaltenes are the heaviest fraction of heavy oils and thus the most difficult to upgrade. Therefore the following section will detail the structure of asphaltenes.

2.2.1. Asphaltenes

Asphaltenes are a solubility fraction defined as insoluble in n-pentane or n-heptane and soluble in benzene or toluene (3). Heavier oils have higher asphaltene content. The asphaltene fraction is composed by molecules of high structural complexity, which can contain polyaromatic hydrocarbons (PAH) and heteroatoms. Exact molecular structures of asphaltenes are difficult to determine and several structures have been proposed (7,11). Asphaltene molecules consist of aromatic and naphthenic rings with aliphatic chains or heteroatoms that work as bridges or side chains. Two models have been proposed for asphaltene molecules, a “continental” type and an “archipelago” type (11). Continental type asphaltenes consist of cores composed of seven aromatic rings surrounded by aliphatic chains whereas archipelago type asphaltenes are composed by smaller aromatic cores united to each other by aliphatic chains. Figure 2.3 shows a hypothetical asphaltene molecule from Maya crude (12).

Heteroatoms are present in asphaltenes in different forms. For example, sulfur is present as organic sulfides, disulfides, mercaptans, and thiophenes; nitrogen is present

as pyridines, quinolines, indoles, and pyrroles; oxygen can be found as carboxylic acids, phenols, esters, amides, ketones and benzofurans. Metals, usually Ni and V, are present as porphyrins.

The determination of the molecular size and weight of asphaltenes has been a topic of debate, given that different analytical techniques provide different results. The nature of the crude oil also influences the size of the asphaltene molecules (11). It was observed that Maya asphaltenes have a wide molecular size range from 3,000 to 10,000 u, when analysed by size exclusion chromatography (SEC), matrix assisted laser desorption ionisation (MALDI) and ultraviolet fluorescence spectroscopy (13). On the other hand, the molecular size range for asphaltenes was observed to be from 300 to 1,400 u when electrospray ionisation, which allows large molecules to vaporise, was used coupled with Fourier Transform Ion Cyclotron Resonance Mass Spectrometry (14).

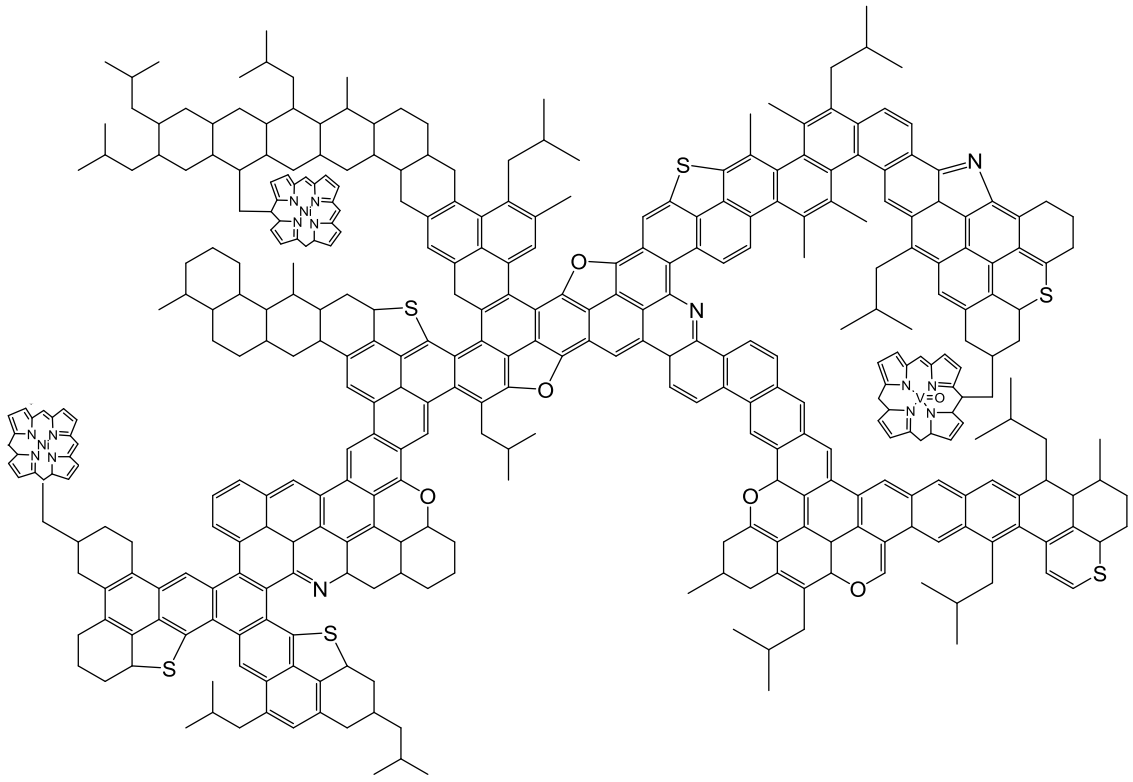

Figure 2.3. Representation of hypothetical Maya asphaltene (12).

Other asphaltene properties are studied with several characterisation techniques, a detailed review is available (11). For example ^{1}C and ^{1}H nuclear magnetic resonance (NMR) identifies aliphatic and aromatic groups; functional groups such as –OH, -CH_3 and –CH_2CH_3 can be identified via Fourier Transmission infrared spectroscopy (FTIR).

2.3. OIL UPGRADING

2.3.1. Oil refinery

A simplified general schematic of a refinery with a hydrocracker is shown in Figure 2.4. Oil first enters the atmospheric distillation unit where it is separated into different boiling point fractions: light naphtha (< 100 °C), naphtha (100-200 °C), kerosene (177-260 °C), light gas oil (LGO) (232-343 °C) and heavy gas oil (HGO) (315-426 °C). The AR is then separated in the vacuum distillation unit into vacuum gas oil (VGO) (426-565 °C) and VR (> 540 °C). After this, depending on the boiling point of the stream, further processing is performed by two different types of processes a) hydrogen addition or b) carbon rejection (6). Hydrogen addition processes, such as hydrotreating (HT), decrease the C to H ratio in products and lower the heteroatom content. Hydrotreating targets the removal of heteroatoms and is therefore classified by the heteroatom it removes; N, S and metals are targeted by hydrodenitrification (HDN), hydrodesulfurisation (HDS), and hydrodemetallisation (HDM), respectively. Carbon rejection processes, such as catalytic cracking (CCU) and coking, further crack molecules to reduce the boiling point of the stream. Hydrocracking (HCR) is a process that combines hydrogen addition and carbon rejection. When hydrotreating and hydrocracking are combined, the operation is called hydroprocessing. Further refining of lighter streams is performed for molecular rearrangement purposes to provide better properties in the end products. Isomerisation (ISOM) converts normal paraffins into iso-paraffins, alkylation (ALKY) creates paraffinic ramifications in aromatics and finally catalytic reforming (CRU) converts linear paraffins into aromatics.

In a refinery heavy oils can be upgraded via two carbon rejection pathways, thermal or catalytic. The former employs high temperatures to separate different fractions and to crack larger molecules into smaller ones. Thermal cracking of heavy oils is in many ways obsolete because of poor yields and unwanted side products, however the heaviest streams are upgraded by visbreaking or coking. Visbreaking consists of mild thermal cracking conditions (<450 °C) to process residua into HGO and lower boiling point streams. Coking consists of severe thermal cracking conditions (> 480 °C) that convert feed into volatiles and coke. The coking capacity of a refinery determines its heavy oil processing capacity.

In catalytic cracking processes, reactions take place with specially designed catalysts with metal active sites that trigger molecular size reduction reactions. These processes include catalytic cracking and hydrocracking. During catalytic cracking larger molecules are converted into smaller ones in the presence of a catalyst at high temperatures (>

450 °C). Coke deposits build up on the catalyst when cracking hydrocarbons, thus the catalyst is periodically removed from the reactor and regenerated. Given that hydrocracking is the main process used for hydrocarbon upgrading in this work, its description is provided in the following section.

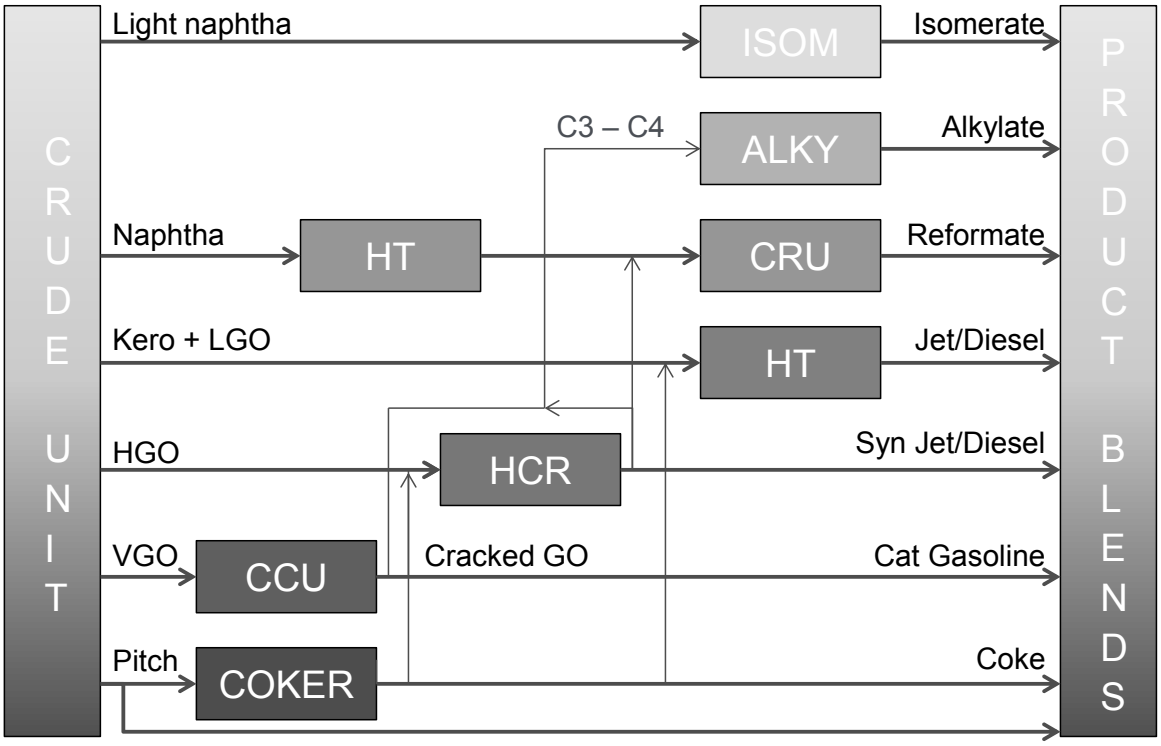

Figure 2.4. Simplified diagram of a refinery.

With the following process units: hydrotreaters (HT), isomerisation plant (ISOM), alkylation plant (ALKY), catalytic reformer (CRU), hydrocracker (HCR), catalytic cracker (CCU) and coker.

2.3.2. Hydrocracking industrial process

Hydrocracking is a carbon reduction and hydrogen addition process thus feeds that have large molecular size components, usually with high aromatic content, are used. These include coker oils, cracked or cycle gas oils, VGO, syncrude, aromatic streams, and heavy-cracked naphtha. AR and VR are also hydrocracked to obtain valuable products. Process conditions are tailored to the properties of the feed, desired products and H_2 availability. Operating conditions that can be varied in industrial hydrocrackers include feed to recycle ratio, fractionator cut point, conversion level and catalyst; conditions are changed because hydrocracking can selectively produce naphtha, jet fuel, or diesel fuel. Temperatures can range from 300 to 450 °C and pressures from 85 to 200 bar; temperatures above 400 °C are used for residua hydrocracking (15). High hydrogen partial pressure, which is very expensive, is employed in the process to ensure an excess of H_2 in the liquid phase and thus H_2 solubility in heavy feeds (9).

Therefore process conditions are optimised for H_2 consumption. For feeds with a high amount of coke precursors, high pressure hydrocracking needs to be used since it decreases coking; however it implies a higher capital investment (16). Refineries are processing heavier feeds, thus hydrocrackers and hydrotreaters have become central units of the plants (4).

Generally, downflow fixed bed reactors with multiple catalytic beds (five or six) are used. Moving bed and ebullated bed reactors are also used. Hydrogen is introduced in the system and in between catalytic beds to ensure exothermic reactions are quenched and to facilitate homogeneous temperature and mass flow of the fluid. Different process designs exist using one stage, two stage, once-through, and other configurations. No two hydrocracking units are the same because they are designed for a particular refinery. A general diagram of a hydrocracker is presented in Figure 2.5. The hydrocarbon feed gets preheated before entering the first reactor, where it is mixed with high pressure H_2. The hydrocarbons are cracked and hydrogenated and can continue into a second stage reactor, after which the pressure of the product stream is decreased before entering a fractionator. The heavier products are recirculated into the first and/or second reactor for further upgrading. H_2 is recycled from the products and fresh make-up H_2 is also used since the process works with H_2 excess.

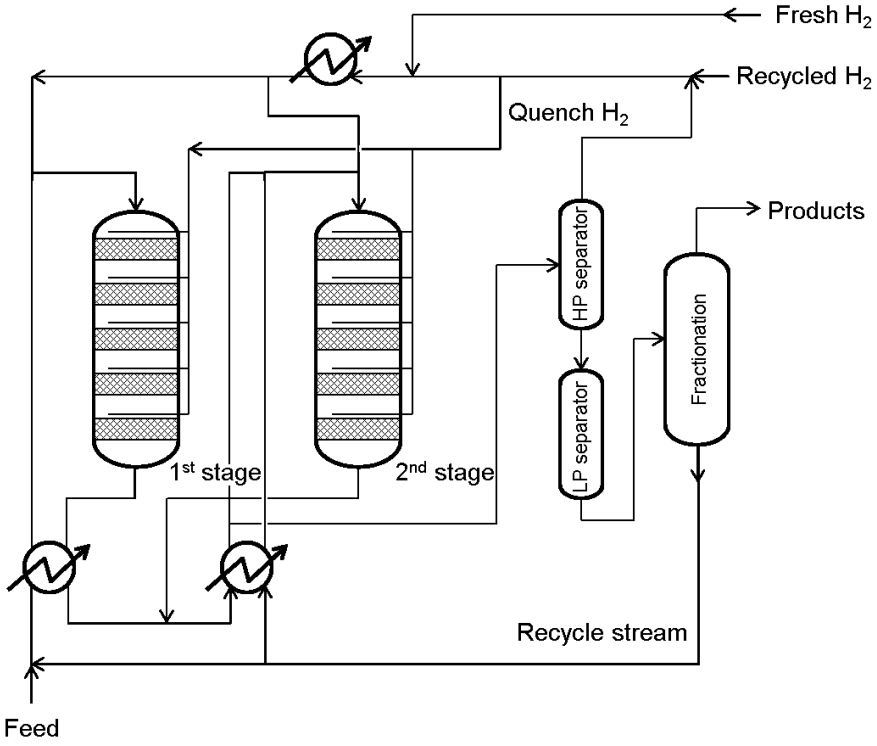

Figure 2.5. General diagram of a hydrocracker (17,18).

Hydrocracking units can have a preceding HDS, HDN, and/or HDM process unit or catalyst bed to remove heteroatoms in order to avoid their coming in contact with and poisoning the hydrocracking catalyst. When two reactor stages are employed, the first unit is designed for low cracking activity whilst the second stage employs a higher severity cracking catalyst (19). The catalysts properties are tailored to the feed composition, thus different catalysts are employed in the catalytic beds. For example, catalysts with larger pores that allow better contact with heavier feeds are used in the top beds whereas catalysts with smaller pores are used in the bottom ones (20). Detailed descriptions of hydrocracker design and unit parameters are available in the literature (9,21). The main licensors of hydrocrackers are the companies UOP, Chevron, IFP, Shell, Exxon, BP and Texaco. Industrial catalysts are offered by Advanced Refining Technologies (Chevron), AkzoNobel, Criterion, Haldor Topsøe, Axens/Procatalyse, and UOP.

2.4. HYDROCRACKING CATALYSTS

Hydrotreating and hydrocracking are fundamental processes in refineries, thus studies on catalysts are abundant. Catalysts for the two processes can have the same composition. This section details the composition of hydrocracking catalysts and also their synthesis methods.

2.4.1. Composition

Hydrocracking catalysts are bimodal because they perform two functions: cracking (carbon rejection) and hydrogenation-dehydrogenation (H_2 addition). The former takes place on acid sites –available usually in the support– and the latter on metal sites. Hydrocracking catalysts have evolved throughout the seven decades that the technology has been available along with process developments and different feed availability (21). The first catalysts consisted of pelletised tungsten sulfide and were followed by iron or nickel supported on montmorillonite or amorphous silica-alumina. After the 1960s, when hydrocracking was becoming commercially widespread, Ni or NiW on silica-alumina were the main catalysts utilised. By mid 1970s hydrocracking was an established technology and did not change dramatically until the 1990s, when demand for gasoline and distillates in the Middle East and Asia grew considerably. Catalysts changed as well, implementing better selectivity and activity and allowing for different product slates for seasonal demand. Catalysts supported on γ-Al_2O_3 which contained Mo or W promoted by Co or Ni have been used for decades. Zeolites were used because they had favourable characteristics over amorphous supports, mainly impacting product selectivity, as well as high acidity.

2.4.1.1. Metals

The standard composition for hydroprocessing catalysts is Mo (or W) promoted by Ni (or Co). Mo and Ni were chosen as active metals for this work because most of the studies on heavy oil hydrocracking used this metal combination and NiMo are more active with heavier feeds than CoMo catalysts (22). The active form of the catalyst is in sulfide form, with the formation of NiMoS structures. MoS_2 stacks, or slabs, have a hexagonal structure and promoters are located at the edges, corners or basal planes (23), as shown in Figure 2.6. Coordinated unsaturated sites (CUS) form on the corners and edges of the MoS_2 stacks. CUS create vacancies that can adsorb molecules with unpaired electrons from the feed (9). The formation of CUS has been known for decades (24,25), nevertheless studies on the formation and reactivity of the vacancies and edge sites continue to this day to design catalysts with higher activity and lower propensity to coking.

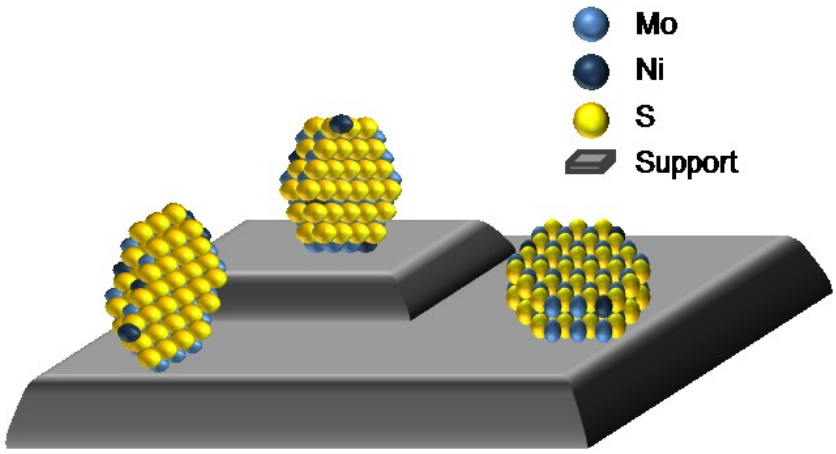

Figure 2.6. Representation of MoS_2 stacks promoted with Ni on a support (other states of Ni not shown) (26).

Recent advances in characterisation technology have provided well-defined images of how CUS form and react. Two examples are mentioned. High resolution transmission electron microscope (HRTEM) images of unsupported NiMo catalysts show how MoS_2 stacks are formed (27). It was observed that Ni introduces defects in the MoS_2 structure, thus creating more CUS. Work on how corner CUS react was obtained using atom-resolved scanning tunnelling microscopy (STM), which provided interesting images of how dibenzothiophene (DBT), a model structure used for HDS studies, adsorbs preferentially on the corner sites to react (28).

Since promoters increase the number of CUS by creating more edge and corner sites, their main effects can include activity enhancement, selectivity improvement, increased

catalyst lifetime, and neutralisation of acid sites (9). The promoter does not affect the metal sulfide size; it just increases its activity.

Dispersion of the active metals on the support is fundamental for their activity because it helps create more NiMoS species. During metal deposition a Mo monolayer is first formed on the support on which Ni particles deposit. An upper limit on metal loading is reached since metals can start agglomerating to form larger particles, with less CUS (29). It was reported that a monolayer of MoO_3 was formed with 4.6 atoms·nm^{-2} for alumina support (30), which would correspond to a 20 wt % loading for a support with a surface area of 120 m^2·g^{-1}. The concentration of metals on the catalysts varies by study, although upper limits of 20 wt % for MoO_3 were observed. Excessive metal content can lead to poor metal distribution and sintering, low metal content can diminish the hydrogenation function of the catalyst. The relationship between the Ni and Mo content in the catalysts is important; selected examples of Ni/(Ni+Mo) atomic ratios for different supports and reactions relevant for this study are shown in Table 2.2. An atomic ratio of Ni/(Ni+Mo) close to 0.3 corresponds to the Ni and Mo sulfides optimal synergy, by having the maximum ratio of Ni to Mo atoms in the slab to generate CUS (31–34).

Besides the Ni/(Ni+Mo) atomic ratio, the loading of metals relates to the number of active sites available on the catalyst. These sites need to be balanced with the cracking activity of the support. Optimal ratios exist as well for number of acid sites to number of hydrogenating sites, depending on the reaction and conditions (35).

Table 2.2. Ni and Mo loadings used in hydroprocessing catalysts.

Reaction	Ni / (Ni + Mo) atomic ratio	MoO_3 loading (wt %)	Support	Source
Thiophene HDS	0.24	n.a.*	unsupported	(36)
Phenanthrene hydrogenation	0.30	8.8-20.6	zeolites	(35)
Thiophene HDS	0.30	14.5	Al_2O_3	(37)
DBT HDS	0.33	< 15	γ-Al_2O_3	(38)
Bitumen upgrading	0.36	n.a.	unsupported	(39)
Thiophene HDS	0.38	8.3	P-Al_2O_3	(40)
n-heptane hydrocracking	0.50	8	zeolites	(41)

*Not applicable.

Noble metals have been used in hydrocracking catalysts, nevertheless noble metals can prove to be inferior to base metals because they are readily poisoned by sulfur. This is made evident by the fact that most commercial hydrocrackers employ base

metal catalysts (42). Furthermore, the higher capital costs of novel metal catalysts over base metal ones need to be considered along their deactivation rates.

2.4.1.2. Supports

Catalytic supports play important roles apart from cracking activity, such as structural support and metal dispersion. The diffusion of large hydrocarbons into the catalytic support is the rate limiting step in heavy oil hydrocracking (43,44). Small pores not only hinder asphaltene access but are also preferential sites for coke deposition (43), leading to pore blockage and surface area loss. Diffusional constraints and catalyst poisoning need to be balanced (20,45). Therefore properties such as pore volume, pore size distribution and –to a lesser extent– surface area (9), have to be taken into account during catalyst design. Structural properties are also important because the catalyst needs to withstand high pressures and temperatures without collapsing. The acidity of the catalyst affects the cracking severity; high cracking severity is selective for lighter naphtha whereas mild cracking activity maximizes middle distillates production. Thus several factors related to the feed and process conditions need to be taken into consideration when choosing a support. Hydroprocessing catalysts for heavy oils are predominantly supported on γ-Al_2O_3 as well as SiO_2-Al_2O_3 and zeolites (46). Mixtures of different oxides are also performed for optimal combinations for specific feeds and reactor configurations (47).

Even though zeolites have a high surface area, their small pore size diameter does not generally allow large hydrocarbon molecules to diffuse to the catalytic sites (48). Zeolites have a structured pore size; it has been proven that this arrangement is not favourable for hydrocracking reactions because shape-selective restraints are imposed on the heavier oil molecules (49). Extensive pre-cracking would have to take place in order for the larger molecules to diffuse into a zeolite-based catalyst. Pillared clays (PILC) have been explored as an alternative catalytic support to zeolites because of their similar properties but larger pores (50–52). PILC are prepared by inserting metal ions between the clay layers that gives structural stability to the clay and creates a gap between the layers and therefore can increase porosity. PILC were used for thiophene HDS (51) and decane hydrocracking (53). Nevertheless, PILC pores are still small to allow access for heavier hydrocarbons (54).

In this thesis different materials were synthesised and used as catalytic support: mesoporous alumina, alumina doped with chromium, mesoporous silica alumina and carbon nanofibres. Given that the materials differ between each other, a description of

the state of the art regarding each one is included in the corresponding chapter where the support is used.

2.4.2. Synthesis

The method employed for metal loading on the support has effects on the catalyst final properties. For example, the metal loading, the metal/promoter ratio, and the particle shape and size of the metal crystals in the support can differ depending on the synthesis conditions (55). There are many methods described in the literature (21,56–59) to synthesise catalysts. A description of the method used throughout this work, incipient wetness, is provided. This procedure is employed in industry as a continuous process. In the incipient wetness technique, the metal active phase is added in a solution to the dry powdered support which allows for a controlled addition of metals (56). The pore volume and surface area of the support determine the volume of solution that can be adsorbed, what is experimentally described as “wettability”. An appropriate solvent needs to have high solubility for the metal salts and at the same time provide diffusion in the pores of the support (60). Water is generally used as solvent. The addition of metals is controlled but is limited by the metal compounds solubility in the solvent, thus intermediate drying steps can be performed between impregnations to achieve the desired loading. Intermediate drying steps are also employed when loading different metals, since the previously impregnated metal can be allowed to first adsorb on the support (21,57). The order of addition of the metals impacts the morphology and the metal loading of the catalyst (44,55,61). In this work Mo was first loaded on the support since a layer of Mo is needed to then obtain promotion by Ni. Catalyst are usually dried and calcined after metal impregnation. The former step is performed to eliminate the solvent and the latter as a thermal treatment to form the oxide form of the metals (56).

Chelating agents have been used in aqueous solution when adding metals to the support by incipient wetness (62). Different effects have been attributed to chelating agents, such as the formation of polymolybdate species that are easier to reduce to MoS_2 (63), less interaction with the support to create higher MoS_2 stacking (64), better promotion of Co on Mo (65), and the complete sulfidation of Mo that creates active NiMoS species (66). In this work diethylenetriamine (DETA) was chosen as chelating agent (67,68). Advantages of the removal of the chelating agent by calcination are mixed (63).

The final step in catalyst synthesis consists in the sulfidation of the catalyst to convert the metal oxides into the active metal sulfides. Sulfidation methods are classified as in-

situ or ex-situ. In situ sulfiding takes place inside the reactor, where added sulfur is converted to H_2S at high temperature and pressure. H_2S then reacts with the metal oxides to form metal sulfides. Sulfur sources can be a sulfur-containing liquid or gas such as a mixture of H_2/H_2S, CS_2/H_2 (69), or dimethyldisulfide (DMDS) and H_2 (70). In ex situ sulfiding the catalyst is contacted with sulfur-containing species prior to reactor loading. A stoichiometric amount of sulfur is added to convert all the metal oxides to metal sulfides. There are two main commercial processes that do this, the sulfiCAT and actiCAT (20).

2.5. HYDROCRACKING REACTION

2.5.1. Mechanism

The mechanisms of thermal and catalytic cracking have been studied since the 1950's (47,71). The balance between cracking and hydrogenation activity has been considered as the basis for bifunctional catalysts (72). Hydrocracking studies started, understandably, with model compounds such as paraffins (73). Figure 2.7 shows the hydrocracking reaction mechanism for paraffins. Metal sites catalyse the dehydrogenation of paraffins into olefins after which the creation of carbenium ion intermediates takes place in acid sites. Then hydrogenation into cracked or isomerised products occurs on metal sites. The different pathways change depending on the balance between metal and acid sites (74). As a catalyst remains in operation, this balance changes because of deactivation and poisoning which does not occur uniformly on the acid and metal sites. H_2 partial pressure plays an important role in the reaction selectivity, as it affects the concentration of olefins that serve as intermediates (74). Temperature, or severity, is usually increased with time to maintain the desired activity. At higher temperatures thermal cracking starts to compete with catalytic cracking and at a certain temperature thermal reactions determine the cracking rate of the hydrocarbons (75). It was proposed afterwards that an interrelationship between metal and acid sites is involved in the reaction mechanism and therefore considering specific functions for each active site would be an oversimplification (18). Moreover, H_2S present in the system, from either excess sulfur for catalyst in-situ sulfidation or HDS reactions, also promote hydrogenation of cracked compounds (hydrogenolysis) (76).

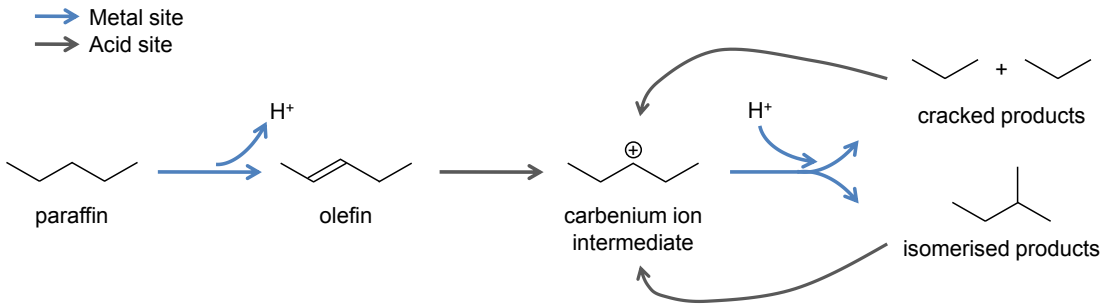

Figure 2.7. Representation of paraffin hydrocracking reaction mechanism (77–79).

The complexity of the hydrocracking reaction mechanism increases along with the complexity of the feed. The mechanism for bitumen coking and hydrocracking is shown in Figure 2.8 (15,80–82). In this case, residue is considered as a compacted core of aromatic and naphthenic rings as well as heteroatoms, where most of the aliphatic side chains were previously removed. Initial thermal cracking reactions target carbons linking aromatic and naphthenic rings (in red). Thus radicals, aromatic and aliphatic, are formed. If H_2 were not available, aromatic radicals polymerise with another radicals, forming larger PAH and eventually coke. The catalytic reaction pathway consists of hydrogenation of a heteroatom ring (in blue) which would in turn thermally decompose into distillates. When a hydrogenation reaction takes place, naphthenic rings convert to gas and aromatic rings to distillates. Catalysts accelerate the reaction with H_2. Coke can also be formed by catalytic dehydrogenation reactions. Reaction mechanisms for heavy oil have been postulated (83) with the formation of carbenium ions considered in asphaltene hydrogenation. The rupture of links between aromatic rings and aliphatic carbons as well as the hydrogenation of aromatic rings in asphaltenes is considered to take place in the catalyst acid sites.

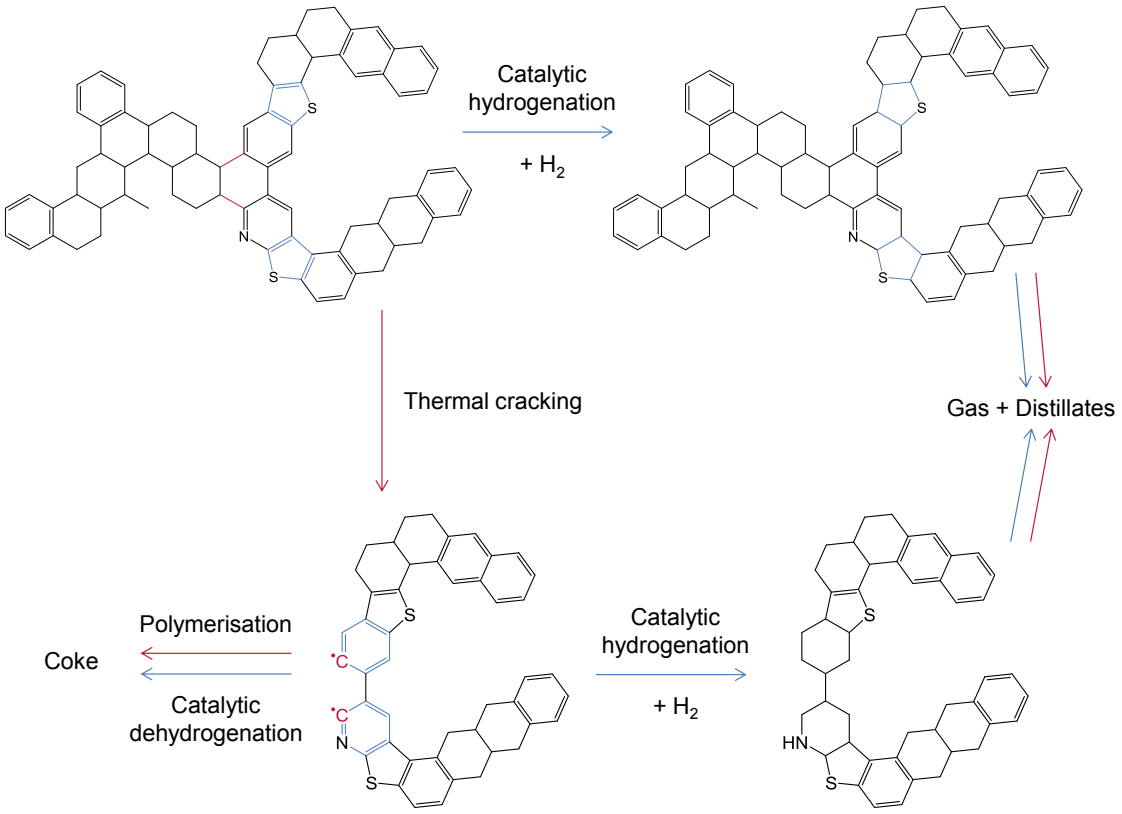

Figure 2.8. Representation of heavy oil hydrocracking reaction mechanism (15,80–82).

Even though the specific mechanism for heavy oil hydrocracking is not precisely known, the cracking propensity of different bonds was investigated (12) and is shown in Figure 2.9. Carbons have a cracking propensity in the following order: aliphatic chains (red) > naphthenic rings (yellow) > heteroatoms (blue and grey) (12). Thus it appears that gas formation is related to the number of aliphatic chains present in the oil as well as the content of naphthenic rings (15). A higher gas production is observed when no catalysts are used, showing that catalytic hydrogenation saturates radicals and carbenium ions that would otherwise undergo further thermal cracking (84). In multi-ring PAH systems the hydrogenation first takes place at a fast rate but the rate of reaction progressively slows down for the last remaining aromatic rings, thus saturated outer rings are easier to crack than central rings (18). This makes the conversion of compounds with many condensed aromatic rings unfavourable. High H_2 partial pressures and temperatures can facilitate the saturation of PAH rings.

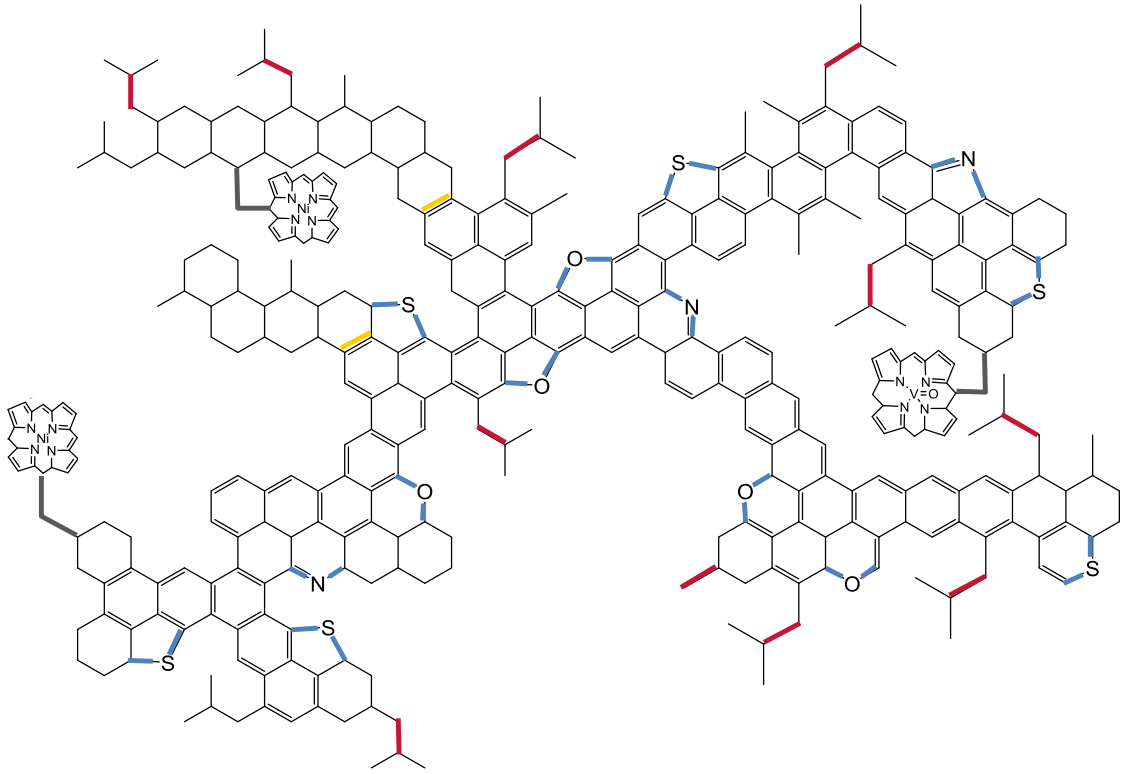

Figure 2.9. Different cracking propensity for aliphatic chains (red) > naphthenic rings (yellow) > heteroatoms (blue and grey) in a Maya asphaltene (12).

Since catalysts mainly act in H_2 transfer (85), it was observed that polymerisation reactions (coke) are diminished while heteroatom removal is increased due to termination reactions by hydrogenation. If H_2 is not available, polymerisation of carbenium ions or free radicals generated in the cracking reactions would supersede hydrogenolysis. Catalyst activity is not considered constant since the catalyst is deactivated by coke deposits, nevertheless hydrocracking reactions continue despite coke formation (80). A study that used alumina (without metal sites) as a catalyst obtained residue conversion, nevertheless severe coking occurred to the extent that the experiment had to be terminated (85).

The mechanisms for HDS and HDM reactions have also been described in the literature (6,83,86). HDS reactions have been studied extensively with model compounds such as thiophene structures (36–38,40). NiMo catalysts had better HDS performance for heavy oil fractions than CoMo catalysts (22). The dispersion of metal sites on catalysts was determinant on the HDS and HDM rates for Maya crude (87). Catalysts with smaller pores (<10 nm) yielded higher HDS conversion whereas larger pores were better suited for HDM reactions (15-20 nm) (88).

The development of kinetic models of heavy oil hydrocracking is not straightforward due to the complexity of the feeds (89). Therefore, different approaches have been reported

for kinetic modelling of hydrocracking of heavy oils, although the most common and used method is the lumping technique (69,90–93). The lumping technique consists of grouping species present in the process based on shared characteristics, such as boiling point, functional group, chain length, molecular weight, polarisability or polarity (91). The discrete lumping method is a traditional approach that groups species by boiling points that cover the whole range of the system; the groups are then linked to one another through reaction pathways. This approach has been used extensively to model hydrotreating and hydrocracking reactions (69,91,94,95).

2.5.2. Influence of catalyst and process conditions

Diffusion into catalytic sites is the rate limiting step for heavy oil hydroprocessing, as was mentioned previously. This property is dependent on the catalyst textural properties in relation to the feed, especially for heavy hydrocarbons. Therefore not only the cracking and hydrogenating ability of the material needs to be considered but also the support pore architecture. Several studies have been published in this area. Hydrocracking of preasphaltene (benzene insoluble) and asphaltene fractions of different coal extracts was performed with catalysts with different median pore sizes, from 12 to 73 nm (44,61). The overall yield of oil was not affected by changes in the catalyst pore sizes but the conversion of asphaltenes was influenced by pore size. An optimal pore size was found for asphaltene conversion depending on the feed, although usually larger pores facilitated asphaltene upgrading. In a different work (96) on AR and VR hydrocracking, activity was lower when using a CoMo/silica-alumina catalyst with pore size of 3 nm than when using a CoMo/alumina with larger pores. NiMo/alumina catalysts with pores between 10 and 20 nm proved better at hydrocracking VR (97). The CoMo/alumina catalysts with larger pore sizes also obtained better conversion of the asphaltene fraction than others with smaller pores (88). Thus the design of catalysts is tailored to a specific feed while considering a) cracking activity, which should balance desired cracking with undesired coking reactions, and b) pore structure, which permits diffusion of hydrocarbon molecules into active sites (98).

Thermal cracking, affected by temperature, is an important factor in heavy feed processing since it may supersede catalytic cracking (83). The contribution of thermal effects on residue upgrading needs to be taken into consideration when operating temperature is above 415 °C for AR (99). The conversion of heavy fractions containing coke precursors above 425 °C can be dominated by thermal cracking (100). Thus

asphaltene upgrading is obtained by simultaneous thermal and catalytic conversion (9). The formation of gases is also related to reaction temperature (69).

2.6. CATALYST DEACTIVATION

2.6.1. Introduction

Catalyst deactivation needs to be taken into account since it dictates the life cycle for commercial operation of a hydrocracker (16). The main causes of hydrocracking catalyst deactivation are coke and metal deposits as well as poisoning caused by heteroatoms, Ni, V and Fe. The definition of coke depends on the study; it usually encompasses the non-volatile carbonaceous deposits that adsorb on the catalyst (101). Metals, present as porphyrins in the feedstock, selectively deposit on active sites of the catalyst. Coke deposits occur mainly at the beginning of reaction whereas metals accumulate on the catalysts over time, as shown in Figure 2.10. A first stage in which rapid coke deposition causes loss in activity is followed by gradual accumulation of metals. Operating temperature is usually increased with time to maintain the activity but no additional significant coking takes place (102). Activity is maintained until finally pores are blocked and catalytic activity is lost.

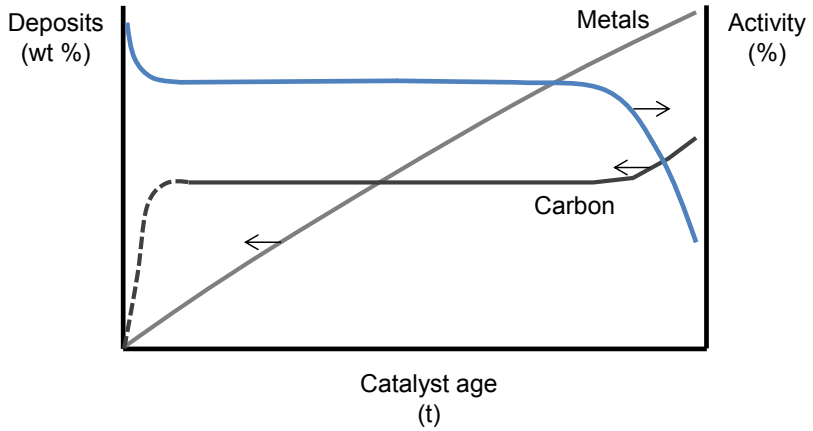

Figure 2.10. Metal and carbon deposits as a function of catalyst age and activity (103).

Catalyst poisoning can take place with organic species, Ni, V, and Fe. High S or N content in the feeds can cause the heteroatoms to adsorb on the catalysts. Sulfur poisons metal active sites whereas nitrogen poisons the acid function (45). The degree of metal and heteroatom poisoning depends on the feed properties so guard reactors with HDS, HDN, or HDM catalysts are often used before a hydrocracker (104). For example when metals in the feed exceed 50 ppm a triple catalyst system with high metal storage capacity HDM catalysts are needed (105). Metal and heteroatom deposition capacity depends on the catalyst pore structure; larger surface area and

porosity can withstand more poisoning (70). Catalysts used to process heavy feeds must have storage capacity for metals and consider deactivation by heteroatoms such as S and N (9). Maya crude contains a high amount of metals (Ni + V > 300 ppm) so special considerations have to be taken when working with it. Many studies have been done on the topic, mainly from Ancheyta et al. (102,104,106,107).

At longer reaction times other changes which are observed include sintering of active sites, which is the formation of larger crystallites, having less CUS, migration of the active sites and pore size collapse, at which point the hydrogenation and metal functions are lost (9). Sintering of metal sites are for the most part irreversible, causing permanent loss of activity (105). Since sintering causes the activity of the system to rapidly decrease, the reaction needs to be terminated.

2.6.2. Coke deposition on catalysts

This work focuses on the short-term deactivation of catalysts thus emphasis is placed on coke formation instead of metal deposition. The nature of coke deposits depends on the interrelationship between operating conditions, hydrocarbon feedstock and catalyst. This section will first cover coke formation and process conditions, then describe how the feed properties influence coke formation and finally detail the relationship between coke deposits and catalyst properties.

2.6.2.1. The nature of coke

Figure 2.11 shows how coke deposits on the catalyst by adsorbing preferentially to the support (acid sites). As can be observed, the hydrogenating function of the sulfided metal crystallites clears the immediate zone from coke deposits (108). Moreover, coke forms as a monolayer of consistent thickness over the support. These deposits cover active sites of the catalysts and therefore reduce its activity (98). It is considered that coke forms preferentially on the acid sites because of basic N molecules present in asphaltenes. Over time, as coke deposits neutralise the acidity of the support, coke deposits are reduced. If neutral supports such as carbon are used, less coke deposits are expected (9).

Even though coke mainly forms during initial reaction stages, it undergoes transformations throughout operation becoming more aromatic (109,110). Reversibly adsorbed aromatics and asphaltenes first form (soft or bulk coke) and then transition into irreversibly adsorbed condensed aromatic clusters (hard or refractory coke) (111). Soft coke can be soluble in toluene and has a higher H/C ratio than hard coke (112). Refractory coke forms on the acid sites (113). In a study (109) using a Mo/Al_2O_3

catalyst to hydroprocess AR, changes in the nature of the coke were observed in a 240 hr experiment. Coke deposits were mainly formed in the first 15 hours although additional coke formation continued until the end of the run. With time the coke became more aromatic in nature and had a larger concentration of S and N heteroatoms than in the initial soft coke.

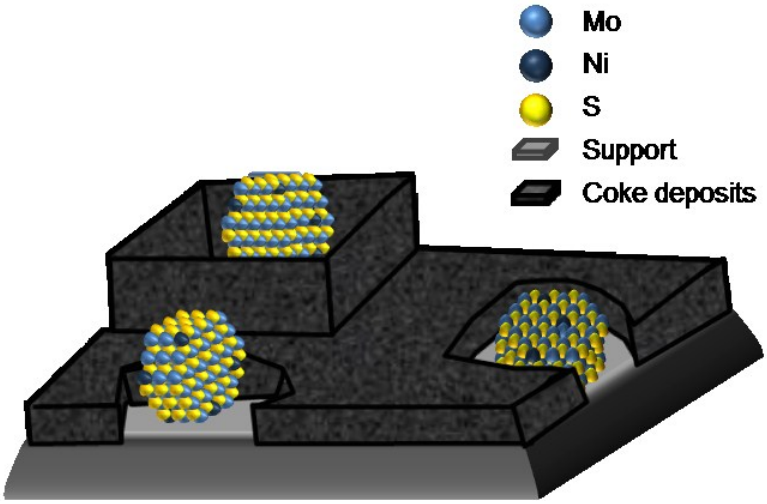

Figure 2.11. Representation of coke deposition on a catalyst (26,108).

Sediments referred to as “sludge” are formed from asphaltene deposits when these are no longer soluble in the aromatic or saturates fractions (114). This phenomenon needs to be avoided during hydroprocessing reactions, thus ideally the catalyst converts a proportion of asphaltenes and resins so that the former remains in solution.

Coke deposition is lower at short contact time reactions whereas at long contact times the higher concentration of coke precursors in the system cause higher coke deposits (115). It was found that in a batch system coke deposition was higher at lower temperatures because coke precursors were not being thermally cracked and thus accumulated in the system and catalyst (116). Conversely, in continuous systems the concentration of coke precursors is constant and therefore higher coke deposits are observed when increasing process severity (117). At high temperatures (410-550 °C) cracking reactions are thermodynamically favoured (82).

Hydrogen partial pressure plays an important role in preventing catalyst deactivation by coke deposits (9,118,119). Higher H_2 solubility in the oil phase helps coke precursors to hydrogenate into liquid products instead of polymerising into coke (Figure 2.8).

2.6.2.2. Influence of feed properties on coke deposition

Studies on heavy oil hydroprocessing have focused on the coke-forming propensity of heavy feeds (102,104,120,121). Since heavier feeds tend to have larger shares of coke

precursors, catalysts deactivate rapidly and are utilised for shorter times than when using lighter feeds (122). Catalyst cycles can be less than one year for residues and heavy feeds whereas cycles for naphtha hydrotreating catalytic activity can be sustained for more than five years.

Heavy feeds generate more coke deposits than lighter feeds because of the higher content of coke precursors, such as asphaltenes (101,123). Nevertheless, not only the concentration of asphaltenes is important but also their structure. More aromatic asphaltenes will yield higher coke deposits than less aromatic asphaltenes (9). It was found that coke deposits were higher for hydrotreated AR (HDS and/or HDM) than for the straight-run AR (121). The feed that was previously hydrotreated and thus had been thermally converted to a certain extent, yielding larger aromatic structures. These in turn produced higher coke deposits than a straight-run AR. Since the adsorption of asphaltenes on the catalyst is mainly responsible for initial coking rates, the coke formation from VR asphaltenes was found to occur rapidly (98). Thus higher coke deposits can be expected with VR. Coke deposits of 10 to 20 wt % of the catalyst can occur when processing heavy feeds such as Maya crude (88,100,104).

2.6.2.3. Influence of catalyst properties on coke deposits

Catalytic properties such as acidity and textural properties such as pore size distribution are related to coke deposition. The acidity of the catalyst promotes cracking reactions which yield higher coke deposits (98). When processing the same feed, AR, the catalyst with higher acidity obtained higher coke deposits (121). As mentioned previously, the size of asphaltene molecules has been a topic of debate; a range from 2-80 nm has been detected with different characterisation methods (123), although most studies consider asphaltene size to be below 10 nm. Thus catalysts would need pores that allow the diffusion of these large molecules.

Textural properties need to be tailored to the feed, especially when using heavy oils. The optimal pore size for which the activity loss is minimal needs to be found during catalyst design (105). The distribution of coke deposits on the support affects how pores are plugged. The comparison of spent catalysts with small pores and large pores show that small pores are susceptible to pore mouth plugging whereas larger pores can accommodate more coke without plugging (88). The reduction of surface area, pore volume and median pore diameter was found to be related to the content of carbon deposits (101). The decrease in pore volume for spent catalysts was found to be proportional to the amount of coke deposits (124). Large molecules have difficulties diffusing into pores below 2 nm, therefore these pores often do not undergo pore mouth

plugging (108). Pores larger than 10 nm had a smaller impact from coke deposits than smaller pores, which had reductions in pore size and pore volume even in short 1 hr contact time reactions (61). Conversely, an increase in average pore diameter for spent catalysts was observed and explained by coverage of the smallest pores with coke deposits (107,111). A deposition of 25 wt % coke on catalyst corresponded to a 60% reduction in surface area (119).

The pore architecture also differentiates the catalyst. For example cylindrical pores can have pore mouth plugging that turns them into ink-bottle type pores (87). Ink-bottle pores have strong steric hindrance issues for heavy hydrocarbons.

Independent from the catalyst textural properties, Ni and Mo particles also undergo changes during deactivation. The Ni particles migrate from Mo stacks, thus reducing the catalyst activity (27). Larger Ni crystals can form and MoS_2 stacks grow, lowering the activity of the CUS (122). The migration and segregation of metals is higher with more severe operating temperatures (124).

Operating conditions influence the changes in pore volume and surface area of fresh and spent catalysts (70). Catalysts generally have a faster deactivation rate if more severe conditions are employed.

2.6.3. Catalyst regeneration

Some of the changes that catalysts undergo during reaction are reversible. Thus catalysts are removed from the reactor and regenerated after their activity decreases to a certain extent so that they can be reused for another operating cycle (122). Regeneration usually involves the removal of coke deposits and some heteroatoms by combustion in a diluted oxygen or air stream at temperatures between 400 and 500 °C. Industrial catalysts are used in several operation-regeneration cycles. Regeneration can partially or totally restore catalytic activity; when properties are completely affected the catalyst is no longer used (125). The net amount of active metals in the catalyst decreases in each cycle and can agglomerate, but catalysts can still remain active for several regeneration cycles. Sulfur and nitrogen heteroatoms can be removed as well during regeneration, but metal deposition of poisons like Ni or V is irreversible and therefore is not eliminated by regenerative oxidation (21). Soft coke can be removed from the catalyst because it is adsorbed in the surface, but refractory coke cannot be removed and starts accumulating in regenerated catalysts.

2.7. ANALYTICAL TECHNIQUES

A brief description of the analytical techniques employed throughout this work is provided in this section.

2.7.1. Catalyst characterisation

Supports as well as fresh and spent catalysts were characterised by several techniques to evaluate their properties. Textural properties were obtained with N_2 adsorption, the crystallinity of the sample was analysed by X-Ray diffraction (XRD) and elemental composition was determined with X-Ray fluorescence (XRF). Different temperature-dependent analysis were used such as temperature programmed desorption (TPD), ammonia-TPD, temperature programmed oxidation (TPO) and temperature programmed reduction (TPR). These techniques were used to obtain information about the type of oxygenated groups, acidity and reducibility of metal sites. Scanning electron microscopy (SEM) was used to observe the morphology of the materials and when used in conjunction with energy dispersive X-Ray spectroscopy (EDX) the dispersion of metals and carbon deposits were evaluated. Transmission electron microscopy (TEM) was used to visualise alumina support morphology as well as catalysts before and after reactions to observe the effects of carbon deposition. TEM was also employed to analyse the shape of catalysts supported on carbon nanofibres.

2.7.1.1. N_2 adsorption

The texture of a material is defined as the detailed geometry inside pores of a particle (126). The texture of porous solids is determined by three variables which are superficial area, particle size and porosity. With these parameters, textural properties such as total pore volume, shape and size of pores, and pore size distribution is obtained. Pore sizes are classified by IUPAC (127) depending on their diameter in the following categories: micropores (< 2 nm), mesopores (2 to 50 nm) and macropores (> 50 nm) as shown in Figure 2.12. Different characterisation techniques exist to analyse textural properties such as gas adsorption and mercury porosimetry; depending on the nature of the material a technique is better suited than another.

In this work N_2 adsorption was employed given that the catalysts and supports had pores mostly in the mesopore range. N_2 is a gas commonly used for this analysis because it is inert and the area that the molecule takes is constant and independent of the material analysed. Nitrogen is introduced into the material at isothermal conditions (-196 °C) and pressure of the gas is allowed to equilibrate. This allows N_2 to adsorb to the surface of the analysed material, which results in a decrease in N_2 pressure. N_2

partial pressure is incremented and different points, corresponding to an amount of adsorbed N_2, are taken, thus creating an adsorption isotherm. Afterwards N_2 partial pressure is decreased and the pressure of the system is allowed to stabilise. The points taken during N_2 partial pressure decrease create the desorption isotherm.

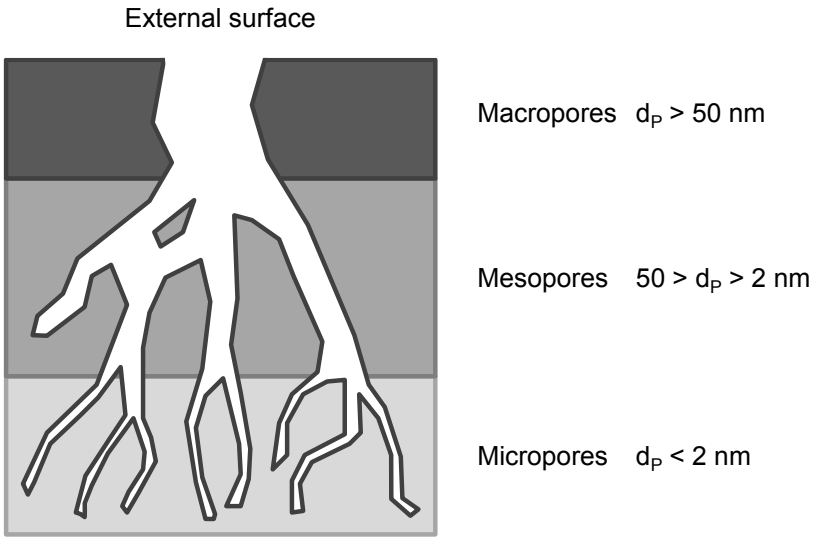

Figure 2.12. Representation of a material with macro, meso and micropores.

The study of isotherms gives information for most of the textural properties of the material, such as surface area, pore volume, pore size distribution and pore architecture. Isotherms were classified by Sing et al. (126) into six types (I-VI), as shown in Figure 2.13a. Type I isotherm represents the existence of chemisorption, adsorption in micropores, adsorption in dissolution or physisorption in homogeneous surfaces. Type II isotherms correspond to adsorption in mono and multilayers, non-porous solids or macropores which have superficial heterogeneity. Type III isotherm occurs when the adsorption between adsorbate-adsorbant is weak. Type IV isotherm is similar to Type II isotherm at low relative pressures but at medium pressures capillary condensation occurs in the mesopores. This isotherm presents a hysteresis loop, which occurs when the amount of adsorbed gas does not coincide with increasing pressure than with decreasing pressure. This is observed because the pores trap the gas, referred to as capillary condensation. Type V isotherm is very rare and difficult to interpret. It corresponds to weak adsorption at low pressures followed by capillary condensation. Finally Type VI isotherm is observed for homogeneous surfaces where a adsorbate layer is formed after the previous one is completed. Each layer forms in a pressure range, thus each step corresponds to a layer.

Hysteresis loops are formed by differences between N_2 uptake in the adsorption and desorption isotherms, adding information about the type of pores present in the

material. Figure 2.13b shows the classification of hysteresis loops. Hysteresis loops transition from type H1, which has vertical and parallel branches, to H4 which has horizontal and parallel branches at most relative pressure values. Types H2 and H3 are thus intermediates. Type H1 corresponds to materials with narrow pore size distribution, Type H2 loops are difficult to interpret because they are observed in materials without a defined pore size distribution. In Type H3 no adsorption limit is observed and corresponds to materials formed by plate-like particles. Type H4 is observed for materials with narrow slit-like pores.

The adsorption-desorption isotherms are commonly interpreted with the Brunauer, Emmet and Teller (BET) method which calculates the monolayer of N_2 adsorbed on the surface of the material and the multilayers of N_2 formed thereafter. With the BET method the surface area, hereafter referred to as S_{BET}, is obtained. The BET equation can be used in this work given the absence of microporosity in the materials. The Barret, Joyner and Halenda (BJH) method calculates the pressure at which N_2 condensation will occur in cylindrical pores covered with multilayers of N_2. The BJH method was used to calculate the pore size of the materials.

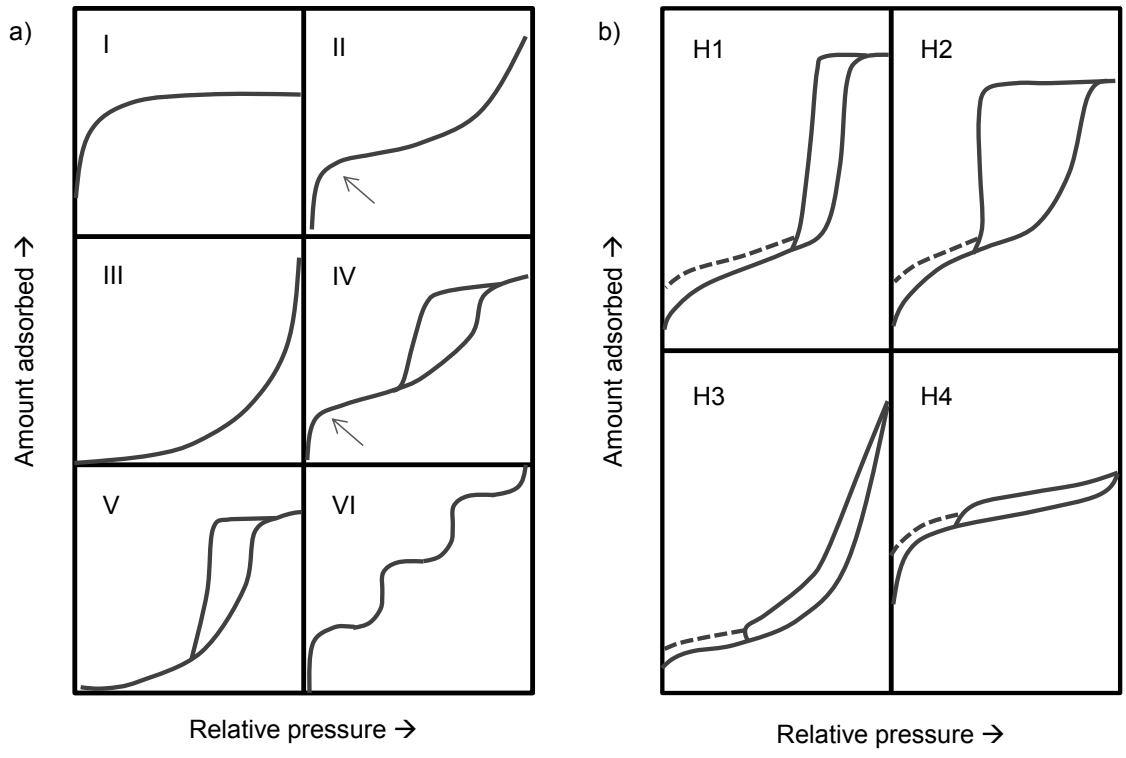

Figure 2.13. Types of physisorption isotherms (a) and types of hysteresis loops (b) (126).

2.7.1.2. X-Ray Diffraction and X-Ray fluorescence

X-Ray studies are non-destructive techniques which employ an X-Ray beam to diffract or interact with electrons of the sample. XRD provides information on the crystallinity of the sample and can identify the sample composition, crystallite size and unit cell size. A beam of radiation with a specific wavelength (λ) is directed at a sample at a specified angle (2θ). The reflected beam from the sample is detected and the interplanar distances (d) of the sample are determined using Bragg's law. In Figure 2.14 a schematic of XRD is shown. Each crystalline material has a characteristic XRD pattern, thus reflections are found in the samples XRD pattern and the presence of crystalline materials is detected.

In X-Ray fluorescence the sample is bombarded with X-Ray photons which eject electrons from the sample atoms, as shown in Figure 2.15. This creates electron vacancies which are filled by electrons from a higher energy level, emitting photons. The radiation is first dispersed using crystals and then detected, producing a plot where elements can be identified because each one fluoresces at a specific energy. The intensity of the signal is correlated to the concentration of each element; therefore a quantitative elemental analysis is performed.

θ: angle of incidence on the crystal
d: spacing of atomic layers parallel to the crystal surface

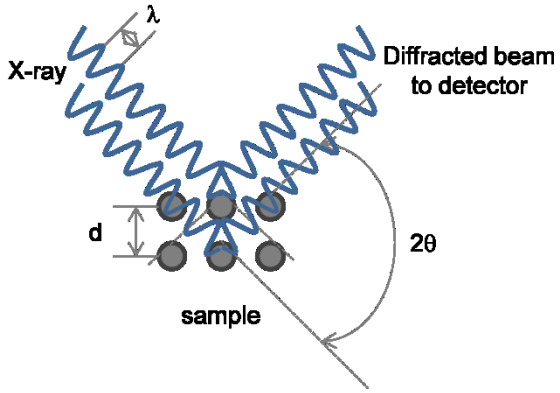

Figure 2.14. Representation of XRD technique.

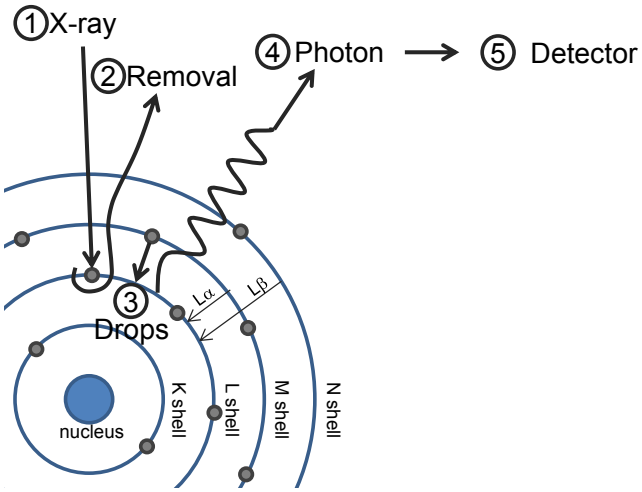

Figure 2.15. Representation of XRF technique.

2.7.1.3. Temperature dependent analyses

In temperature programmed desorption, the thermal decomposition of carbonaceous materials of a sample is measured in terms of CO and CO_2 with a mass spectrometre. This gives information of the types of functional groups available on the surface of the sample because different groups decompose at different temperatures. It was used to analyse carbon nanofibres.

The acidity of the materials was studied with NH_3-TPD because ammonia is a strong base that has very low steric hindrance when interacting physically or chemically with a material through its OH species. In this analysis NH_3 is added to the sample and then temperature is increased to observe NH_3 desorption. At first weakly physisorbed NH_3 is desorbed, followed by strongly chemisorbed NH_3. Weak acidity corresponds to low NH_3 desorption temperatures whereas strong acidity corresponds to high NH_3 desorption temperatures. Acid sites can be defined as weak, medium and strong, with NH_3 desorbing temperatures of <200 °C, 200–400 °C and >400 °C respectively (128). The NH_3-TPD curves are integrated by temperature intervals to determine the amount of acid sites by type.

TPO is performed to evaluate the degree of ordering in carbonaceous materials because graphitic carbons (highly ordered) combust at higher temperatures than amorphous ones. TPO was used to evaluate functional groups in functionalised carbon nanofibres.

During TPR the sample is heated in a reducing environment (H_2) and thermal conductivity of the gas stream is used to measure the disappearance of the reducing agent (H_2). Thus H_2 concentration is proportional to the rate of catalyst reduction. The

reduced species can be identified and metal-metal and metal-support interactions are observed.

2.7.2. Hydrocarbon analyses

Hydrocarbons were analysed by size exclusion chromatography (SEC), ultraviolet fluorescence (UV-F) spectroscopy and inductively coupled plasma spectroscopy (ICP).

2.7.2.1. Size exclusion chromatography

SEC is used to analyse molecular weight distribution of the samples. Molecules elute according to their hydrodynamic volume which is related to their molecular size with a calibration curve. A low concentration solution dissolved in a solvent, used as the eluent, is injected into a packed column. Larger molecules cannot enter the pores of the packing and thus elute rapidly. In contrast, smaller molecules can access more pores and have longer paths, therefore taking longer time to elute. If the molecules are too large to enter the column porosity they are “excluded”, thus a peak at short elution time appears. After the excluded peak a valley can be present which signifies a change in molecular conformation (129), after which a second peak of the molecules that could enter the porosity appears. The second peak is called “retained”. Thus samples that have broad molecular size distribution present a bimodal distribution with an excluded peak, for molecules with a large three dimensional configuration, and a retained peak. A relative measure of molecular mass is obtained by elaborating a calibration curve with standards. This method is useful to determine molecular size distribution for asphaltenes (11) and has been used in the research group extensively (13,129,130).

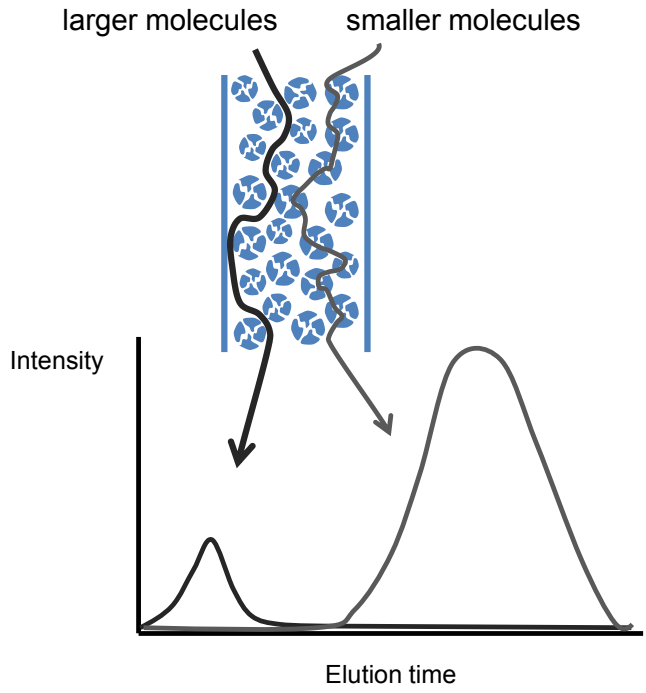

Figure 2.16. Schematic of SEC principle.

2.7.2.2. Ultraviolet-fluorescence spectroscopy

Ultraviolet-fluorescence spectroscopy is used to obtain information of the aromatic ring structure of oil samples (11). A shift to longer wavelengths occurs with increasing conjugation of the aromatic rings (131). The synchronous UV-F spectra of a complex mixture of aromatics will have contributions from all species and thus definite aromatic structures cannot be determined. However, it has proven useful to compare relative size of PAH groups.

2.7.2.3. Inductively coupled plasma spectroscopy

Samples are first digested to homogenise them and to be able to vaporise them. Digested samples are vaporised into a stream of argon plasma produced by a magnetic field with an inductively coupled coil. The atomised compounds in the sample are thermally excited, releasing photons which are detected with an emission spectrometre (OES). Each element has a specific radiation wavelength, thus elemental composition is obtained. The intensity of the measurement is correlated with the elemental concentration by using calibration standards.

Chapter 3: Experimental

In the present study, catalysts were developed and then tested in batch hydrocracking experiments to evaluate their effectiveness in upgrading a vacuum residue. Two independent experimental procedures were developed: catalyst synthesis and hydrocracking experiments. Consequently, this chapter will be divided into these two sections. Section 3.1 explains the synthesis techniques and materials characterisation which are common to different chapters. Independently, each results chapter contains an experimental section focusing on the synthesis of the catalytic supports. Section 3.2 elaborates on the reaction system that was employed, explains why reaction conditions were chosen, and how the experimental data was analysed. It concludes with the description of the characterisation techniques for hydrocarbon products.

All reactants employed in this work were obtained from Sigma Aldrich unless specified otherwise. Gas cylinders were sourced from BOC.

3.1. CATALYSTS

3.1.1. Synthesis

Hydrocracking catalysts are classified as bifunctional because they perform two actions: hydrogenation/dehydrogenation and cracking. All catalysts developed for this work had the same metals, Mo promoted by Ni, a standard combination for this process (9,132). On the other hand, four different catalytic supports were designed and prepared: mesoporous alumina, mesoporous alumina doped with Cr, mesoporous silica alumina and finally carbon nanofibres. Given that each support differs greatly from the others, for clarity purposes the synthesis and characterisation will be included in the relevant chapters where the material is applicable. The only support that is common to several chapters is mesoporous alumina; yet Chapter 4 describes the synthesis of the alumina to obtain materials with different pore sizes and Chapter 5 deals with different metal concentration.

The method of impregnation for metals Ni and Mo employed for all supports was incipient wetness. Since the metal content and synthesis conditions varied depending on the support, the metal impregnation procedure is reported in each chapter as well.

3.1.2. Characterisation techniques

Supports and catalysts were analysed by various techniques, detailed in this section. The techniques were available in three different facilities: Imperial College in London, UK, the Mexican Petroleum Institute in Mexico City, Mexico, and the Carbochemistry Institute in Zaragoza, Spain.

Spent catalysts were also characterised by thermogravimetric analysis (TGA) to determine coke deposits, but as this analysis pertains to reaction product hydrocarbons it is reported in Section 3.2.2.

3.1.2.1. X-Ray Fluorescence

Elemental analyses with energy dispersive X-Ray Fluorescence were performed with a Bruker XRF-S2 Ranger with a Cu source at the IMP.

The equipment was tested with different oxide concentrations for Mo/Al_2O_3 and Ni/Al_2O_3 catalysts, as shown in Figure 3.1a and b, respectively. The Mo/Al_2O_3 catalysts were designed with different concentrations covering the range that was expected for this project. The Mo plot shows that the MoO_3 target concentrations are very close to the measurement provided with XRF. A straight line was added as a trendline for the data and its slope was very close to 1.0, therefore it was determined that this technique could be employed for elemental analysis of Mo. Additionally, two Ni/Al_2O_3 catalysts with different concentration were measured three times, which proved the technique consistent and adequate for this study.

3.1.2.2. X-Ray Diffraction

X-Ray powder diffraction for the materials described in Chapters 4, 6 and 8 were acquired at ICB-CSIC in a PANalytical diffractometre equipped with a Ni-filtered CuKα radiation (λ=1.54 x 10^{-10} m) and a secondary graphite monochromator, using a θ-2θ configuration. Counts were accumulated every 0.01º and the step time was 3 s. Wide angle scans were performed at a 2θ range of 10-80º, step of 0.01º and step time 5s.

Further powder XRD patterns for the materials described in Chapters 5 and 7 were carried out at IMP with a Bruker AXS D8 Discovery with GADDS equipment. Diffraction patterns were measured between 4 and 70° in the 2θ range using two frames with a

scanning time of 300 s. Measurements were taken at ambient temperature using CuKα radiation (λ=1.54 x 10^{-10} m).

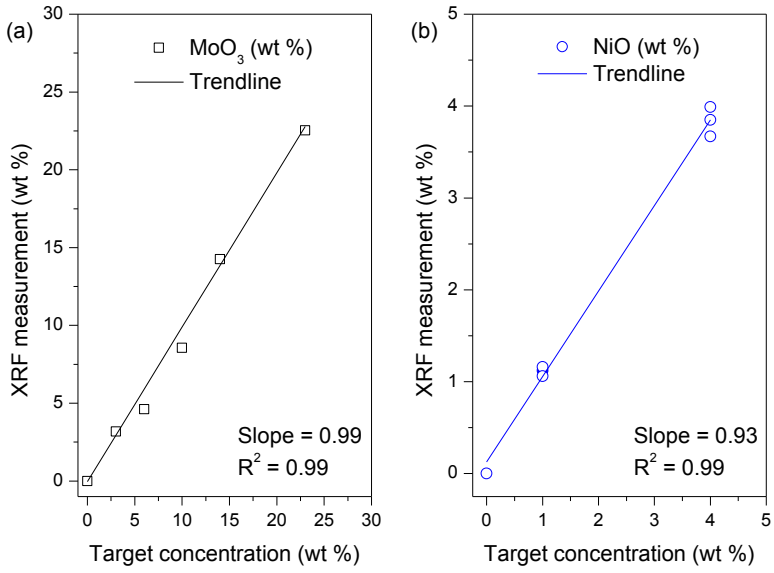

Figure 3.1. XRF elemental analysis for Mo/Al_2O_3 and Ni/Al_2O_3 catalysts.

3.1.2.3. N_2 Adsorption

A Micromeritics Tristar analyser available at Imperial College was used to evaluate the textural properties of the materials. Approximately 200 mg of sample were dried at 110 °C under N_2 flow prior to performing N_2 adsorption tests based on the standard method of N_2 adsorption at -196 °C. The BET method was used to calculate the surface area and the pore size distribution was calculated with the BHJ method based on adsorption-desorption isotherms.

3.1.2.4. Temperature Programmed Desorption

Temperature programmed desorption tests were performed in an AutoChem II 2920 apparatus. Approximately 100 mg of sample were placed in a quartz reactor and were heated at a rate of 10 °C·min^{-1} from room temperature to 1000 °C under constant Ar flow (50 mL·min^{-1}). A quadrupole mass spectrometre (Pfeiffer-Vacuum Omnistar) coupled to the system was used to detect the desorbed gases. The equipment was previously calibrated with a known concentration of CO and CO_2 in Ar (1 % wt). The CO and CO_2 profiles were calculated by integrating the area under the concentration curve versus volume.

3.1.2.5. NH_3 Temperature Programmed Desorption

NH_3 temperature programmed desorption was performed to determine the relative acidity of the samples at ICB-CSIC in a Micromeritics PulseChemisorb 2700. A sample consisting of 200 mg was outgassed in Ar flow to desorb water and impurities from the sample. To do this, the sample was heated at a rate of 10 °C·min^{-1} from room temperature to 600 °C and held at this temperature for 60 min. The sample was then cooled down to 50 °C and ammonia was introduced into the system; the physically adsorbed ammonia was purged afterwards. The system was heated at a rate of 10 °C·min^{-1} to 600 °C and the chemisorbed ammonia was determined with a thermoconductivity detector (TCD).

The TCD read the NH_3 concentration, which was converted into μmol·g^{-1}·min^{-1} units and then plotted against the temperature. The number of acid sites was determined by integrating the area under the curve for each type of acidity (weak, medium and strong) and expressed in molecules of NH_3 adsorbed per temperature interval.

3.1.2.6. Temperature Programmed Oxidation

A Setaram Thermogravimetric analyser was used for TPO analysis. 12±2 mg of sample were heated under air flow using a heating rate of 10 °C·min^{-1} from room temperature to 1000 °C. The derivative of the weight loss curve was analysed.

3.1.2.7. Temperature Programmed Reduction

A Micromeritics PulseChemisorb 2700 was employed to perform temperature programmed reduction at ICB-CSIC to investigate the reducibility of the oxide species of the calcined catalysts. TPR profiles were obtained by passing a 10% H_2/Ar flow of 50 mL·min^{-1} through approximately 200 mg of sample. The temperature was increased with a rate of 10 °C·min^{-1} within a temperature range from 45 °C to 600 or 900 °C and the H_2 consumption was determined with a TCD.

3.1.2.8. Microscopy

3.1.2.8.1. Transmission Electron Microscopy

Transmission Electron Microscopy was performed on the supports and the catalysts in oxide form. A Jeol 2011 microscope equipped with a LaB_6 gun and operating at 200 kV was used at University of Zaragoza (in collaboration with ICB-CSIC) for this purpose. Elemental analysis was performed on localised areas by Electron Dispersive X-Ray Spectroscopy with a PGT energy selective X-ray analyser with a Cu source on volumes

smaller than 10^3 nm^3 and a detection limit of 1%. The samples were finely grounded, suspended in ethanol and dispersed. A drop of this solution was then deposited on a classical TEM lacey carbon copper grid. TEM micrographs were taken focusing on parts of the samples lying across the grid holes to obtain information free of the contribution of the supporting carbon film.

3.1.2.8.2. Scanning Electron Microscopy – Energy Dispersive X-Rays

The morphology and metal dispersion of the catalysts in oxide form was examined with a Hitachi S-3400 N SEM equipped with a Röntec XFlash of Si(Li) EDX analyser at ICB-CSIC. Powder samples were first spread on SEM slabs and sputtered with gold. A qualitative elemental analysis was performed with EDX microanalysis at 2300x magnification.

3.2. HYDROCRACKING EXPERIMENTS

3.2.1. Experimental procedure

3.2.1.1. Microbomb reactor description

A batch microbomb reactor designed in-house was used throughout this work. The system has been utilised in the research group extensively (133–135). Other works in the literature also employ a similar reaction system (108,136).

A diagram for the microbomb reactor is shown in Figure 3.2. All pressure fittings were made out of stainless steel 316 grade and were purchased from Swagelok. The reactor consisted of a ½ in. bored-through union tee with both ends plugged and was connected to a ¼ in. control line with a reducing port connector. The control line of the reactor had a pressure relief valve to allow safe operation, gas inlet and outlet manual valves, and a pressure transducer (GE Druck UNIK 5000) to monitor the system pressure. A heat exchanger that operated with tap water was placed near the control line to condense gases and to protect the pressure transducer from high temperature. A type K thermocouple (RS components) inserted from the top of the pressure line measured the temperature in the centre of the reactor. A second thermocouple monitored the temperature in the control line.

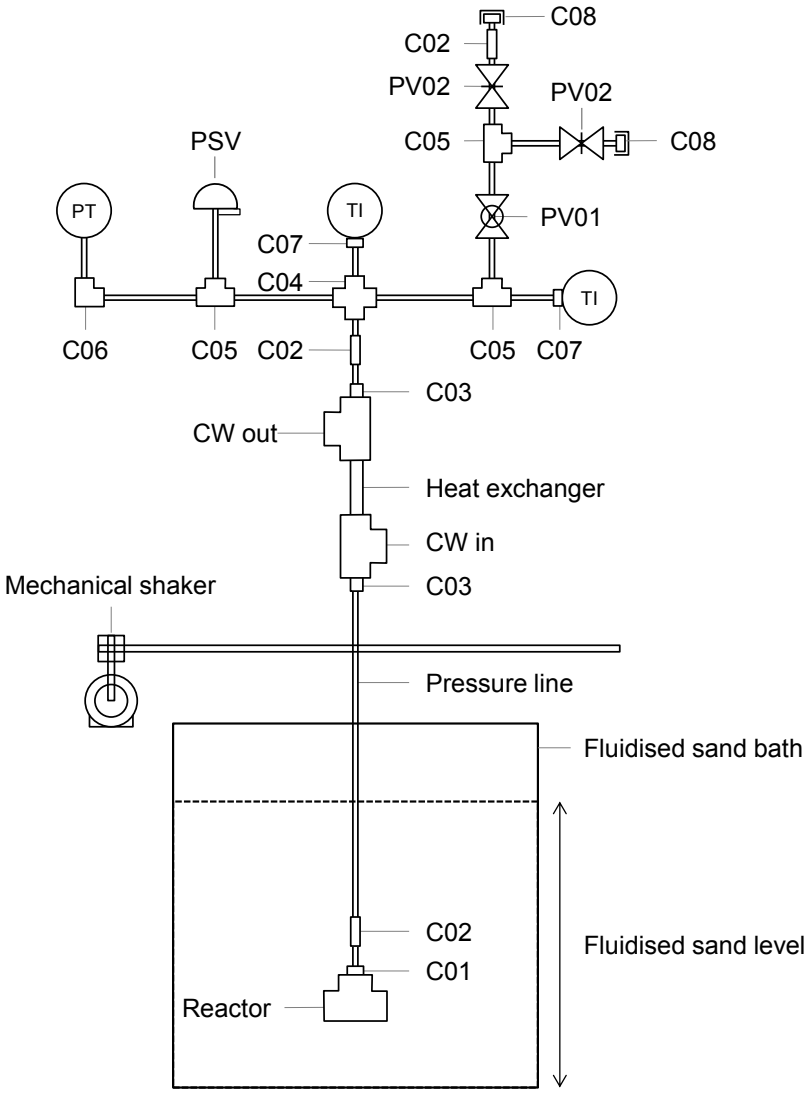

Figure 3.2. Microbomb reactor diagram.

Where: PT: pressure transducer, TI: temperature indicator, PSV: relief valve, PV01: ball valve, PV02: needle valve, C01: ½ in. to ¼ in. reducing port connector, C02: ¼ in. straight union, C03: ¼ in. to ½ in. reducer, C04: ¼ in. union cross, C05: ¼ in. union tee, C06: ¼ in. union elbow, C07: ¼ in. to thermocouple reducer, C08: ¼ in. cap.

The control line and heat exchanger were attached for stability to a metal plate which was mounted on a mechanical shaker assembly above a sand bath. The pressure line and reactor were immersed in the heated fluidised sand bath (Techne model SBL-2D) during reaction. The shaker performed horizontal agitation at 80 cpm to improve contact between the catalyst and feed. The sand bath had a maximum operating temperature of 500 °C, which was measured with an external type K thermocouple placed at its centre, connected to a temperature controller. Reaction temperature inside of the reactor consistently was 10 °C below the sand bath temperature. The sand bath and reactor were located inside an open top safety cabinet during operation.

3.2.1.2. Reactor operation

The diagram available in Figure 3.3 illustrates the operating procedure for the hydrocracking tests. First, the sand bath was heated to the required reaction temperature. A clean ½ in. tee with plugged ends was charged with the desired amount of VR in powder form, given that it is solid at ambient conditions. 1 g of VR were used for experiments with catalysts supported on mesoporous alumina, mesoporous alumina doped with Cr and mesoporous silica alumina whereas 0.5 g of VR were used for experiments with catalysts supported on CNF. The catalyst was added in oxide form in a 1:4 wt/wt ratio with the VR. CS_2 was added for in-situ sulfiding because when CS_2 is heated in a H_2 atmosphere, H_2S is produced which allows for the catalysts sulfidation. 800 μL of CS_2 were used per gram of catalyst, corresponding to an excess of 10 times the theoretical sulfur needed to convert Mo to MoS_2 and Ni to Ni_2S_3, the active phase of the catalyst (137).

If a catalyst was reutilised, it was coated with coke deposits. The catalyst to feed weight ratio was maintained but the catalyst weight was considered without coke deposits. No CS_2 was added during reutilisation reactions. No CS_2 was added when using catalysts supported on CNF (Chapter 8).

The reactor was then attached to the ¼ in. pressure line via a straight union and a high pressure H_2 cylinder was connected to the control line. The system was pressurised and checked for leaks, if leaks were encountered the system was depressurised and the leaks suppressed. Afterwards, the reactor was pressurised to 150 bar with H_2 and depressurised to 7 bar three times, to ensure no air was present in the system. Finally, the microbomb was pressurised with H_2 to the cold operating pressure, 150 bar, and the system was closed and disconnected from the gas cylinder. The cooling water inlet and outlet lines were connected and the thermocouples and pressure transducer were checked to function properly. The reactor was bolted on the shaker system and immersed in the hot fluidised sand. The shaker system was turned on and zero time was registered when the target temperature was reached inside the reactor. Since the fluidised sand bath allowed the system to reach the target temperature within three minutes, preheating periods were neglected. After the desired reaction time elapsed, the reactor was removed from the shaker assembly and quickly quenched, first in cold water then with ice, to room temperature. This ensured all thermal or catalytic reactions stopped immediately. Initial and final temperatures and pressures were recorded for the cold and hot system. The system was depressurised by venting the gases extremely slowly with a flex line into a nearby fume cupboard. This way H_2S fumes,

produced from CS_2 decomposition, and other light gases were not vented to the atmosphere.

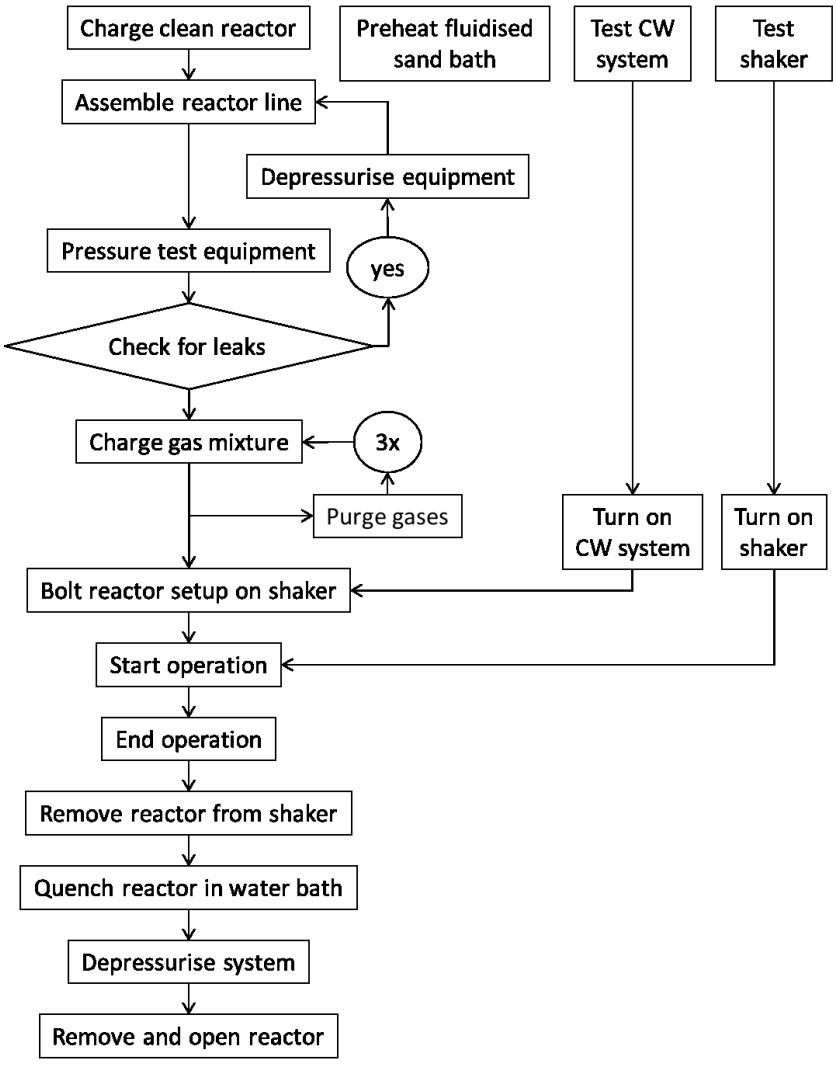

Figure 3.3. Microbomb reactor operation.

3.2.1.3. Product recovery and fractionation

Figure 3.4 illustrates the product recovery procedure along with their subsequent analyses. A solvent mixture of $CHCl_3$/CH_3OH 4:1 vol/vol was used to carefully recover all products after opening the reactor. This solvent mixture was used because it was found to dissolve most hydrocarbons and it presented a lower viscosity than pure $CHCl_3$, which facilitated its removal (54). The pressure line was washed with solvent to ensure all products were recovered. The solid products were separated from the liquid by vacuum filtration using a Whatman PTFE membrane filter of 1 μm pore size. The filter cake was washed with solvent to ensure soluble materials were removed, then it was dried in vacuum at 60 °C for 3 hours to remove traces of solvent. Separately, the solvent in the liquid products was removed first in a rotary evaporator at 60 °C at

atmospheric pressure and then the remaining liquid products were dried to constant weight with N_2 flow. The sample was considered dry when there was a change of less than 1 wt % in 60 min. The filter cake consisted of coked catalyst and was analysed by TGA for carbonaceous deposits. In selected experiments, the liquid product sample was analysed by XRF spectroscopy to determine S content and ICP spectrometry to determine metal content.

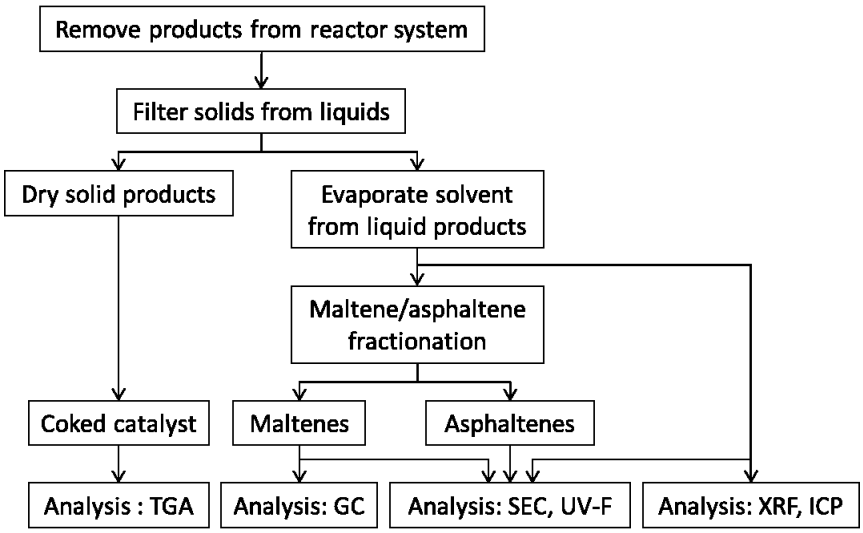

Figure 3.4. Product recovery and analysis sequence.

The liquid products were further separated into maltene and asphaltene fractions. To achieve this, a 100 mg sample of liquid products was mixed with 6 mL of heptane for 2 hours and then centrifuged at 2000 rpm for 20 minutes. The supernatant was recovered and 4 mL of heptane were added to the rest of the sample. This procedure was repeated usually twice or until the supernatant was clear. Subsequently, toluene was added to the heptane insolubles, mixed for 2 hours and centrifuged at the same conditions. The heptane soluble and heptane insoluble/toluene soluble fractions were passed through a syringe filter (Whatman Puradisc 13, 1.0 μm, PTFE) and then dried with N_2 flow to constant weight to obtain the maltene/asphaltene weight ratio. Finally, they were dried at 80 °C for two hours. The maltene fraction was analysed by GC and selected samples were examined by SEC and UV-F spectroscopy.

The same experimental procedure was followed for the recovery and analysis of reutilisation reactions products.

3.2.1.4. Reaction conditions

Feed. Maya crude vacuum residue was used as feed for all hydrocracking experiments. The VR was sourced with help from the IMP and was used as received, without dilution. The main properties of the VR, provided by IMP, are described in Table 3.1.

Table 3.1. VR properties

Boiling point interval	°C	540+
Specific gravity at 15 °C		1.08
°API gravity		-0.34
Viscosity at 100 °C	cSt	265,546
Sulfur content	wt %	7.02
Conradson carbon	wt %	25.54
Asphaltene content	wt %	33.6*
Ni	ppm w/w	93**
V	ppm w/w	227**

*Asphaltene content determined with the same method as reaction products, described in Section 3.2.1.3.

**Ni and V content determined with ICP-OES as reaction products, described in Section 3.2.2.5.

Pressure. Since VR is a feed extremely difficult to upgrade (9), high H_2 pressure was chosen because this would enable better upgrading of the high boiling point fractions, specially asphaltenes (138), as well as reducing coke formation (108,139). Ancheyta et al. reported on studies of the effect of pressure in hydroprocessing (140). It was found that other operating parameters, such as temperature, have a higher impact on reaction products. Therefore in this work the initial pressure of the system was set for all experiments to 150 bar in cold conditions. This pressure rose to 180-190 bar during reaction, depending on the operating temperature.

Temperature. Preliminary studies were performed at 350 °C and it was observed that no VR conversion took place at this temperature. Three higher temperatures were selected: 400, 425 and 450 °C. No higher temperatures were tested because it was observed that gas yields were around 50 wt % at 450 °C, and therefore reactions above this temperature would have had extremely high gas yields. Experiments employing temperature ramps and two temperature stages were performed because other studies observed that when utilising a gradual increase of temperature in the system (139,141) or using two temperature stages (142) gas production was reduced. The following temperature ramps were tested: 350 to 400 °C and 400 to 450 °C. In these experiments the reactor was immersed in the sand bath set to the initial temperature and when the reactor reached the target temperature the sand bath temperature was immediately increased to the final reaction temperature. Two temperature stages were

also tested: 350 to 400 °C, 350 to 450 °C, and 400 to 450 °C. For experiments with two temperature stages, the reactor was held at the initial temperature for 1 hr and then the sand bath temperature was increased to the final reaction temperature. When the reactor reached this temperature reaction was held for an additional hour. The sand bath heated at a rate of approximately 0.83 °C·min^{-1}. These preliminary tests helped determine that gas yields remained the same either with temperature ramps, two temperature stages, or isothermal heating. Therefore isothermal conditions were employed for all experiments.

Time. The purpose of this work is to study the initial rate of deactivation for several catalysts as well as determining product distribution and VR conversion. The contact time was set for 60 minutes for both initial reactions (where the catalysts were used for the first time) and reutilisation reactions (where fresh feed was used with coked catalyst).

3.2.1.5. Data analysis

The conversion of materials boiling above 450 °C, $C_{>450°C}$, and the conversion of the asphaltene fraction, $C_{Asphaltenes,}$ were calculated in this work. The conversions were calculated with Equation 1 and 2 for $C_{>450°C}$ and $C_{Asphaltenes}$, respectively. It is well accepted that coke forms from polymerised asphaltenes. This study focuses on the initial deactivation of the catalysts, thus carbonaceous deposits are considered as part of the >450 °C materials. This allows for a distinction between active catalysts and catalysts that lead to a large carbon deposition, forgoing upgrading of the feed (134).

$$C_{>450°C} = \frac{m_F \cdot x^F_{>450°C} - m_{LP} \cdot x^{LP}_{>450°C} - m_{SP} \cdot x^{SP}_{carbon}}{m_F \cdot x^F_{>450°C}} \qquad \text{Equation 1}$$

$$C_{Asphaltenes} = \frac{m_F \cdot x^F_{Asphaltenes} - m_{LP} \cdot x^{LP}_{Asphaltenes} - m_{SP} \cdot x^{SP}_{carbon}}{m_F \cdot x^F_{Asphaltenes}} \qquad \text{Equation 2}$$

where m_F, m_{LP}, and m_{SP} are the weight of the feed, liquid products and solid products recovered after reaction, respectively; $x^F_{>450°C}$ and $x^{LP}_{>450°C}$ are the mass fraction boiling above 450°C for the feed (with a value of 1.0) and liquid products, correspondingly. $x^{LP}_{>450°C}$ was calculated by adding the maltene fraction that did not elute in GC measurements, i.e. with a boiling point above 450 °C, to the asphaltene fraction of the sample. $x^{SP}_{carbon}$is the amount of carbonaceous material deposited on the catalyst

determined with TGA measurements in grams of carbon per gram of catalyst units. $x^{F}_{Asphaltenes}$ and $x^{LP}_{Asphaltenes}$ are the asphaltene mass fractions for the feed and liquid products, respectively.

In the literature conversions generally do not take into consideration coke deposits, such as in Equation 3 and 4 for $C'_{>450°C}$ and $C'_{Asphaltenes}$, respectively. Results for $C_{>450°C}$ and $C'_{>450°C}$ (comparing Equation 1 and 3) are plotted in Figure 10.1 in Appendix 1, which shows that if a catalyst is used for the first time $C_{>450°C}$ and $C'_{>450°C}$ vary importantly, since in the first reaction most of the coke is formed. On the other hand, when the catalyst is reutilised coke formation is minimal therefore $C_{>450°C}$ is very similar to $C'_{>450°C}$. The same circumstance occurs in Figure 10.2 in Appendix 1 when Equation 2 and 4 are used to compare $C_{Asphaltenes}$ and $C'_{Asphaltenes}$. Therefore including coke deposits into conversion definitions has an important impact in evaluating catalysts in initial reaction stages.

$$C'_{>450°C} = \frac{m_F \cdot x^F_{>450°C} - m_{LP} \cdot x^{LP}_{>450°C}}{m_F \cdot x^F_{>450°C}} \qquad \text{Equation 3}$$

$$C'_{Asphaltenes} = \frac{m_F \cdot x^F_{Asphaltenes} - m_{LP} \cdot x^{LP}_{Asphaltenes}}{m_F \cdot x^F_{Asphaltenes}} \qquad \text{Equation 4}$$

The definition of coke varies between authors because the use of different solvents result in different coke levels (143). Throughout this work coke or carbonaceous deposits are defined as the materials adsorbed to the catalyst that are not extractable in $CHCl_3/CH_3OH$ 4:1 vol/vol and were determined by TGA measurements.

Gases were not collected after reaction given that light ends are generally not affected by catalytic activity (75,138). Their yield was calculated by mass balance according to Equation 5.

$$\text{Gas Yield} = \frac{m_F - m_{LP} - m_{SP} \cdot x^{SP}_{carbon}}{m_F} \qquad \text{Equation 5}$$

Thermal experiments without catalyst were performed to observe the extent of thermal reactions at 400, 425 and 450 °C. The $C_{>450°C}$ and $C_{Asphaltenes}$ conversions and the product distribution of the reactions are shown in Table 10.1 in Appendix 1.

3.2.1.6. Repeatability and error estimation

Tests to assess experimental repeatability and to determine random error were carried out. A catalytic experiment was performed three times under the same conditions and maltene/asphaltene fractionation was completed four times with the same sample, VR.

The standard deviation, standard error and error percentage were calculated with Equations 6 to 8 where X_i is the i-th measure of value of X, M is the sample mean and N the number of samples.

$$\text{Standard deviation, } (SD) = \sqrt{\frac{\Sigma (X_i - M)^2}{N-1}} \qquad \text{Equation 6}$$

$$\text{Standard error, } (SE) = \pm \frac{SD}{\sqrt{N}} \qquad \text{Equation 7}$$

$$\text{Error (\%)} = \pm \left(\frac{SE}{M} \right) \cdot 100 \qquad \text{Equation 8}$$

The standard deviation and error percentage of the experimental repeatability studies shown in Table 3.2 were satisfactorily low; therefore all results in this work will be reported as the actual measurement for each experiment.

Table 3.2. Error analysis for catalytic tests and maltene/asphaltene fractionation.

Experiment / measurement	Mean	SD	SE	Error (±%)
Catalytic reaction N=3				
Liquid products recovered (wt % of feed)	0.91	0.034	0.019	2.15
Solid products recovered (wt % of catalyst)	1.05	0.047	0.027	2.57
x_{carbon}^{SP} on spent catalyst (%)	0.25	0.005	0.003	1.04
Maltene and asphaltene fractionation N=4				
Maltene content (wt %)	0.66	0.009	0.005	0.68
Asphaltene content (wt %)	0.34	0.009	0.005	1.34

3.2.2. Feed and product characterisation

All feed and product characterisations were developed and carried out at Imperial College.

3.2.2.1. Gas Chromatography

A Perkin Elmer Clarus 500 Chromatographer fitted with flame ionisation detector (FID) was used for simulated distillation to quantify the boiling point distribution below 450°C in the maltene fraction. The gas chromatographer (GC) was equipped with a SGE capillary column (HT-5, 25 m long, 0.1 μm film thickness) and was operated with a split ratio 1:20 using He as a carrier gas with a flow rate of 10 $mL \cdot min^{-1}$. The ASTM D2887 method was employed with the following oven temperatures: 35 °C for 1.0 min, then a ramp of 15 $°C \cdot min^{-1}$ until 350 °C when the temperature was held for 2.0 min. The FID and injector temperatures were 370 and 350 °C, respectively. H_2 was fed to the flame at a flow rate of 45 $mL \cdot min^{-1}$ together with an air flow of 450 $mL \cdot min^{-1}$. Samples were always diluted in $CHCl_3$ before injection, with approximately 20 mg of sample dissolved in 200 μL.

A calibration was performed using Standard Gas Oil (SGO) to convert gas chromatographic retention times into a boiling point distribution. This was performed by plotting the sample elution profile against the real boiling point distribution of the SGO (contained in a data sheet provided with the sample) along the oven temperature. This way, the oven temperatures or retention times could be correlated to the real boiling point of the sample, as is shown in Figure 3.5. Therefore, the real 450 °C boiling point was found at a specific retention time.

Afterwards a calibration with different dilutions of SGO was performed to correlate the area of the GC signal intensity to sample concentration. In this manner, the wt % of a maltene sample that eluted before a real boiling point temperature of 450 °C ($Maltene_{<450°C}$) was determined. The maltene fraction boiling over 450 °C ($Maltene_{>450°C}$) did not elute from the column and was calculated with the SGO calibration. Another calibration was developed, using the same Standard Gas Oil, to obtain the column retention times that correspond to the following boiling fractions: Heavy Naphtha (<205 °C), Kerosene (205-260 °C), Diesel (260-340 °C), Gas Oils (340-425 °C) and residue (>425 °C). This calibration was used to calculate the concentration of these fractions in the maltenes.

At least two injections were performed for each sample to ensure repeatability.

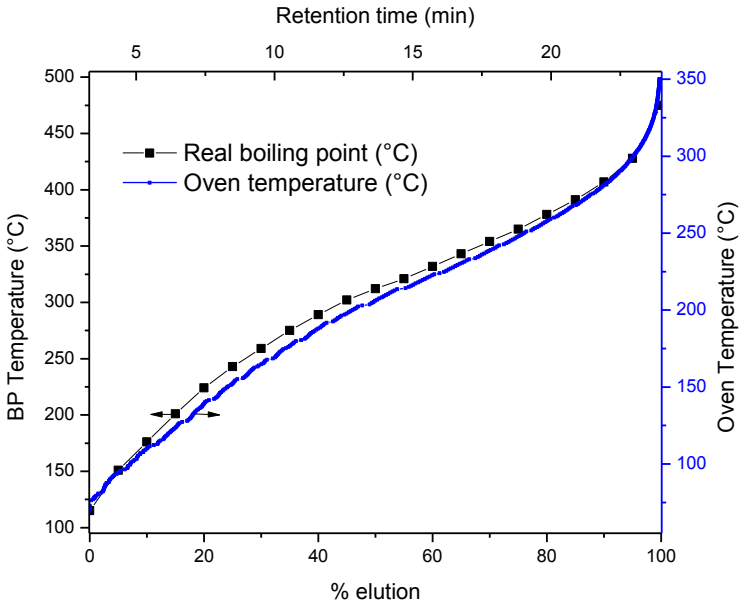

Figure 3.5. Boiling point distribution for SGO.

3.2.2.2. Thermogravimetric analysis

The amount of carbonaceous deposits on the catalysts after hydrocracking reactions was determined with a Perkin-Elmer TGA1 thermogravimetric analyser. Samples of approximately 3 mg were combusted under 40 mL·min^{-1} of air flow from 50 to 900 °C at a rate of 10°C·min^{-1}. Samples were held at isothermal conditions for the initial and final temperatures to allow the weight to stabilise; at 50 °C temperature was maintained for 15 min and at 900 °C for 30 min. The carbonaceous deposits were calculated as the difference between the initial stabilised weight and the final stabilised weight.

Selected catalysts were reutilised, therefore the amount of coke deposits in the second reactions accounted for the deposits of the initial reaction plus the contents formed in the reutilisation. Coke deposits are reported in weight per weight unit of catalyst for these calculations since this allows the estimation of the reutilisation reaction coke by subtracting the initial deposits from the total coke. Coke was reported as solids for the product yield distribution by multiplying the value in weight per weight unit of catalyst to the mass of catalyst.

Coke deposits on carbonaceous supports had to be calculated in a different manner since the combustion of the carbon support also contributed to weight loss. Thus fresh and spent catalysts were combusted in the aforementioned conditions. Afterwards the derivative of the weight loss of the fresh and spent materials was integrated in the region where coke deposits occurred (300-500 °C). The area related to coke deposits was calculated from subtracting the area of the fresh catalyst from the area of the spent

catalyst. The percentage of the area corresponding to coke in regards to the total area was determined. This was converted into the percentage of weight loss relative to coke deposits.

3.2.2.3. Size Exclusion Chromatography

SEC was performed on the asphaltene fraction in a system consisting of a "Mixed D" packed column with polystyrene/polydivinylbenzene (Polymer Laboratories, UK) operated with N-methyl-2-pyrrolidone (NMP) sourced from Rathburn Chemicals and chloroform mixtures (6:1 vol/vol) as the mobile phase in conjunction with a Perkin-Elmer LC 290 variable wavelength UV-absorbance detector operating at 300 nm. The column was maintained at 80 °C during the measurements as this reduced the solvents viscosity and allowed for better separation of the samples. The solvent was pumped at a flow of 0.5 $mL \cdot min^{-1}$. The area of the chromatographs was normalised to allow for comparison between different sample concentrations. This equipment has previously been used to determine the molecular weight distribution of petroleum derived materials and has been described in detail elsewhere (129,130).

Calibration was performed with standard polystyrene (PS) compounds as well as PAH, nitrogenated and oxygenated structures (Polymer Laboratories), obtaining two curves shown in Figure 3.6: one for materials with large molecular mass (MM) (600 to 52,000 u) and another one for materials with lower molecular mass (80 to 530 u). The exclusion limit of the column for polystyrene is around 200,000 u.

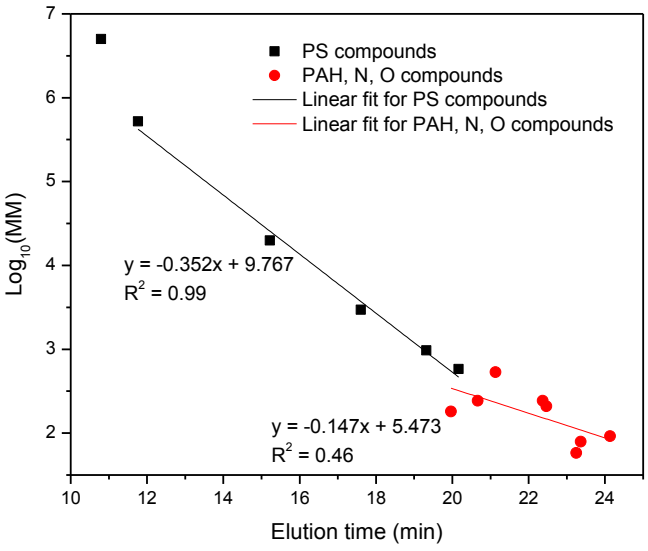

Figure 3.6. Mixed-D column calibration data for PS and PAH, N and O compounds.

3.2.2.4. Ultraviolet-fluorescence Spectroscopy

Ultraviolet Fluorescence studies were conducted with a Perkin-Elmer LS50 Luminescence Spectrometre in the static cell mode. Only synchronous UV-F spectra obtained with a 20 nm difference between excitation and emission wavelength are shown in this work. A quartz cell with 1 cm path length was used and scanned at 240 $nm \cdot min^{-1}$. Samples were diluted with chloroform until the signal lied in 70-100 a.u. Dilution was increased to observe if the fluorescence signal intensity decreased to ensure self-absorption effects were avoided. The procedure is described in detail elsewhere (13).

3.2.2.5. Inductively Coupled Plasma

The determination of Ni and V heteroatom content in the VR and reaction products was performed with a Perkin Elmer inductively coupled plasma optical emission spectrometre (Optima 2000 DV). The equipment has a double monochromator optical system and 40 MHz solid state RF generator. The analytical emission lines for Ni and V were 231.6 and 292.5 nm, respectively.

Samples were prepared by microwave closed digestion with nitric acid. 20±0.5 mg of sample were placed in a screw cap PTFE digestion bomb with 1 mL of concentrated HNO_3 (65% vol). The samples were digested in a Mars 5 (CEM Corp.) microwave with the following program: 2 min at 300 W, 1 min at 0 W, 10 min at 450 W, 1 min at 0 W and 10 min at 450 W. The samples were then allowed to cool down to room temperature and placed in a freezer for 1 hr. The digested contents were carefully recovered and their volume adjusted to 10 mL in a volumetric flask using 5 vol % HNO_3 solution. Calibration standards were prepared using inorganic solution standards in 1 M HCl solutions from BDH Spectrosol®.

This technique was utilised to determine the hydrodemetallisation activity of the catalyst. Ni and V conversions were calculated using Equation 9 and 10, respectively. HDM conversion was calculated from Equation 11.

Ni conversion, $C_{Ni} = \frac{m_F \cdot x_{Ni}^F - m_{LP} \cdot x_{Ni}^{LP}}{m_F \cdot x_{Ni}^F}$ Equation 9

V conversion, $C_V = \frac{m_F \cdot x_V^F - m_{LP} \cdot x_V^{LP}}{m_F \cdot x_V^F}$ Equation 10

HDM conversion $= \frac{m_F \cdot \left(x_{Ni}^F + x_V^F\right) - m_{LP} \cdot \left(x_{Ni}^{LP} + x_V^{LP}\right)}{m_F \cdot \left(x_{Ni}^F + x_V^F\right)}$ Equation 11

where x_{Ni}^F, x_{Ni}^{LP}, x_V^F and x_V^{LP} are the mass fraction of Ni and V for the feed (F) and liquid products (LP), respectively.

Samples were prepared by triplicate to evaluate the reproducibility of the preparation procedure. Also, the metal content for a selected sample was measured three times to evaluate the reproducibility of the measurements. The standard deviation, standard error and error percentage were calculated with Equation 6 to 8. The total error for each element was calculated by adding the sample preparation plus the sample measurement errors. Table 3.3 shows the standard deviation and error values, which were satisfactorily low. The reported results consist of the average values of the measurements performed for each sample.

Table 3.3. Error analysis for ICP-OES measurements for Ni and V determination.

Experiment / measurement	Mean	SD	SE	Error (±%)
Sample preparation N=3				
Ni (ppm)	92.9	0.8	0.5	0.5
V (ppm)	227.2	1.8	1.1	0.5
Sample measurement N=3				
Ni (ppm)	63.1	1.8	1.0	1.6
V (ppm)	43.6	1.8	1.0	2.4
Total error for Ni				2.1
Total error for V				2.9

3.2.2.6. X-Ray Fluorescence

Product samples were analysed with energy dispersive XRF to determine sulfur content. Measurements were performed with a Bruker S4 Pioneer with a Cu source. Approximately 100 mg of sample were dissolved in 10 mL of toluene and mixed during 120 min. Afterwards a 3 mL aliquot of the solution was placed in a sample cup with prolene film (4 μm thickness) and XRF spectra measurements were taken with a

program developed in-house for oil samples, which focused on S. The sulfur content is reported as conversion, HDS, which was calculated with Equation 12.

$$\text{Sulfur conversion, HDS} = \frac{m_F \cdot x_S^F - m_{LP} \cdot x_S^{LP}}{m_F \cdot x_S^F} \qquad \text{Equation 12}$$

where x_S^F and x_S^{LP} are the mass fraction of S for the feed and liquid products, respectively.

Chapter 4: Synthesis of mesoporous alumina using structure directing agents

In this chapter the synthesis procedure of mesoporous aluminas using soft (surfactants) and hard (nanofibres) structure directing agents will be described, along the materials characterisation. Aluminas of different porosity were synthesised. The synthesis and characterisation of NiMo catalysts supported on these aluminas are also detailed.

4.1. INTRODUCTION

As mentioned previously, heavy oils contain a larger share of asphaltenes, containing predominantly polycyclic aromatic hydrocarbon structures, when compared to lighter oils. The limiting step in the hydrocracking reaction is the diffusion of PAHs through the porous network to reach the catalyst active sites. Therefore the presence of large pores in the catalytic support is highly recommended for heavy feed processing (43,44,61). The diffusion of large molecules mainly depends on the pore structure –pore size, pore size distribution and pore volume– and less significantly the surface area of the catalyst (9). The presence of mesopores favour the access of asphaltenes from heavy oils into catalysts, promoting hydrodemetallisation and hydrodesulfurisation (46).

Different types of alumina have been extensively used as catalytic support for hydrotreating and hydrocracking processes because of their acidity and large surface areas. They vary from amorphous to crystalline forms (γ, κ, and α alumina) and the tailoring of pore size has been explored for several decades (144). However, organised mesoporous alumina has received little attention for upgrading heavy oils; a few examples of hydrotreating and hydrocracking studies can be found in the literature (145–150). It was reported that mesoporous aluminas have a greater capability to disperse Mo species, compared to conventional aluminas, achieving higher activity during thiophene HDS reactions (147).

It was also observed that the size of the mesopores influenced the diffusion of thiophene leading to higher HDS rates with larger pores even with constant Mo loading. Another advantage to these materials is the almost absence of micropores, which allows metals to deposit only on pores that are accessible to large feed molecules.

The properties of organised mesoporous aluminas (OMA) are available in several reviews (146,151–153). Different procedures are used for the synthesis of the materials (154–158). Structure directing agents, i.e. the templates with which the materials are given shape, are commonly used and afterwards removed by solvent exchange or calcination. These agents are classified as cationic, anionic, non-ionic, non-surfactant and nanocasting (153); these templates can also be divided in soft, such as surfactants and other organic molecules, and hard, like polymers and carbons. This chapter will concentrate on the use of two types of structure directing agents, soft non-ionic surfactants (Pluronic F127 and P123) and a hard template (carbon nanofibres). Thus a brief summary of the state of the art with these materials is provided. Aluminium isopropoxide and aluminium nitrate were employed as Al precursor in this work.

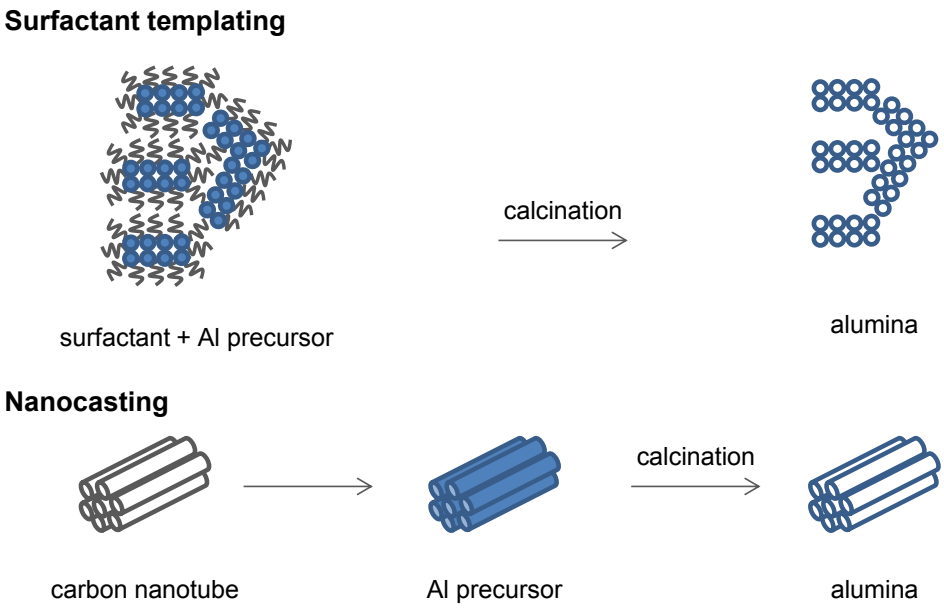

Figure 4.1. Schematic pathway for organised mesoporous alumina synthesis.

A schematic of the preparation of the materials is shown in Figure 4.1. Briefly, the synthesis of OMA using non-ionic surfactants consists in mixing the surfactant in solution with an aluminium precursor. The mixture is usually aged, dried and then the surfactant is removed via calcination in air. Poly(ethylene oxide) (PEO) surfactants have been used in di-block $(R\text{-}EO)_n$ copolymers (such as Tergitol, Igepan) or ethylene

oxide (EO) and propylene oxide (PO) tri-block $(EO)_n(PO)_m(EO)_n$ copolymers (Pluronics). The Pluronic copolymers have different water solubilities, which allow for variation in swelling of the surfactant molecules. The nanocasting synthesis route is different because the carbon agent is impregnated with a solution containing the Al precursor, similar to the incipient wetness impregnation used for catalyst synthesis. The obtained slurry is then dried and the carbon is subsequently removed by calcination. Al precursors such as alkoxides, nitrates, and chlorides have been used, with a summary available elsewhere (153). The porosity of the resulting alumina depends on the selection of the synthesis conditions as well as the Al precursor and structure directing agent. Since the surfactant or carbon decomposes during calcination, careful consideration of the heating rate needs to be taken to avoid structural collapse (153).

Pluronic F127, $(EO)_{106}(PO)_{70}(EO)_{106}$, has been used as a structure directing agent with aluminium isopropoxide and aluminium nitrate. A brief description of how Pluronic F127 has been employed is included. Aluminium isopropoxide ($Al(O\text{-}i\text{-}Pr)_3$) reacts with water to form alumina particles which can condense, resulting in a material with lower surface area (159). Therefore $Al(O\text{-}i\text{-}Pr)_3$ is used in solution in a non-aqueous solvent. For example, $Al(O\text{-}i\text{-}Pr)_3$ was dissolved in a mixture of ethanol and propanol and afterwards Pluronic F127 was added using a controlled amount of water to allow spacings between the alumina particles to form (160). The material was aged for 24 hr at three different temperatures (room temperature, 80 and 150 °C) and calcined at 600 °C. The H_2O:Al ratio was varied from 2 to 20, with pore diameter of the resulting materials increasing from 14 to 26 nm with increasing water content as a result of the increase in diameter of the Pluronic F127 micelles. Another synthesis procedure was performed by dissolving Pluronic F127 in ethanol and HNO_3 or organic acid with HCl and then adding aluminium isopropoxide (161). The solvents were evaporated and the mixture was aged for 48 hr and afterwards calcined at 400 or 900 °C. The pore size of the resulting aluminas varied from 8 to 10.8 nm; the materials were highly ordered with a 2D hexagonal structure. Another synthesis procedure was based on the formation of a gel upon the mixing of an aqueous solution of aluminium nitrate mixed with Pluronic which was then aged overnight at room temperature and subsequently aged at 80 °C or 150 °C for 24-48 hr, filtered and calcined at 600 °C (162). The materials had a smaller pore diameter but larger surface area with lower ageing temperature and presented a Type IV isotherm typical of mesoporous materials.

$(EO)_{20}(PO)_{70}(EO)_{20}$, or Pluronic P123, has been used for similar synthesis methods as Pluronic F127. For example, aluminium nitrate was used in aqueous solution and mixed with P123 and afterwards aged and calcined, resulting in an alumina with a pore

size of 2 or 8 nm depending on the ageing temperature (162). In other work, an aluminium chloride precursor was used in ethanol solution, obtaining an alumina with a pore size distribution centred at 14 nm and a surface area of 300 $m^2 \cdot g^{-1}$; no ordered mesostructure was obtained (163). A different route consisted of mixing aluminium nitrate using Pluronic P123 in an aqueous solution and afterwards adding ammonium hydroxide to adjust the pH. The slurry was then aged and calcined, synthesising an alumina with a surface area of 336 $m^2 \cdot g^{-1}$ and a pore size of 4 nm (157). Aluminium tert butoxide in HCl solution was mixed with Pluronic P123 in ethanol solution, aged and then calcined to produce highly ordered mesoporous aluminas with pore sizes from 4 to 15 nm, surface areas of 200-400 $m^2 \cdot g^{-1}$ and a structure similar to the mesoporous SBA-15 which has a hexagonal arrangement (164). The same procedure as with F127 in acid solution and $Al(O\text{-}i\text{-}Pr)_3$ was also employed (161), obtaining a highly ordered hexagonal arrangement consistent with cylindrical pores observed in the H1 hysteresis loop for N_2 adsorption-desorption isotherms of the material.

Different carbonaceous materials have been employed for the nanocasting synthesis route, such as aerogels, nanotubes and nanofibres. Carbon aerogels with different textural properties were used with aluminium nitrate in aqueous solution to obtain materials with surface area around 300 $m^2 \cdot g^{-1}$ with a bimodal pore distribution at 8 and 20-30 nm (165). Low aluminium loadings were not successful since the pore structure collapsed, concluding that Al_2O_3:C ratios higher than 0.3 were favourable. The CMK-3 carbon aerogel has also been used as nanocasting agent for its structure, an inverse replica of the mesoporous silica SBA-15, as summarised in (153). The use of carbon nanotubes as structure directing agents for alumina synthesis has also been explored using aluminium nitrate (166), aluminium chloride (167) and aluminium tri-sec-butoxide (168); alumina nanotubes with varying pore sizes (3 to 10 nm) and surface areas (140-400 $m^2 \cdot g^{-1}$) were synthesised. Other carbon nanoarrays have been used for nanocasting with $Al(NO_3)_3$ in an absolute ethanol solution, obtaining a bimodal mesoporosity (169).

The main objective of the study presented in this chapter was to synthesise aluminas with different porosity via surfactant templating and nanocasting. Furthermore, an evaluation of the effects of synthesis conditions on the resulting aluminas textural properties was performed. NiMo catalysts were prepared on selected aluminas.

4.2. ALUMINA SYNTHESIS

4.2.1. Surfactant templating

Alumina support was synthesised by adapting a procedure available in the literature (160). Aluminium isopropoxide ($Al(O\text{-}i\text{-}Pr)_3$) was dissolved in ethanol and 2-propanol (anhydrous 99.5%). Afterwards a non-ionic surfactant (Pluronic F127 or P123) was added while stirring the mixture at 50 °C and, when it was dissolved, water was added with additional ethanol and propanol, creating an emulsion. First 88% of the total volume of the alcohols was used to dissolve the $Al(O\text{-}i\text{-}Pr)_3$ and remaining volume was added along with the water. Usually 50 g of $Al(O\text{-}i\text{-}Pr)_3$ were used with 115 mL of ethanol, 112 mL of propanol, 34.7 g of surfactant, and a varying amount of water (8.8, 48.5 or 88 mL) which yielded approximately 11.5 g of final product. DI water was used; absolute ethanol was purchased from VWR UK. The mixture was aged overnight at a specific temperature (ambient, 50, or 80 °C) after which it was vacuum filtered (Whatman 541, hardened ashless, 22 μm) to remove most of the solvents, obtaining a wet paste. The remaining surfactant and solvents were removed by subsequent drying steps at 150 °C for 1 hr, and calcination at 350 °C for 2 hr and 550 °C for 4 hours in a muffle furnace with air flowing at 200 $mL \cdot min^{-1}$. The heating rate during the drying and calcination was also varied; 1, 5.5 and 10 $°C \cdot min^{-1}$ ramps were used. Finally, the material was sieved to 45-250 μm.

The aluminas were named as S# when surfactant was used as structure directing agent. The synthesis conditions for the materials are summarised in Table 4.1. The following conditions were used: two surfactants (Pluronics F127 and P123), three H_2O:Al ratios (2, 11 and 20), three ageing temperatures (ambient, 50 and 80 °C) and three calcination rates (1, 5.5 and 10 $°C \cdot min^{-1}$).

An experimental design of a Central Composite Circumscribed Design (CCC), shown in Figure 4.2, was employed for alumina synthesis using Pluronic F127. The effect of synthesis variables H_2O:Al ratio, ageing temperature and calcination heating rate on the textural properties of the resulting aluminas (S_{BET}, total pore volume and average pore diameter) was assessed. An additional axial point (Alumina S10) was added to observe the effect of ageing temperature with constant H_2O:Al ratio and calcination heating rate. Alumina S11 was synthesised using Pluronic P123 as surfactant instead of F127 with the same conditions as Alumina S6 to observe changes when changing the surfactant.

Table 4.1. Synthesis conditions for aluminas prepared by surfactant templating.

Alumina name	Surfactant	H_2O:Al ratio	Ageing temperature (°C)	Calcination rate (°C·min^{-1})
S1	F127	2	20	1
S2	F127	2	20	10
S3	F127	2	80	1
S4	F127	2	80	10
S5	F127	20	20	1
S6	F127	20	20	10
S7	F127	20	80	1
S8	F127	20	80	10
S9	F127	11	50	5.5
S10	F127	20	50	10
S11	P123	20	20	10

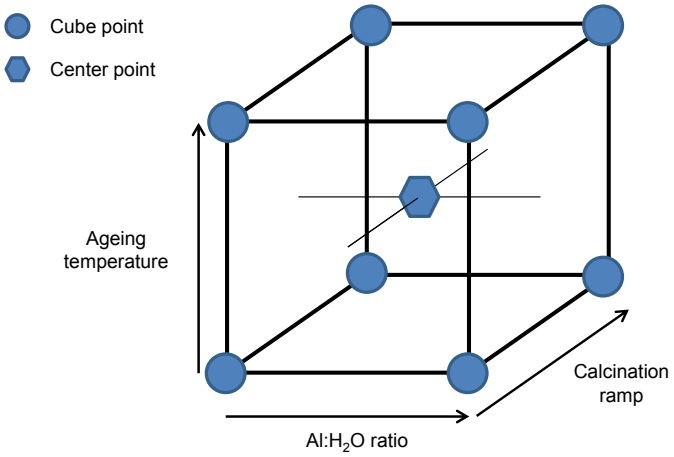

Figure 4.2. Central Composite Circumscribed Design (CCC) employed for alumina synthesis with Pluronic F127 surfactant templating.

4.2.2. Nanocasting

The aluminas prepared via the nanocasting route were synthesised using two Al precursors, aluminium nitrate and aluminium isopropoxide. The carbon nanofibres used as structure directing agent were sourced from Applied Science Inc. (ASI), Cedarville, USA and consisted of Pyrograf III^{TM} carbon (PR-24-XT-PS). The material is pyrolytically stripped (i.e. without PAH on the surface) and is available as free flowing powder, formed by stacked-cup carbon nanofibres of 50-200 μm in length.

The Al:C molar ratio used was 0.5, and the experimental wettability of the nanofibres was taken into consideration for the concentration of the precursor solutions. Each precursor was prepared with a different solution: an aqueous one was prepared with

$Al(NO_3)_3$ whereas $Al(O\text{-}i\text{-}Pr)_3$ was dissolved in 50:50 vol/vol ethanol:propanol. Two subsequent impregnations were performed for each precursor to achieve the desired Al loading with an intermediate drying step at 80 °C overnight. After the second impregnation, the materials were dried at 150 °C for 1 hr and then at 350 °C for 2 hr to decompose the Al precursor to form alumina. Finally, the nanofibres were removed by calcination in air at 800 °C for 4 hours in a muffle furnace under flowing air at 200 $mL \cdot min^{-1}$. Two heating rates were employed during the drying and calcination (1 and 10 $°C \cdot min^{-1}$). Thus two different aluminas were synthesised for each Al precursor. Finally, the materials were sieved to 45-250 μm. The aluminas were named as NC# and their synthesis conditions are summarised in Table 4.2.

Table 4.2. Synthesis conditions for aluminas prepared by nanocasting.

Alumina name	Al precursor	Impregnation solution	Calcination rate ($°C \cdot min^{-1}$)
NC1	$Al(NO_3)_3$	H_2O	1
NC2	$Al(NO_3)_3$	H_2O	10
NC3	$Al(O\text{-}i\text{-}Pr)_3$	ethanol:propanol	1
NC4	$Al(O\text{-}i\text{-}Pr)_3$	ethanol:propanol	10

4.3. ALUMINA CHARACTERISATION

The aluminas (S and NC series) were analysed by N_2 adsorption-desorption to evaluate the impact of the synthesis conditions on their textural properties. Selected materials were also analysed by TEM and SEM.

4.3.1. Textural properties

4.3.1.1. Surfactant templating

Table 4.3 shows the textural properties of the materials determined by N_2 adsorption-desorption studies. To analyse the CCC design for aluminas synthesised with Pluronic F127 (S1 to S9), Figure 4.3 illustrates the influence of the synthesis conditions on the resulting textural properties of the materials. It was observed that aluminas S1 to S4, synthesised with a H_2O:Al ratio of 2, presented lower average pore diameters (APD) and higher surface area (S_{BET}) of the group, with the highest pores obtained for a H_2O:Al ratio of 20. This was expected because the surfactant micelles swelled and increased in diameter when using higher water content, as previously reported (160). The effects of the ageing temperature and calcination rate on the textural properties

were not clearly observed (Figure 4.3) as a combination of factors seemed to be involved.

Table 4.3. Textural properties of the calcined aluminas synthesised by surfactant templating determined by N_2 adsorption-desorption.

Sample	S_{BET} ($m^2 \cdot g^{-1}$)	Total pore volume ($cm^3 \cdot g^{-1}$)	Average pore diameter* (nm)
S1	392.4	1.04	9.2
S2	338.6	0.93	11.0
S3	374.2	0.95	8.1
S4	393.1	1.05	9.2
S5	353.6	1.68	17.9
S6	341.2	1.21	12.0
S7	312.7	1.30	15.4
S8	313.1	1.41	16.0
S9	339.8	1.50	15.5
S10	311.7	1.13	13.0
S11	350.3	1.88	20.3

*BJH model applied to the adsorption branch of the isotherms.

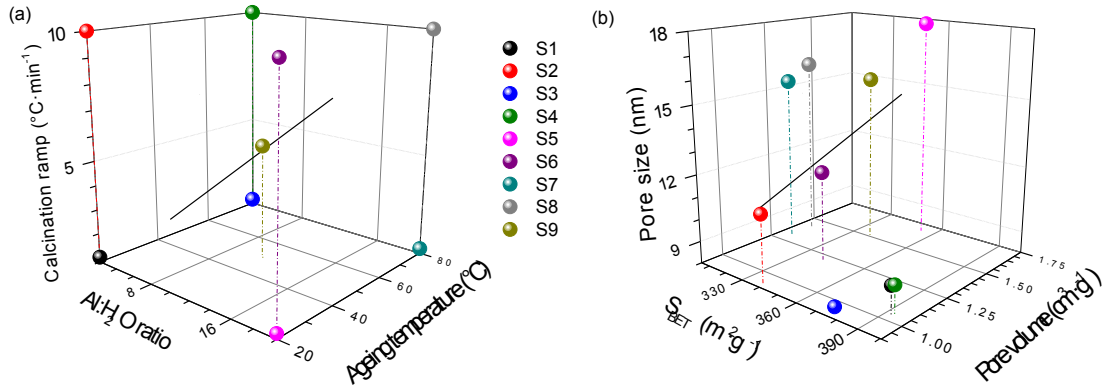

Figure 4.3. Influence of synthesis conditions (a) on textural properties (b) for S1 to S9 aluminas.

The main variable that influenced textural properties was H_2O:Al ratio ($X_{H2O:Al}$). Additionally ageing temperature (X_{AT}) and calcination heating rate (X_{CHR}) had effects on the pore volume. Further analysis of the influence of synthesis conditions was performed by observing N_2 adsorption-desorption isotherms along the PSD curves of the synthesised aluminas. Given that $X_{H2O:Al}$ was the most influential synthesis variable, Figure 4.4 groups aluminas with $X_{H2O:Al}$ of 2 whereas Figure 4.5 with $X_{H2O:Al}$ of 20. A diagonal in the CCC design to compare synthesis variables is presented in Figure 4.6. Finally Figure 4.7 shows aluminas synthesised using a $X_{H2O:Al}$ of 20 and X_{HR} 10 °C·min^{-1} but different X_{AT} or surfactant.

$X_{H2O:Al}$ values of 2 – Figure 4.4. The N_2 adsorption-desorption isotherms and pore size distribution (PSD) of the aluminas synthesised using a $X_{H2O:Al}$ of 2 and Pluronic F127

surfactant are shown in Figure 4.4. S1 and S2 were synthesised with X_{AT} of 20 °C; S3 and S4 with an ageing temperature of 80 °C. All isotherms were Type IV, hysteresis loops H3 were observed for S1 and S2 whereas S3 and S4 had hysteresis H1. The hysteresis loop H3 is representative of slit-like platelets and H1 for capillary condensation taking place in mesopores (126). At higher P/Po values the materials had fairly different hysteresis loop shapes. Narrow hysteresis loops were observed for S1 and S2, different than the slightly broader ones obtained for S3 and S4. This showed that X_{AT} influenced the pore architecture, which reflected on the PSD curves of the materials, shown in the inset figure. Narrower PSD profiles were obtained for S3 and S4 than for S1 and S2. The isotherms had a similar shape in relative pressures below 0.6. The N_2 uptake capacity for the materials was similar at P/Po values close to 1, which was then observed in similar S_{BET} for these aluminas (Table 4.3). At high P/Po values the curve for most of the aluminas continued upwards which is indicative of macroporosity (126), instead of ending in a horizontal line which only occurred for S3. Since the isotherm for S3 ended in a horizontal plateau, it was expected to observe a narrower PSD profile for this material. Larger contribution of pores with smaller size (below 4 nm) were observed for S1 and S2 than for S3 and S4, showing an additional effect of X_{AT}. S1 and S3 were calcined at 1 °C·min^{-1} whereas S2 and S4 using a rate of 10 °C·min^{-1}. The effect of X_{CHR} was observed as a decrease in the maximum pore volume in the PSD curves with lower X_{CHR}.

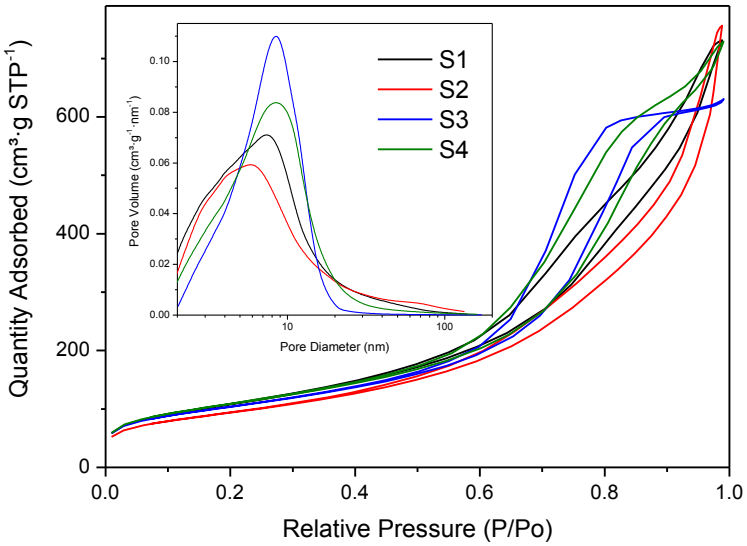

Figure 4.4. N_2 adsorption-desorption isotherms with pore size distribution (inset) for S series calcined aluminas prepared with H_2O:Al ratio of 2.

In summary, for $X_{H2O:Al}$ of 2, a higher X_{AT} resulted in a narrower PSD curves and a different pore architecture of slit-shaped pores. It was reported that when water and triblock copolymer systems had higher temperatures (a) a lower surfactant concentration was needed to form micelles and (b) the radius size of the micelles increased (170). Thus, the effect of X_{AT} was to increase the size or shape of surfactant micelles. In this case S3 and S4 had larger pore volumes at the maximum pore sizes than S1 and S2 as well as different hysteresis loops. The X_{CHR} determined the pore volume at the APD. The calcination ramp determined how rapidly the surfactant decomposed. Then the pore volumes for the materials calcined at a higher rate (10 °C·min^{-1}) were lower than for the ones calcined at a lower rate (1 °C·min^{-1}) because the combustion of the surfactant was more aggressive.

$X_{H2O:Al}$ values of 20 – Figure 4.5. In this Figure N_2 adsorption-desorption isotherms and pore size distribution of the aluminas synthesised using a $X_{H2O:Al}$ of 20 and Pluronic F127 surfactant are shown. In this case all aluminas presented a Type IV isotherm with hysteresis loops H3, which correspond to materials with plate-like particles and slit shaped pores (126), independent of X_{AT}. As with the aluminas prepared using a $X_{H2O:Al}$ of 2 (Figure 4.4), the isotherms of all aluminas were very similar in the micropore region (low P/Po). The hysteresis loops started to form at a relative P/Po around 0.7, thus the amount of water used in the synthesis did not affect the microporosity of the materials. A difference between lower and higher $X_{H2O:Al}$ was the N_2 uptake capacity; the latter had higher nitrogen uptake (800-110 cm^3·g STP^{-1}) than the low H_2O:Al ratio (600-700 cm^3·g STP^{-1}) which reflected on lower S_{BET}. The shapes of the isotherms of the four aluminas were very similar, as were the PSD profiles observed in the inset figure. S5 and S6 were aged at 20 °C whereas S7 and S8 at 80 °C. X_{AT} did not have a significant effect, in contrast with aluminas using $X_{H2O:Al}$ of 2, where different hysteresis loops were observed when changing X_{AT}. A larger S_{BET} was observed for S5 and S6 than for S7 and S8 (Table 4.3). This suggested that when using a $X_{H2O:Al}$ of 20 the effect of X_{AT} was observed in a reduction of S_{BET}. When X_{AT} was 20 °C, differences were observed when varying X_{CHR} (at 1 or 10 °C·min^{-1}). No changes were observed with different X_{CHR} when X_{AT} was 80 °C. For example, a 6 nm difference was obtained between the APD of S5 and S6 while only a 0.6 nm difference was observed for S7 and S8 (Table 4.3). Thus, S5 and S6 present differences in the isotherms in the P/Po region close to 1. A horizontal line is observed for S6, indicative of a narrow pore size distribution and an absence of macropores. Therefore, the impact of X_{AT} with a $X_{H2O:Al}$ of 20 was not as important as with a $X_{H2O:Al}$ of 2. It was mentioned previously that an increase in X_{AT} could cause the formation of larger micelles. It appears that the $X_{H2O:Al}$

of 20 determined the size of the micelles, which remained unaffected with increasing ageing temperature. On the other hand, X_{CHR} had a stronger effect when X_{AT} was 20 °C, but not when it was 80 °C.

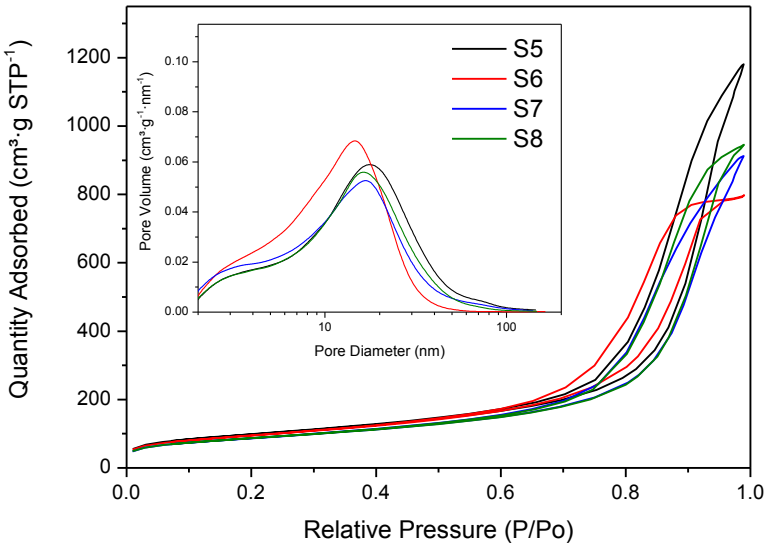

Figure 4.5. N_2 adsorption-desorption isotherms with pore size distribution (inset) for S series calcined aluminas prepared with H_2O:Al ratio of 20.

Diagonal in CCC design – Figure 4.6. The N_2 adsorption-desorption isotherms and PSD profiles for aluminas S1, S8 and S9, which correspond to a diagonal from the lower value for the synthesis variables (S1) to the higher values (S8), passing through the centre point (S9) are shown in Figure 4.6. The three isotherms are Type IV and a transition from a hysteresis loop H1 to H3 occurs when the $X_{H2O:Al}$ is increased from 2 to 5.5. S1 has more micropores than the other aluminas, as detected in the low P/Po region with a hysteresis loop at lower P/Po than for S8 and S9. The isotherm shape for S8 and S9 was almost identical, only S9 had higher N_2 uptake throughout the curve. The average textural properties of S8 and S9 were very similar (Table 4.3). Possibly $X_{H2O:Al}$ higher than 11 created micelles of similar size. The main difference observed was the higher N_2 uptake capacity for S9, hence higher S_{BET}. The PSD profiles (inset) offer a clearer picture of how the synthesis variables affected the textural properties. The formation of larger surfactant micelles that yielded larger pores occurred with higher $X_{H2O:Al}$; this was mentioned previously and was very clear when comparing Figure 4.4 and 4.5.

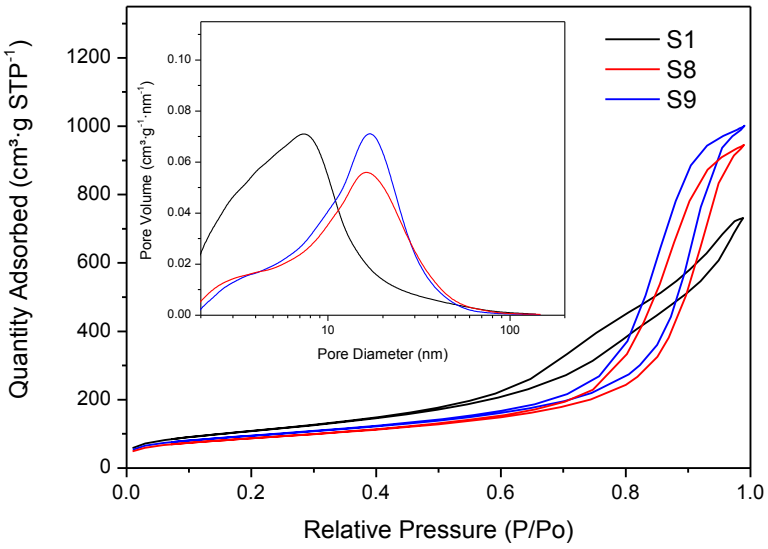

Figure 4.6. N_2 adsorption-desorption isotherms with pore size distribution (inset) for S series calcined aluminas prepared with extreme cube point synthesis conditions.

$X_{H2O:Al}$ of 20 and X_{HR} 10 °C·min^{-1} – Figure 4.7. The N_2 adsorption-desorption isotherms for aluminas prepared using Pluronic F127 and P123 surfactants are shown in Figure 4.7. The PSD profiles are provided in an inset figure. S6 and S8 have already been shown in Figure 4.6 but are included again for comparison purposes. All isotherms were Type IV with a H3 hysteresis loop. S10 was prepared using the intermediate X_{AT} of 50 °C (S6: 20 °C and S8: 80 °C) and showed that higher X_{AT} reduces the pore volume. The isotherm for S10 had the same N_2 uptake capacity as S6 but the same shape of the isotherm as S8. The PSD curve was shifted to lower pore diameters for S10 than S8; S6 had higher pore volumes. The N_2 uptake capacity of S11 which was synthesised using P123, was higher than for the other materials. This related to its higher APD of 20 nm, compared to the same alumina prepared using F127 (S6) which had an APD of 12 nm. However, this material did not present a narrow PSD curves, but had a broad distribution which could not classify as purely bimodal.

An increase in pore size with higher H_2O:Al ratios had also been observed previously for aluminas prepared via surfactant templating (160). Overall, the isotherms from Figure 4.4 to 4.7 present similar shapes as the ones obtained for mesoporous aluminas synthesised with surfactant templating of Pluronic F127 and P123 (162). Those materials had a reduction in S_{BET}, an increase in pore volume and APD when the ageing temperature was increased. This study showed that the calcinations rate could also affect the pore volume but it was dependent on the H_2O:Al ratio as well as the ageing temperature employed.

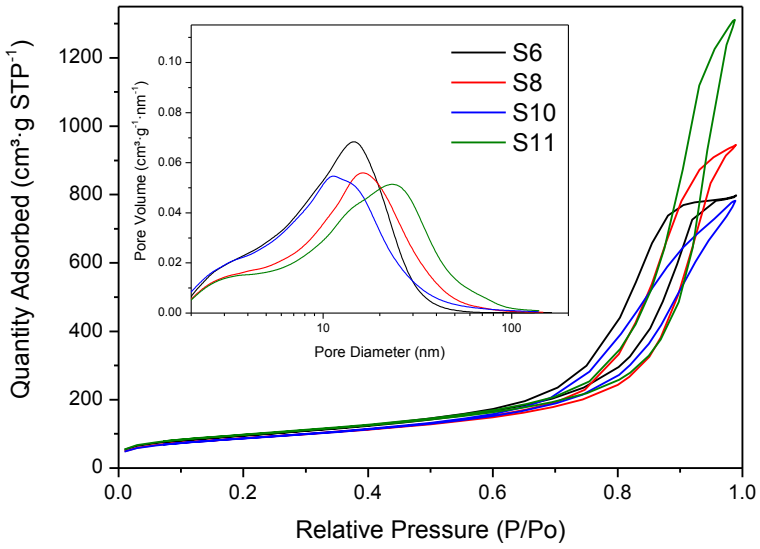

Figure 4.7. N_2 adsorption-desorption isotherms with pore size distribution (inset) for S series calcined aluminas prepared with H_2O:Al ratio of 20 and calcination rate of 10 °C·min^{-1}.

To gain better understanding of the effects of the synthesis conditions on textural properties an ANOVA statistical study of these aluminas was performed as part of a project with collaboration with ICB-CSIC (171). Additional experimental points were used to obtain a Box-Wilson Central Composite Design Face Centred (CCF, α:±1). Full details are not reported here as they are out of the scope of this chapter; a brief summary of the findings of this work is provided. A model for variables H_2O:Al ratio ($X_{H2O:Al}$), ageing temperature (X_{AT}) and calcination heating rate (X_{CHR}) was obtained. The effect of such variables on textural properties S_{BET} (Y_{SBET}), total pore volume (Y_{PV}) and APD (Y_{APD}) was analysed. A satisfactory adjustment of the experimental data was achieved with the quadratic response models. The most significant model variable affecting Y_{SBET}, Y_{PV} and Y_{APD} was $X_{H2O:Al}$. No influence of the terms X_{AT} and X_{CHR} was observed for any textural property. On the other hand, the interaction of X_{AT} and X_{CHR} was found to be significant for Y_{SBET} and Y_{PV}. Selected aluminas were characterised with N_2 adsorption, XRD and TEM, finding that the formation of platelets of different length occurred with varying $X_{H2O:Al}$, which allowed for different pore size distributions.

4.3.1.2. Nanocasting

The textural properties for the aluminas prepared via the nanocasting route are presented in Table 4.4. The choice of Al precursor had an important effect on the S_{BET} and total pore volume of the resulting aluminas. NC3 and NC4, synthesised using Al(O-i-Pr)$_3$, had significantly higher S_{BET} than NC1 and NC2, synthesised using Al(NO$_3$)$_3$. It appeared that the decomposition of the organic compounds in Al(O-i-Pr)$_3$ occurred without destroying the alumina matrix as with the nitrates present in Al(NO$_3$)$_3$. Additionally, the calcination heating rate had an effect for NC3 and NC4. NC3 was calcined at 1 °C·min^{-1} all its textural properties were higher than NC4, which was calcined at 10 °C·min^{-1}. Thus, a lower heating rate facilitated a better decomposition of the organics.

Table 4.4. Textural properties of the calcined aluminas synthesised by nanocasting determined by N_2 adsorption-desorption.

Sample	S_{BET} ($m^2 \cdot g^{-1}$)	Total pore volume ($cm^3 \cdot g^{-1}$)	Average pore diameter* (nm)
NC1	35.3	0.10	14.6
NC2	46.8	0.11	11.6
NC3	118.4	0.43	16.6
NC4	75.2	0.15	9.2

*BJH model applied to the adsorption branch of the isotherms.

Figure 4.8 shows the N_2 adsorption-desorption isotherms and PSD curves for the aluminas synthesised by the nanocasting route. All isotherms had the same shape, Type IV with a H3 hysteresis loop that was formed at P/Po of 0.4 but which presented a sharp change in direction, from horizontal to vertical, at P/Po of ca. 0.9. This change in slope of the isotherm can be found for capillaries with heterogeneous sizes and different geometries (126). The change in the slope of the isotherm is reflected in a bimodal pore size distribution (observed in the inset figure), with a peak occurring at 3 nm and another one at 30 nm for all materials. The choice of Al precursor had a strong effect on the textural properties, as mentioned previously. When Al(NO$_3$)$_3$ was used (NC1 and NC2) low N_2 uptake was observed in the isotherms, with low S_{BET} for the corresponding materials. The pore volumes of NC1 and NC2 were low as well. Conversely, NC3 and NC4, which were produced using Al(O-i-Pr)$_3$, had higher N_2 uptake in their respective isotherms, and also higher pore volume in the PSD profiles. Furthermore, the choice of calcination rate was important in conjunction with the Al precursor. The 10 °C·min^{-1} rate favoured higher S_{BET} and pore volume and a lower APD for NC2 than the 1 °C·min^{-1} rate for NC1. Conversely, higher textural properties were obtained when Al(O-i-Pr)$_3$ was prepared using a 1 °C·min^{-1} calcination rate. NC3 was the only alumina

synthesised by nanocasting that retained a considerable surface area (118 $m^2 \cdot g^{-1}$) and maintained sufficient volume in the larger sized pores.

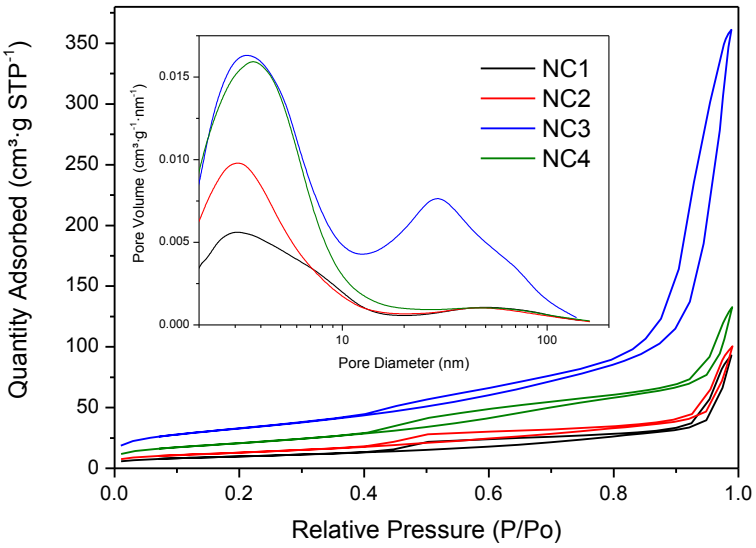

Figure 4.8. N_2 adsorption-desorption isotherms with pore size distribution (inset) for NC series calcined aluminas.

4.3.2. Electron microscopy study

4.3.2.1. Surfactant templating

TEM images of aluminas from selected cube points of the CCC design (S2, S3, S5 and S6) are shown in Figure 4.9 at low (20,000X), medium (40,000X) and high (100,000X) magnification. It was observed that the pore architecture of S2 and S3 had a random worm-like motif which can be found for aluminas synthesised by the surfactant templating method (155). In the high magnification micrographs for S2 and S3 short corrugated platelets are detected, as has been reported previously (160,172). No discernible differences were noted in the low and medium magnifications between S2 and S3 micrographs, but in the high magnification images an enlargement of platelets for S2 compared to S3 was shown, resulting in larger APD for the former (Table 4.3). An immediate difference in the micrographs for S5 and S6 was observed with an enlargement in the slit-shaped platelets. These platelets had a ca. 60-80 nm length compared to the ca. 20 nm length for the aluminas prepared using a H_2O:Al ratio of 2. S5 and S6 were aged at the same temperature but with a different calcination rate, 1 °C·min^{-1} for the former and 10 °C·min^{-1} for the latter. Longer platelets were observed for S5 than for S6, showing that the faster calcination rate caused lower APD as well as pore volume (Table 4.3).

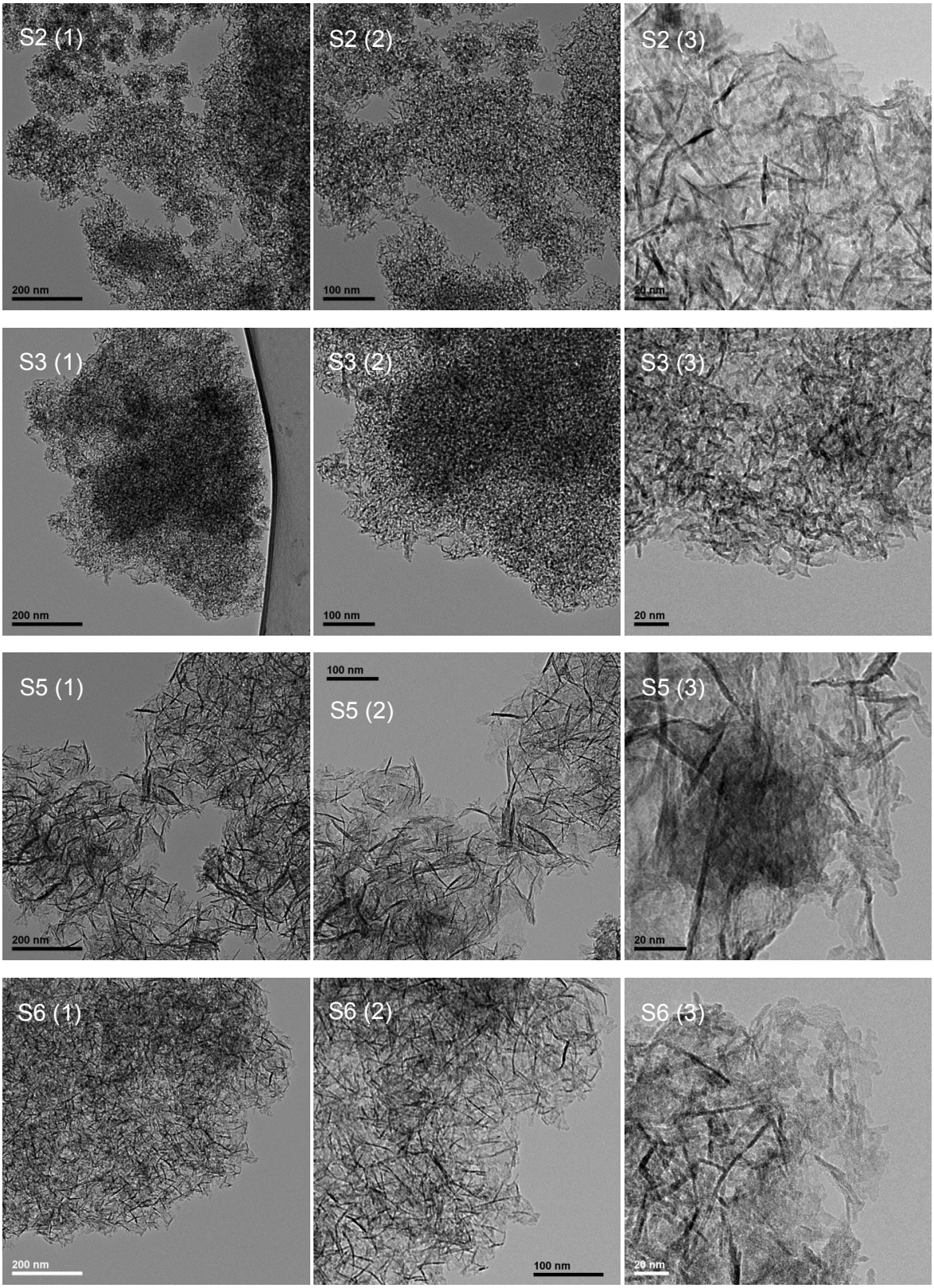

Figure 4.9. (1) Low (20,000X), (2) medium (40,000X) and (3) high (100,000X) magnification TEM images of alumina samples CCC design cube points (S2, S3, S5 and S6).

Figure 4.10 displays TEM images for centre point alumina S9 and also S10 at low (20,000X), medium (40,000X) and high (100,000X) magnification. Alumina S9 had an intermediate H_2O:Al ratio of 11 to the aluminas from Figure 4.9, and the platelets had a length of ca. 40 nm. The platelets for S10 were similar to the ones from S5 and S6. Therefore, the H_2O:Al ratio was determinant in increasing the platelets length and a consequentially larger APD and wider PSD curves. The surfactant micelles would swell into larger particles when higher amounts H_2O were used, thus larger and longer pores were formed when the surfactant was removed. When the platelets became larger when using higher H_2O:Al ratios a transition between a wormlike architecture to a slit-like one was observed (157), confirming the transition in hysteresis loops observed in Figure 4.4 to 4.6.

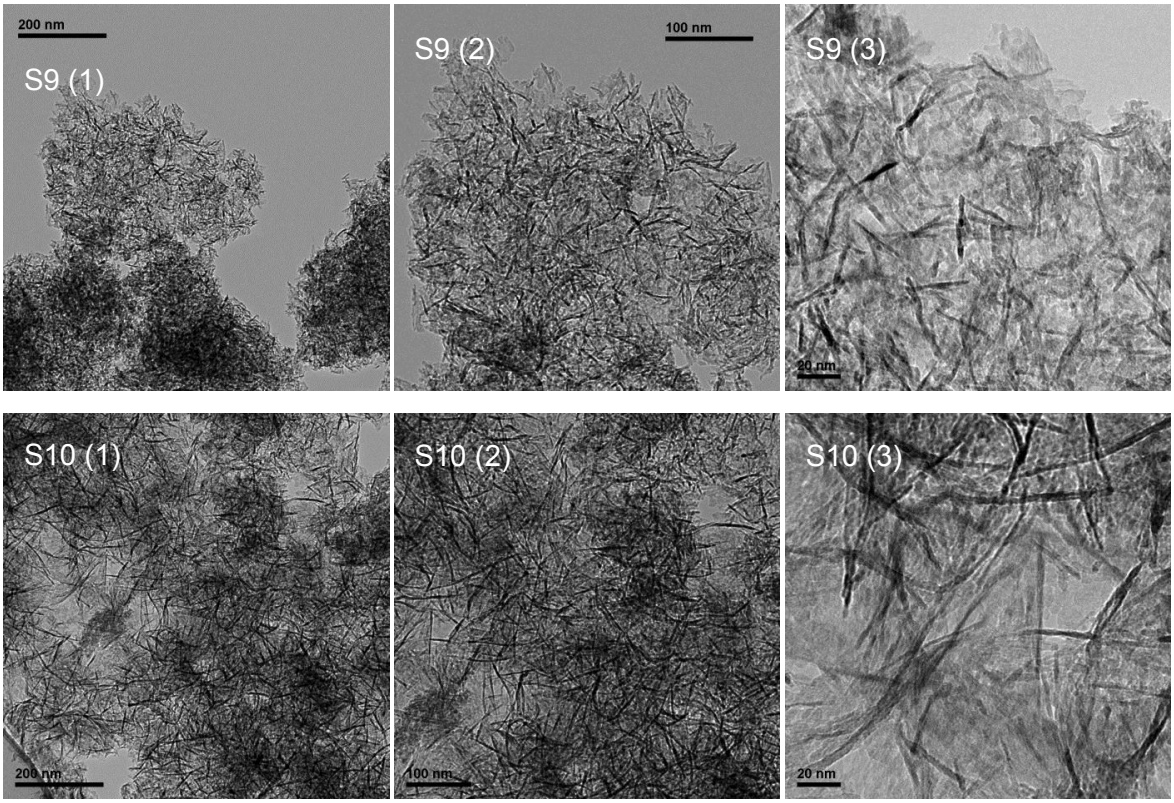

Figure 4.10. (1) Low (20,000X), (2) medium (40,000X) and (3) high (100,000X) magnification TEM images of alumina samples CCC centre and axial points (S9 and S10).

4.3.2.2. Nanocasting

Figure 4.11 shows low (5,000X), and high (10,000X) magnification SEM images for the four aluminas prepared by nanocasting. NC1 and NC2 were prepared using aluminium nitrate as Al precursor whereas NC3 and NC4 using aluminium isopropoxide. All aluminas appeared to be amorphous in nature, unlike materials synthesised with an ordered carbon precursor (169). NC1 showed it was formed by long fibres in its high

resolution micrograph, though little surface area or pore volume was present in this material.

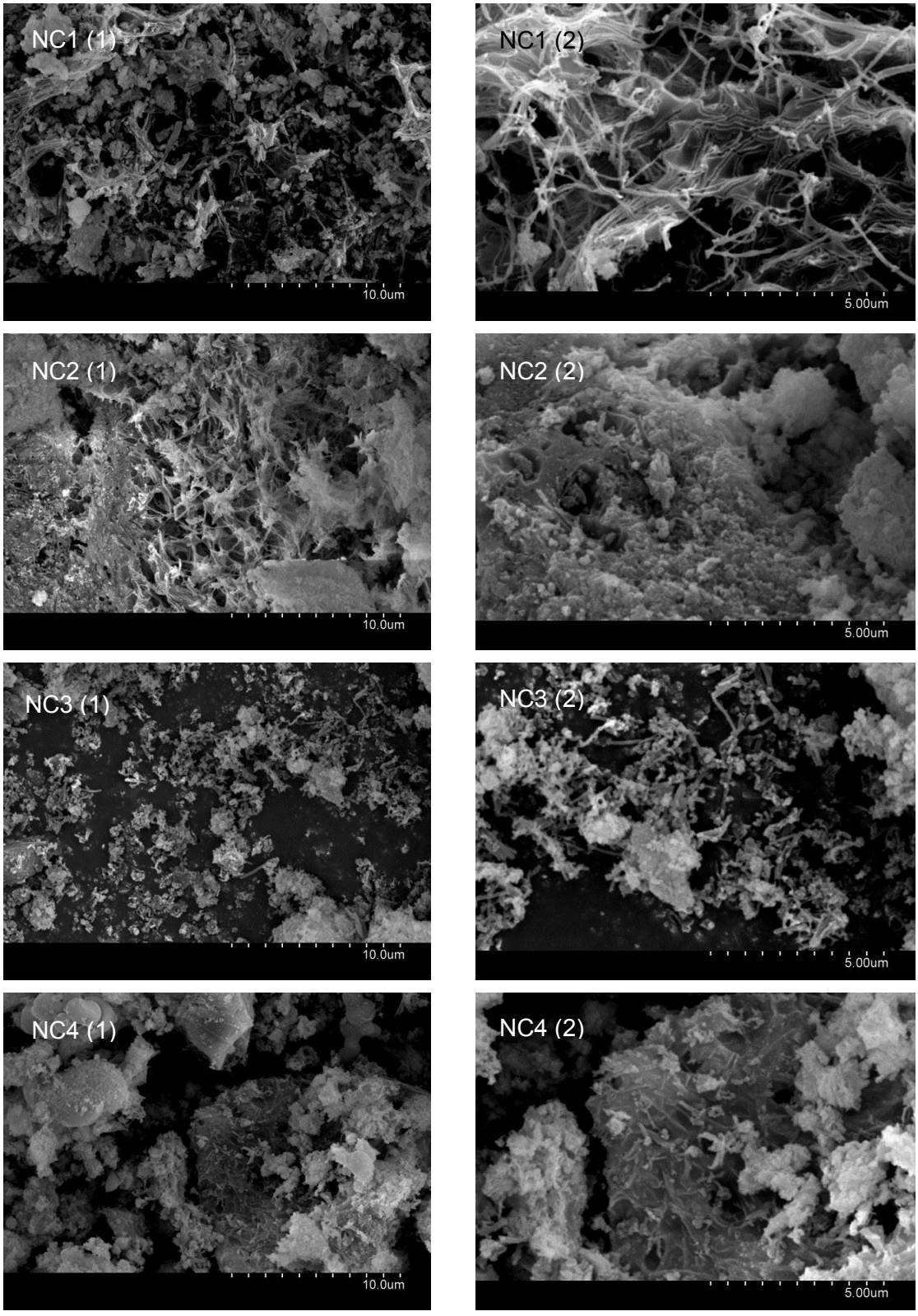

Figure 4.11. SEM micrographs of alumina samples prepared by nanocasting at (1) low (5,000X), and (2) high (10,000X) magnification.

Figure 4.12 shows TEM images at low (10,000X), medium (40,000X) and high (100,000X) magnification of NC1 and NC3, prepared with $Al(NO_3)_3$ and $Al(O\text{-}i\text{-}Pr)_3$, respectively. Some particles in NC1 retained the shape of the carbon template but others collapsed. NC3 maintained the shape of the carbon nanofibres; hollow fibres were formed with a width of approximately 80 nm and several microns in length. High temperature calcination at 800 °C did not destroy the shape of the nanofibres of NC3, as has been reported previously with alumina prepared using $Al(NO_3)_3$ and calcined at 500 °C (166). This material was the one prepared by nanocasting that retained significant surface area and pore volume. Local elemental analysis performed with Electron Dispersive X-Ray Spectroscopy (EDX) showed that both samples were composed of Al_2O_3 and carbon was successfully removed (results not shown).

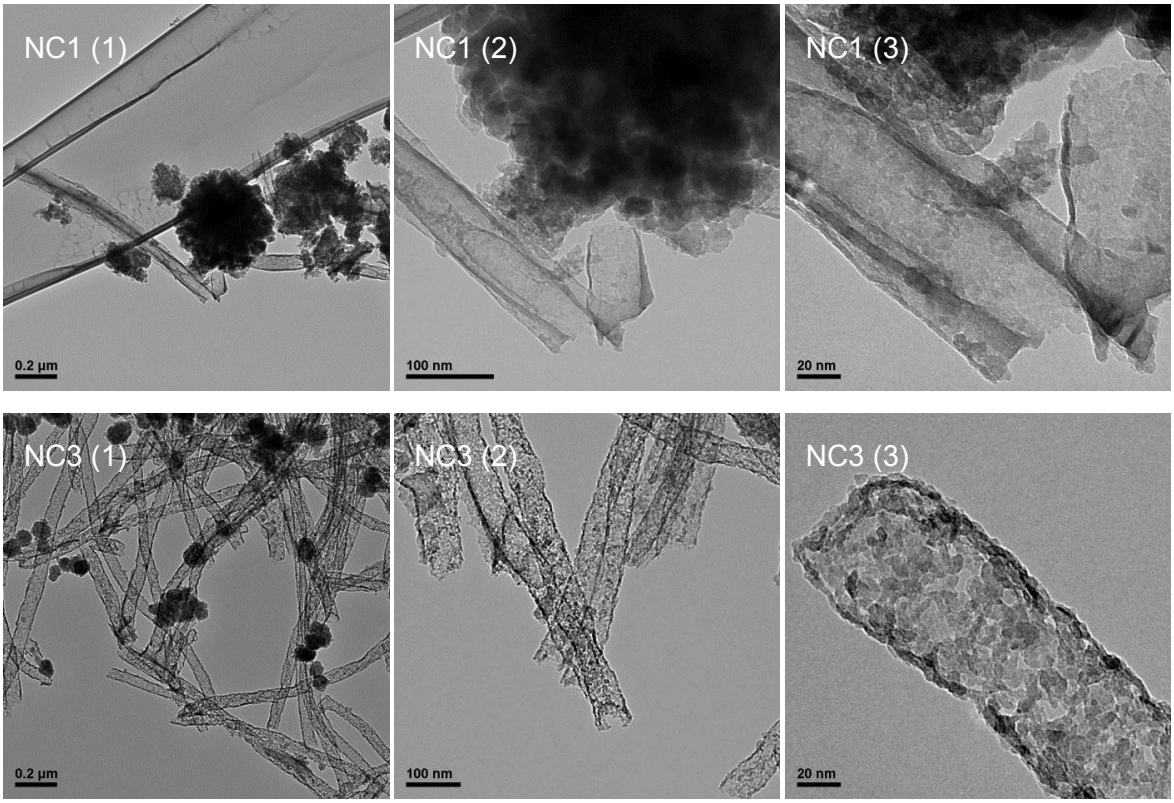

Figure 4.12. (1) Low (10,000X), (2) medium (40,000X) and (3) high (100,000X) magnification TEM images of alumina samples NC1 and NC3 prepared by nanocasting.

Aluminas prepared by nanocasting can prove interesting catalytic supports because of lack of microporosity and reduced diffusional limitations, given that the spacing between pores can allow large hydrocarbon molecules access to the active sites. Additionally, selective deposition of metals in the bimodal porosity of the support could permit different metal composition inside and outside the fibres. Thus the metal composition and loading could be tailored to the molecules that could access the inner or outer surfaces of the fibres.

4.4. CATALYSTS

4.4.1. Selection of aluminas as catalytic support

Aluminas S3, S5, S6 and NC3 were selected to impregnate metals. These were chosen for their different textural properties that would thus yield catalysts with different porosity, surface area and pore volume. S_{BET} for the S series aluminas is very similar, nevertheless different APD of 8.1, 12.0 and 17.9 nm were selected. From Figure 4.4 and 4.5 it can be observed that the PSD curves are different for the aluminas, for example S3 has a narrower pore size distribution than S5 or S6. The two latter aluminas differed in the APD (S5 was larger) and the presence of macropores (S6 had none). NC3 was selected because it was the alumina prepared by nanocasting that retained significant surface area as well as pore volume and had a large APD of 16.6 nm. Further characterisation was performed on these materials; XRD patterns and TPD-NH_3 studies are presented in Figure 4.13 and 4.14, respectively. In the former figure it was observed that no diffraction lines were present for S3. The absence of diffraction lines typically occurs to materials without an ordered oxide phase (157). The other aluminas had three broad intensity peaks at approximately 38°, 46° and 67°, which are typically assigned to gamma alumina. Thus S5, S6 and NC3 had a greater presence of ordered materials than S3. The H_2O:Al ratio used in alumina synthesis can impact the phase of the alumina that is formed, obtaining higher crystallinity with higher ratios (159,160,168), as observed with S3 (H_2O:Al ratio of 2) compared to S5 and S6 (H_2O:Al ratio of 20).

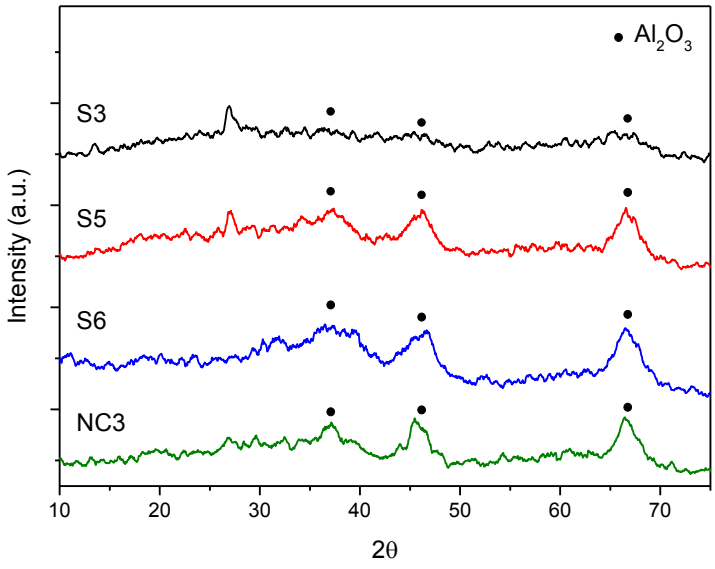

Figure 4.13. Powder XRD patterns of calcined S and NC series aluminas.

The TPD-NH_3 profiles for the aluminas (Figure 4.14) showed that the S3, S5 and S6 aluminas had slightly different acidities above 400 °C. When calculating the NH_3 micromoles desorbed per m^2 of material, S3, S5 and S6 had similar values in the temperature range from 400 to 600 °C, "strong acidity", which would be the one active during reaction. NC3 presented a lower strong acidity, possibly due to the lower surface area of the material. All materials presented strong acid sites, required for reactions above 400 °C. The amount of strong acid sites occurred in the following decreasing order: S5 > S3 > S6 > NC3.

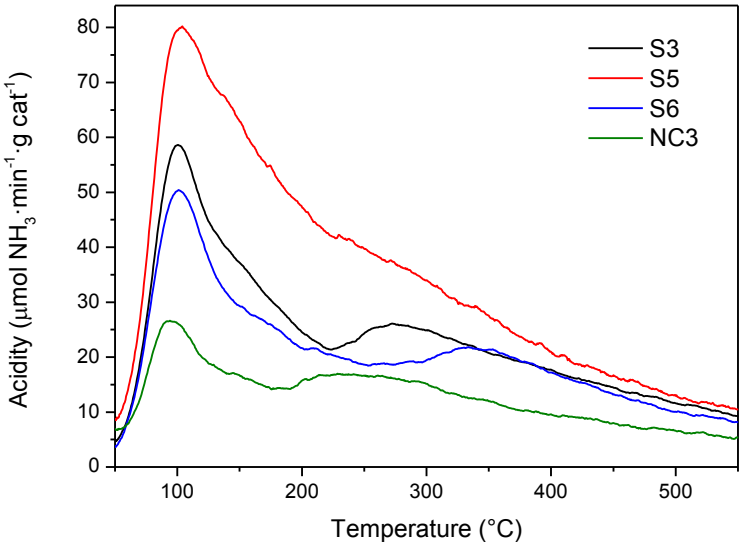

Figure 4.14. NH_3-TPD profiles for the calcined S and NC series aluminas.

Table 4.5. Acid sites available in supports S3, S5, S6 and NC3 by temperature interval.

Sample	NH_3 content* (μmol $NH_3 \cdot g^{-1}$)			
	50-200 °C	200-400 °C	400-600 °C	50-600 °C
S3	486	407	250	1143
S5	850	666	295	1810
S6	401	354	215	971
NC3	210	240	136	586

*NH_3 data calculated from integrated areas from Figure 4.14, acidity values calculated with an ammonia concentration calibration and taking into account the sample mass.

4.4.2. Catalyst synthesis

The aluminas were impregnated using Ni and Mo to prepare catalysts. The catalyst supported on S6 was used and is included in Chapter 5. The other materials were not used for reaction with VR due to time constraints but will be studied as part of future work.

A nominal NiO loading of 3 wt % and MoO_3 loading of 14 wt % were chosen to have an atomic ratio of Ni/(Ni+Mo) close to 0.3. The catalysts were prepared via the incipient wetness impregnation method. A DETA/H_2O solution, of 10:1 DETA:H_2O volume ratio, containing ammonium tetrathiomolybdate (ATM) was used to first impregnate the dry alumina supports. The dilution and added volume of the metal solutions were based on the experimental wettability of each alumina, i.e. the pore volume. Afterwards, the materials were dried overnight at 80 °C. Then Ni aqueous solutions, using $Ni(NO_3)_2.6H_2O$ as the metal precursor, were prepared by tailoring their concentration to the desired metal loading. The Mo-containing alumina materials were impregnated with the corresponding Ni solution and dried overnight at 80 °C. Finally, the materials were calcined using the following temperature program: 150 °C for 2 h, 350 °C for 3 h, and finally 550 °C for 4 h; the temperature rate employed was 10 °C·min^{-1}. The calcination of catalysts was carried out in a muffle furnace under flowing air at 200 mL·min^{-1}. The materials were named Ni3Mo14/*x* where *x* is the name of the corresponding alumina support.

4.4.3. Catalyst characterisation

The textural properties of catalysts synthesised with S3, S5, S6 and NC3 are presented in Table 4.6. The S_{BET} for the S series-supported catalysts were above 250 m^2·g^{-1}, the pore volume of the catalysts varied between 0.56 and 0.97 cm^3·g^{-1} and a range of pore sizes between 7.8 to 13 nm. Most of the S_{BET} of the support was maintained; nevertheless pore volume and APD were reduced due to metal loading, showing that the metals penetrated the supports pores. As expected, Ni3Mo14/NC3 had marked different textural properties than the other catalysts with lower S_{BET}, lower pore volume and a larger pore diameter due to the different alumina support used. This catalyst conserved the higher pore volume of the original support.

Table 4.6. Textural properties of the calcined catalysts synthesised on S and NC aluminas determined by N_2 adsorption-desorption. The percentage of the corresponding textural property of the supports which was retained is noted in parenthesis.

Sample	S_{BET} ($m^2 \cdot g^{-1}$)		Total pore volume ($cm^3 \cdot g^{-1}$)		Average pore diameter* (nm)	
Ni3Mo14/S3	279.4	(75%)	0.62	(65%)	7.8	(96%)
Ni3Mo14/S5	274.0	(77%)	0.97	(58%)	13.0	(73%)
Ni3Mo14/S6	342.5	(99%)	0.66	(54%)	10.4	(86%)
Ni3Mo14/NC3	95.3	(80%)	0.31	(72%)	15.2	(92%)

*BJH model applied to the adsorption branch of the isotherms.

Figure 4.15 shows the N_2 adsorption-desorption isotherms of the catalysts. Since the isotherms of the respective supports have been detailed previously, only a brief description will be provided in this section. Ni3Mo14/S3 maintained the Type IV isotherm with H1 hysteresis loop as its support; Ni3Mo14/S5 and Ni3Mo14/S6 had a hysteresis loop H3. The N_2 uptake capacity of the catalysts varied in the microporous region and in P/Po values close to 1. Ni3Mo14/S3 had a clear horizontal line at high P/Po, indicative of narrow pore size distribution and the absence of macropores. The isotherm of Ni3Mo14/NC3 differs from the others because it is supported on the alumina synthesised by nanocasting.

The PSD profiles for the catalysts are shown in Figure 4.16. Different distributions were obtained, from narrow (Ni3Mo14/S3) to broad (Ni3Mo14/S5 and Ni3Mo14/S6). Average pore diameters varied from approximately 5 to 15 nm with different pore volume. Ni3Mo14/NC3 presented a very different morphology with a bimodal distribution with peaks at 4 and 20 nm and is presented in a separate Y axis given that the pore volumes were significantly smaller than for the S series aluminas.

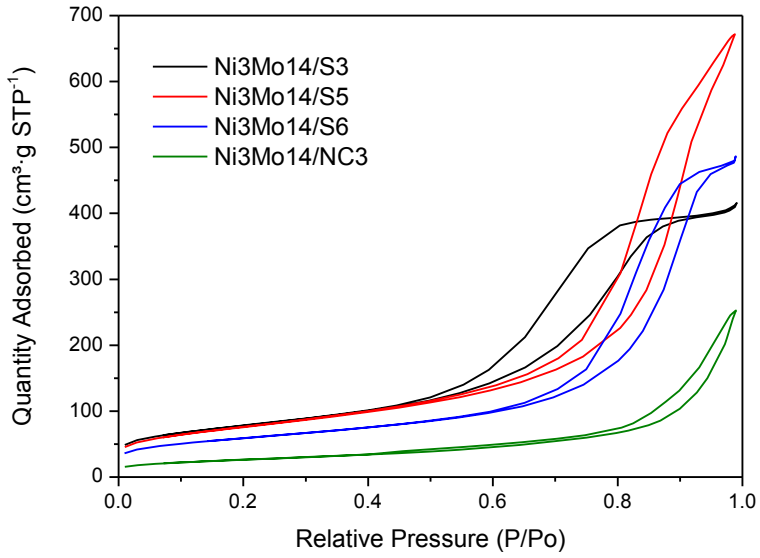

Figure 4.15. N_2 adsorption-desorption isotherms for calcined catalysts supported on S and NC series aluminas.

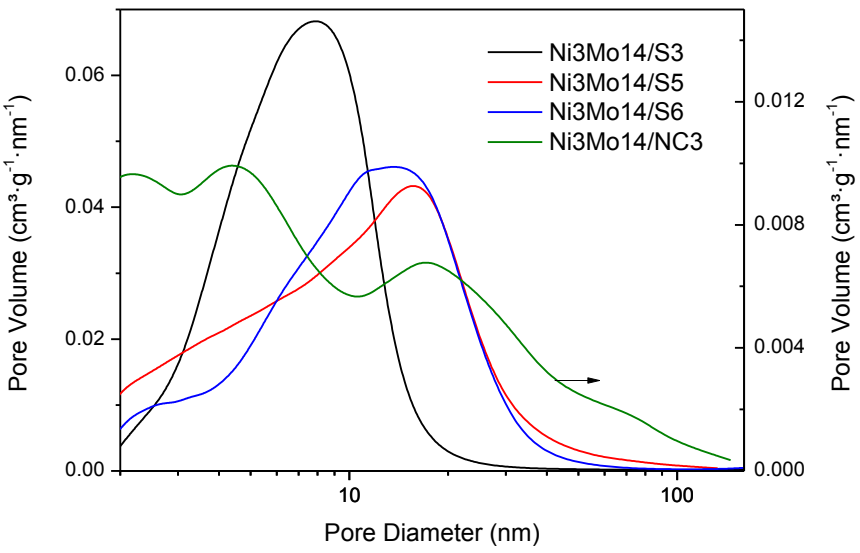

Figure 4.16. Pore size distribution for calcined catalysts supported on S (left Y axis) and NC (right Y axis) series aluminas.

The TPD-NH_3 profiles for the catalysts are shown in Figure 4.17. It was observed that Ni3Mo14/S6 was the catalyst that had stronger acidity and Ni3Mo14/NC3 had almost no strong acid sites.

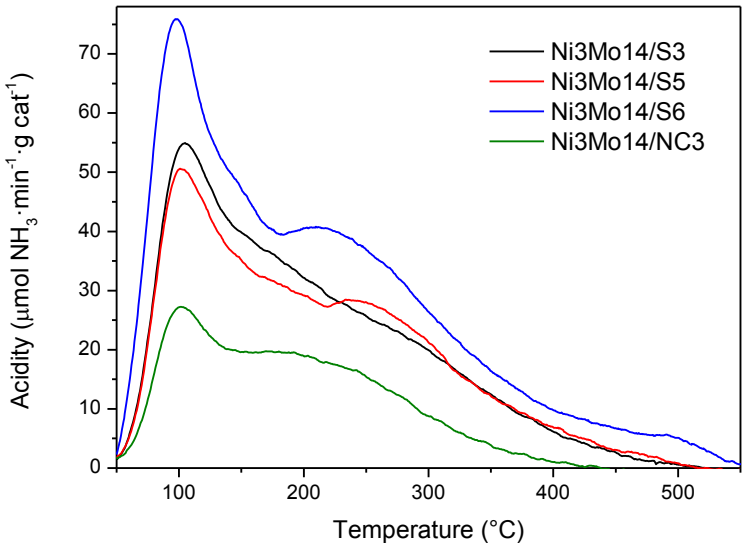

Figure 4.17. NH_3-TPD profiles for the calcined NiMo catalysts on S and NC series aluminas.

Figure 4.18 shows the temperature reduction profiles for Ni3Mo14/S3, Ni3Mo14/S5, Ni3Mo14/S6 and Ni3Mo14/NC3. Three main peaks were observed for each catalyst, where a low temperature Mo reduction peak first appears, followed by the Ni reduction and lastly by a high temperature Mo reduction. The first Mo peak corresponds to a reduction of octahedral Mo and the second to a reduction of tetrahedral species (Mo^{6+} → Mo^{4+} → Mo^{0}) (173–175). Ni species are reduced in a single step (176). The reducibility of metal oxides depends on the synthesis technique (177), metal loading (178) and the type of support, for example peaks are obtained at different temperatures for alumina, silica-alumina, or zeolites (174,179). Therefore comparing different reports proves difficult.

It is interesting to observe that the three reduction peaks occurred at slightly different temperatures for the catalysts, with the first peak for Ni3Mo14/S3 appearing at lower temperatures than for Ni3Mo14/NC3. This could show that the textural properties of the support and its acidity (Figure 4.14) can also affect to some extent the reducibility of the metal oxides. The reducibility of the metal oxides occurred in the following decreasing order: S3 > S5 > S6 > NC3. The strong acid sites of S3 and S5 were almost identical, and these two catalysts had lower metal reduction temperatures than S6, which had more strong acid sites. Thus the catalyst with metal sites available at lower temperatures would be expected to have higher catalytic activity. Ni3Mo14/NC3 did not present three distinct reduction peaks as the other catalysts. Possibly the Ni peak overlapped with the first Mo peak and was therefore not observed.

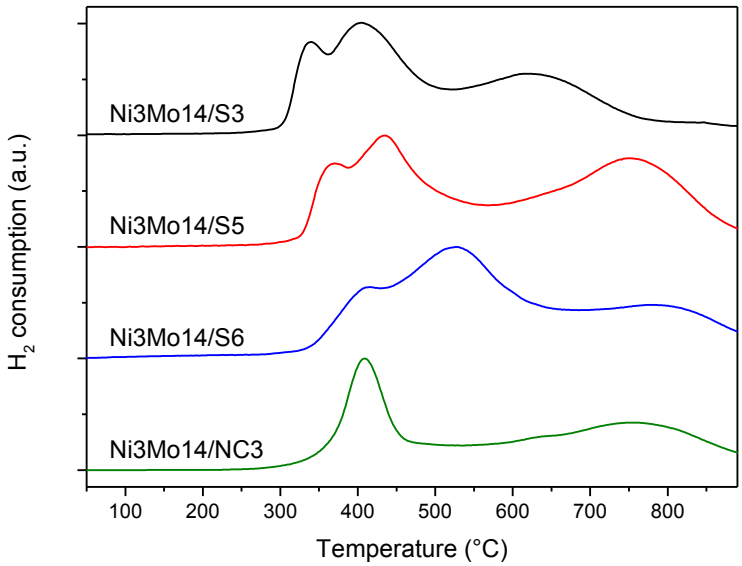

Figure 4.18. TPR spectra of calcined NiMo catalysts supported on S and NC series aluminas.

4.5. CONCLUSIONS

Mesoporous alumina can have advantageous properties as catalytic support for upgrading heavy feeds because it can allow large molecules to enter into the catalyst active sites. Mesoporous materials have been synthesised using different procedures with structure directing agents to obtain organised mesoporous aluminas. In this chapter, aluminas were synthesised via the surfactant templating and nanocasting methods. The process variables of H_2O:Al ratio, ageing temperature and calcination rate were evaluated when preparing the aluminas using surfactants. The synthesis conditions had significant effects on the textural properties of resulting aluminas and were also observed in TEM images.

An analysis for alumina synthesis was described. The H_2O:Al ratio was determinant for the materials surface area, total pore volume as well as average pore diameter. This happened because the surfactant micelles would swell and increase in diameter depending on the amount of water used. Additionally, the interaction of H_2O:Al ratio and ageing temperature influenced the surface area and pore volume. When a lower H_2O:Al ratio was used, the ageing temperature possibly modified the size of the surfactant micelles. It was observed that when a larger H_2O:Al ratio was used the ageing temperature did not influence the micelle size, and therefore did not impact the resulting textural properties. The calcination heating rate influenced the combustion of the surfactant and organic materials from the alumina matrix. The interaction of ageing

temperature and calcination heating rate had an impact in the surface area of the materials.

For aluminas prepared by nanocasting, high S_{BET} and pore volume were obtained when $Al(O\text{-}i\text{-}Pr)_3$ was used as Al precursor (instead of aluminium nitrate) and a slow calcination rate was employed. It appeared that the combustion of $Al(O\text{-}i\text{-}Pr)_3$ occurred without destroying the alumina matrix. A lower heating rate facilitated a better decomposition of the organics during calcination which led to better textural properties for the alumina calcined at 1 $°C \cdot min^{-1}$.

NiMo catalysts were prepared on selected aluminas, obtaining catalysts with different average pore size, PSD profiles and pore volume.

Chapter 5: Effect of metal loading in $NiMo/Al_2O_3$ catalysts for VR hydrocracking

An alumina from Chapter 4 was selected as catalytic support. The effects of metal loading of $NiMo/Al_2O_3$ catalysts on VR hydrocracking are evaluated in this chapter. Results are correlated to the fresh and spent catalyst characterisation.

5.1. INTRODUCTION

Heavy oils are challenging to upgrade because they possess a large share of compounds detrimental to hydrocracking catalysts. Carbonaceous deposits adsorbed on the surface of the catalyst are the main cause of short-term deactivation. The ability of the catalyst to adsorb these deposits while maintaining activity poses interesting challenges for heavy oil hydrocracking. Thermal and catalytic reaction pathways occur in parallel during hydrocracking of heavy feeds. Bifunctional hydrocracking catalysts provide the necessary hydrogenation capacity, through its metal sites, to avoid or reduce coking (7). The use of large porosity catalytic supports has been proven to be beneficial to allow large asphaltene-like molecules, such as the ones present in the feed used in this study, to enter catalysts pores and diffuse in its active sites (61). Large pores are also fundamental in avoiding pore mouth blocking in the catalysts (46). The pore size of a catalyst is an important characteristic which may determine its application, but its metal loading needs to be designed as well. The balance between the catalyst acid sites, present in the support, and metal sites can be tailored to different product selectivities. If acid sites dominate the reaction, products would not be fully hydrogenated and polymerise into carbonaceous deposits. On the other hand, excess hydrogenation capacity causes a shortage in the availability of cracked molecules for reaction. This chapter addresses how varying metal content in the catalysts changes product distribution and its effects on spent catalyst textural properties.

The catalysts used in this chapter consist of the NiMo combination supported on mesoporous alumina, the same combination used throughout this thesis. This material can have a better dispersion of metal particles (180) and seems to be a promising alternative to conventional γ-aluminas for hydrocracking heavy feeds. The metals are deposited on the supports in oxide form and are afterwards sulfided to create the active phase of the catalyst, where Ni atoms decorate the edges of MoS_2 slabs forming NiMoS. The relationship between the Ni and Mo content in the catalysts is important and an atomic ratio of Ni/(Ni+Mo) close to 0.3 corresponds to the Ni and Mo sulfides optimal synergy, by having the maximum amount of Ni edge atoms to Mo edge and other atoms in the slab (31–34,181).

The influence of metal loading on hydroprocessing catalysts has been studied in previous works for model compounds and heavy feeds. HDS of model compounds was performed and catalysts with higher NiMo concentration achieved better conversions (182). It was found that the dispersion of the metals is also important, not only the concentration. When MoO_3 crystallites are formed –which happens with an 18 wt % loading on SBA type mesoporous molecular sieves– catalytic activity decreases for HDS of model compounds (183). During atmospheric gas oil hydrotreating it was found that higher MoO_3 loadings, if they are well dispersed, achieved higher HDS activity (29), similar to the effect found with model compounds. An optimal Mo content was found during hydroprocessing of VR with NiMo/alumina catalysts. This occurred at a lower Mo content than the previously mentioned studies, Mo content was varied between 0 and 8.3 wt % an optimal HDM conversion was reached at 4 wt % (184). Another study used different catalyst compositions although its main objective was to find the optimal pore size for hydrotreating of Maya crude oil (107). Research on the impact of metal loading in hydrocracking catalysts for heavy oil is scarce, which prompted this investigation.

The main objective for this chapter is to study $NiMo/Al_2O_3$ catalysts with different metal loadings during hydrocracking of vacuum residue with three reaction temperatures. The impact of the metal content was analysed in terms of initial coke deposition, VR conversion and product distribution.

Three $NiMo/Al_2O_3$ catalysts were developed maintaining the atomic ratio of Ni/(Ni+Mo) constant. These catalysts were then used to hydrocrack VR in a batch reactor at three temperatures: 400, 425 and 450 °C. Catalysts were recovered and characterised by TGA to determine the amount of coke deposits and by N_2 adsorption to explore the variation of their textural properties when compared to the fresh catalysts. Afterwards the catalysts were reutilised under the same conditions with fresh VR as feed, to

simulate how fresh feed comes in contact with catalysts in a continuous reactor. All reactions lasted 60 minutes at 185 bar H_2 pressure. Reaction products were separated into their maltene and asphaltene fractions and then maltenes were further analysed by GC to determine the boiling point distribution. These results allowed for a calculation of conversion values of the fraction boiling above 450 °C as well as for asphaltenes. The spent catalysts characterisation showed how the textural properties were affected after the initial reaction, and if further changes happened after reutilisation.

5.2. MATERIALS

5.2.1. Synthesis

5.2.1.1. Support

The alumina selected for this chapter was Alumina S6, its synthesis is described in Chapter 4 section 4.2.1, hereafter referred to as "alumina" or "Al_2O_3".

5.2.1.2. Catalysts

The catalysts have been named as Ni*x*Mo*x* where *x* is the loading of the corresponding metal oxide in wt %. The catalysts are: Ni1Mo6/Al_2O_3, Ni2Mo10/Al_2O_3 and Ni3Mo14/Al_2O_3. The atomic ratio of Ni/(Ni+Mo) for each catalyst was designed to be close to 0.3. The synthesis procedure described in Section 4.4.2 was used.

Catalyst synthesis was carried out at the Mexican Petroleum Institute (IMP) employing a TECAN MPS9500 liquid handling robot with pH, agitation, and temperature controls. The system was controlled by Symyx software which enabled the use of planned concentrations and liquid additions to the powder support. The calcination of the supports and catalysts was carried out at IMP in a tube muffle furnace under flowing air at 200 $mL \cdot min^{-1}$ at 500 °C for 4 hours.

5.2.2. Characterisation

XRF was used to measure the metal oxide loadings on the calcined catalysts in powder form (Table 5.1) observing that the nominal loadings were met. The atomic ratio of Ni/(Ni+Mo) was confirmed to be close to 0.3 for all the materials. The textural properties of the materials are presented in Table 5.2 where it was observed that all catalysts present a pore size in the mesoporous range. The pore volume and average pore diameter of the catalysts were reduced, as expected, when compared to the original support due to partial covering of pores by the metal oxides. Surface area of the catalysts increased depending on their metal content although the APD remained

similar for all materials. S_{BET} for Ni3Mo14/Al_2O_3 was similar to the Al_2O_3 support. A higher concentration of Mo could increase the S_{BET} of the material while decreasing its pore diameter (185). N_2 adsorption-desorption isotherms and pore size distribution profiles for the catalysts are presented in Figure 10.3 in Appendix 1.

Table 5.1. Metal oxide content determined by XRF.

Sample	NiO (wt %)	MoO_3 (wt %)	Ni/(Ni+Mo) atomic ratio
Al_2O_3	0	0	
Ni1Mo6/Al_2O_3	1.22	5.96	0.28
Ni2Mo10/Al_2O_3	2.11	9.54	0.30
Ni3Mo14/Al_2O_3	2.98	13.88	0.29

Table 5.2. Textural properties of the support and calcined catalysts determined by N_2 adsorption-desorption.

Sample	S_{BET} ($m^2 \cdot g^{-1}$)	Total pore volume ($cm^3 \cdot g^{-1}$)	Average pore diameter* (nm)
Al_2O_3	341.2	1.21	12.0
Ni1Mo6/Al_2O_3	282.2	0.60	11.5
Ni2Mo10/Al_2O_3	294.2	0.53	10.5
Ni3Mo14/Al_2O_3	342.5	0.66	10.4

*BJH model applied to the adsorption branch of the isotherms.

Ammonia TPD profiles for the support and catalysts are shown in Figure 5.1. It was observed that an increase in Ni/Mo loading resulted in an increase in weak acidity but a decrease in strong acidity. This occurred when metals covered the surface of Al_2O_3 and blocked acid sites. For hydrocracking reactions where catalysts are involved, larger numbers and stronger acid sites would correlate to higher cracking acidity (148). Since all of the catalysts present varying amounts of strong acidity, it is expected that cracking reactions could take place at this temperature range, even though the steric hindrance to reach acid sites is lower for NH_3 than that for large hydrocarbon molecules.

Table 5.3 shows the ratio of acid to metal sites in the catalysts. The acidity of the catalysts was characterised by NH_3-TPD study with strong acid sites present over 400 °C. The number of acid sites, n_A, are expressed as desorbed NH_3 molecules per gram of catalyst. The number of metal sites, n_M, were determined with the metal oxide content (XRF) and are expressed in atoms of Ni + Mo available per gram of catalyst.

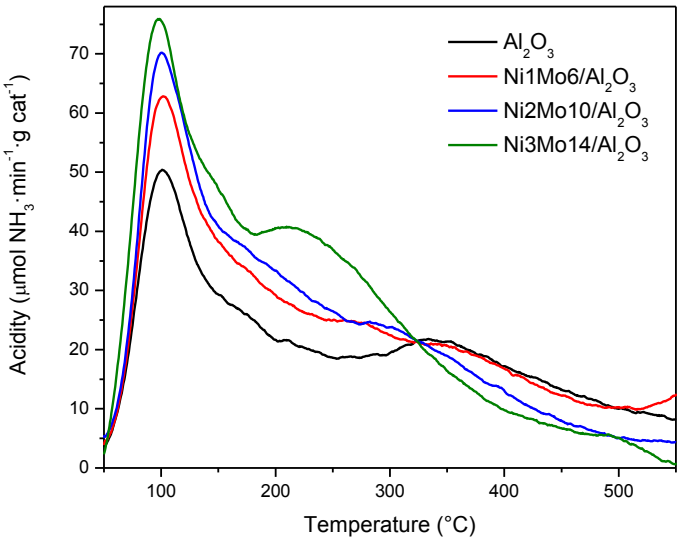

Figure 5.1. NH_3-TPD profiles for the calcined Al_2O_3 and NixMox/Al_2O_3 catalysts.

Table 5.3. Acid and metal sites available in the fresh catalysts. NH_3, Ni and Mo content expressed in molecules*.

Sample	n_A** $(NH_3 \cdot g^{-1}) \cdot 10^{-20}$	n_M $[(Ni+Mo) \cdot g^{-1}] \cdot 10^{-20}$	n_A/n_M $NH_3 \cdot (Ni+Mo)^{-1}$
Ni1Mo6/Al_2O_3	1.96	3.66	0.54
Ni2Mo10/Al_2O_3	0.77	6.19	0.12
Ni3Mo14/Al_2O_3	0.52	9.29	0.06

*NH_3 data calculated from integrated areas from Figure 5.1, acidity values calculated with an ammonia concentration calibration and taking into account the sample mass. Ni and Mo data available in Table 5.1.

**Only strong acidity accounted for (>400 °C temperature range).

Figure 5.2 displays the XRD diffraction patterns of the Al_2O_3 and catalysts. The Al_2O_3 diffractogram shows no lines characteristic of an ordered oxide phase, indicative of a mesostructure with amorphous framework (157). Three broad intensity peaks are observed which match the diffractogram reported in the alumina synthesis (160). These peaks are typically assigned to gamma alumina, suggesting some degree of ordering. The catalyst diffractograms show no Ni or Mo oxide crystallite reflections; their diffraction patterns correspond to the one for Al_2O_3. This can suggest that Ni and Mo oxides were highly dispersed in the supports and had a size of less than 4 nm, the detection limit of XRD technique (149,180,186–188). On the other hand, some Mo could be present as MoS_2 species –since the Mo precursor, ATM, contains S– which are poorly crystalline solids that XRD would not detect (189).

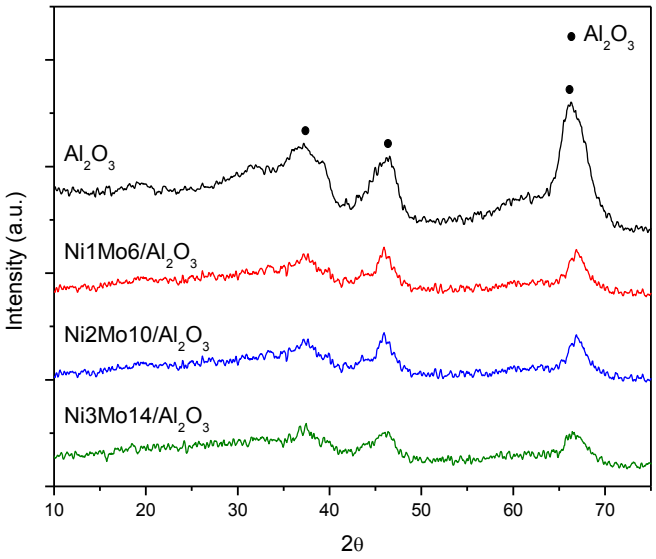

Figure 5.2. Powder XRD patterns of calcined Al_2O_3 and $NiMo/Al_2O_3$ catalysts.

Temperature programmed reduction profiles are shown in Figure 5.3 where three peaks are observed for each catalyst. Mo supported on alumina presents two main peak regions: one at low temperature around 370 °C and the other at high temperature around 830 °C (173–175). These peaks correspond to first, a reduction of octahedral Mo and afterwards the reduction of tetrahedral species (MoO_3 → MoO_2 → Mo). The first Mo reduction peak for $Ni1Mo6/Al_2O_3$ appears from 250 to 700 °C with a peak around 600 °C. This peak migrates to lower temperatures with increasing Mo content to 540 °C and 520 °C for $Ni2Mo10/Al_2O_3$ and $Ni3Mo14/Al_2O_3$, respectively. As Mo species are increasingly available and have less interaction with Al_2O_3 they were reduced at lower temperatures. The high temperature Mo reduction peak was observed at similar temperature for the three catalysts. The NiO species are reduced in a single step without intermediate formation into bulk Ni, with a peak commonly shifting to lower temperatures with increasing Ni content (176). With higher Ni loadings, an additional peak appears at around 250 °C. For $Ni1Mo6/Al_2O_3$ a single peak occurs around 500 °C, merging with the first Mo reduction, and shifts to lower reduction temperatures for $Ni2Mo10/Al_2O_3$ and $Ni3Mo14/Al_2O_3$. These last catalysts start presenting a low temperature Ni reduction as well.

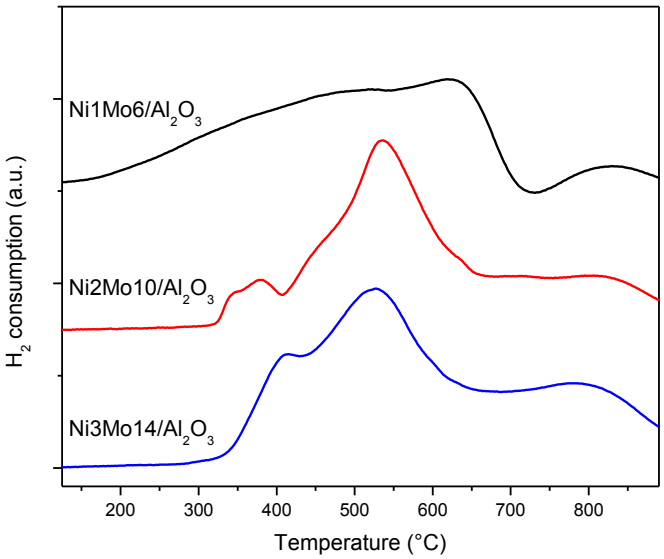

Figure 5.3. TPR spectra of calcined NiMo catalysts supported on Al_2O_3.

5.3. RESULTS AND DISCUSSION

Results were divided into two parts as follows: Section 5.3.1 which focuses on VR conversion, asphaltene upgrading and the corresponding product distribution and Section 5.3.2 which deals with changes in the spent catalysts.

5.3.1. Reaction products

5.3.1.1. Conversion

The conversion values of the >450 °C fraction ($C_{>450°C}$) and asphaltenes ($C_{Asphaltenes}$) for initial, reutilisation and thermal reactions are shown in Figure 5.4 and 5.5, respectively. Numerical values for these figures are available in Table 10.2 (Appendix 1) and in Table 10.1 for thermal runs (without catalyst). As previously mentioned in Chapter 3, for both conversion definitions coke formation was taken into account as unconverted products (Equations 1 and 2), so an increase in coke production affected the resulting values negatively.

From Figure 5.4 it was seen that $C_{>450°C}$ consistently increased for initial and reutilisation reactions when reaction temperature was increased, indicating that thermal cracking occurred alongside catalytic reactions. With increasing temperature –severity– during hydrocracking, thermal cracking rates increase and can surpass hydrogenation reactions which were not favoured by temperature (39,75,190). A 3, 7 and 14% increase in $C_{>450°C}$ occurred when metal content was increased from Ni1Mo6/Al_2O_3 to

Ni3Mo14/Al_2O_3, at the 400, 425 and 450 °C initial reactions, respectively. At 400 and 425 °C Ni1Mo6/Al_2O_3 led to slightly higher $C_{>450°C}$ than Ni2Mo10/Al_2O_3, nevertheless at 450 °C Ni2Mo10/Al_2O_3 performed as Ni3Mo14/Al_2O_3. It will be discussed in a latter section that Ni2Mo10/Al_2O_3 did not obtain the expected conversions at low temperatures. Sulfided metal sites catalyse hydrogenation-dehydrogenation reactions; therefore Ni3Mo14/Al_2O_3 would present the highest hydrogenation rates of the three studied catalysts.

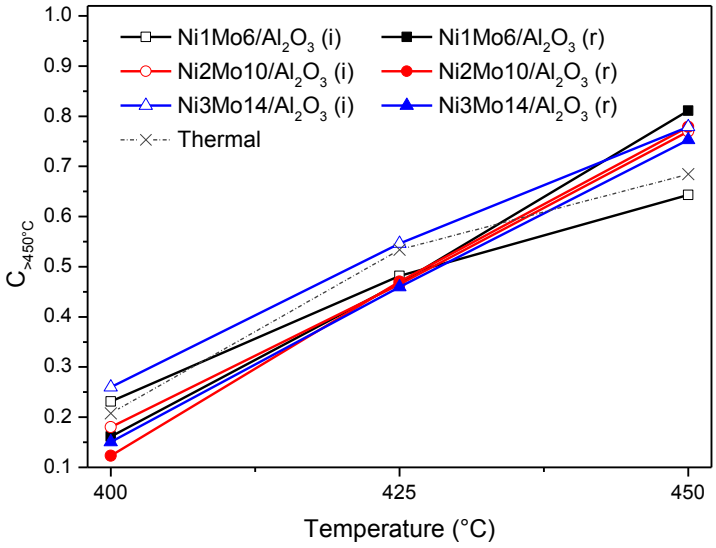

Figure 5.4. $C_{>450°C}$ for different NixMox/Al_2O_3 catalysts, for (i) initial reactions and (r) reutilisation reactions. Reactions were at 185 bar H_2 pressure for 60 minutes.

It is accepted that coke formation occurs mostly at the beginning of reaction. Its effect should mostly be felt on initial reaction $C_{>450°C}$ because it would be expected that conversion values rose when no new coke was formed, yielding higher $C_{>450°C}$ values. Nevertheless, a decrease in $C_{>450°C}$ values was observed for reutilisation reactions at 400 °C for all catalysts. At 425 °C, $C_{>450°C}$ stabilised for Ni1Mo6/Al_2O_3 and Ni2Mo10/Al_2O_3 but decreased for Ni3Mo14/Al_2O_3 and at 450 °C $C_{>450°C}$ increased for Ni1Mo6/Al_2O_3 and stabilised for Ni2Mo10/Al_2O_3 and Ni3Mo14/Al_2O_3. $C_{>450°C}$ values for reutilisation reactions did not increase with increasing metal content, therefore no trend was observed and thermal cracking dominated this conversion.

The $C_{>450°C}$ results compare well with a study (75) where coker gas oil (with 74% of the material boiling above 343 °C) was hydrocracked with a NiMo/γ-alumina in a flow reactor. In reactions above 420 °C the cracking rate was not influenced by the presence of a catalyst, but was dominated by thermal cracking, as was observed in this work. This would explain why, overall, $C_{>450°C}$ values for reutilisation reactions did not

increase with increasing metal loading. Similar conversion values were obtained for VR (b.p. above 424 °C) hydrocracked in a flow reactor at 430 °C (85). Even though conversion was not defined to include coke deposits as in the aforementioned work, coke deposits in a continuous system reach steady state and would thus be close to zero.

Figure 5.5 shows $C_{Asphaltenes}$ for initial and reutilisation reactions for $Ni1Mo6/Al_2O_3$, $Ni2Mo10/Al_2O_3$ and $Ni3Mo14/Al_2O_3$ along with thermal experiments. For initial reactions, overall, an increase in temperature resulted in an increase in $C_{Asphaltenes}$. This effect was very different from $C_{>450°C}$ in which asphaltene conversion did not rely so heavily on reaction temperature. For example, in $Ni1Mo6/Al_2O_3$ initial reactions $C_{Asphaltenes}$ varied 6% when reaction temperature was increased from 400 to 450 °C whereas $C_{>450°C}$ values increased 41% in this same temperature range. For $Ni2Mo10/Al_2O_3$ $C_{Asphaltenes}$ doubled when increasing reaction temperature from 400 to 450 °C but for $Ni3Mo14/Al_2O_3$ asphaltene conversion increased only 13%. The effect of metal loading was clearly observed for $C_{Asphaltenes}$ in initial reactions, where an increase in metal loading led to higher conversion values. $Ni2Mo10/Al_2O_3$ at 400 °C deviated from this trend because $C_{Asphaltenes}$ was higher for $Ni1Mo6/Al_2O_3$. This catalyst underperformed as well in its 400 °C reutilisation reaction but was very active at higher temperatures. All catalysts achieved higher $C_{Asphaltenes}$ during reutilisation reactions when compared to initial reactions. Spent catalysts are less acidic than fresh ones hence trigger less asphaltene adsorption on the surface (191), perhaps allowing asphaltenes to follow upgrading reaction pathways. In reutilisation reactions temperature played a role as well. Conversion values for $Ni1Mo6/Al_2O_3$ and $Ni2Mo10/Al_2O_3$ increased by 26 and 48%, correspondingly, when reaction temperature was risen from 400 to 450 °C. On the other hand, $C_{Asphaltenes}$ increased only 7% for $Ni3Mo14/Al_2O_3$, which could be explained by a limit in asphaltene upgrading capabilities for this catalyst. It was observed that if only thermal cracking was taking place, almost no asphaltene upgrading would occur. Given that no hydrogenation activity would be available without a catalyst, asphaltenes polymerised instead of converting into lower boiling point materials. Results from this section were in line with asphaltene conversions values of 60% reported for VR hydrocracking at 430 °C (85) and with values of 70% for hydrocracking of asphaltenes at 400 °C (although in the presence of toluene as a solvent in a 1:1.15 wt/wt ratio higher values should be expected) (192). The latter study stated that catalytic and thermal pathways take place in parallel during asphaltene upgrading. During VR hydrocracking on a $NiMo/Al_2O_3$ catalyst, asphaltene conversion increased in only 4% when catalyst content was increased from 1 to

10% (138). This work showed that an increase in metal content has a significantly higher impact than an increase in the oil to catalyst ratio. Other works state that asphaltene upgrading increased significantly above 425 °C (191,193,194) for VR and heavy feeds. In conclusion, metal loading did not greatly influence $C_{>450°C}$, which appeared to be dominated by thermal cracking, but was an important factor for asphaltene upgrading.

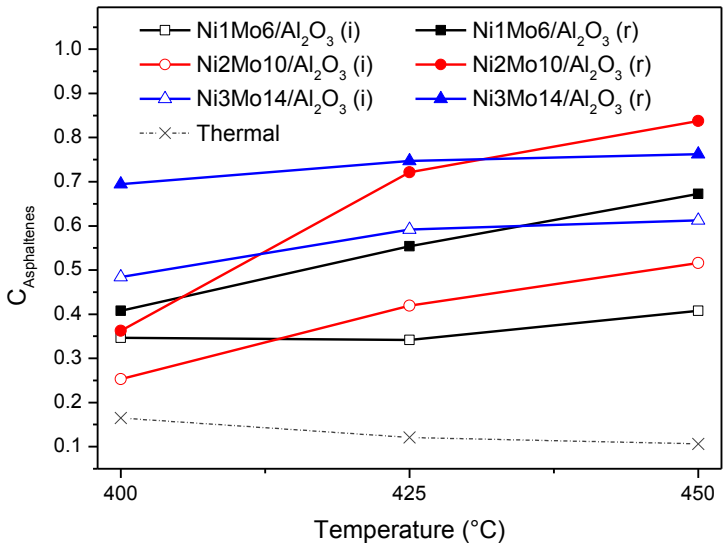

Figure 5.5. $C_{Asphaltenes}$ for different $NixMox/Al_2O_3$ catalysts for (i) initial reactions and (r) reutilisation reactions. Reactions were at 185 bar H_2 pressure for 60 minutes.

5.3.1.2. Yields

The product distribution for the three catalysts is shown in Figure 5.6a and b for initial and reutilisation reactions, respectively. The reaction products were expressed in feed wt % and were grouped into the following fractions (with increasing boiling point): Gas, $Maltenes_{<450°C}$, $Maltenes_{>450°C}$, Asphaltenes and Solids. As explained in Section 3.2.1.5, Gas was calculated by Equation 5, liquid products were fractioned into Asphaltenes and Maltenes, then the content of $Maltenes_{<450°C}$ and $Maltenes_{>450°C}$ was determined by GC, and the carbonaceous deposits were reported as Solids, determined by TGA. The Solids reported for reutilisation reactions are the materials formed in this reaction i.e. coke deposits from the first reaction were not accounted for. Detailed data used for Figure 5.6 is found in Table 10.3 and 10.4 (Appendix 1) for initial and reutilisation reactions, respectively.

Effect of temperature in initial reactions. The Gas fraction increased steadily with temperature for all catalysts, from a yield close to zero at 400 °C to 30-40 wt % at

450 °C. This trend was consistent with literature data (19,195,196) and indicates that thermal cracking took place in parallel with catalytic reactions. This could be attributed to breakage of side chains or chains between aromatic rings that were subsequently removed from the asphaltene structure. Thermal reactions (Table 10.1 in Appendix 1) showed that when a catalyst was employed, a reduction in gas production occurred. $Maltenes_{<450°C}$ increased when reaction temperature was raised, although only by 10% from low to high temperature reactions. Another product that varied significantly with temperature for all catalysts were $Maltenes_{>450°C}$, which decreased from above 60 wt % at 400 °C for all catalysts to around 30 or 20 wt % at 450 °C for Ni1Mo6/Al_2O_3 and the others, respectively. This would explain that the main upgrading pathway for this fraction was via thermal reactions. Asphaltenes yields were almost unaffected by temperature, except for Ni2Mo10/Al_2O_3. Solids varied with reaction temperature, with higher yields at lower temperatures for all catalysts. This was consistent with results reported for the hydrocracking of atmospheric residue with NiMo/alumina catalyst in a batch reactor (116). The authors explained this observation via a reduction of coke precursors in the system, which does not happen in continuous feeding systems because the concentration of these precursors is constant. Coke can also evolve by hydrogenating into lighter compounds and is specially reactive in initial stages of reaction (108). Nevertheless, when unsupported catalysts were used in a batch reactor an increase in coke was expected with increasing reaction temperature (39,136,197). It then appears that the alumina support played an important role in allowing coke deposits to behave in a dynamic form. In general, temperature influenced product yields in an important manner for Gas and $Maltenes_{>450°C}$ and had some effect in increasing $Maltenes_{<450°C}$ and reducing Asphaltenes and Solids.

Effect of catalyst in initial reactions. A rise in metal loading accounted for a larger amount of available metal sites for hydrogenation reactions. The n_A/n_M ratio of the catalysts changed the balance of cracking activity and hydrogenation activity (Table 5.3). The n_A/n_M ratio for the catalysts followed: Ni1Mo6/Al_2O_3 > Ni2Mo10/Al_2O_3 > Ni3Mo14/Al_2O_3. The catalyst with the higher n_A/n_M had lower hydrogenation activity per site, which was reflected in the highest Solids yield. Asphaltene content in the products was affected by the catalyst metal loading given that higher hydrogenation capacity would increase asphaltene upgrading. As expected, Ni3Mo14/Al_2O_3 presented lower Asphaltenes yield. It was mentioned previously that $Maltenes_{>450°C}$ yields were mostly affected by temperature. In addition to thermal cracking, catalytic effects on this fraction were observed in 450 °C reactions using Ni2Mo10/Al_2O_3 and Ni3Mo14/Al_2O_3 which led to higher conversion. The $Maltenes_{<450°C}$ yields were very similar for all catalysts at all

temperatures except for Ni3Mo14/Al_2O_3, which had a higher activity at 425 and 450 °C. Finally, Gas production was higher for Ni2Mo10/Al_2O_3 and Ni3Mo14/Al_2O_3, which showed that at high temperatures high boiling point fractions hydrogenated completely into Gas (196). The decrease in Asphaltenes and Solids yields showed that catalytic activity took place. Ni2Mo10/Al_2O_3 and Ni3Mo14/Al_2O_3 presented higher activity at higher temperatures.

Effect of temperature and catalyst in reutilisation reactions. Temperature affected reutilisation reactions in the same manner as in initial reactions. Increasing temperature caused Gas and $Maltenes_{<450°C}$ yields to increase, $Maltenes_{>450°C}$ yields to decline, and the reduction of Asphaltenes yields. Solids from reutilisation reactions appeared to remain unaffected by changes in temperature. The trends for catalytic activity for initial reactions held for reutilisation reactions.

Overall effect of reutilisation of catalysts. The most important change that occurred to the product yield when catalysts were reutilised at any temperature was the decline in new coke build-up. It is well accepted that coke deposition reaches steady state after increasing rapidly in the first hours of contact with hydrocarbon feeds (43,198). Solid production occurred for most reutilisation reactions, nevertheless the yields were significantly lower than for initial reactions. These trends were in agreement with (54,108,134) where the same approach of catalyst reutilisation was employed. This evidence corroborated what was discussed in Section 5.3.1.1 –when less coke was factored into the equations used to calculate $C_{>450°C}$ and $C_{Asphaltenes}$ (Equation 1 and 2) greater conversion values were obtained. Ni2Mo10/Al_2O_3 had a 2% yield of Solids in its reutilisation at 400°C, the higher value for this fraction during reutilisations. This indicated that coke deposits for this catalyst had not stabilised yet, and could account for lower $C_{>450°C}$ and $C_{Asphaltenes}$ at these conditions. The Solids yield for Ni3Mo14/Al_2O_3 at 450 °C was 1.3%, which could indicate that this catalyst was also stabilising. Coke deposits were still forming in the reutilisation reaction thus the reduction in $C_{>450°C}$ could be caused by the negative impact of coke on conversion values. Coke deposits are formed by the polymerisation of asphaltene molecules into larger structures mostly formed by aromatics. If less coke deposits were generated, asphaltenes could follow alternative reaction pathways. An increase in Asphaltenes yield was observed for some reutilisation reactions, compared to initial reactions, which could be attributed to asphaltenes that did not polymerise but remained unreactive. This was the case for reactions at 400 °C for all catalysts so it appeared that thermal cracking of this fraction was needed to trigger their upgrading. Ni2Mo10/Al_2O_3 and Ni3Mo14/Al_2O_3 remained highly active at 425 and 450 °C for asphaltene upgrading and

showed lower Asphaltene yields in their reutilisation. Asphaltenes were converted into $Maltenes_{>450°C}$ since this fraction observed its yields increase for all reutilisations. Ni1Mo10/Al_2O_3 presented constant Asphaltene yields for its 450 °C reutilisation but interestingly the $Maltenes_{>450°C}$ fraction upgraded into $Maltenes_{<450°C}$. This could reveal that stabilisation of the catalysts allowed for selectivity to increase into desirable products ($Maltenes_{<450°C}$). The Gas yield for Ni3Mo14/Al_2O_3 decreased in its 450 °C reutilisation, possibly due to the decreased cracking function of the catalyst given that its acid sites would be covered by coke. In conclusion, the strategy of reutilising catalysts provided a way to assess their effectiveness when coated with carbon deposits. Since these deposits formed mainly in the first reaction, asphaltenes and heavy maltenes could follow reaction pathways into lower boiling point materials in the catalyst reutilisation.

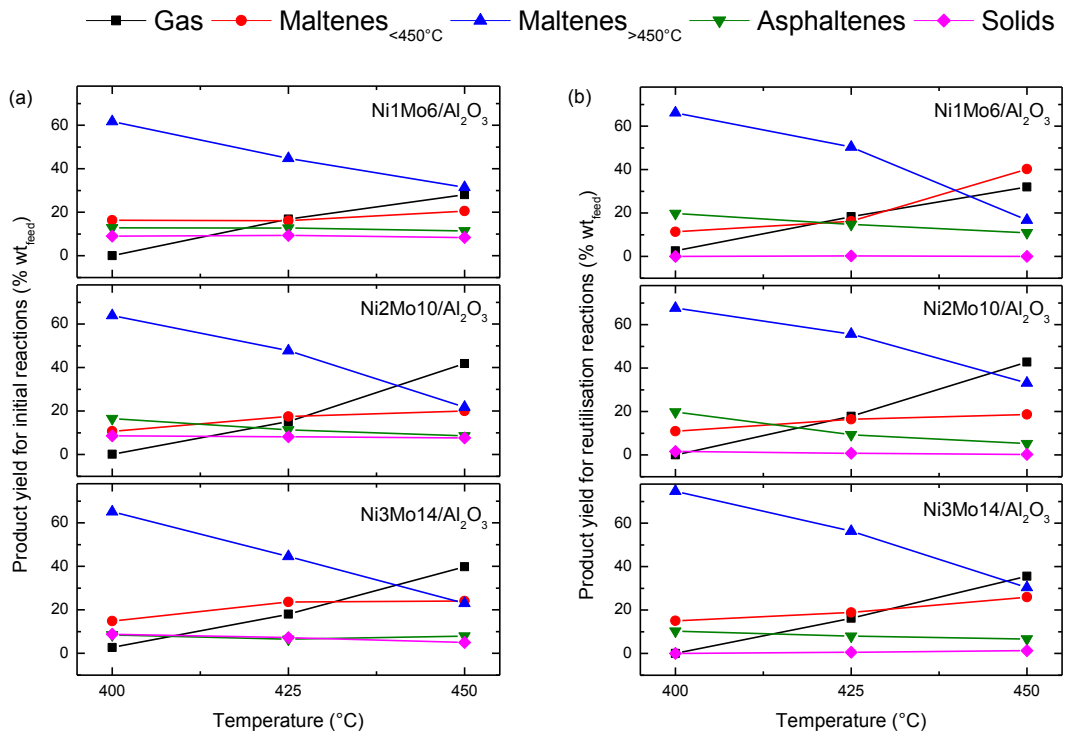

Figure 5.6. Product yields for (a) initial and (b) reutilisation reactions with NixMox/Al_2O_3 catalysts. All reactions lasted 60 minutes with an initial 185 bar H_2 pressure.

5.3.1.3. Selectivity

The product distributions for $Maltenes_{<450°C}$, calculated from GC SimDis of this fraction, are displayed in Figure 5.7. Data for this section are available in Table 10.5 (Appendix 1). The fractions were considered within the following boiling point distribution ranges: up to 204 °C for heavy naphtha, 204-260 °C for kerosene, 260-343 °C for diesel, 343-427 °C for gas oils and finally 427-450 °C for residue. It was

observed that the product yields did not vary between the different catalysts. Even though the upgrading into $Maltenes_{<450°C}$ was dependent of catalytic activity, the product distribution of lower boiling point materials was not affected by it, the same product distribution was obtained.

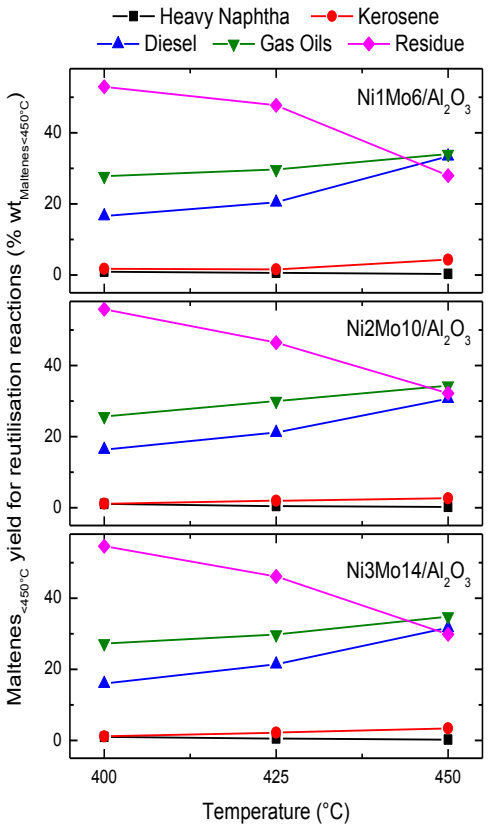

Figure 5.7. Product yields for $Maltenes_{<450°C}$ for reutilisation reactions with NixMox/Al_2O_3 catalysts. All reactions lasted 60 minutes with an initial 185 bar H_2 pressure.

Figure 5.8 shows the maltene to asphaltene (M/A) ratio of products for the reutilisation reactions. This ratio was calculated as the total maltene yields ($Maltenes_{<450°C}$ + $Maltenes_{>450°C}$) to Asphaltene yield for liquid products, i.e. not accounting for Gas and Solids production. Data for this section are available in Table 10.6 (Appendix 1).

Higher hydrogenation capacity and lower n_A/n_M ratio of the catalysts reduced the asphaltene content. There were some thermal effects on the resulting M/A ratio for all catalysts since higher temperature reactions led to a higher ratio. For Ni1Mo6/Al_2O_3 a constant rise in the M/A ratio was observed with increasing temperature –the M/A ratio increased from 3.9 to 5.2 from the 400 to the 450 °C reutilisation reactions. Ni2Mo10/Al_2O_3 presented a substantial increase in the products M/A ratio, from 4.0 to 9.9, when temperature was increased. This accounted for a 50% reduction in Asphaltenes yield. In the TPR study for the catalysts (Figure 5.3) it was observed that

the reducibility of NiO and MoO_3 migrated to lower temperatures with increasing metal loading. Therefore Ni2Mo10/Al_2O_3 had more active sites at lower temperatures than Ni1Mo6/Al_2O_3, which would account for the rise in its activity and resulting increase in M/A ratio at 425 and 450 °C. Ni2Mo10/Al_2O_3 outperformed Ni3Mo14/Al_2O_3 at 450 °C, even though the latter had a higher metal content. This could relate to the relatively high increase in coke deposits of Ni3Mo14/Al_2O_3 in its reutilisation reaction and tie to the decrease in $C_{>450°C}$ at these conditions. On the other hand, Ni3Mo14/Al_2O_3 presented a fairly constant M/A ratio at all temperatures, indicating that it was active at all temperatures. From its TPR study it was observed that it was more easily reducible, then it achieved a maximum activity from the lower reaction temperature, 400 °C, by reaching the catalytic activity threshold. Its n_A/n_M was the lowest of the three catalysts and it appeared that the metal function had a better balance for asphaltene upgrading.

The M/A ratio for VR was 2, and in thermal runs, without catalysts, it decreased to 1.2 at 450 °C (data for thermal runs available in Table 10.1). Therefore, catalytic asphaltene upgrading was achieved with the catalysts used in this study.

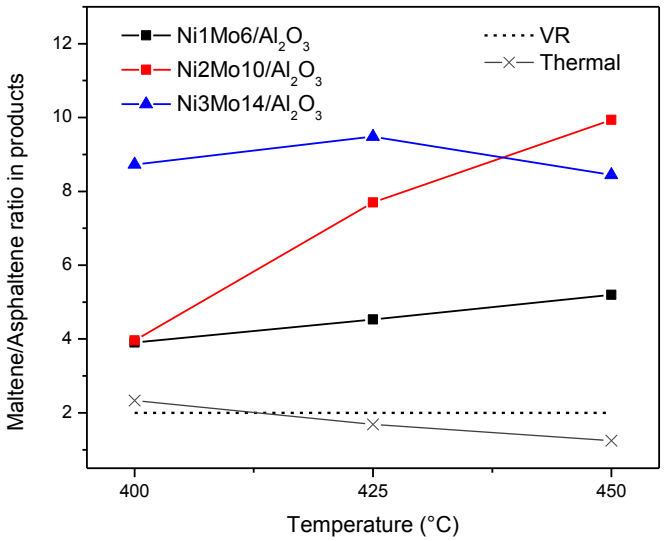

Figure 5.8. Maltene to asphaltene ratio in VR and reutilisation reaction products. All reactions lasted 60 minutes with an initial 185 bar H_2 pressure.

Carbonaceous deposits and gas products were found to be directly tied to reaction temperature, as it has been mentioned before. A study comparing catalytic and thermal reactions found that gas production was mostly independent of catalytic activity (75). In Figure 5.9 it was identified that for reutilisation reactions all catalysts followed the same trend for the sum of coke (Solids yield) and gas production. There were only significant differences between the catalysts for reactions at 450 °C; the catalyst with lower metal

content presented lower coke and gas production. Gas production was higher for Ni2Mo10/Al_2O_3. It was observed that the stability of coke deposits on the catalyst could influence the selectivity to gases. Thermal gas and coke production were significantly higher, showing that the catalysts suppressed thermal cracking (84).

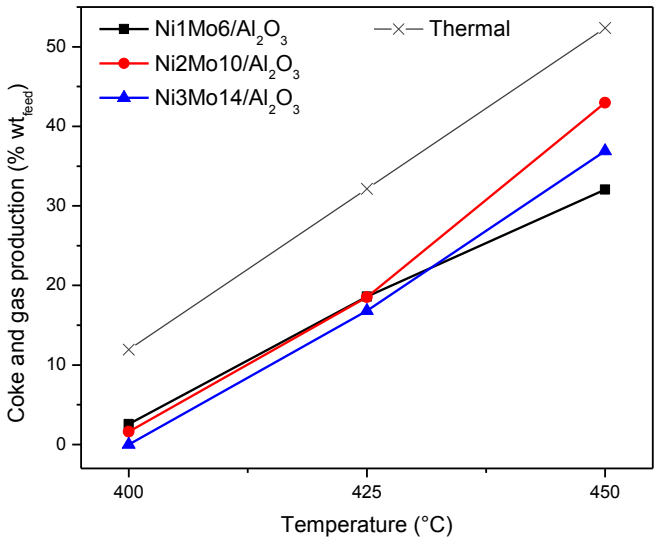

Figure 5.9. Coke and gas production expressed as wt % of feed in reutilisation reaction products. All reactions lasted 60 minutes with an initial 185 bar H_2 pressure.

5.3.2. Spent catalysts

After each reaction spent catalysts were characterised with TGA for coke deposits and N_2 adsorption-desorption to evaluate changes in their textural properties.

5.3.2.1. Coke deposits

The contents of Table 5.4 show the amount of coke deposited on the catalysts at all the reaction conditions and relates to the Solids yield reported previously (Section 5.3.1.2). The values in this section are expressed as gram of coke per gram of catalyst, instead of as a yield. This variable would not be highly influential in this study since the initial S_{BET} for all catalysts was in the same range. It was mentioned in Section 5.3.1.2 already that coke deposits decreased with increasing reaction temperature in a batch system. Coke deposits also varied with the catalysts metal loading –higher hydrogenation to cracking activity (Ni3Mo14/Al_2O_3) led to lower coke deposits at all temperatures. During reutilisation reactions there was an increase in coke deposits for Ni2Mo10/Al_2O_3 and Ni3Mo14/Al_2O_3, indicating that they had not stabilised yet. The reutilisation reaction of Ni3Mo14/Al_2O_3 at 400 °C was an exception. Since the n_A/n_M ratio was lower for these catalysts coke formation occurred at a slower pace. Coke

deposits had a higher increase in the 400 °C reutilisation reactions for $Ni2Mo10/Al_2O_3$. Coke deposition for $Ni1Mo6/Al_2O_3$ was close to zero for reutilisation reactions. Possibly all catalysts would obtain the same stable coke deposits eventually at each reaction temperature since these deposits would neutralise acidity. This study confirmed that a higher metal loading, or reduced acidity, slows down initial coke deposition (191). The values of coke observed in this study would be expected for a heavy feed such as VR, given that the higher the asphaltene content of the feed, the higher wt % of carbon that deposited on the catalysts. For AR a carbon content of above 15 wt % was expected in the first hours of reaction (113).

Table 5.4. Coke on catalyst determined by TGA analysis.

Sample	g coke per g catalyst at different reaction temperatures* (°C)					
	400 (i)	400 (r)	425 (i)	425 (r)	450 (i)	450 (r)
$Ni1Mo6/Al_2O_3$	0.41	0.41	0.38	0.39	0.35	0.35
$Ni2Mo10/Al_2O_3$	0.35	0.44	0.33	0.36	0.31	0.32
$Ni3Mo14/Al_2O_3$	0.36	0.36	0.28	0.31	0.20	0.25

*(i) for initial and (r) for reutilisation reactions.

5.3.2.2. Textural properties

The textural properties described in Table 5.5 demonstrated that all catalysts suffered changes after reaction. Overall, catalysts underwent a reduction in S_{BET}, pore volume and average pore diameter. This same effect had been reported previously in the literature (61,108). Other studies (107,111) argue that average pore diameter increases with declining S_{BET} and pore volume after hydrocracking reactions. This was explained by coke covering the catalyst pores and immediately reducing S_{BET} and pore volume but blocking the mouth of the smallest pores, hence increasing APD. The change in S_{BET} and pore volume was related to the coke deposits, with higher coke deposits causing a higher reduction in these properties.

It was reported (61) that the impact of coke in pores with large diameter (above 10 nm) was less than the effect of coke in smaller pores, observing a reduction in pore size and volume even in short 1 hr contact time reactions. Other results suggested that pores below 2 nm did not allow residue molecules to penetrate because of steric hindrance and therefore could not cause pore mouth plugging (108). Therefore, the decrease or increase of pore diameter in a spent catalyst can depend on the properties of the feed it comes in contact with, if the catalyst is present as an extrudate or in powder form and its initial pore size distribution.

Table 5.5. Textural properties of the fresh and spent catalysts determined by N_2 adsorption. All reactions lasted 60 minutes with an initial 185 bar H_2 pressure.

Sample	T* (°C)	S_{BET} ($m^2 \cdot g^{-1}$)	Total pore volume ($cm^3 \cdot g^{-1}$)	Average pore diameter** (nm)
Ni1Mo6/Al_2O_3	fresh	282.2	0.60	11.5
	400 (i)	57.8	0.09	6.7
	400 (r)	92.5	0.15	6.1
	425 (i)	167.6	0.23	5.4
	425 (r)	139.5	0.22	5.8
	450 (i)	73.7	0.12	6.0
	450 (r)	107.6	0.18	6.4
Ni2Mo10/Al_2O_3	fresh	294.2	0.53	10.5
	400 (i)	141.7	0.29	7.3
	400 (r)	104.0	0.23	7.6
	425 (i)	136.1	0.29	7.3
	425 (r)	121.4	0.26	7.8
	450 (i)	183.2	0.32	6.5
	450 (r)	144.6	0.30	7.3
Ni3Mo14/Al_2O_3	fresh	342.5	0.66	10.4
	400 (i)	145.6	0.26	6.3
	400 (r)	141.9	0.24	5.9
	425 (i)	229.4	0.40	5.8
	425 (r)	201.0	0.37	6.1
	450 (i)	229.6	0.46	6.9
	450 (r)	180.3	0.38	7.0

*(i) for initial and (r) for reutilisation reactions.

**BJH model applied to the adsorption branch of the isotherms

The N_2 adsorption-desorption isotherms for spent Ni1Mo6/Al_2O_3, Ni2Mo10/Al_2O_3 and Ni3Mo14/Al_2O_3 are represented in Figure 5.10, 5.11 and 5.12, respectively. Isotherms for all spent catalysts retained the shape of the fresh ones: a Type IV isotherm with hysteresis loop H3, which matched materials formed by plate-like particles assembled in parallel (126). The isotherms also matched the shape of the Al_2O_3 isotherm reported in its synthesis (160) and verified in the alumina support used (Figure 4.5). The shape and position of the hysteresis cycles in most of the spent catalysts started at slightly lower relative pressures than the hysteresis loops of the fresh catalysts. This was indicative of the retention of the mesoporosity of the original materials. Since the hysteresis loops did not increase, deactivation by pore mouth plugging was minimal (46). Coke deposits affected the N_2 uptake capacity, as observed in the isotherms. Higher coke deposits corresponded to lower N_2 volumes in relative pressure values near 1. Reductions in N_2 uptake capacity were observed through decreased S_{BET} of the materials (Table 5.5). The N_2 uptake capacity decreased for spent catalysts

in the whole P/Po range, therefore it was expected that coke was deposited evenly in pores of different sizes.

Spent Ni1Mo6/Al_2O_3 catalysts had a similar isotherm shape as the fresh catalyst. The isotherms of the catalysts from initial reactions at 400 and 450 °C had lower N_2 uptake values (throughout all relative pressures) than the ones for reutilisation reactions even though they presented constant coke deposits. This reflected the reduction in S_{BET} in these initial reactions which then recovered to higher values for the corresponding reutilisations. Since coke deposits were permeable and reactive, they could first block most of the surface area and then react to form more compact –or aged– coke in the subsequent reaction. The isotherm for the reutilisation reaction at 425 °C fell out of order in the maximum N_2 uptake because this catalyst had not stabilised in coke content. Higher N_2 uptake capacity at low relative pressures corresponded to more pores in the smaller pore sizes, as was also observed in Figure 5.13.

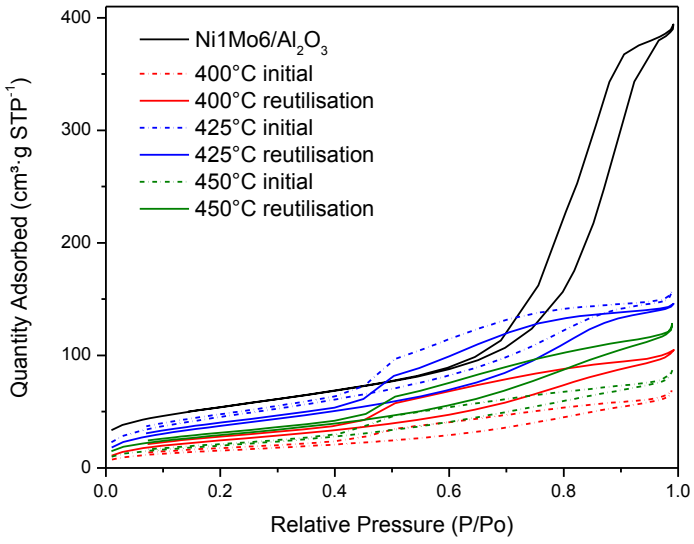

Figure 5.10. N_2 adsorption-desorption isotherms of fresh and spent Ni1Mo6/Al_2O_3 catalysts. All reactions lasted 60 minutes with an initial 185 bar H_2 pressure.

Isotherms for spent Ni2Mo10/Al_2O_3 and Ni3Mo14/Al_2O_3 achieved higher N_2 uptake in the following order for reaction temperatures: 450 > 425 > 400 °C. This order matched decreasing coke content. Finally, the isotherm for the initial and reutilisation reactions of Ni3Mo14/Al_2O_3 at 400 °C had a relatively different shape than the fresh catalyst. The stable coke deposits at this temperature could imply denser coke was forming; these coke deposits could cause its pore structure to change to some extent, evidenced by the variations in its isotherm shape.

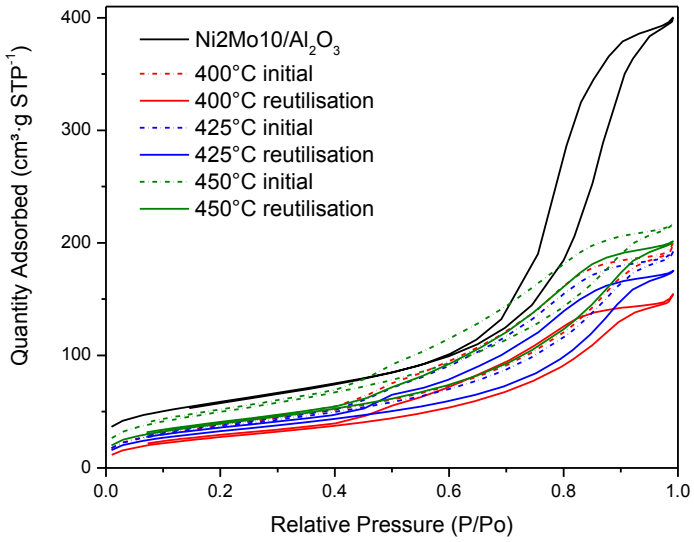

Figure 5.11. N_2 adsorption-desorption isotherms of fresh and spent $Ni2Mo10/Al_2O_3$ catalysts. All reactions lasted 60 minutes with an initial 185 bar H_2 pressure.

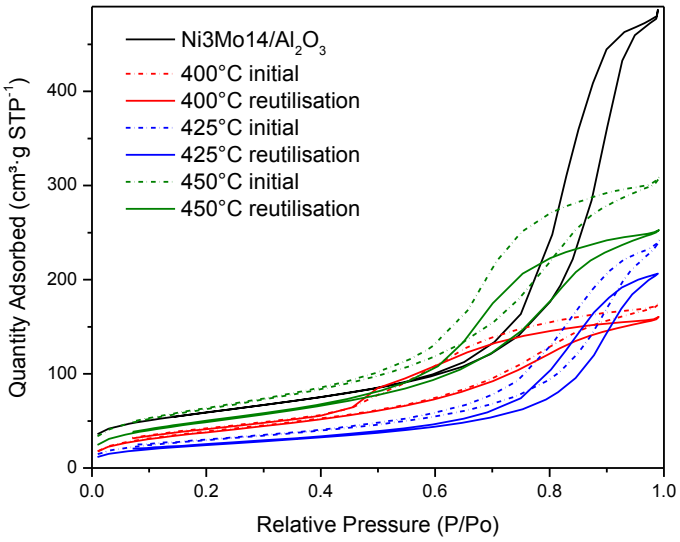

Figure 5.12. N_2 adsorption-desorption isotherms of fresh and spent $Ni3Mo14/Al_2O_3$ catalysts. All reactions lasted 60 minutes with an initial 185 bar H_2 pressure.

The microporosity of the materials was observed at low relative pressures of the isotherms. At relative pressures close to 1.0 the presence of macropores were observed if the isotherms did not remain horizontal (126). The microporous region of the isotherms for spent catalysts had a reduction in its N_2 uptake capacity compared to fresh catalysts, showing that the smallest pores were lost. The shape of the isotherms

at high relative pressures did not change for spent catalysts; therefore the macroporosity of the materials was not affected.

In this work, catalysts presented similar coke deposits while maintaining the isotherm shape whereas in other published studies (70,87) it was observed that isotherms drastically changed shape. Therefore it appears that the structure of this alumina, plate-like particles assembled in parallel, permitted high coke deposits while maintaining its textural properties.

Changes in the pore size distribution profiles for $Ni1Mo6/Al_2O_3$, $Ni2Mo10/Al_2O_3$ and $Ni3Mo14/Al_2O_3$ are shown in Figure 5.13, 5.14 and 5.15, respectively. The PSD curves for all fresh catalysts are represented in Figure 10.3 (Appendix 1). The PSD profiles for catalysts spent in reutilisation reactions had lower pore volume than for catalysts spent in initial reactions. The only exception to this were the reutilisations at 400 and 450 °C for $Ni1Mo6/Al_2O_3$, conditions at which coke deposits were stable (Table 5.4). These figures also revealed that lower coke deposits resulted in a lower effect on PSD profile; the PSD curve had pore volumes in decreasing order for reutilisations at: 450, 425 and 400 °C.

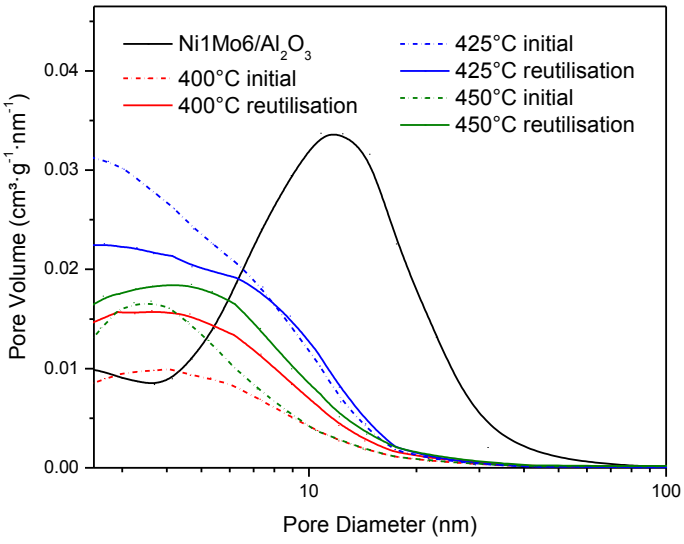

Figure 5.13. Pore diameter distribution as a function of pore volume for spent $Ni1Mo6/Al_2O_3$ catalysts. All reactions lasted 60 minutes with an initial 185 bar H_2 pressure.

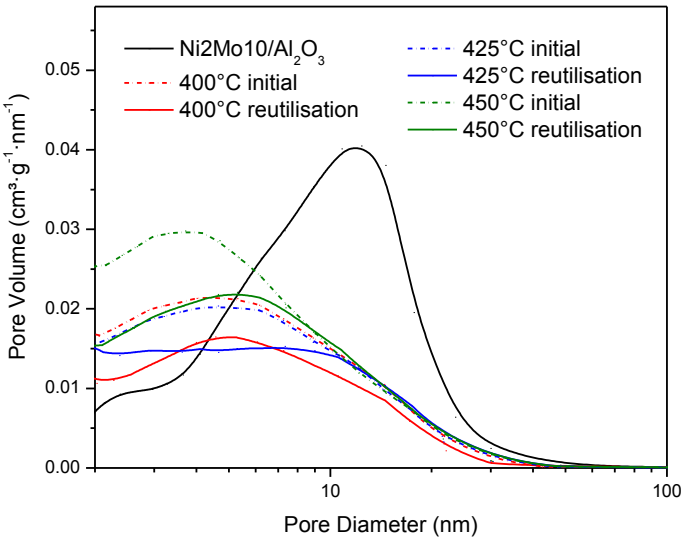

Figure 5.14. Pore diameter distribution as a function of pore volume for spent $Ni2Mo10/Al_2O_3$ catalysts. All reactions lasted 60 minutes with an initial 185 bar H_2 pressure.

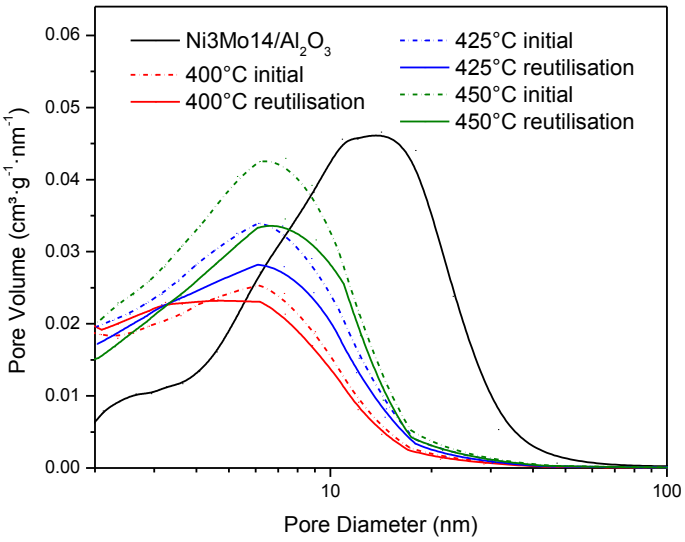

Figure 5.15. Pore diameter distribution as a function of pore volume for spent $Ni3Mo14/Al_2O_3$ catalysts. All reactions lasted 60 minutes with an initial 185 bar H_2 pressure.

In all spent catalysts the pore volume decreased in the whole range of pore sizes, suggesting coke was deposited in the whole pore size range causing the narrowing of the pores, as observed with coked CoMo/alumina (199).

5.3.3. Effects of coking

In this section the relationship between coke deposits, conversions and textural properties are discussed. Reaction conditions influenced coke deposits which then in turn affected conversion values and textural properties. Coke deposits for spent catalysts are reported in Table 5.4. $Ni1Mo6/Al_2O_3$ presented the narrowest range of values, from 0.35 to 0.41, then $Ni2Mo10/Al_2O_3$, from 0.31 to 0.44, and finally $Ni3Mo14/Al_2O_3$ with values from 0.20 to 0.36. This showed that the range of values from lower to higher coke deposition increased with increasing metal deposition.

5.3.3.1. On conversion

Figure 5.16a and b illustrate how coke deposits, reported from Table 5.4, affected $C_{>450°C}$ and $C_{Asphaltenes}$, respectively. Generally, $C_{>450°C}$ values followed a trend opposite to coke deposition. Higher coke deposits accounted for lower $C_{>450°C}$. Minimum and maximum $C_{>450°C}$ were similar for all catalysts, whereas minimum and maximum $C_{Asphaltenes}$ depended on the catalyst. Coke deposits did not affect $C_{Asphaltenes}$ as greatly as $C_{>450°C}$; for $Ni3Mo14/Al_2O_3$ $C_{Asphaltenes}$ were almost independent of coke content. In some cases $Ni1Mo6/Al_2O_3$ and $Ni2Mo10/Al_2O_3$ obtained different $C_{Asphaltenes}$ with the same coke content.

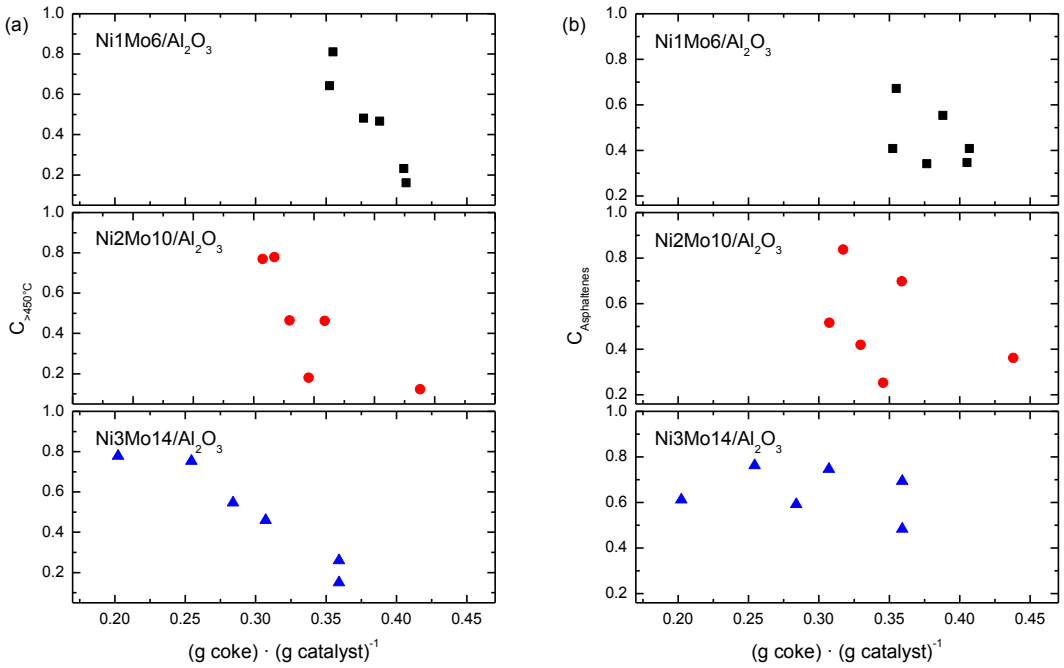

Figure 5.16. (a) $C_{>450°C}$ and (b) $C_{Asphaltenes}$ for initial and reutilisation reactions of $NiMo/Al_2O_3$ catalysts. All reactions lasted 60 minutes with an initial 185 bar H_2 pressure.

5.3.3.2. On textural properties

The relationship between coke content and relative S_{BET} is displayed in Figure 5.17. Relative S_{BET} was calculated by normalising the values of the spent with the fresh catalysts. A general trend was observed for $Ni2Mo10/Al_2O_3$ and $Ni3Mo14/Al_2O_3$: increasing coke content caused a decrease in relative S_{BET}. This trend was also observed (101) where a sample with 24 wt % carbon (corresponding to 0.19 g coke·g catalyst^{-1}) retained 60% of the fresh catalyst S_{BET}. The dispersion of values for coke deposits, as mentioned previously, depended on the metal content of the catalysts. This trend was not held for $Ni1Mo6/Al_2O_3$ as this catalyst presented an increase in S_{BET} when coke deposits had stabilised.

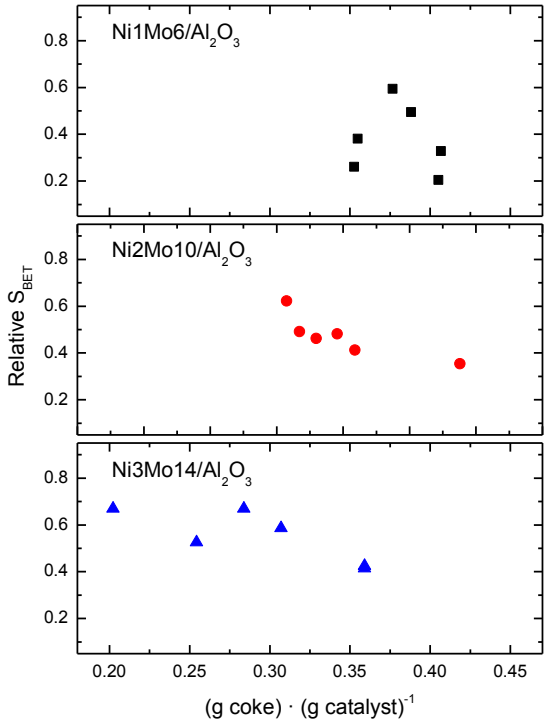

Figure 5.17. Surface area of the spent $NiMo/Al_2O_3$ relative to the surface area of the fresh catalysts. All reactions lasted 60 minutes with an initial 185 bar H_2 pressure.

Figure 5.18 shows how relative pore volume decreased with increasing coke deposits. The relative pore volume was calculated by normalising the values of the spent with the fresh catalysts. In all cases, a higher reduction in relative S_{BET} than in relative pore volume occurred, opposed to a study where catalyst pellets were used (101). At similar coking values, $Ni1Mo6/Al_2O_3$ had the furthest reduction in pore volume and S_{BET}, then $Ni2Mo10/Al_2O_3$ and lastly $Ni3Mo14/Al_2O_3$. Even at the same reaction conditions (reutilisation reactions at 425 °C for $Ni2Mo10/Al_2O_3$ and $Ni3Mo14/Al_2O_3$) with the same

coke deposits of 0.36 (g coke)·(g catalyst)$^{-1}$ the catalyst with lower n_A/n_M ratio better maintained its textural properties. Additionally, in the higher coking scenario –the 400 °C reutilisation– Ni2Mo10/Al_2O_3 suffered less reduction in S_{BET} and pore volume than the other catalysts. As mentioned before, Ni1Mo6/Al_2O_3 did not have a trend of decreasing pore volume with increasing coke content. Nevertheless it was observed that the pore volume increased when coke deposits stabilised.

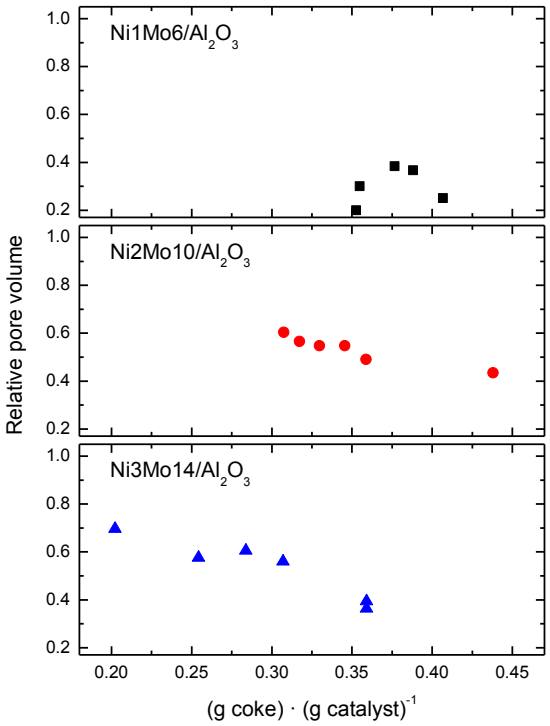

Figure 5.18. Pore volume of the spent NiMo/Al_2O_3 relative to the pore volume of the fresh catalysts. All reactions lasted 60 minutes with an initial 185 bar H_2 pressure.

In Figure 5.19 it was observed that Ni1Mo6/Al_2O_3 had the larger reduction in APD of the three catalysts at any condition. It was interesting to observe that even though coke deposits almost stabilised for this catalyst at all conditions, it still had changes in the textural properties in the reutilisation reactions. For example, at 400 °C the APD decreased to 0.58 times the original APD in the initial reaction and decreased further to 0.53 (of the original APD as well) in the reutilisation. It has been shown that coke is reactive and can evolve into different configurations, becoming more aromatic in nature with time (109,110). Refractory coke (hard coke) forms on the catalysts acid sites (113) whereas soft coke adsorbs on the catalyst and can react because it consists of aromatics and asphaltenes (200). The results presented here support this theory. Even a small increase in coke deposits caused a decrease in APD. For Ni2Mo10/Al_2O_3 and Ni3Mo14/Al2O3 the APD values varied from 0.62 to 0.74 and from 0.56 to 0.67

times the fresh catalyst APD, respectively. The amount of coke deposits did not have a clear correlation with changes in the APD for spent catalysts. Conversely, more coke generally caused a further reduction in S_{BET} and pore volume.

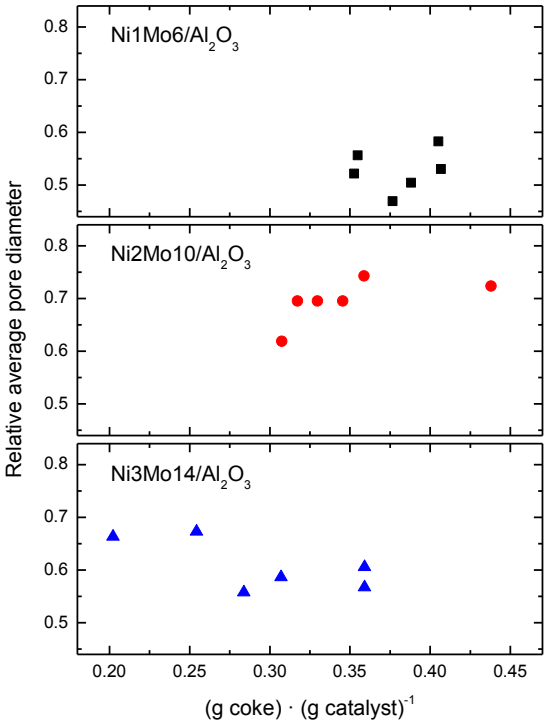

Figure 5.19. Average pore diameter of the spent NiMo/Al_2O_3 relative to the APD of the fresh catalysts. All reactions lasted 60 minutes with an initial 185 bar H_2 pressure.

5.4. CONCLUSIONS

The influence of metal loading in NiMo/Al_2O_3 catalysts has been studied for the initial stages of hydrocracking reactions. Highly dispersed catalysts were synthesised on a mesoporous Al_2O_3; they retained the mesoporosity after metal impregnation. The catalysts presented strong acidity, which is required for bifunctional catalysts used in hydrocracking reactions. A higher metal content allowed the Ni and Mo oxides to reduce at lower temperatures during TPR analysis, suggesting higher availability of metal active sites for Ni3Mo14/Al_2O_3. This catalyst also presented the lowest n_A/n_M ratio which possibly reflected on lower coke deposits.

When hydrocracking VR it was observed that thermal and catalytic reactions occurred concurrently, which was expected because of the reaction conditions. Conversions for the >450 °C fraction and asphaltenes, $C_{>450°C}$ and $C_{Asphaltenes}$, were in line with results from the literature that employed continuous reactors, even though a batch reactor was used in this work. Metal loading proved to be moderately influential for $C_{>450°C}$ in which

thermal reactions dominated. For $C_{Asphaltenes}$ the impact of metal loading was more important: higher metal loading led to higher asphaltene conversions. The catalyst with higher metal loading (Ni3Mo14/Al_2O_3) achieved a maximum asphaltene conversion that was stable across all reaction temperatures, showing that catalytic pathways predominated over thermal ones. For the other catalysts thermal reactions played a more important role in asphaltene upgrading, as it was observed that $C_{Asphaltenes}$ rose significantly with increasing temperature.

The relationship between thermal and catalytic reactions was analysed in more detail via product distribution. Thermal reactions were dominant mainly for gas production but were important for upgrading the fraction of maltenes boiling above 450 °C. The impact of temperature was not so influential for asphaltene upgrading. Coke deposits decreased with increasing temperature and varied depending on the catalysts n_A/n_M ratio. It was found that the hydrogenation capacity of the catalysts was important in reducing the amount and the rate of formation of coke deposits. However, coke stabilised earlier for the catalyst with the lower metal loading, which confirmed its higher initial acidity through a higher cracking rate.

The strategy of reutilising catalysts proved to be successful in understanding their activity and deactivation at short reaction time intervals. The activity of the catalysts was mostly maintained during their reutilisation. Most of the coke build-up occurred in the first reaction, so in the reutilisation reactions the heaviest fractions underwent different reaction pathways than polymerisation. When the catalysts were reutilised lower yields of Asphaltenes and $Maltenes_{>450°C}$ were obtained, higher yields of $Maltenes_{<450°C}$ were observed and gas production remained relatively constant.

All catalysts suffered a reduction in their surface area, pore volume and average pore diameter. Even though pore volume decreased for all pore sizes, no evidence of pore mouth plugging was shown. The shapes of the N_2 adsorption isotherm hysteresis loop were maintained for the spent catalysts, therefore the materials retained their original mesoporosity. The N_2 uptake capacity decreased for the spent catalysts which explained the reductions in S_{BET}. These mesoporous materials appeared to accommodate large amounts of coke deposits while maintaining their textural properties. Catalysts with higher metal loading could better maintain their textural properties than catalysts with lower metal content, even with comparable coke deposits. Moreover, Ni3Mo14/Al_2O_3 achieved lower coke and gas yields than the other catalysts. Therefore a NiO content of 3 wt % and MoO_3 loading of 14 wt % was chosen for subsequent work.

The dynamic nature of coke was proven with the catalysts reutilisation. First, catalysts could maintain their activity, which showed that coke build-up did not present a barrier for the feed molecules to come in contact with the catalyst active sites. Therefore coke deposits were permeable to the feed and reactive. The textural properties of the reutilised catalysts changed even with constant coke deposits. This could be explained by coke becoming more aromatic in nature with reaction time.

Chapter 6: NiMo catalysts supported on Cr-doped Al_2O_3 for VR hydroprocessing

In this chapter, a novel Cr-doped mesoporous alumina, "Al_2O_3-Cr", was used as support for NiMo catalysts and subsequently evaluated for VR hydrocracking. Results obtained in hydrocracking reactions were correlated to the fresh and spent catalyst characterisation and compared to the Ni3Mo14/Al_2O_3 catalyst from Chapter 5. Results also include reactions with supports Al_2O_3 and Al_2O_3-Cr.

6.1. INTRODUCTION

Catalysts with weaker bonds between active metals and support can present higher activity of the metal sites (24). Since dopants affect the interaction of the support with the active metals, their use has been explored to improve support acidity or metal dispersion for hydrotreating catalysts. Alkali and alkaline elements have been employed as doping agents for alumina to reduce the acidity that leads to higher coking rates. A review of the elements and their method of deposition can be found in the literature (201). Dopants were generally added by incipient wetness after the metals were loaded on the support, although the order and method of addition of basic dopants altered the later dispersion of the catalyst metal sulfides. Mixed oxide supports with alkaline metals have also been prepared by coprecipitation with alumina precursors (63). Halogens have also been utilised as dopants for alumina, silica-alumina and zeolites during hydrocracking reactions (21,52). Phosphorous has been used to dope alumina since it can increase the acidity and dispersion of metals (202).

Transition metals have also been used as dopants for alumina support prepared via sol gel, with Fe and Cu doped materials presenting larger pore diameter than a pure alumina (203). Cr can form a monolayer on alumina support (204) and has also been used as a doping agent to improve metal dispersion for different supports such as zeolites, zirconia, silica, alumina and pillared clays. A brief summary of relevant literature of Cr as a doping agent is described presently.

Zeolites were modified with Cr^{3+} by ion exchange and then impregnated with Mo and Ni (205). These materials achieved higher activity for thiophene HDS than the corresponding unmodified zeolites. Textural properties of the materials were not reported, but the destruction of the crystal lattice of zeolites caused by Cr ions could have increased the pore size of the catalysts and therefore facilitated HDS. ZrO_2 was also doped with Cr since the latter oxides are easier to reduce, also chromium sulfide has a high thermal stability which would allow better metal dispersion (206). Chromium was introduced onto the ZrO_2 support in its synthesis and then Ni and Mo were loaded on zirconia doped with varying amounts of Cr_2O_3. The catalysts were tested for tetralin hydroprocessing and thiophene HDS; they presented higher hydroprocessing activity but lower HDS activity than an industrial $NiMo/Al_2O_3$ catalyst. Catalytic activity was higher when Cr_2O_3 content was 10 instead of 90 wt %, because a synergy between the activities of the Mo and Cr occurred. High contents of Cr counteracted on the promoting effect of Ni on Mo given that the Cr-Ni interaction was very strong.

In most studies, Cr is added as a dopant through incipient wetness impregnation. For example, different Cr concentrations were added to mesocellular silica foam to obtain highly dispersed catalysts, which were later tested for propane oxidative dehydrogenation, a reaction that is commonly catalysed with Cr supported on silica (207). In this study it was reported that higher Cr content increased the number of acid sites in the materials. It was observed elsewhere that Cr can help to reduce the migration of metals when they are deposited on a zeolite support, therefore increasing their dispersion (208). The Cr-doped catalyst presented a high hydrogenating activity for gas oil. Mesoporous silica was impregnated with Ni and Cr by incipient wetness to evaluate the effect of Cr on hydroprocessing reactions (209). Cr aided in increasing Ni dispersion by decreasing the Ni particle size. At the same time, the Cr^{3+} ions increased the stability of the catalyst. Small amounts of Cr increased the strong acidity of the material, although loadings higher than 4 wt % did not add further acidity. The catalyst with the higher Cr content had less coke deposits at the end of the reaction. The authors propose that Cr forms an alloy with Ni which protects it from coke deposition as well as poisoning by sulfur molecules which adsorb on the Cr. The catalyst with higher Cr content (5.2 wt %) presented the higher activity, conversion and stability when hydrogenating tetralin with dibenzothiophene at moderate temperatures. Finally, it was published that a monolayer of Cr_2O_3 is created on an alumina support with 12 wt % content; at higher loadings surface Cr species are formed (210). This result is consistent with other literature for mesoporous alumina doped with Cr (211) although it

was reported that 5 wt % Cr was sufficient for crystalline Cr_2O_3 formation with a MCM-41 silica (212).

Pillared clays have also been used as catalyst support given that they possess large pores, high surface area and acidity required for hydrotreating reactions. Elements such as Al, Ti, Cr, Fe, Zr, and Sn have been deposited between the clay layers to provide structural stability (213). A Cr-alumina PILC had less coke deposits than an Al-PILC, showing that Cr has catalytic activity and helps suppress coke formation during the dehydrogenation of cyclohexane (156). Further studies with a Cr-based montmorillonite PILC concluded that this material presented sufficient thermal resistance for hydrocracking reactions as well as strong acidity (214). Ti, Cr and Al based montmorillonite PILC were prepared and then tested as hydrocracking catalysts for coal extract and petroleum residue in previous work in this research group (215–217). The authors credit the performance of the Cr-montmorillonite to its large basal spacings, strong acidity and thermal resistance. A study with longer reaction times found that the Cr-montmorillonite PILC still retained cracking capabilities even though it had a large drop in surface area and pore blockage after some hours of operation. SEM-EDX micrographs of the catalyst showed that the areas surrounding chromium clusters presented significantly smaller coke deposits (54).

Given that Cr can have positive effects as a doping agent for hydrocracking catalysts, a Cr-doped alumina was synthesised and used as catalytic support for Ni and Mo in this study. Cr should be incorporated in the alumina support without the presence of Cr_2O_3 crystallites, thereby affecting the support-metal interaction instead of the promoter-metal one. The first approach that was explored was adding Cr by incipient wetness with Mo and Ni. Experimental results employing these catalysts were not satisfactory, as conversions for these materials were lower than the ones for bimetallic NiMo catalysts. Therefore a novel approach was developed by adding Cr as a dopant to the mesoporous alumina matrix: the procedure to synthesise mesoporous alumina utilised in Chapter 4 was modified for these purposes. This synthesis procedure has not been reported in the literature. Ni and Mo were afterwards loaded on the Cr-doped Al_2O_3; Ni and Mo concentrations were chosen from the best performing catalyst of Chapter 5. The synthesis is similar to a mesoporous Cr_2O_3/Al_2O_3 which uses a non-ionic surfactant as a structure directing agent and is used to catalyse alkene dehydrogenation reactions (211).

The main objective for this chapter was to study how the Cr-doped alumina support changed catalytic properties and how these in consequence affected product distribution during VR hydrocracking reactions. Therefore, results from catalyst

Ni3Mo14/Al_2O_3 from Chapter 5 are included throughout this chapter for comparative purposes. At the same time, experiments using Al_2O_3-Cr and Al_2O_3 supports as catalysts –with knowledge that no hydrogenation function would occur– are also included. The same reaction system, conditions, and product recovery scheme as in Chapter 5 were employed. The spent catalysts characterisation showed how the textural properties were affected after the initial reaction, and if further changes happened after reutilisation.

6.2. MATERIALS

6.2.1. Synthesis

6.2.1.1. Support

A novel mesoporous alumina support doped with Cr was synthesised by adapting a procedure from the literature (160). Aluminium isopropoxide was dissolved in ethanol and propanol with 1, 8 and 6 molar ratios, respectively. Afterwards a non-ionic surfactant (Pluronic F127) was added in a 0.01 molar ratio while stirring the mixture at 50 °C until it was dissolved. Then an aqueous solution containing $Cr(NO_3)_3 \cdot 9H_2O$ was added in a 20 molar ratio, creating an emulsion. The chromium salt concentration, 4.8 wt %, was calculated to obtain a desired 6 wt % Cr_2O_3 in the calcined alumina. All molar ratios are expressed in reference to aluminium isopropoxide. The mixture was aged overnight at room temperature and later dried as a thin film at ambient temperature for 24 hr inside a fume cupboard. The surfactant and solvents were removed by subsequent drying steps at 150 and 350 °C and during calcination at 550 °C for 8 hours. Finally, the material was sieved to 50-250 μm. The Cr-doped alumina was named Al_2O_3-Cr.

6.2.1.2. Catalysts

A NiMo catalyst supported on the Cr-doped alumina described in Section 5.2.1.1 has been synthesised by the incipient wetness method following the procedure described in Chapters 4 and 5. Briefly, Mo was impregnated in the dry support with ATM solution in DETA/H_2O and dried overnight. Then $Ni(NO_3)_2.6H_2O$ in aqueous solution was impregnated and the catalyst was dried and calcined in a muffle furnace with flowing air at 150 mL·min^{-1}. The catalyst, Ni3Mo14/Al_2O_3-Cr, was designed with 3 wt % NiO and 14 wt % MoO_3 loadings, chosen from the best performing catalyst from Chapter 5.

A Cr-containing catalyst was also synthesised by incipient wetness. Mo was first impregnated on the Al_2O_3 support and after drying the Cr salt was added in aqueous solution simultaneously with the Ni salt. The catalyst was dried and calcined as the previously described catalyst. It was named Ni3Mo14Cr6/Al_2O_3.

6.2.2. Characterisation

The textural properties of the Al_2O_3-Cr and Ni3Mo14/Al_2O_3-Cr are given in Table 6.1, where they are compared with Al_2O_3 and Ni3Mo14/Al_2O_3 from Chapter 5. It was observed that all materials presented a pore size in the mesoporous range. S_{BET} of Ni3Mo14/Al_2O_3-Cr was reduced when compared to the support and Ni3Mo14/Al_2O_3 maintained the Al_2O_3 S_{BET}. The average pore diameter (APD) after metal deposition of Ni3Mo14/Al_2O_3-Cr decreased less than Ni3Mo14/Al_2O_3, maintaining an APD very similar to its support. Also, Ni3Mo14/Al_2O_3-Cr retained more pore volume after metal impregnation.

Table 6.1. Textural properties of the calcined support and catalyst determined by N_2 adsorption.

Sample	S_{BET} ($m^2 \cdot g^{-1}$)	Total pore volume ($cm^3 \cdot g^{-1}$)	Average pore diameter* (nm)
Al_2O_3-Cr	365.3	1.05	9.7
Ni3Mo14/Al_2O_3-Cr	274.7	0.74	9.1
Al_2O_3	341.2	1.21	12.0
Ni3Mo14/Al_2O_3	342.5	0.66	10.4

*BJH model applied to the adsorption branch of the isotherms.

The reduction in surface area of Ni3Mo14/Al_2O_3-Cr was corroborated by lower N_2 adsorption in high relative pressures in its isotherm (Figure 6.1). This figure also shows that the N_2 adsorption-desorption isotherms of the Al_2O_3-Cr and catalyst had the same shape as in the Al_2O_3 support, a Type IV isotherm with hysteresis loop H3, which matches materials formed by plate-like particles assembled in parallel (126). These results show that Al_2O_3-Cr permitted high metal oxide deposition while maintaining the support pore size distribution relatively unaffected. This should allow larger molecules, such as the ones present in VR, to access the pores without steric hindrance issues. Figure 6.1 (inset) shows the pore size distribution curves of the two supports and two catalysts. Ni3Mo14/Al_2O_3-Cr presented a decrease in pore volume with its PSD profile remaining very similar to the support due to partial coverage of the surface by metal oxides.

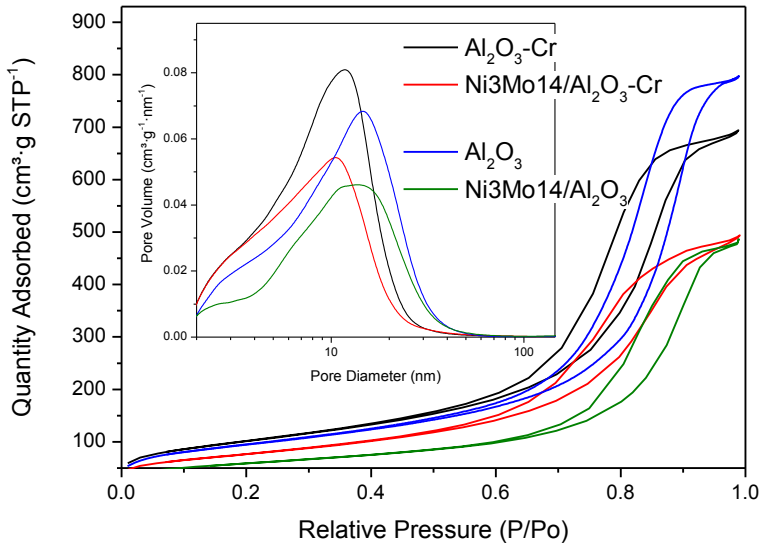

Figure 6.1. N_2 adsorption-desorption isotherms for the calcined Al_2O_3-Cr, Ni3Mo14/Al_2O_3-Cr, Al_2O_3 and Ni3Mo14/Al_2O_3.

Ammonia TPD profiles are shown in Figure 6.2. Al_2O_3-Cr in the Al_2O_3 matrix did not add acidity to the support, contrary to literature reports with Cr added by incipient wetness to silica (207,209). Ni3Mo14/Al_2O_3-Cr presented an increase in weak acidity (<200 °C) but a decrease in strong acidity (>400 °C) when compared to Al_2O_3-Cr. The catalyst still had strong acidity (>400 °C) which is required for cracking reactions above this temperature. Strong acid sites for Ni3Mo14/Al_2O_3-Cr were reduced to 63% of the acid sites of the support whereas sites for Ni3Mo14/Al_2O_3 were reduced to 40% of the values for Al_2O_3 (Table 6.2). The ratio of acid to metal sites (n_A/n_M) for Ni3Mo14/Al_2O_3-Cr and Ni3Mo14/Al_2O_3 can be seen in Table 6.2. The number of acid sites, n_A, are expressed as desorbed NH_3 molecules per gram of catalyst. The number of metal sites, n_M, were determined with the metal oxide content and are expressed in atoms of Ni + Mo available per gram of catalyst. The NiMo catalysts had very similar n_A/n_M ratio thus the same hydrogenation to cracking function could be expected.

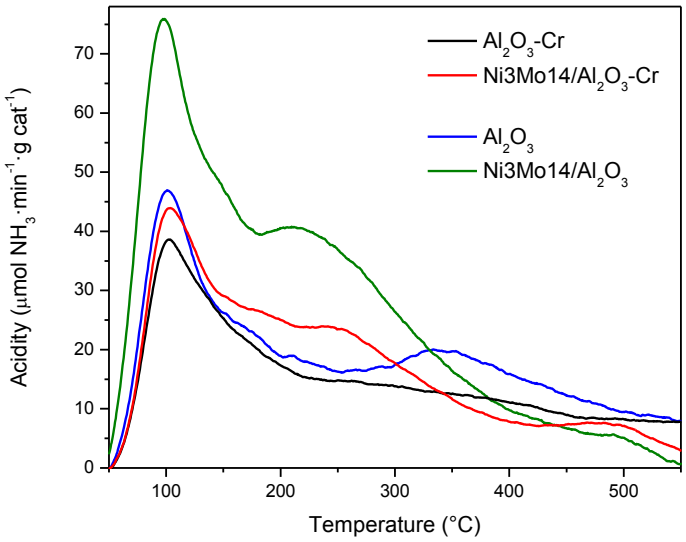

Figure 6.2. NH_3-TPD profiles for the calcined Al_2O_3-Cr, Ni3Mo14/Al_2O_3-Cr, Al_2O_3 and Ni3Mo14/Al_2O_3.

Table 6.2. Acid and metal sites available in the fresh catalysts. NH_3, Ni and Mo content expressed in molecules*.

Sample	n_A** $(NH_3 \cdot g^{-1}) \cdot 10^{-20}$	n_M $[(Ni+Mo) \cdot g^{-1}] \cdot 10^{-20}$	n_A/n_M $NH_3 \cdot (Ni+Mo)^{-1}$
Al_2O_3-Cr	1.11	–	–
Ni3Mo14/Al_2O_3-Cr	0.70	9.37	0.07
Al_2O_3	1.29	–	–
Ni3Mo14/Al_2O_3	0.52	9.29	0.06

*NH_3 data was calculated from integrated areas from Figure 5.1; acidity values were calculated with an ammonia concentration calibration and taking into account the sample mass.

**Only strong acidity accounted for (>400 °C).

The XRD patterns for the catalysts and supports are shown in Figure 6.3. An absence of peaks for all materials revealed that a non-ordered pore structure was present. Since no peaks for bulk Cr_2O_3, NiO or MoO_3 were observed, this could indicate that their dispersion was high and that the crystallites had a size smaller than 4 nm (186). The three broad, low intensity peaks displayed in Al_2O_3 are typically assigned to gamma alumina. The reduction in intensity of these peaks in Al_2O_3-Cr suggested that the degree of ordering was reduced when Cr was added. It was reported that increasing Cr content in zeolites decreased their crystallinity (205); amorphous spectra was observed for Cr-doped zeolites and mesoporous alumina (206,211).

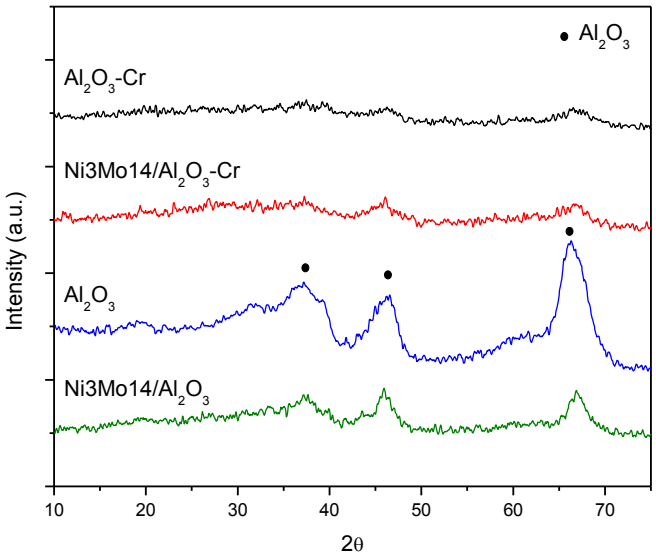

Figure 6.3. Powder XRD patterns of calcined Al_2O_3-Cr, Ni3Mo14/Al_2O_3-Cr, Al_2O_3 and Ni3Mo14/Al_2O_3.

The mesoporous structure of Al_2O_3-Cr and Al_2O_3 can be observed in TEM micrographs in Figure 6.4 (at 20,000X and 100,000X magnifications) for each material. No order was displayed in the pores of Al_2O_3-Cr but their shape was similar to the mesoporous Al_2O_3. This indicated that Cr did not affect the mesoporosity of the original alumina, as previously observed from the N_2 adsorption study. A worm-like motif with a random channel system was observed, representative of aluminas synthesised with surfactant templating method (157) which would match the plate-like particles assembled in parallel identified by the N_2 adsorption-desorption isotherm in Figure 6.1. The Al_2O_3-Cr platelets had a shorter length of ca. 20 nm than the Al_2O_3 ones of ca. 40-60 nm.

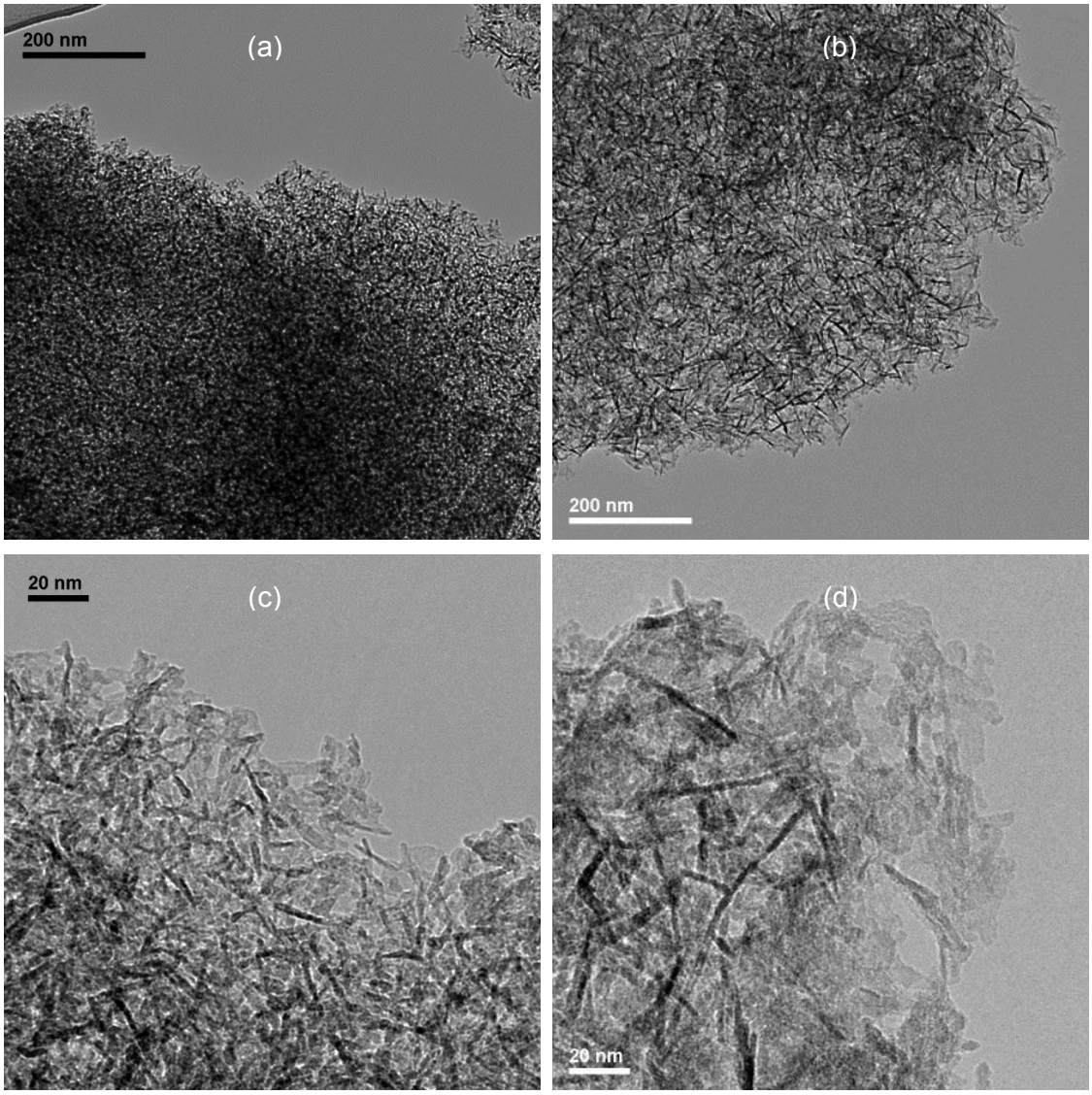

Figure 6.4. TEM images of supports Al_2O_3-Cr (a and c) and Al_2O_3 (b and d) at low (20,000X) and high (100,000X) magnification.

Figure 6.5 shows TEM images for Ni3Mo14/Al_2O_3-Cr and Ni3Mo14/Al_2O_3 at medium and high magnification (50,000X and 100,000X). A very homogeneous dispersion for metals was observed for Ni3Mo14/Al_2O_3-Cr. The catalyst had a darker coloration than Al_2O_3-Cr from Figure 6.4, due to the coating of pores with Ni and Mo oxides. In contrast, crystallites can be observed in the images for Ni3Mo14/Al_2O_3. These images show Cr increases the metal oxide dispersion in Al_2O_3 supported catalysts, as previously observed with zeolites and silica as support (208,209).

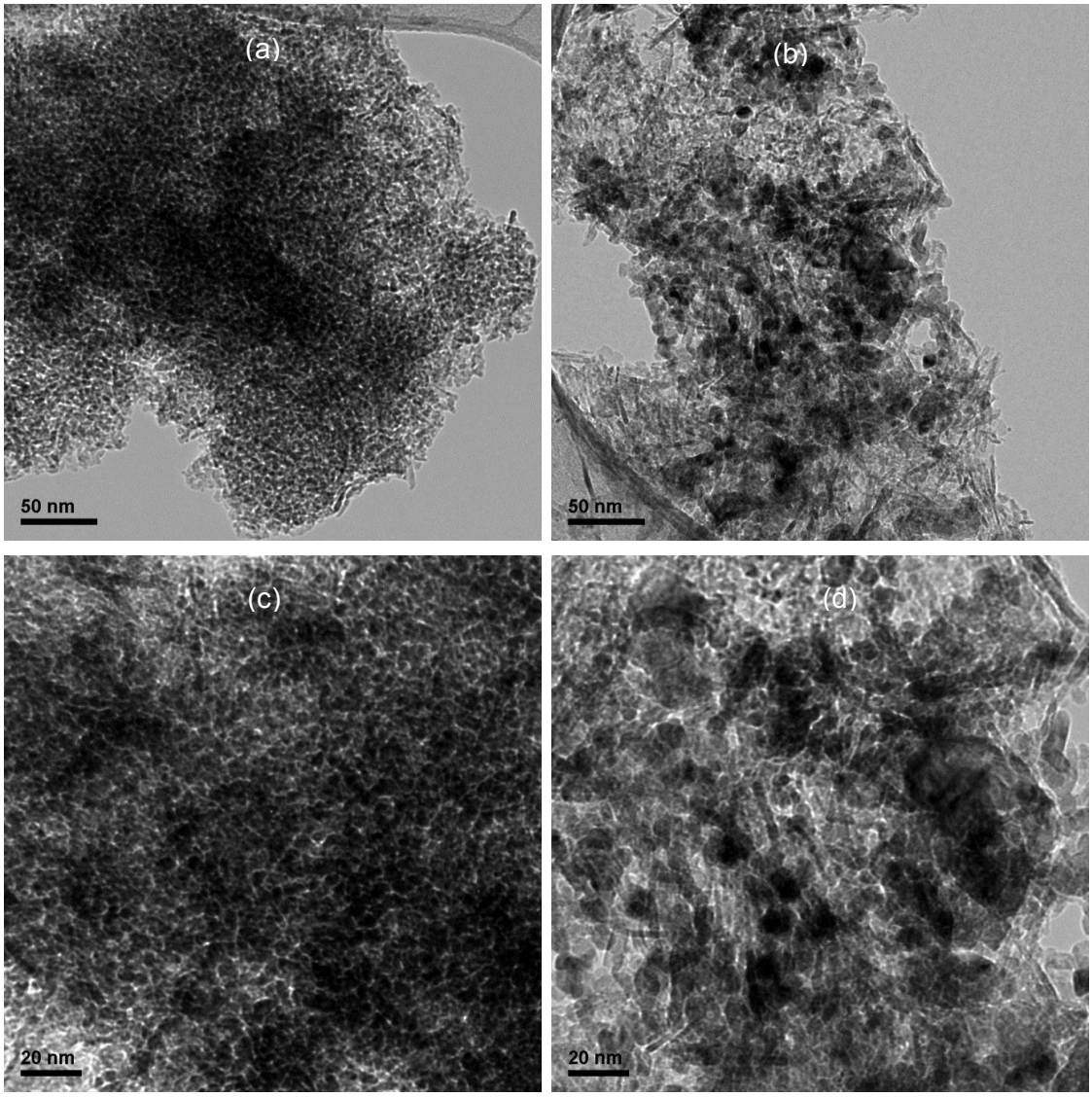

Figure 6.5. TEM images of Ni3Mo14/Al_2O_3-Cr (a and c) and Ni3Mo14/Al_2O_3 (b and d) at medium (50,000X) and high (100,000X) magnification.

Additionally, local elemental analysis was performed by Electron Dispersive X-Ray Spectroscopy (EDX) on two sections for Ni3Mo14/Al_2O_3-Cr, shown in Figure 6.6. The presence of the elements in the support (Al, Cr) and active metals (Ni, Mo) was corroborated. Cu was also detected as this element was present in the grid used to support the samples for analysis.

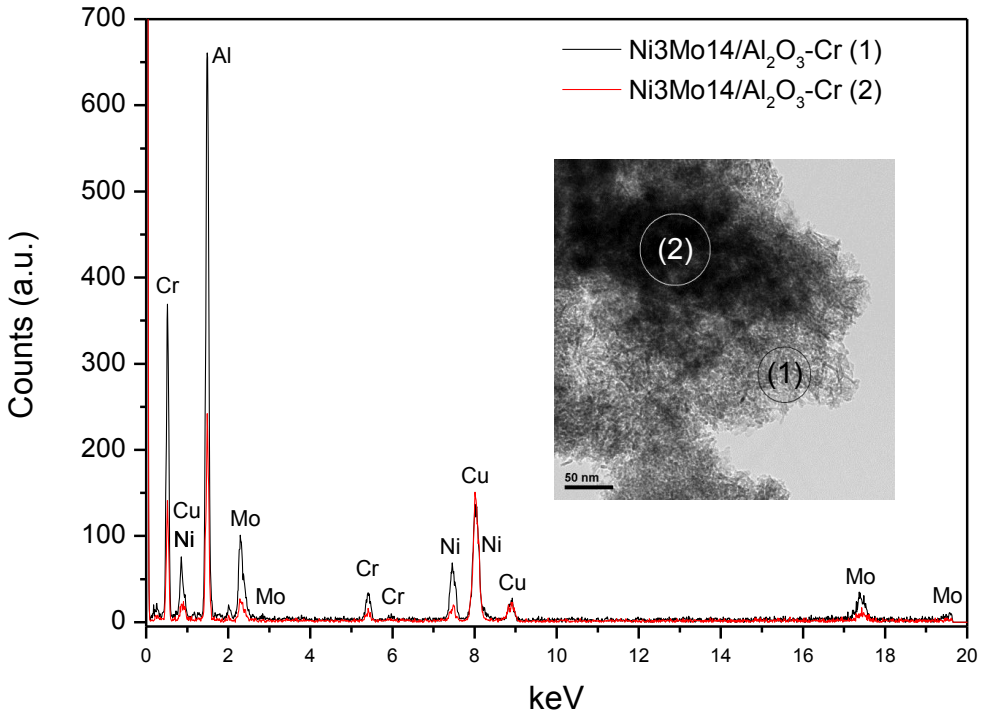

Figure 6.6. EDX analysis on two TEM micrograph areas at 50,000X magnification (inset) for Ni3Mo14/Al_2O_3-Cr.

Temperature reduction profiles for Al_2O_3-Cr, Ni3Mo14/Al_2O_3-Cr and Ni3Mo14/Al_2O_3 are shown in Figure 6.7. It was reported that bulk Cr_2O_3 presents two reduction peaks (212). A single one was observed for Al_2O_3-Cr around 325 °C, at a lower temperature than in a mesoporous Cr_2O_3/Al_2O_3 synthesised by a surfactant templating method similar to the one used in this work (211). As was previously reported in Section 4.4.3, two reduction steps (MoO_3 → MoO_2 → Mo) around 370 and 830 °C are observed for Mo supported on alumina (173–175). NiO species typically present one reduction peak around 500 °C (176). For Ni3Mo14/Al_2O_3 the first Mo reduction was at 520° C and the Ni reduction around 400 °C.

Ni and Cr supported on silica showed a reduction of Ni^{2+} into $NiCr_2O_4$ around 470 °C (209). Mo was reported to be easier to reduce with increasing Cr content in doped γ-alumina (218). In catalysts supported on mesoporous silica, Cr presented a reduction peak at 420 °C, Mo at 522 °C and the CrMo catalyst had a peak which combined the two metals reductions at a temperature in the centre of the monometallic catalysts (ca. 440 °C) as well as the high temperature Mo peak (219). Two reduction peaks were observed for Ni3Mo14/Al_2O_3-Cr, the first one around 410 °C and the second at 750 °C. The first peak had a shoulder and merged the low temperature Mo reduction

with the Ni and Cr reductions. The first Mo and Ni peaks appeared at lower temperatures than in Ni3Mo14/Al_2O_3, indicating that the 6 % wt Cr oxide present in the support matrix aided in increasing the reducibility of the metals. The shift to higher temperatures for the Cr peak could indicate it lowered the interactions between Ni, Mo and Al_2O_3. The amount of H_2 consumed in the Ni3Mo14/Al_2O_3-Cr TPR study was 167% greater than the one for Ni3Mo14/Al_2O_3. Therefore, more Ni and Mo oxides would be available to act as catalytic active sites after sulfidation.

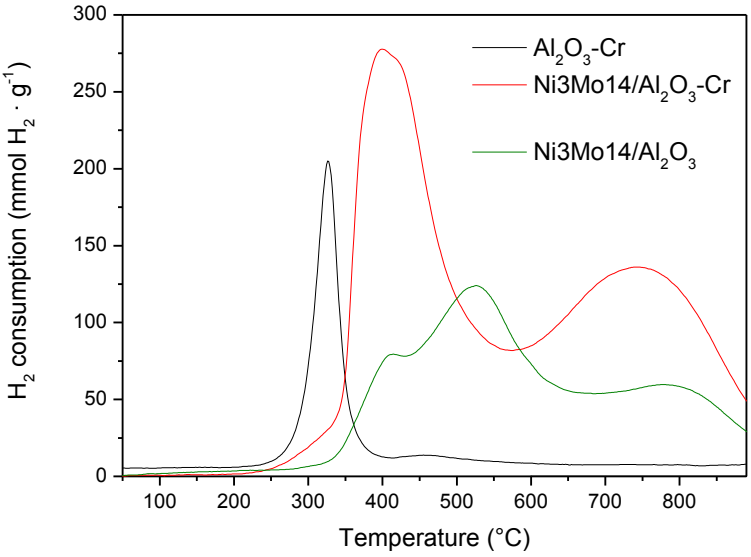

Figure 6.7. TPR spectra of calcined Al_2O_3-Cr and Ni3Mo14/Al_2O_3-Cr.

6.3. RESULTS AND DISCUSSION

The results are divided into two parts as follows: Section 6.3.1 which focuses on VR conversion, asphaltene upgrading and the corresponding product distribution and Section 6.3.2 which deals with changes in the spent catalysts. Experiments were performed at 400, 425 and 450 °C with Ni3Mo14/Al_2O_3-Cr and Ni3Mo14/Al_2O_3 and at 400 and 450 °C with Al_2O_3-Cr and Al_2O_3 supports.

6.3.1. Reaction products

6.3.1.1. Conversion

The conversion values for Ni3Mo14/Al_2O_3-Cr and Ni3Mo14/Al_2O_3 of the >450 °C fraction ($C_{>450°C}$) and asphaltenes ($C_{Asphaltenes}$) are shown in Figure 6.8a and b, respectively. Results include initial and reutilisation reactions as well as thermal reactions. Data for this figure are available in Table 10.1, 10.2 and 10.7 (Appendix 1). As previously

mentioned in Chapter 3, both conversion definitions take coke formation into account as unconverted products (Equation 1 and 2), so increases in coke production affected the resulting values negatively.

$C_{>450°C}$ increased linearly with temperature for initial and reutilisation reactions of Ni3Mo14/Al_2O_3-Cr and Ni3Mo14/Al_2O_3, with similar results as the thermal reaction. This was consistent with observations that thermal cracking dominates in heavy fraction hydrocracking (75). At 450 °C all catalytic reactions had higher $C_{>450°C}$ than the thermal reaction, possibly due to the better sulfidation of the metal active sites. The reutilised Ni3Mo14/Al_2O_3-Cr obtained higher $C_{>450°C}$ at 450 °C than the other catalysts. This could happen because coke formation occurs mainly in the first reaction therefore when the catalyst was reutilised larger molecules followed an upgrading pathway instead of converting into coke. Initial reactions using Ni3Mo14/Al_2O_3 led to higher $C_{>450°C}$ than Ni3Mo14/Al_2O_3-Cr, nevertheless differences are within experimental error. $C_{>450°C}$ were generally higher for Ni3Mo14/Al_2O_3-Cr than for Ni3Mo14/Al_2O_3 in reutilisation reactions. This could be due to coke formation during reutilisation reactions; Ni3Mo14/Al_2O_3-Cr had higher coke deposits in its initial use and less deposition in its reutilisation than Ni3Mo14/Al_2O_3.

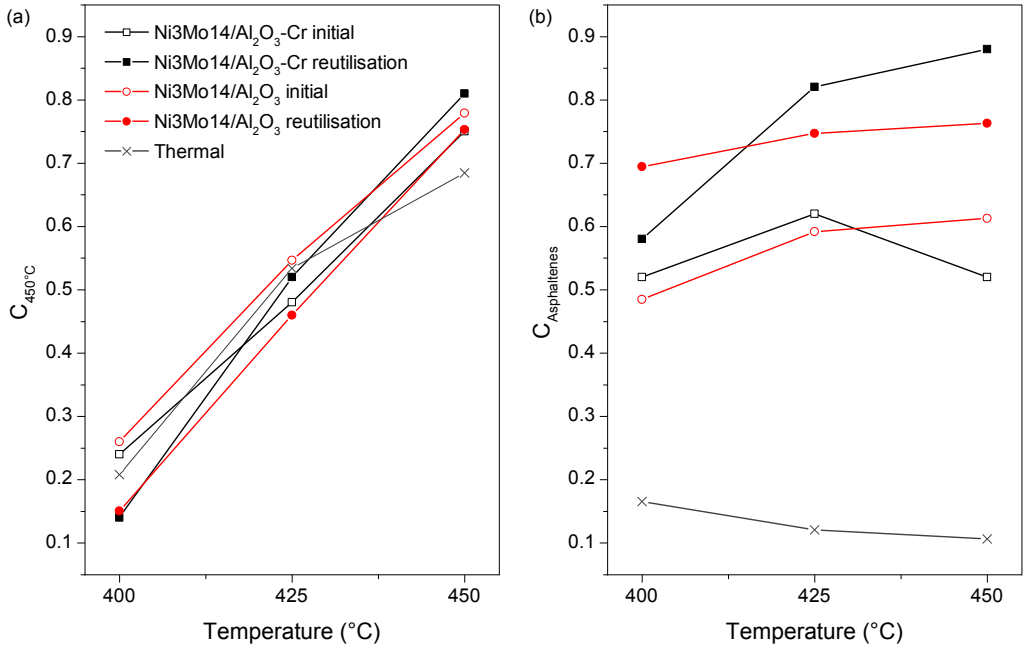

Figure 6.8. $C_{>450°C}$ and $C_{Asphaltenes}$ for Ni3Mo14/Al_2O_3-Cr, Ni3Mo14/Al_2O_3 catalysts for initial and reutilisation reactions and for thermal reactions. All experiments were at 185 bar H_2 pressure for 60 minutes.

On the other hand, $C_{Asphaltenes}$ were significantly higher for catalytic –either with Ni3Mo14/Al_2O_3-Cr or Ni3Mo14/Al_2O_3– than for thermal reactions. It was reported that catalytic activity mainly concerns hydrogenation, coke build-up suppression and heteroatom removal when upgrading heavy fractions (85). Thus when asphaltenes crack, thermally or catalytically, they can react with other cracked asphaltenes or with H_2 in the system (190). Hydrogen transfer to asphaltenes occurs only in the presence of a catalyst and since hydrogen transfer is not favoured by thermal reactions, asphaltenes polymerise and form larger PAH. This causes the decrease in asphaltene conversion with increasing process severity for thermal reactions. It was reported that a catalyst can prevent coking at severe reaction conditions, therefore increasing asphaltene upgrading (7). Results from this section for both catalysts are in good agreement with the literature (85). $C_{Asphaltenes}$ was similar for initial reactions of Ni3Mo14/Al_2O_3-Cr and Ni3Mo14/Al_2O_3 at 400 and 425 °C. At the initial 450 °C reaction, Ni3Mo14/Al_2O_3 yielded better asphaltene conversion than Ni3Mo14/Al_2O_3-Cr. Spent catalysts covered in coke deposits are less acidic than fresh ones (98), so less coke formation would be expected in the reutilisation reactions and this would have allowed higher $C_{Asphaltenes}$ in reutilisation reactions than in initial reactions. $C_{Asphaltenes}$ for reutilisation reactions were higher with higher reaction temperatures for both catalysts, showing that when more severe thermal cracking took place the molecules reacted via hydrogenation. In the reutilisation at 425 and 450 °C, asphaltene conversions were higher for Ni3Mo14/Al_2O_3-Cr than for Ni3Mo14/Al_2O_3. This could be due to higher availability of metal sites, as seen in the TPR study (Figure 5.3). The changes in pore size and other textural properties of the catalysts will be discussed hereafter.

It was mentioned previously that Cr was first added as a metal by incipient wetness and that results were not encouraging. To give an example of these results, Table 6.3 contains data for Ni3Mo14Cr6/Al_2O_3. This catalyst was considerably outperformed by Ni3Mo14/Al_2O_3-Cr for asphaltene conversion. Thus Cr was added as a doping agent to the alumina prior to Ni and Mo deposition.

Table 6.3. Asphaltene content in reaction products and conversion for reactions using Ni3Mo14/Al_2O_3-Cr and Ni3Mo14Cr6/Al_2O_3. All reactions lasted 60 minutes at 450°C with an initial 185 bar H_2 pressure.

Catalyst	Asphaltenes (wt %) in products	$C_{Asphaltenes}$
Ni3Mo14/Al_2O_3-Cr	5.1	0.88
Ni3Mo14Cr6/Al_2O_3	15.2	0.54

Figure 6.9a shows $C_{>450°C}$ for Al_2O_3-Cr and Al_2O_3 supports which helped elucidate the extent of the hydrogenating function of Cr in the Al_2O_3 matrix. As would be expected, $C_{>450°C}$ values were similar for both supports and thermal reactions. $C_{Asphaltenes}$ were different from thermal reactions (Figure 6.9b) where at 400 °C thermal upgrading of asphaltenes proved higher than with either support. When an alumina was used as a catalyst, high coke deposits occurred, to the extent that experiments had to be discontinued (85). Thermal and catalytic cracking were combined at 400 °C and in the absence of a hydrogenating function high coke yields were produced, hence the observed low and/or negative $C_{Asphaltenes}$ values. For Al_2O_3 negative conversions were obtained. At 450 °C either support achieved higher conversions than in the thermal reaction. Values for initial reactions were lower than for reutilisation of the materials, suggesting that most of the coke deposition occurred in the initial reaction stages. It was observed that chromium can act as a hydrogenation catalyst (220).

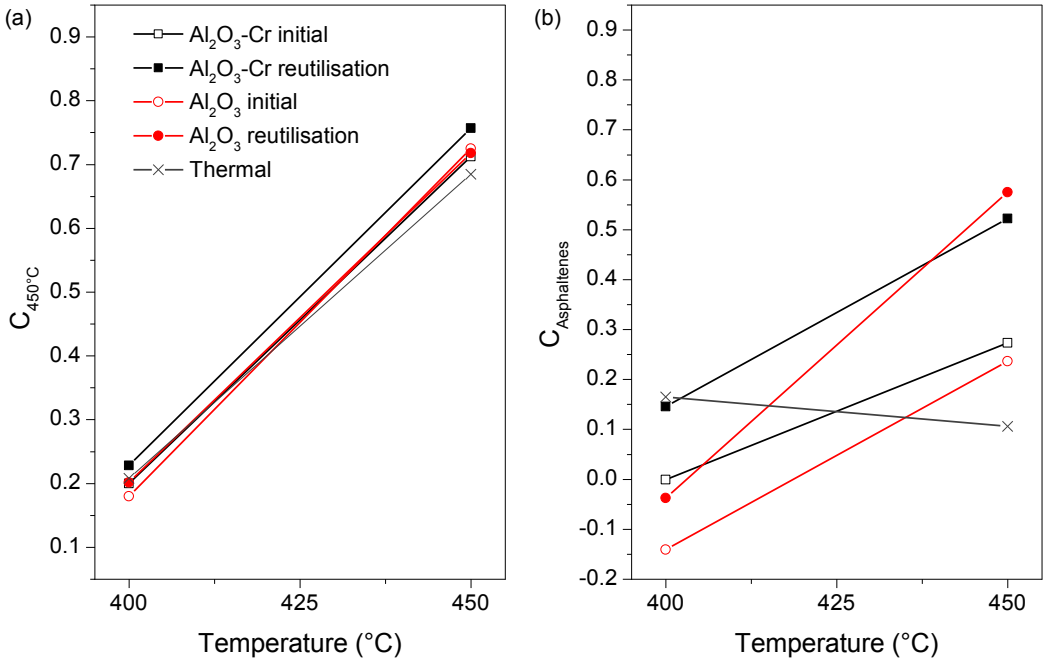

Figure 6.9. $C_{>450°C}$ and $C_{Asphaltenes}$ for Al_2O_3-Cr and Al_2O_3 for initial and reutilisation reactions and for thermal reactions. All experiments were at 185 bar H_2 initial pressure for 60 minutes.

The TPR study (Figure 6.7) showed that Cr was reduced at lower temperatures than the ones employed in any of the reactions. Therefore if it possessed any hydrogenation activity, it would be available. Even though in this process Al_2O_3-Cr did not appear to be active for hydrogenation reactions, at 400 °C higher $C_{Asphaltenes}$ were achieved with Al_2O_3-Cr than Al_2O_3. Since both supports had similar strong acidity (Table 6.2), the

variations of $C_{Asphaltenes}$ at 400 °C could be due to the hydrogenation function from Cr. At 450 °C initial conversions for both supports were higher (ca. 0.20) than in thermal reaction (ca. 0.10), but significantly lower than the $C_{Asphaltenes}$ obtained with catalysts (>0.50) (Figure 6.8b). During reutilisation, values increased to approximately 0.55, but were still lower than the values above 0.70 from catalytic reactions, showing that significant hydrogenation was taking place in the catalytic reactions. At higher reaction temperatures thermal cracking and the cracking function of either support were combined in reutilisation reaction, yielding less asphaltenes than in thermal reactions. Since Al_2O_3-Cr did not have higher $C_{Asphaltenes}$ than Al_2O_3, no immediate effect of the hydrogenation activity of Cr was observed.

6.3.1.2. Yields

Figure 6.10a and b show the product distribution for initial and reutilisation reactions with Ni3Mo14/Al_2O_3-Cr and Ni3Mo14/Al_2O_3, respectively. Data for these figures are available in Tables 10.3, 10.4, and 10.8 (Appendix 1). Yields for initial and reutilisation reactions for both catalysts for Gas increased and for $Maltenes_{>450°C}$ decreased when reaction temperature was increased. This indicated that the yields were driven by thermal reactions. All other product yields did not show such significant changes with increasing reaction temperature.

The overall effect of catalyst reutilisation for both materials was observed in a decrease in Solids yield in the reutilisation reaction whereas most of the other product yields remained similar to the initial reaction values. Solids yields for Ni3Mo14/Al_2O_3-Cr were constant at all temperatures in the initial reactions with higher values than Ni3Mo14/Al_2O_3. The latter presented a decrease in Solids production with increasing temperature for initial reactions. Small Solids yields were obtained in reutilisation reactions using both catalysts. In initial reactions Asphaltene yields were very low for Ni3Mo14/Al_2O_3-Cr and similar for all temperatures; for the reutilisations a higher yield was obtained at 400 °C which decreased with reaction temperature. This was consistent with what was mentioned previously with $C_{Asphaltenes}$. In the initial reaction more asphaltenes were polymerised into coke (Solids) and in the reutilisation of the catalysts the process temperature affected asphaltene upgrading since thermal cracking was more severe. For the other catalyst, Asphaltene and Solids yields were similar in the initial reaction at all temperatures. $Maltenes_{<450°C}$ yields were similar for initial and reutilisation reactions for Ni3Mo14/Al_2O_3-Cr. These increased from ca. 10 to 20 wt % from 400 to 425 °C, but did not increase further when temperature was raised to 450 °C. This possibly came at the expense of gas production which was mostly

thermally driven, as mentioned previously, and very high at 450 °C. On the other hand, Ni3Mo14/Al_2O_3 showed an increase in $Maltenes_{<450°C}$ in its reutilisation reaction temperature was increased.

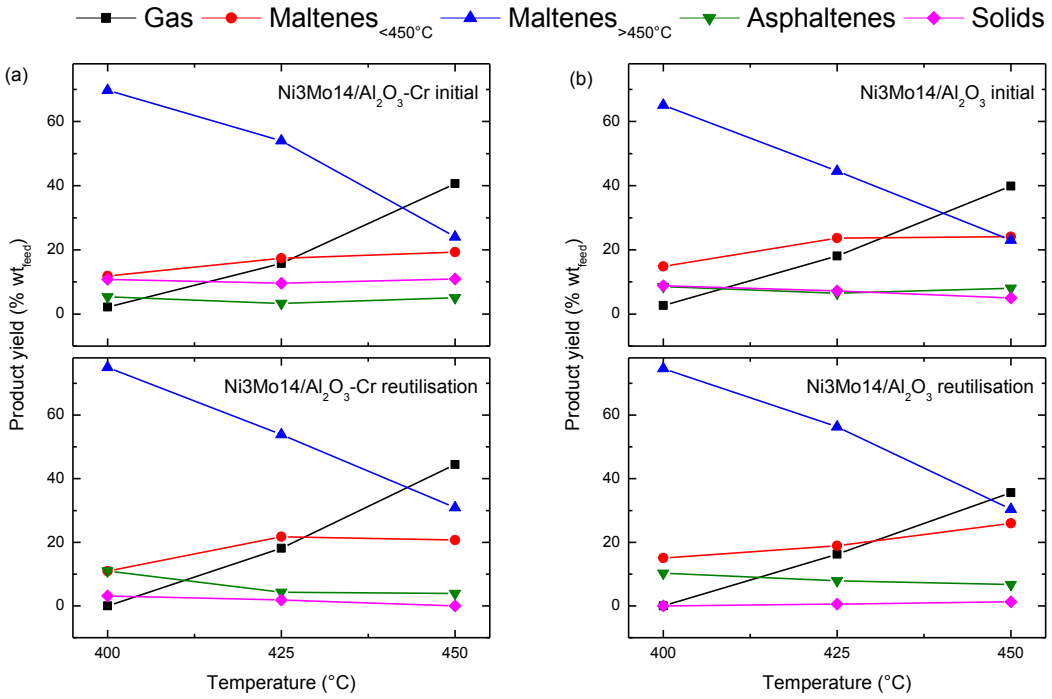

Figure 6.10. Product yields for initial and reutilisation reactions with Ni3Mo14/Al_2O_3-Cr (a) and Ni3Mo14/Al_2O_3 (b). All reactions lasted 60 minutes with an initial 185 bar H_2 pressure.

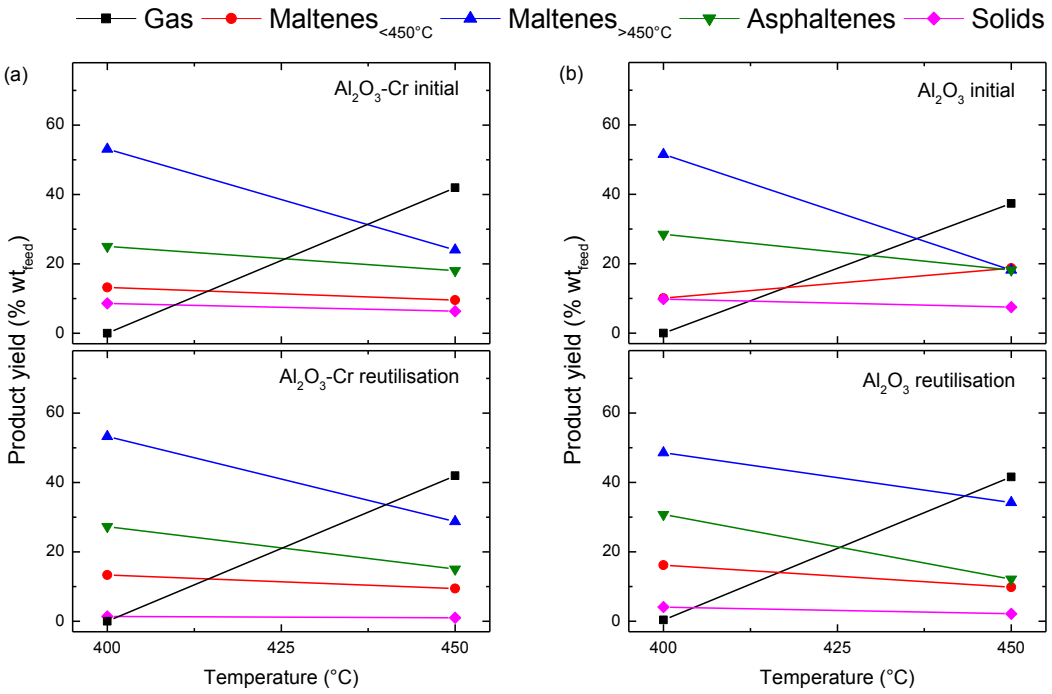

Figure 6.11. Product yields for initial and reutilisation reactions with Al_2O_3-Cr (a) and Al_2O_3 (b). All reactions lasted 60 minutes with an initial 185 bar H_2 pressure.

The product distribution for reactions with supports Al_2O_3-Cr and Al_2O_3 are available in Figure 6.11a and b, respectively (data are in Table 10.9 and 10.10 in Appendix 1). The same thermal trends were observed as in the catalysts, as expected: an increase in Gas and a decrease in $Maltenes_{>450°C}$ took place with increasing reaction temperature. A small decrease in $Maltenes_{<450°C}$ occurred with increasing temperature, nevertheless these values were significantly lower than the ones for Ni3Mo14/Al_2O_3-Cr and Ni3Mo14/Al_2O_3 catalysts. The lack of catalytic activity was also observed in high Asphaltenes yields. Solids yields had the same behaviour as in catalytic reactions; they were high in initial reactions but close to zero in the support reutilisations. The reutilisation of the materials mainly changed the Solids yield but had no major effect on the other products.

6.3.1.3. Selectivity

The product distribution for reutilisation reactions for $Maltenes_{<450°C}$, calculated from GC SimDis analysis of this fraction, are displayed in Table 6.4 for Ni3Mo14/Al_2O_3-Cr and Ni3Mo14/Al_2O_3. Data for this section are expressed as $Maltenes_{<450°C}$ wt %. Fractions are considered within the following boiling point distribution ranges: initial boiling point to 204 °C for heavy naphtha, 204-260 °C for kerosene, 260-343 °C for diesel, 343-427 °C for gas oils and finally 427-450 °C for residue.

Both catalysts had very similar product distributions. Close to zero yields were observed for the lowest boiling point materials, heavy naphtha and kerosene, at any temperature. Residue yields decreased with temperature, converting into diesel and gas oils which increased with rising temperature. At 400 and 425 °C reactions, no differences were observed between initial and reutilisation reactions for $Maltenes_{<450°C}$ fraction yields, indicating that catalytic activity remained constant. The residue yields at 450 °C were lower for the reutilisation than for the initial reactions, although an increase in kerosene was observed. The main difference between the catalysts was that Ni3Mo14/Al_2O_3-Cr presented less kerosene yields at 425 and 450 °C at the expense of less residue upgrading.

Maltene to asphaltene (M/A) ratios in reutilisation reaction products are displayed in Figure 6.12a for Ni3Mo14/Al_2O_3-Cr, Ni3Mo14/Al_2O_3, Al_2O_3-Cr, Al_2O_3 and thermal reactions. Total maltene contents were taken into account, i.e. $Maltenes_{<450°C}$ + $Maltenes_{>450°C}$. Ni3Mo14/Al_2O_3 had similar M/A ratios at any reaction temperature, thus its activity was constant with a limit in its upgrading capacity. The behaviour of Ni3Mo14/Al_2O_3-Cr was different. Its maximum activity was achieved at the middle temperature, 425 °C. A substantial increment in the M/A ratio occurred when

temperature was increased from 400 to 425 °C. Then the M/A ratio decreased for the 450 °C reaction. This is related to the $Maltenes_{<450°C}$ yields observed at 425 °C (Figure 5.6a). Even though asphaltene content decreased at 450 °C, gas yield at this temperature was very high, reducing $Maltenes_{>450°C}$ and decreasing the M/A ratio. The easier reducibility of the metal sites of Ni3Mo14/Al_2O_3-Cr when compared to Ni3Mo14/Al_2O_3 could account for more asphaltene upgrading.

Table 6.4. Product yields for $Maltenes_{>450°C}$ fraction for Ni3Mo14/Al_2O_3-Cr and Ni3Mo14/Al_2O_3; 60 min reactions with an initial 185 bar H_2 pressure.

Sample/Reaction		T (°C)	Heavy naphtha (wt %)	Kerosene (wt %)	Diesel (wt %)	Gas Oils (wt %)	Residue (wt %)
Ni3Mo14/Al_2O_3-Cr	Initial	400	0.8	1.1	15.0	28.0	55.1
		425	0.5	2.1	22.0	31.8	43.6
		450	0.3	4.0	35.5	34.8	25.4
	Reutilisation	400	1.4	1.5	15.7	27.8	53.6
		425	1.0	1.5	21.9	32.4	43.2
		450	0.5	1.3	30.9	37.1	30.2
Ni3Mo14/Al_2O_3	Initial	400	0.7	0.9	14.7	27.9	55.8
		425	0.4	2.1	24.2	33.4	39.9
		450	0.4	0.9	29.8	38.8	30.1
	Reutilisation	400	1.0	1.1	16.0	27.3	54.6
		425	0.5	2.2	21.4	29.8	46.1
		450	0.2	3.4	31.7	34.9	29.8

Gas and coke production can be observed in Figure 6.12b for all catalysts and supports as well as thermal reactions. The increase in gas was thermally driven, as discussed previously. Gas and coke production for all materials were lower than in thermal reactions. Catalysts provided hydrogenation which stopped molecules from cracking all the way to gas and prevented coking (7). Nevertheless, Ni3Mo14/Al_2O_3 led to less coke and gas production at all temperatures than Ni3Mo14/Al_2O_3-Cr. The latter had slightly higher acidity (Table 6.2) which could trigger higher cracking and coking rates.

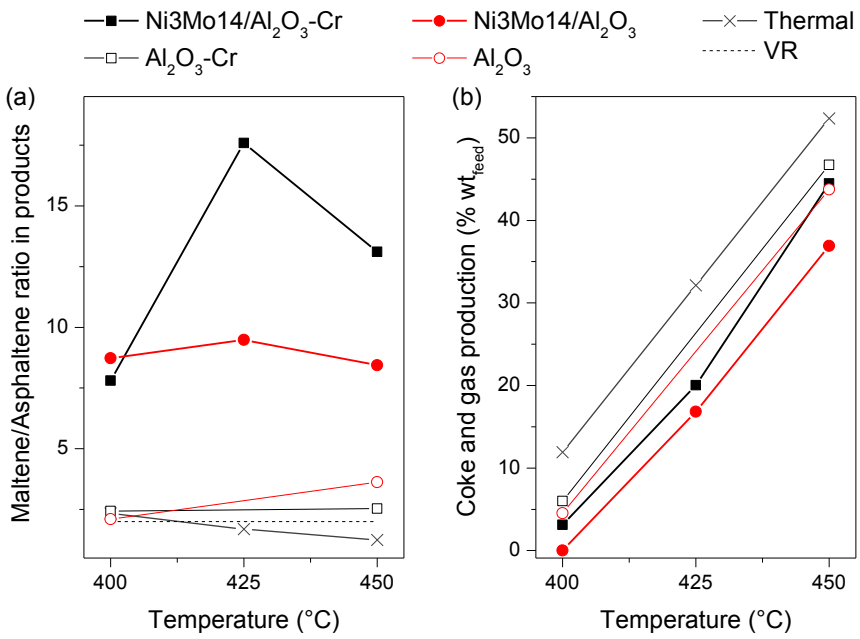

Figure 6.12. (a) Maltene to asphaltene ratio in VR and reutilisation reaction products. (b) Coke and gas production expressed as wt % of feed in reutilisation reaction products. All reactions lasted 60 minutes with an initial 185 bar H_2 pressure.

6.3.1.4. HDS and HDM

Sulfur content on the products were obtained with XRF analysis. Hydrodesulfurisation conversions for Ni3Mo14/Al_2O_3-Cr and Ni3Mo14/Al_2O_3 are presented in Table 6.5, calculated from Equation 12. High HDS rates were achieved for both catalysts, with values slightly increasing with higher reaction temperatures. No significant differences were observed between the catalysts for initial reactions. On the other hand, during reutilisation reactions Ni3Mo14/Al_2O_3-Cr maintained HDS conversions similar to the ones for initial reactions whereas Ni3Mo14/Al_2O_3 had a decrease in HDS conversions. It was reported that up to 30-40% of sulfur conversion occurs due to thermal cracking and that additional conversion is catalytic (7). The HDS rates for the first hour of reaction in this study were significantly higher than for a CoMo/Al_2O_3 catalyst used for Maya crude diluted with diesel hydrotreating at 380 °C (87). Even though HDS decreased with time on stream (TOS), initial rates were less than 0.60. Another hydrotreating study using a NiMo/Al_2O_3 catalyst, also with Maya crude diluted with diesel, at 380 °C achieved an HDS of ca. 0.7 (106).

The feed used in this thesis has a considerably higher initial sulfur content (7 wt %) than the Maya crude from the quoted literature (2 wt %). Thus products had a similar sulfur content, with values around 1 wt %. Sulfur-containing molecules that underwent HDS could be present in the VR as mercaptans, sulfides and simple thiophenic rings. On the other hand, the sulfur that remained in the products could be part of complex PAH

structures (alkylated dibenzothiophenes and polynuclear organic sulfur compounds) which have a lower propensity to react (221).

Table 6.5. HDS for initial and reutilisation reactions of Ni3Mo14/Al_2O_3-Cr and Ni3Mo14/Al_2O_3. All reactions lasted 60 minutes with an initial 185 bar H_2 pressure.

Catalyst	Reaction temperature	initial		reutilisation	
		S (wt %)	HDS	S (wt %)	HDS
Ni3Mo14/Al_2O_3-Cr	400 °C	1.2	0.85	1.6	0.78
	425 °C	0.9	0.90	1.0	0.89
	450 °C	0.7	0.95	0.8	0.94
Ni3Mo14/Al_2O_3	400 °C	1.2	0.87	1.5	0.79
	425 °C	0.7	0.93	1.2	0.85
	450 °C	0.7	0.95	1.5	0.87

Ni and V content in the 425 °C reaction products using Ni3Mo14/Al_2O_3-Cr and Ni3Mo14/Al_2O_3 were determined with ICP-OES analysis. Equation 9, 10 and 11 were used to calculate Ni and V conversion (C_{Ni}, C_V) and total HDM, respectively. Encouraging hydrodemetallisation conversions were obtained, as can be seen in Table 6.6. Total Ni + V content in the VR feed was 320 ppm. Very favourable HDM rates (>0.90) were obtained for both catalysts, with slightly higher rates for removal of both metals with Ni3Mo14/Al_2O_3-Cr than with Ni3Mo14/Al_2O_3. The HDM for reutilisation reactions was very similar to the initial reactions; therefore HDM activity was maintained in the spent catalysts. Higher HDM rates were observed in this work than in hydrotreating Maya crude diluted with diesel at 380 °C with a CoMo/Al_2O_3 (87) or a NiMo/Al_2O_3 (106), which had ca. 0.55 and 0.60 values, respectively. The Maya crude had less initial Ni and V content than the VR used in this work, obtaining a product with approximately 70 ppm metals, significantly higher than in this work. Therefore both mesoporous alumina and mesoporous alumina doped with Cr had high HDM activity in short reaction times.

Table 6.6. HDM conversion for initial and reutilisation reactions at 425 °C of Ni3Mo14/Al_2O_3-Cr and Ni3Mo14/Al_2O_3. All reactions lasted 60 minutes with an initial 185 bar H_2 pressure.

Catalyst	Reaction	Ni (ppm)	V (ppm)	C_{Ni}	C_V	HDM
Ni3Mo14/Al_2O_3-Cr	425 °C initial	0.80	8.93	0.99	0.97	0.98
	425 °C reutilisation	5.61	5.98	0.95	0.98	0.97
Ni3Mo14/Al_2O_3	425 °C initial	6.04	5.28	0.95	0.98	0.97
	425 °C reutilisation	8.15	17.64	0.93	0.94	0.93

6.3.2. Spent catalysts

After each reaction spent catalysts were characterised with TGA for coke deposits and N_2 adsorption-desorption to evaluate changes in their textural properties. SEM-EDX was performed on the spent catalysts of the reutilisation reactions and TEM micrographs were taken on the catalysts after the reutilisation at 425 °C.

6.3.2.1. Coke deposits

Coke deposits on Ni3Mo14/Al_2O_3-Cr, Ni3Mo14/Al_2O_3, Al_2O_3-Cr and Al_2O_3 are shown in Table 6.7, expressed as gram of coke per gram of catalyst. These data correspond to the solids yield reported in Table 10.3, 10.4, and 10.8 to 10.10 (Appendix 1). Coke deposits are further discussed in this section in association to changes in the catalysts textural properties. In the initial reactions with Ni3Mo14/Al_2O_3-Cr coke deposition was similar for all temperatures. For reutilisation reactions with Ni3Mo14/Al_2O_3-Cr, a 30% increase in coke occurred at 400 °C and less coke build-up took place with increasing reaction temperature (20% at 425 °C and 0% at 450 °C). The higher increase in coke at the 400 °C reutilisation was reflected in a lower $C_{>450°C}$ for this reaction. Coke precursors polymerise at low reaction temperatures and undergo thermal cracking at high temperatures, thus higher coke formation is observed at lower reaction temperatures in a batch system (116). The decrease in coke deposits in the reutilisation reaction at 450 °C using Ni3Mo14/Al_2O_3-Cr was probably due to the reactivity of coke in initial stages of reaction (108).

Coke deposits were consistently lower for Ni3Mo14/Al_2O_3 than for Ni3Mo14/Al_2O_3-Cr at all reaction conditions. The latter catalyst had slightly higher acidity than the former although the n_A/n_M ratio for both catalysts was similar (Table 6.2). Despite higher coke deposits, Ni3Mo14/Al_2O_3-Cr achieved higher $C_{Asphaltenes}$ at 400 and 425 °C than Ni3Mo14/Al_2O_3 in initial reactions. In the reutilisation reactions a similar increase in coke deposits (22%) was obtained for both catalysts at 400 °C. Ni3Mo14/Al_2O_3-Cr had higher $C_{Asphaltenes}$ in the 425 °C reutilisation than Ni3Mo14/Al_2O_3, despite larger coke formation for the former catalyst. At the higher reaction temperature, Ni3Mo14/Al_2O_3 showed an increase in coke whereas Ni3Mo14/Al_2O_3-Cr had no additional deposits. The main difference in coke formation between the catalysts was that for Ni3Mo14/Al_2O_3 coke deposits increased linearly with temperature whereas for Ni3Mo14/Al_2O_3-Cr temperature did not have such a strong effect, especially in the initial reactions. This could indicate that the Cr-doped catalyst reached the coking steady state sooner than Ni3Mo14/Al_2O_3.

It was reported that when alumina is used as catalytic material significant coke deposits occur (85). In this case, coke deposits for Al_2O_3 were higher than their respective catalyst, very probably due to the higher acidity of the material. At 400 °C, Al_2O_3-Cr had higher $C_{Asphaltenes}$ than Al_2O_3 despite higher coke content. In the 400 °C reutilisation deposits for both supports were similar. Unexpectedly, at 450 °C coke deposition was lower for the Al_2O_3-Cr support than for the catalyst.

Higher conversions for the >450 °C fraction were reported using NiMo/Al_2O_3 than using a Cr-PILC when hydrocracking heavy coal liquids at 440 °C (54). The Cr-PILC showed higher coke deposits in the first use of the catalysts. When the catalysts were reutilised, however, coke deposits for the Cr-PILC were very low whereas a significant increase was observed for the NiMo/Al_2O_3. The same behaviour was observed in this work with the Cr-doped alumina. A NiMo/γ-alumina with similar metal loading was used to hydrocrack Cold Lake VR at 430 °C and 140 bar (85). The spent catalyst had 20% carbon deposits (equivalent to 0.25 g of coke per g of catalyst) with an asphaltene conversion of 0.58. Ni3Mo14/Al_2O_3-Cr at 425 °C and 185 bar presented 0.45 g of coke per g of catalyst in its reutilisation reaction with an asphaltene conversion of 0.82. This showed that Ni3Mo14/Al_2O_3-Cr can retain and even present better catalytic activity despite higher coke deposits.

Table 6.7. Coke on catalyst for Ni3Mo14/Al_2O_3-Cr, Ni3Mo14/Al_2O_3, Al_2O_3-Cr and Al_2O_3 determined by TGA analysis. All reactions lasted 60 minutes with an initial 185 bar H_2 pressure.

Sample	g coke per g catalyst at different reaction temperatures* (°C)					
	400 (i)	400 (r)	425 (i)	425 (r)	450 (i)	450 (r)
Ni3Mo14/Al_2O_3-Cr	0.43	0.56	0.38	0.45	0.44	0.42
Al_2O_3-Cr	0.51	0.57	–	–	0.26	0.30
Ni3Mo14/Al_2O_3	0.36	0.36	0.28	0.31	0.20	0.25
Al_2O_3	0.41	0.59	–	–	0.31	0.39

*(i) for initial and (r) for reutilisation reactions.

6.3.2.2. Electron microscopy study of spent catalysts

Figure 6.13 shows SEM micrographs for spent Ni3Mo14/Al_2O_3-Cr in reutilisation reactions at 400, 425 and 450 °C. An amorphous surface was observed for all spent catalysts. EDX elemental distribution profiles are presented as well in for each temperature for Al (red), Cr (green), Mo (blue), Ni (yellow), and C (pink). All the images presented a homogeneous distribution of the support elements (Al and Cr), the metal sites (Mo and Ni) as well as carbon deposition. The same behaviour was observed for Ni3Mo14/Al_2O_3, with SEM micrographs and EDX distribution profiles shown in Figure 6.14. The same format as Figure 6.13 was used.

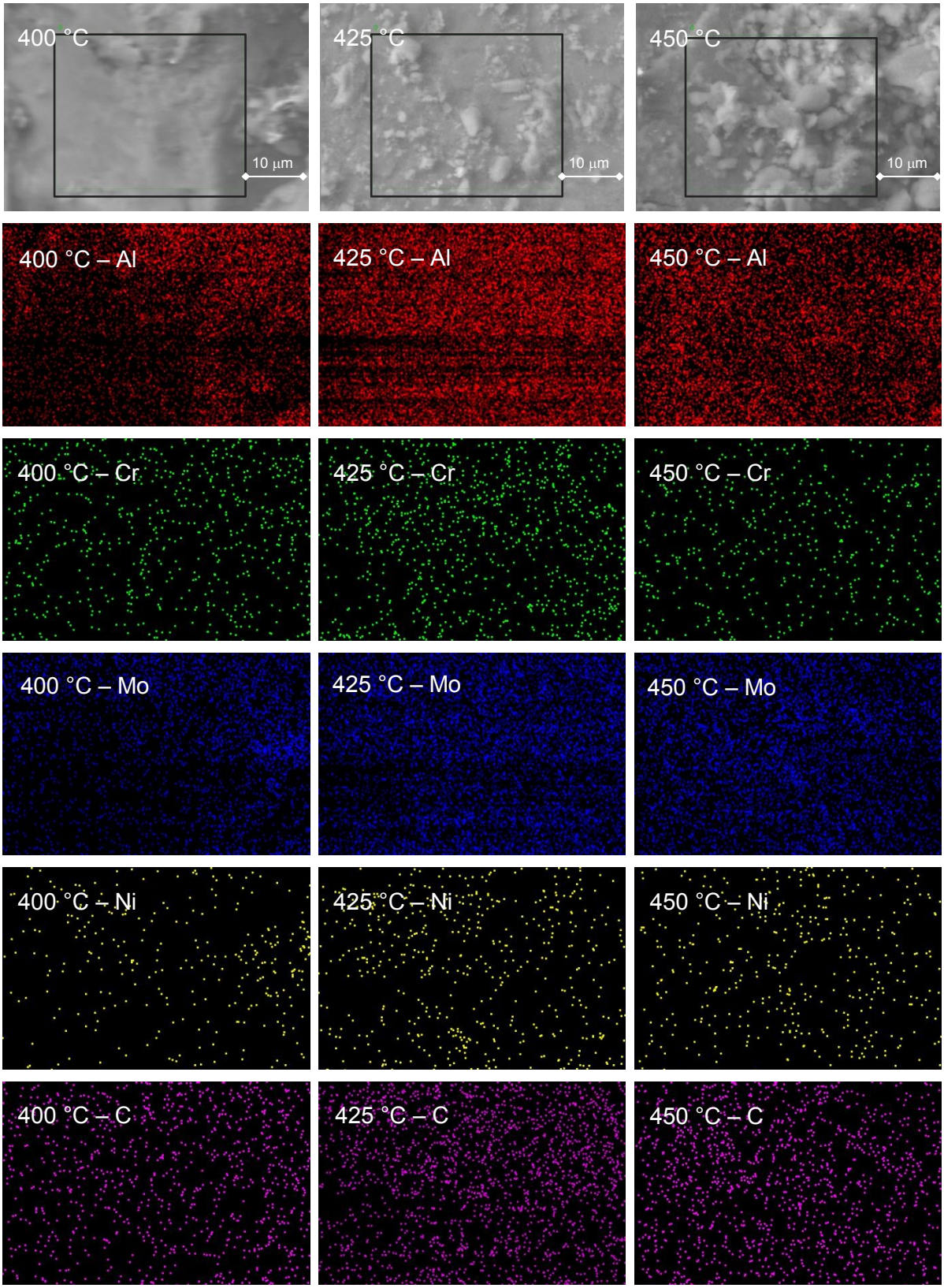

Figure 6.13. SEM micrographs (2,300X) for spent Ni3Mo14/Al_2O_3-Cr for reutilisation reactions at 400, 425 and 450 °C.
Elemental composition distribution profiles performed with EDX for each temperature are shown for the following elements: Al (red); Cr (green); Mo (blue); Ni (yellow); and C (pink).

Interestingly, the EDX profiles for Ni3Mo14/Al_2O_3-Cr (of the SEM analysed areas) measured less carbon than for Ni3Mo14/Al_2O_3, the opposite to values obtained from TGA measurements. This could indicate that coke deposits for Ni3Mo14/Al_2O_3-Cr entered the pores of the catalyst whereas coke deposits for Ni3Mo14/Al_2O_3 did not access all pores of the material and were collected in the surface of the catalyst.

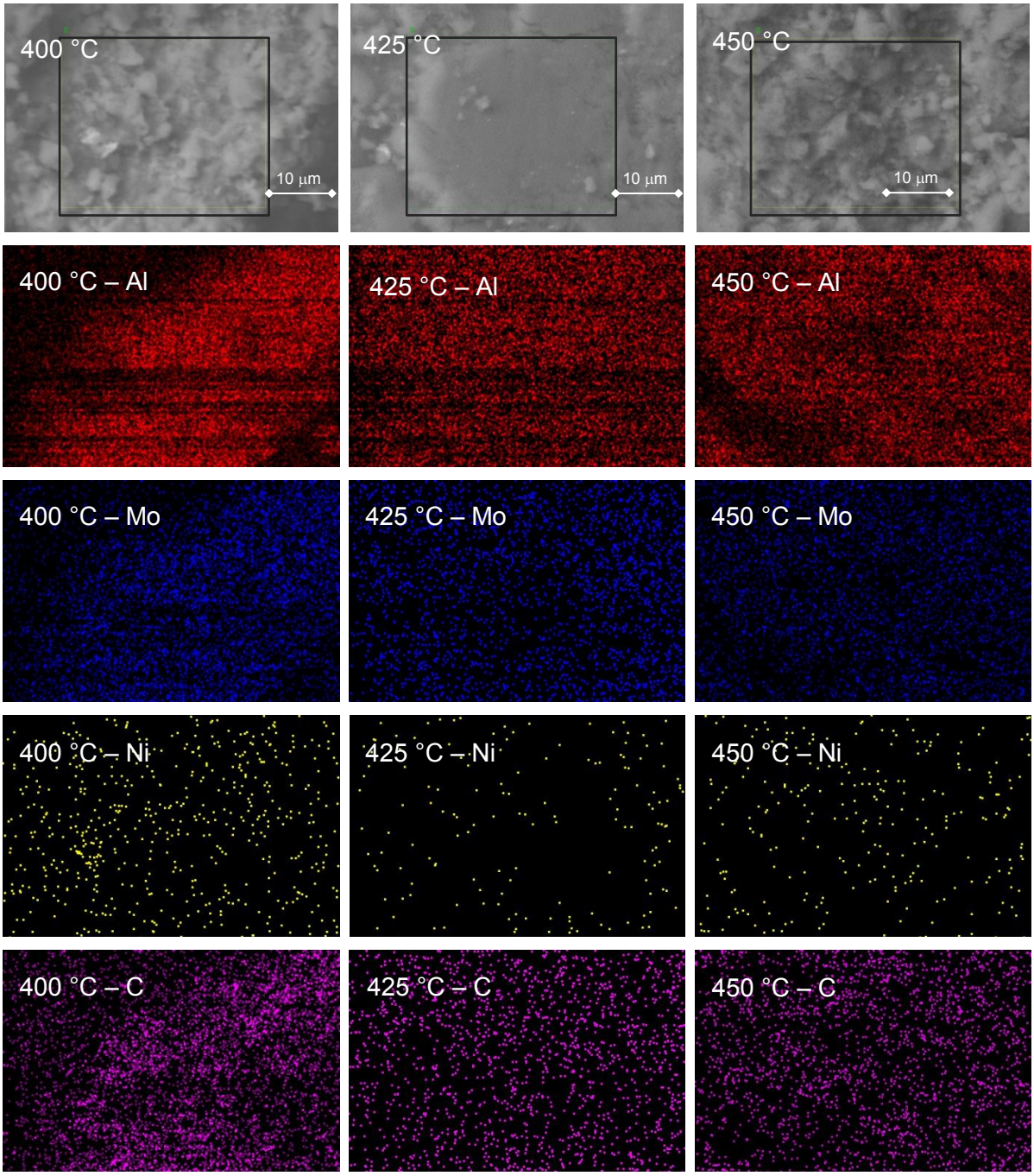

Figure 6.14. SEM micrographs (2,300X) for spent Ni3Mo14/Al_2O_3-Cr for reutilisation reactions at 400, 425 and 450 °C.
Elemental composition distribution profiles performed with EDX for each temperature are shown for the following elements: Al (red); Mo (blue); Ni (yellow); and C (pink).

Figure 6.15 shows TEM images at low (20,000X), medium (50,000X) and high (100,000X) magnification for spent Ni3Mo14/Al_2O_3-Cr and Ni3Mo14/Al_2O_3 after the 425 °C reutilisation reactions. The difference between the catalysts consisted mainly in the distribution of the coke deposits. Ni3Mo14/Al_2O_3-Cr showed uniform deposits which contrasted with coke agglomeration in superficial regions for Ni3Mo14/Al_2O_3 (circled). This would help understand why carbon EDX profiles for Ni3Mo14/Al_2O_3 were higher than for Ni3Mo14/Al_2O_3-Cr, even though the latter had higher total coke content (measured by TGA). It was observed that Ni3Mo14/Al_2O_3-Cr retained the same plate-like shapes as the fresh catalyst (Figure 6.5).

Additional high magnification TEM images for both catalysts are available in Figure 6.16, where more details of coke deposits were observed. For both catalysts MoS_2 layers were identified (circled). Slabs for Ni3Mo14/Al_2O_3-Cr were ca. 5 nm in length with a low stacking degree and were available in random directions (Figure 6.16c and e). Slabs for Ni3Mo14/Al_2O_3 generally had the same direction, longer length (> 10 nm) and had a higher stacking degree (Figure 6.16 d). From these images it was concluded that Cr-doping allows for better uniformity in coke deposition in the alumina support. This possibly allowed a larger amount of coke to enter the porosity of the catalyst, triggering higher coke deposits. On the other hand, even though some coke could enter the pores of Ni3Mo14/Al_2O_3, higher superficial coke deposits were formed.

TEM-EDX profiles for spent Ni3Mo14/Al_2O_3-Cr and Ni3Mo14/Al_2O_3 at 425 °C are shown in Figure 6.17. For the two catalysts, Ni and Mo peaks were observed along C and the support elements (Al and Al/Cr), reflecting on the dispersion of active metals observed in Figure 6.13 and Figure 6.14 from SEM-EDX. The Cu peaks correspond to the grid used to support the samples for analysis.

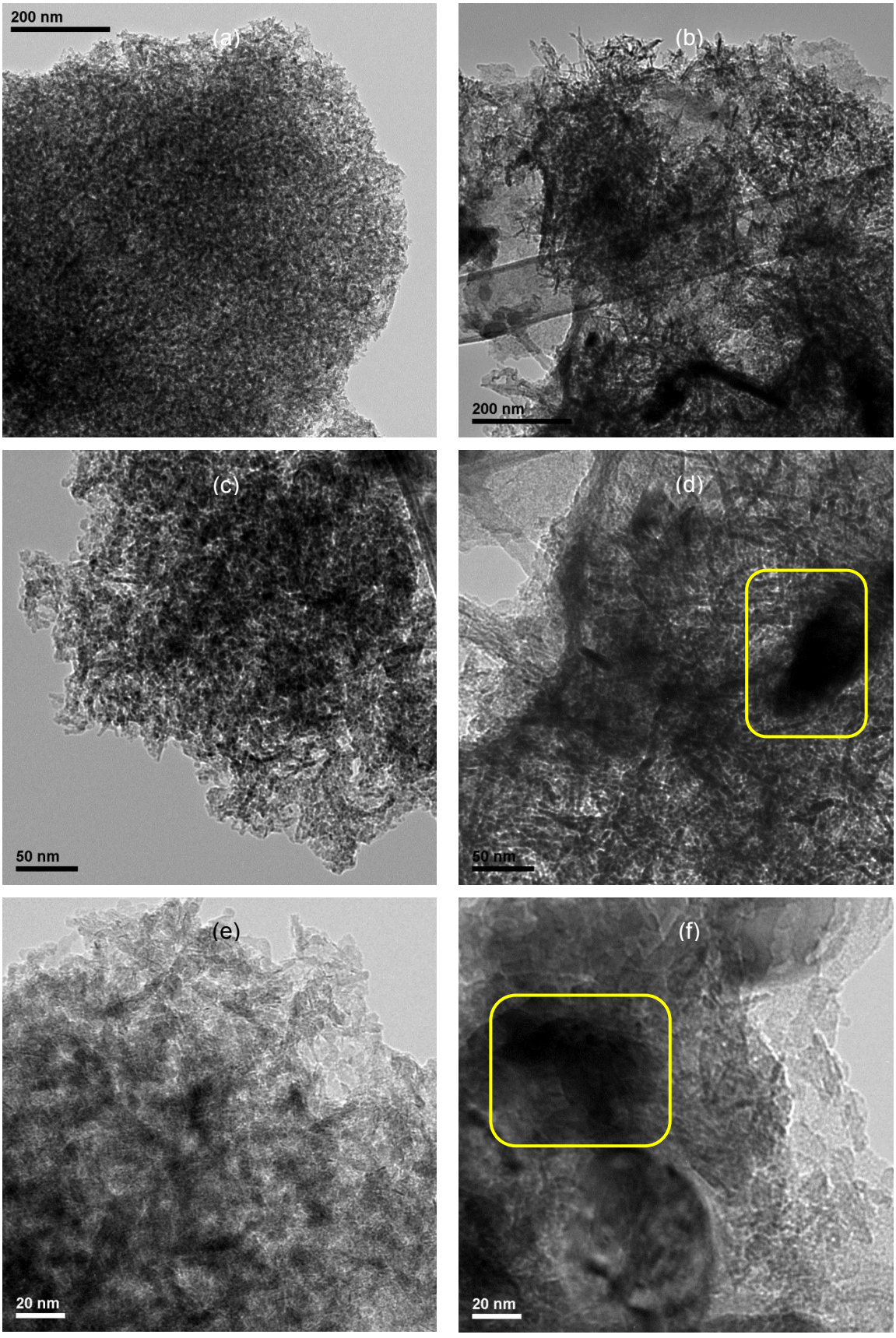

Figure 6.15. TEM images of 425 °C reutilisation spent catalysts Ni3Mo14/Al_2O_3-Cr (a, c, e) and Ni3Mo14/Al_2O_3 (b, d, f) at low (20,000X), medium (50,000X) and high (100,000X) magnification.

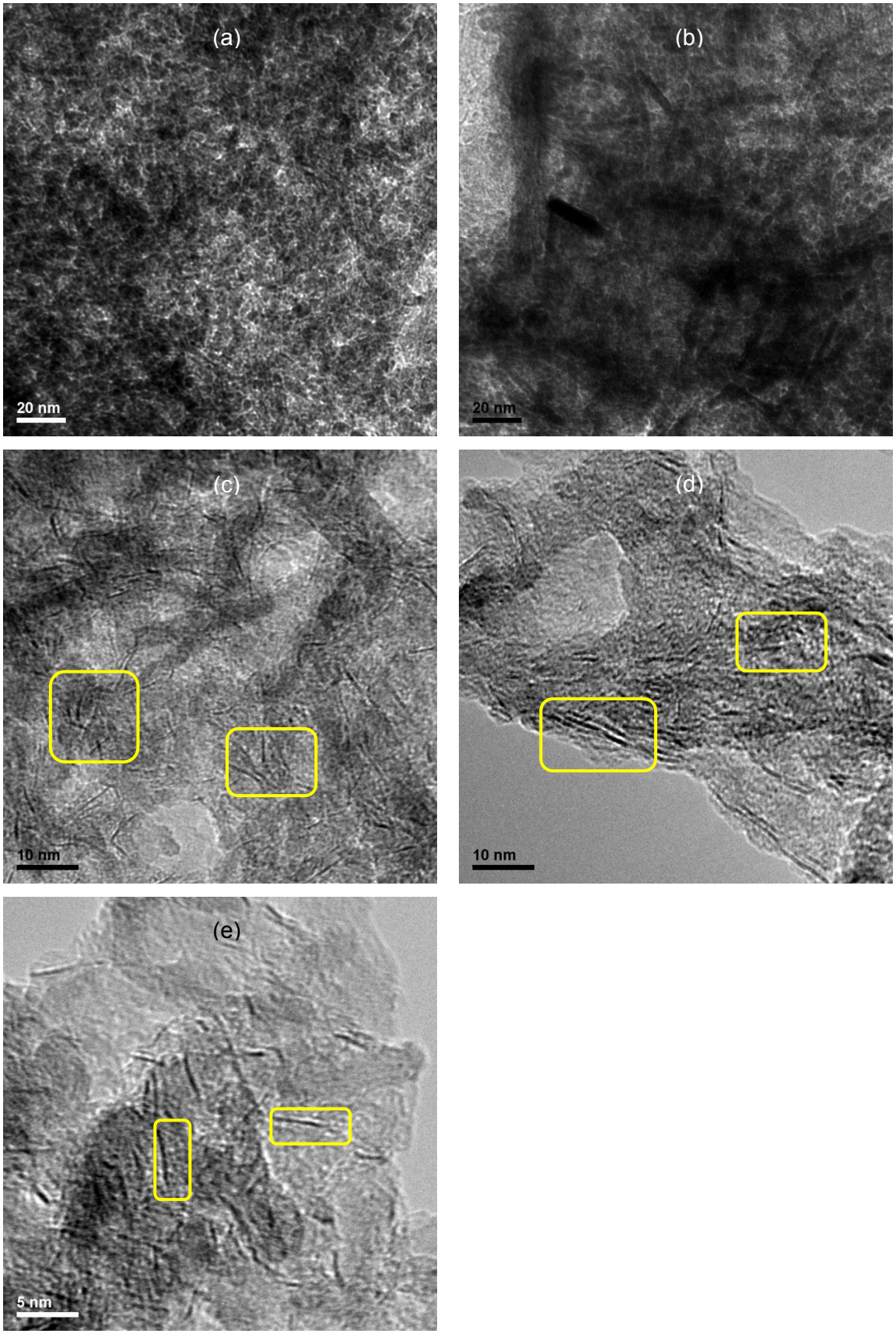

Figure 6.16. TEM images of spent catalysts (425 °C reutilisation) Ni3Mo14/Al_2O_3-Cr (a, c, e) and Ni3Mo14/Al_2O_3 (b, d) at high magnifications (100,000X, 250,000X and 500,000X).

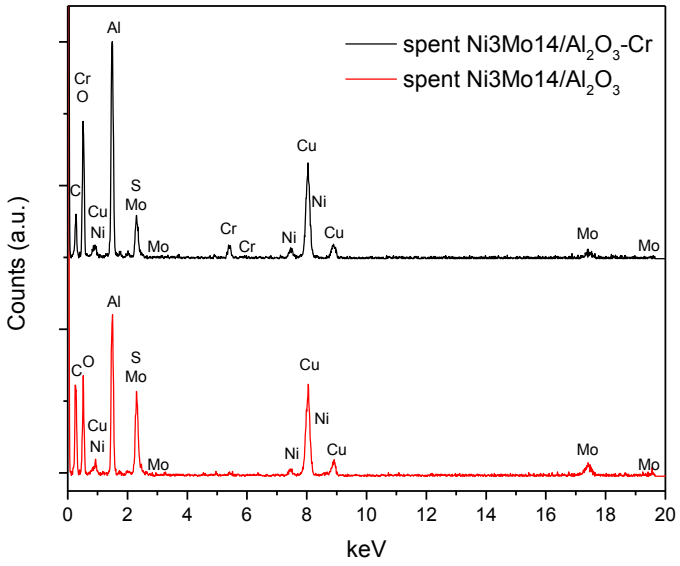

Figure 6.17. EDX analysis on TEM micrograph areas (Figure 6.16 100,000X magnification) for spent Ni3Mo14/Al_2O_3-Cr and Ni3Mo14/Al_2O_3 at 425 °C reutilisation.

6.3.2.3. Textural properties

Changes in textural properties of spent Ni3Mo14/Al_2O_3-Cr, Ni3Mo14/Al_2O_3, Al_2O_3-Cr and Al_2O_3 are shown in Table 6.8. Properties of the fresh catalysts and supports are included (from Table 6.1). A reduction in the S_{BET} and pore volume occurred for all of the spent materials. Textural properties vary after reaction because coke covers the surface of the catalyst, thereby reducing its S_{BET} and pore volume (100,111). Changes in APD for the spent materials were varied. Coke can block the smallest pores thereby increasing the average pore diameter. When the APD is reduced, coke deposits evenly on the support blocking pores of different sizes. In the initial reaction at 400°C using Ni3Mo14/Al_2O_3-Cr and for both reactions at 400°C using Al_2O_3-Cr the APD of the spent materials was higher than for the fresh ones.

Figure 6.18a, b, c and d contain the N_2 adsorption-desorption isotherms for fresh and spent Ni3Mo14/Al_2O_3-Cr, Ni3Mo14/Al_2O_3, Al_2O_3-Cr and Al_2O_3, respectively. The shape of the isotherms match a Type IV with hysteresis loop H3, which is found in materials formed by plate-like particles assembled in parallel (126). The shape and position of the hysteresis loops are similar between fresh and spent materials. Macroporosity is present in the materials since the isotherms did not show a horizontal line at P/Po values close to 1.0. The catalysts and supports showed small changes in isotherm shape even with very high coke deposits; therefore pore mouth plugging was minimal. These plate-like particles showed an advantage over reports for cylindrical pores which,

when covered with coke, were modified into ink-bottle types that greatly reduced the S_{BET} and had steric hindrance issues when processing heavy fractions (87).

Table 6.8. Textural properties of spent Ni3Mo14/Al_2O_3-Cr, Ni3Mo14/Al_2O_3, Al_2O_3-Cr and Al_2O_3 determined by N_2 adsorption. All reactions lasted 60 minutes with an initial 185 bar H_2 pressure.

Sample	T* (°C)	S_{BET} ($m^2 \cdot g^{-1}$)	Total pore volume ($cm^3 \cdot g^{-1}$)	Average pore diameter** (nm)
Ni3Mo14/Al_2O_3-Cr	Fresh	274.7	0.74	9.1
	400 (i)	171.3	0.43	8.5
	400 (r)	173.9	0.47	9.2
	425 (i)	181.3	0.48	9.4
	425 (r)	129.4	0.35	9.3
	450 (i)	159.6	0.46	9.7
	450 (r)	167.7	0.47	9.7
Al_2O_3-Cr	Fresh	365.3	1.05	9.7
	400 (i)	186.2	0.49	9.4
	400 (r)	188.1	0.43	8.2
	450 (i)	246.2	0.78	11.0
	450 (r)	234.8	0.72	10.8
Ni3Mo14/Al_2O_3	Fresh	342.0	0.66	10.4
	400 (i)	145.6	0.26	6.3
	400 (r)	141.9	0.24	5.9
	425 (i)	229.4	0.40	5.8
	425 (r)	201.0	0.37	6.1
	450 (i)	229.6	0.46	6.9
	450 (r)	180.3	0.38	7.0
Al_2O_3	Fresh	341.2	1.21	12.0
	400 (i)	164.8	0.68	14.1
	400 (r)	200.5	0.74	12.9
	450 (i)	203.9	0.79	13.2
	450 (r)	252.4	0.95	13.1

*(i) for initial and (r) for reutilisation reactions

**BJH model applied to the adsorption branch of the isotherms

Ni3Mo14/Al_2O_3-Cr. A decrease in N_2 uptake in low relative P/Po was observed for spent catalysts, showing some decrease in the microporosity of the material while the mesoporosity was maintained. At 425 °C the spent catalysts presented the sharper reduction in N_2 uptake in low P/Po values; since the mesopores in the material were still accessible, there were no steric hindrance effects and conversion for this temperature remained unaffected. N_2 uptake increased at the 400 °C reutilisation, despite higher coke deposits than the initial reaction. This could be due to changes in the nature of the coke deposits; more graphitic or aromatic coke would be more compact.

Ni3Mo14/Al_2O_3. The isotherms of this catalyst, fresh and spent, have been discussed in detail in Section 5.3.2.2. This catalyst as well as Ni3Mo14/Al_2O_3-Cr had a higher decrease in N_2 uptake for their isotherms at 425 °C, which is not the condition at which the highest coke deposits were formed. The shape and position of the isotherms for the spent catalysts had more variations than for Ni3Mo14/Al_2O_3-Cr with even less coke formation. Therefore Ni3Mo14/Al_2O_3-Cr could accommodate higher coke yields without significant variation in its textural properties.

Supports. Both supports had a reduction in the N_2 uptake in low relative pressure, with further decrease in the 400 °C reactions that have larger coke deposits. It is interesting to observe that the isotherms had less N_2 uptake in the reutilisation reactions for Al_2O_3-Cr whereas the opposite occurred for Al_2O_3. Reutilisation reactions accounted for higher coke deposits than the initial ones in all conditions. Hence, the increase in N_2 uptake for Al_2O_3 could happen because deposits change their configuration into more asphaltenic and compact coke. This was also observed with an increase in S_{BET} for the reutilised Al_2O_3.

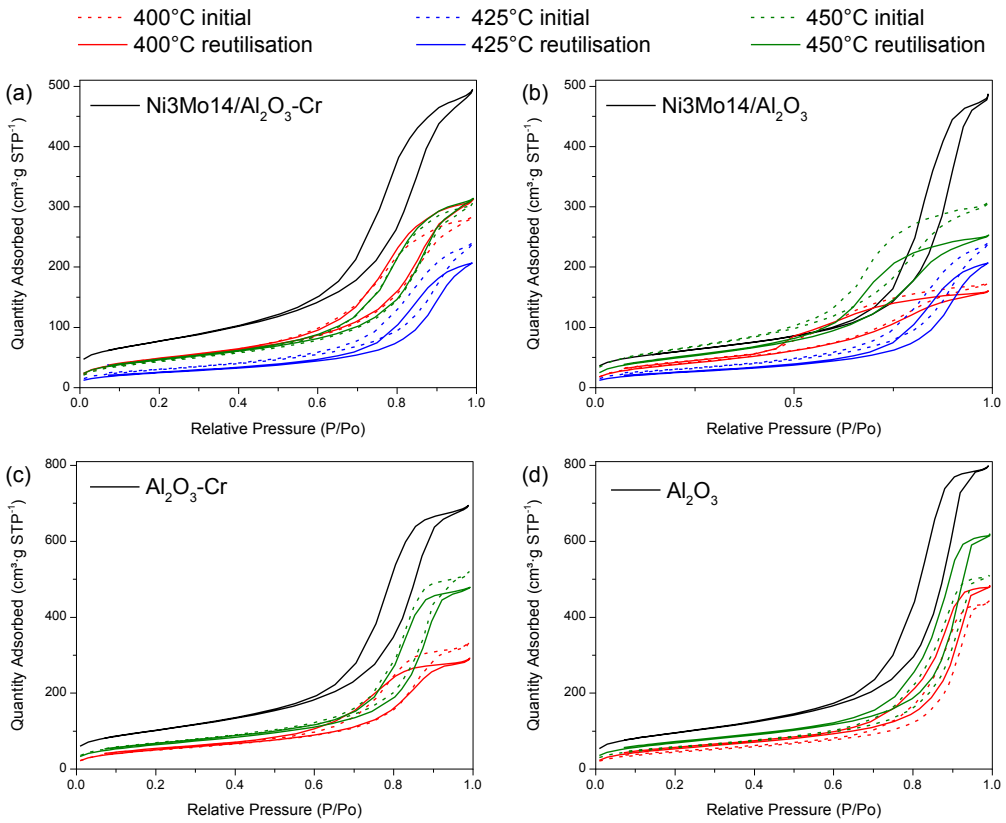

Figure 6.18. N_2 adsorption-desorption isotherms of fresh and spent Ni3Mo14/Al_2O_3-Cr, Ni3Mo14/Al_2O_3, Al_2O_3-Cr and Al_2O_3. All reactions lasted 60 minutes with an initial 185 bar H_2 pressure.

The pore size distribution profiles for the spent and fresh Ni3Mo14/Al_2O_3-Cr, Ni3Mo14/Al_2O_3, Al_2O_3-Cr and Al_2O_3 are present in Figure 6.19a, b, c and d, respectively. Similar PSD curves were maintained for all materials, with a proportional decrease in pore volume throughout.

Ni3Mo14/Al_2O_3-Cr. At 400 °C, a 30% increase in coke deposits from the initial to the reutilisation reaction caused slight shifts in the PSD curves to lower pore volumes at lower pore sizes and higher pore volumes at higher pore sizes. It was mentioned previously that coke is reactive; therefore the accumulation of coke at the 400 °C reutilisation could point towards changes in the nature between newer and older deposits. Given that more coke deposits did not affect the textural properties of the catalyst –the S_{BET} for this catalyst was almost unaffected in its reutilisation– more graphitic, compact coke could be forming (109,110). The PSD curves for spent Ni3Mo14/Al_2O_3-Cr catalysts changed to lower pore volumes from initial and reutilisation reactions at 425 °C. At 450 °C coke deposits did not vary in the reutilisation and the same PSD profile was obtained for the reutilised catalyst. It is interesting that even though the catalysts had different coke deposits at each reaction temperature they retained very similar PSD curves, indicating that Ni3Mo14/Al_2O_3-Cr could accommodate high coke yields without significant variation in its textural properties.

Ni3Mo14/Al_2O_3. The pore size distribution profile of this catalyst has been discussed in detail in Section 5.3.2.2. The main difference to point out between spent Ni3Mo14/Al_2O_3 and spent Ni3Mo14/Al_2O_3-Cr was the decrease in pore volume that the former had at larger pore diameters. Ni3Mo14/Al_2O_3-Cr on the other hand had a constant loss of pore volume throughout all the pore diameters. This would suggest different coke deposition which could be caused by more superficial coke was formed on Ni3Mo14/Al_2O_3 than on Ni3Mo14/Al_2O_3-Cr, where an even decrease in pore volume was observed in all pore diameters.

Supports. Spent Al_2O_3-Cr and Al_2O_3 had similar PSD profiles when fresh. For both, the range between 4 and 20 nm was the most affected in pore volume reduction for the spent materials. The PSD curves for Al_2O_3-Cr at 400 and 450 °C had the same profile, although a higher reduction in pore volume occurred at 400 °C reactions, given that at this temperature higher coke deposits were obtained. Al_2O_3 had higher coke deposits at 400 °C than at 450 °C, but the PSD at the two temperatures were very similar for pore diameters below 10 nm. Perhaps smaller pores in this material were more easily blocked with coke deposits than in Al_2O_3-Cr, which would correspond to the APD obtained with spent catalysts.

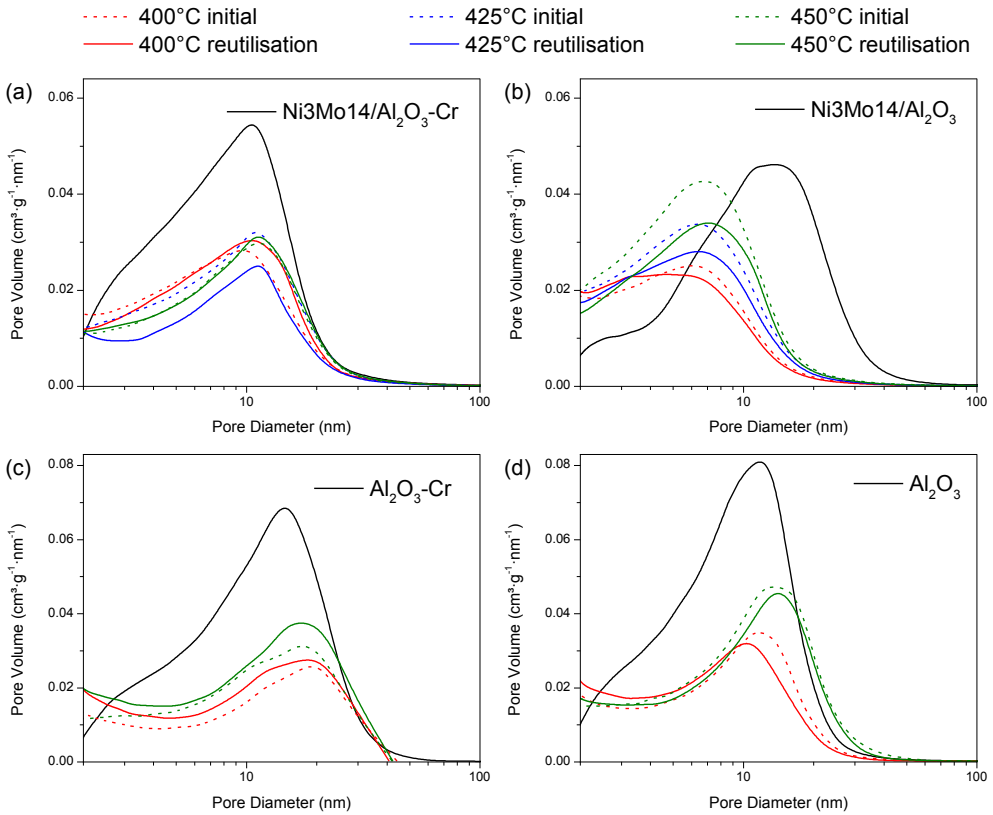

Figure 6.19. Pore diameter distribution as a function of pore volume for fresh and spent Ni3Mo14/Al_2O_3-Cr, Ni3Mo14/Al_2O_3, Al_2O_3-Cr and Al_2O_3. All reactions lasted 60 minutes with an initial 185 bar H_2 pressure.

6.3.3. Effects of coking

6.3.3.1. On conversion

The relationship of coke and conversions ($C_{>450°C}$ and $C_{Asphaltenes}$) is shown in Figure 6.20 for Ni3Mo14/Al_2O_3-Cr, Ni3Mo14/Al_2O_3, Al_2O_3-Cr and Al_2O_3. Data for these plots are available in Table 6.7, Table 10.2 and 10.7 (Appendix 1). Higher coke deposits generally led towards less $C_{>450°C}$ for Ni3Mo14/Al_2O_3-Cr and Ni3Mo14/Al_2O_3. The main difference between the catalysts was the range in coke deposits, a narrower range for the former catalyst was observed than for the latter catalyst. Then it appears that reaction temperature for the former catalyst was not so influential in its coke deposits. In contrast, coke deposition was somewhat influential for Ni3Mo14/Al_2O_3-Cr although mostly it did not affect $C_{Asphaltenes}$ for Ni3Mo14/Al_2O_3. For Al_2O_3-Cr and Al_2O_3 supports a general trend was observed that higher coke deposits yielded less $C_{>450°C}$ or $C_{Asphaltenes}$. The influence of coke deposits was observed to be proportional to the asphaltene content in the feed (101). In this work the same feed was utilised for all reactions;

therefore reaction conditions are also related to carbon deposition as well as conversion.

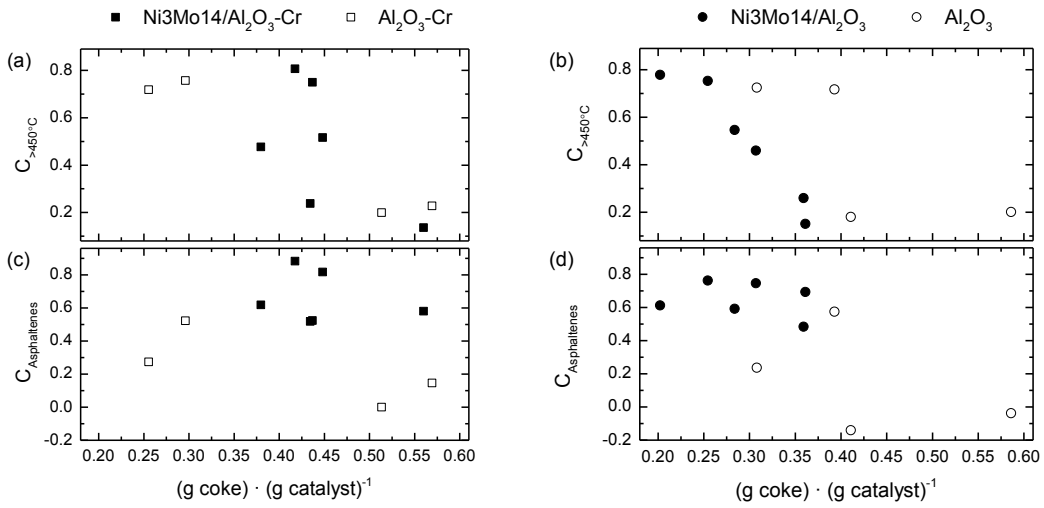

Figure 6.20. Coke content relation to $C_{>450°C}$ (a, b) and $C_{Asphaltenes}$ (c, d) for initial and reutilisation reactions of Ni3Mo14/Al_2O_3-Cr, Ni3Mo14/Al_2O_3, Al_2O_3-Cr and Al_2O_3. All reactions lasted 60 minutes with an initial 185 bar H_2 pressure.

6.3.3.2. On textural properties

The relationship between coke content and relative S_{BET}, relative pore volume and relative APD is displayed in Figure 6.21 a-f for Ni3Mo14/Al_2O_3-Cr, Ni3Mo14/Al_2O_3, Al_2O_3-Cr and Al_2O_3. The relative values were calculated by dividing the property of the spent material by the fresh one.

For Ni3Mo14/Al_2O_3-Cr at coke contents below 0.45 g coke per g catalyst changes in relative textural properties seemed to be proportional to coke content, the catalyst with higher coke yields fell out of the trend. Nevertheless, it was argued previously that for this reaction more graphitic/aromatic coke could be forming given that relative textural properties remain unaffected. The relative textural properties of Al_2O_3-Cr were observed to be proportionally affected by coke deposits, as well as the ones for Ni3Mo14/Al_2O_3. Relative S_{BET} and pore volume for Al_2O_3 did not decrease with coke deposits and APD remained unaffected, possibly because of the formation of more graphitic coke deposits.

The loss of surface area with coke deposition has been reported before (106). Results for Ni3Mo14/Al_2O_3-Cr contrast with changes in textural properties for a CoMo/Al_2O_3 catalyst used for hydrotreating Maya heavy crude diluted with diesel at 380 °C and 50 bar (87). The catalyst presented an 80% reduction in S_{BET}, 40% reduction in pore volume and only retained 10% of its original APD (22 nm). Even though the

$CoMo/Al_2O_3$ catalyst had a large initial pore diameter, coke deposited on the pore mouth thereby decreasing diffusivity of reactant molecules. The authors concluded that a heavy oil catalyst needs to present a large pore diameter; these results suggest that the spatial configuration of the support and the uniformity of coke deposition play key roles in maintaining catalyst activity as well.

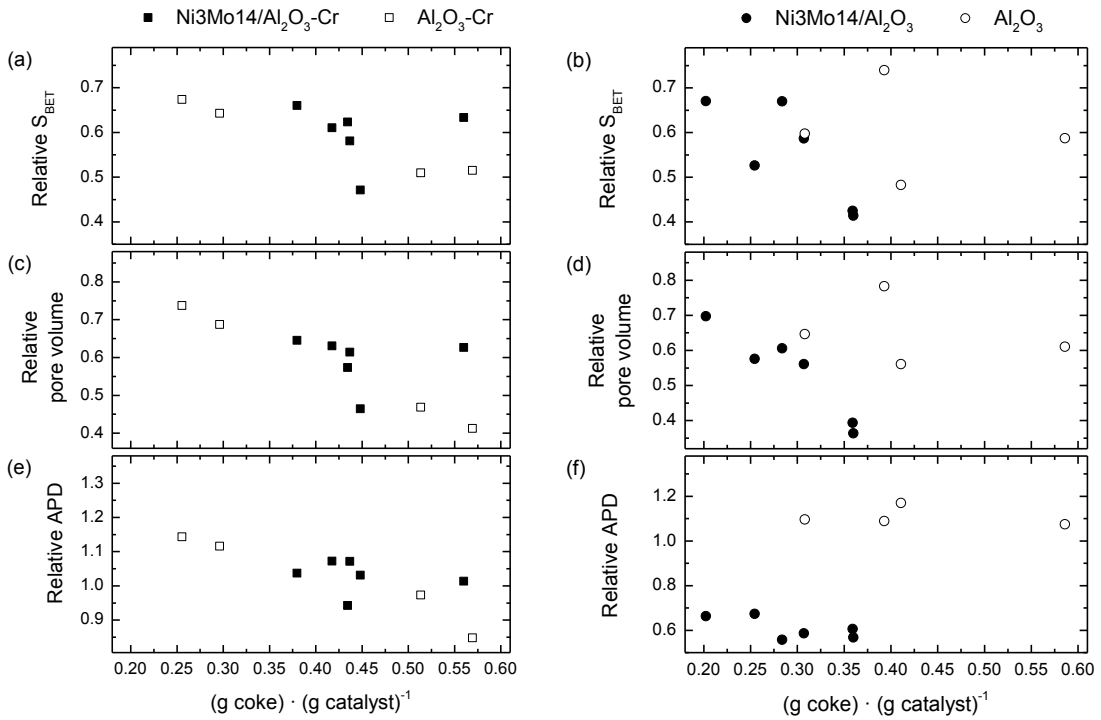

Figure 6.21. Coke content relation to relative textural properties of spent $Ni3Mo14/Al_2O_3$-Cr, $Ni3Mo14/Al_2O_3$, Al_2O_3-Cr and Al_2O_3: (a, b) S_{BET}, (c, d) pore volume and (e, f) APD. All reactions lasted 60 minutes with an initial 185 bar H_2 pressure.

6.4. CONCLUSIONS

The influence of Cr as a dopant in mesoporous Al_2O_3 for NiMo catalysts was investigated for initial reaction stages of VR hydrocracking. The Al_2O_3-Cr support permitted high metal oxide deposition while the textural properties remained relatively unaffected. Al_2O_3-Cr presented strong acidity, required for bifunctional hydrocracking catalysts; acidity was slightly reduced after metal deposition. The Cr-doped catalyst had slightly higher acidity than the one supported on Al_2O_3. XRD patterns showed that a high dispersion of active metal sites in the catalyst was achieved for Al_2O_3-Cr. A decrease in the peaks for gamma alumina suggested that less ordering was present when Cr was inserted in the alumina matrix. TEM micrographs showed that Cr did not affect the mesoporosity and structure of the alumina and that metals were homogeneously dispersed for $Ni3Mo14/Al_2O_3$-Cr. Therefore the novel synthesis method reported here proved effective for introducing Cr in the alumina matrix.

Larger metal crystallites were formed in Ni3Mo14/Al_2O_3 which were not observed in Ni3Mo14/Al_2O_3-Cr. TEM images therefore showed that Cr can help disperse metal oxides in Al_2O_3 supported catalysts. TPR analysis conveyed that Ni and Mo were reduced at lower temperatures in Ni3Mo14/Al_2O_3-Cr than in Ni3Mo14/Al_2O_3, making active metal sites more available for the former material. A shift to higher temperatures for the Cr peak could indicate it formed stronger interactions with Ni and Mo than with the Al_2O_3.

Thermal and catalytic pathways were observed to occur simultaneously in hydrocracking reactions. Conversions for the fraction boiling above 450 °C, $C_{>450°C}$, were observed to be directly related to reaction temperature, with similar values obtained at a certain temperature for any material. On the contrary, asphaltene conversion, $C_{Asphaltenes}$, had a strong catalytic effect. Given that at high temperatures thermal cracking takes place, molecules could be catalytically hydrogenated, yielding better $C_{Asphaltenes}$. Initial conversions were similar for Ni3Mo14/Al_2O_3-Cr and Ni3Mo14/Al_2O_3, but in reutilisation reactions at 425 and 450°C better $C_{Asphaltenes}$ were observed for Ni3Mo14/Al_2O_3-Cr. This could be due to the better metal dispersion and the reducibility of the NiMo sites at lower temperatures. Al_2O_3-Cr could act as a hydrogenation catalyst, and higher $C_{Asphaltenes}$ than Al_2O_3 were observed at 400 °C. At 450 °C it did not appear to be highly active for hydrogenation reactions and yielded similar $C_{Asphaltenes}$ as Al_2O_3. The maximum maltene to asphaltene ratio for Ni3Mo14/Al_2O_3-Cr was obtained at 425 °C, possibly because of higher gas yields at 450 °C. The maltene to asphaltene ratio was significantly higher for this catalyst than for Ni3Mo14/Al_2O_3 above 425 °C, even though the latter had less gas and coke production. HDS and HDM rates for Ni3Mo14/Al_2O_3-Cr and Ni3Mo14/Al_2O_3 were very similar; HDS was similar to other catalysts reported in the literature; very encouraging HDM rates were obtained with these catalysts.

Coke deposits decreased with increasing reaction temperature. In initial reactions and in reutilisations using Ni3Mo14/Al_2O_3-Cr, less coke was accumulated at higher temperatures. Coke deposits were very reactive at 450 °C, with no gains in total coke deposits in its reutilisation. SEM-EDX measurements of the two catalysts revealed that metal sites were still present after coke deposited on the materials, suggesting that coke did not block the metal sites. Ni3Mo14/Al_2O_3-Cr had higher asphaltene conversion than Ni3Mo14/Al_2O_3 –as well as for different catalysts reported in the literature– despite higher coke formation. This shows that Ni3Mo14/Al_2O_3-Cr can retain and even present better catalytic activity despite higher coke deposits. More superficial coke was detected for Ni3Mo14/Al_2O_3 than for Ni3Mo14/Al_2O_3-Cr. Thus Cr not only aided in metal

dispersion in catalyst synthesis, but also in coke dispersion during reaction. This possibly allowed for a larger amount of coke to enter the porosity of the catalyst, triggering higher coke deposits.

Generally, spent catalysts and supports had a reduction in surface area and pore volume and had a small increase in average pore diameter when compared to the fresh materials. Spent Ni3Mo14/Al_2O_3 catalysts had a decrease in APD. No evidence of pore mouth plugging was observed even with high coke deposits. The shape and position of the isotherms for the spent Ni3Mo14/Al_2O_3 had more variations than for Ni3Mo14/Al_2O_3-Cr with less coke formation. Pore volumes were maintained for Ni3Mo14/Al_2O_3-Cr at the lowest pore diameters. Therefore Ni3Mo14/Al_2O_3-Cr could accommodate higher coke yields without significant variation in its textural properties. The plate-like particles formed by Al_2O_3-Cr and Al_2O_3 showed an advantage over other materials, such as cylindrical pores, because they did not present pore mouth plugging. These results suggest that besides the large pore diameter which is needed for heavy oil catalytic upgrading, spatial configuration of the support and the uniformity of coke deposition play key roles in maintaining catalyst activity. The Cr dopant possibly aided in dispersing not only the Ni and Mo metal sites but also coke in the spent catalysts.

Chapter 7: NiMo catalysts supported on mesoporous silica alumina for VR hydrocracking

A catalyst supported on mesoporous silica alumina, Ni1Mo6/MSA, was synthesised and tested in VR hydrocracking. To evaluate and compare the influence of the support on the reactions against alumina, catalyst Ni1Mo6/Al_2O_3 and Al_2O_3 from Chapter 5 and 6, respectively, are included. Results are correlated to the fresh and spent catalyst characterisation.

7.1. INTRODUCTION

Different types of alumina, e.g. γ-alumina, have been widely used as a catalytic support for hydrotreating and hydrocracking processes because of their acidity and large surface areas. However, mesoporous materials have received little recent attention for upgrading heavy oils despite having been used in some hydrotreating and hydrocracking studies (146,148,149,180). Mesoporous aluminas have a greater capability to disperse Mo species, compared to conventional aluminas, achieving higher activity during HDS reactions (180). NiMo catalysts supported on mesoporous silica alumina had a higher stability and performed better than amorphous silica alumina or USY zeolites during vacuum gas oil hydrocracking (148). Higher asphaltene conversions were obtained with CoMo supported on mesoporous silica alumina when compared to conventional alumina-supported catalysts during the hydrocracking of Maya crude oil (149). Therefore, mesoporous supports seem to be a promising alternative to the conventional aluminas for the upgrading of heavy oil fractions.

The objective of this chapter was to compare catalysts supported on mesoporous silica alumina and mesoporous alumina with different textural properties. Results from catalyst Ni1Mo6/Al_2O_3 from Chapter 5 are included throughout this chapter for comparative purposes as well as results from Al_2O_3 from Chapter 6 to compare against MSA. These catalysts were tested in the hydrocracking of a VR from Maya crude oil. The conversion of VR and asphaltenes into lighter hydrocarbons obtained with both supports and catalysts was determined, and the coke deposition process was studied. The catalysts were utilised for two consecutive runs with fresh feed to evaluate coke deposition during reutilisation of the materials.

7.2. MATERIALS

Ni1Mo6/Al_2O_3 and Al_2O_3 from Chapters 5 and 6, respectively, are introduced again in this chapter for comparison purposes. The synthesis procedure for the materials is available in Section 5.2.1.2 and 4.2.1; characterisation results are included.

7.2.1. Synthesis

7.2.1.1. Support

MSA was synthesised according to a literature procedure detailed elsewhere (222). Approximately 8.1 g of aluminium isopropoxide were dissolved in 194 mL of tetrapropylammonium hydroxide at 60 °C and afterwards cooled to room temperature. Then a mixture of 389 mL of tetraethyl orthosilicate with 580 mL of ethanol was added to the Al solution, forming a gel. The mixture was aged overnight at room temperature and later dried at 100 °C and calcined at 550 °C for 8 hours. Finally, the material was sieved to 50-250 μm. The resulting material had a Si/Al weight ratio of 9.

7.2.1.2. Catalysts

The catalysts were named as Ni*x*Mo*x*/support where *x* is the loading of the corresponding metal oxide in wt %. The catalysts are: Ni1Mo6/Al_2O_3 and Ni1Mo6/MSA. The atomic ratio of Ni/(Ni+Mo) for each catalyst was designed to be close to 0.3.

The catalysts were prepared with the same procedure as described in Section 5.2.1.2. Catalyst synthesis was carried out at the Mexican Petroleum Institute (IMP) employing a TECAN MPS9500 liquid handling robot with pH, agitation, and temperature controls. The system was controlled by Symyx software which enabled the use of planned concentrations and liquid additions to the powder support. The calcination of the

supports and catalysts was carried out at IMP in a tube muffle furnace under air flowing at 200 mL·min^{-1} and 500 °C for 4 hours.

7.2.2. Characterisation

XRF spectroscopy was used to measure the metal loadings present in the supports. The nominal loading values of metal oxides were confirmed (Table 7.1). The textural properties of the materials are detailed in Table 7.2. Both supports presented a mesoporous structure. The MSA presented a mesoporous structure with the pore diameter centred at 4.7 nm and a surface area of 723 $m^2 \cdot g^{-1}$, which was diminished by 20% once metals were deposited.

Table 7.1. Metal oxide content determined by XRF.

Sample	Al_2O_3 (wt %)	SiO_2 (wt %)	NiO (wt %)	MoO_3 (wt %)	Ni/(Ni+Mo) atomic ratio
MSA	10.0	90.0			
Ni1Mo6/MSA	6.0	87.0	1.0	6.0	0.29
Al_2O_3	100	0			
Ni1Mo6/Al_2O_3	92.8	0	1.2	5.9	0.28

Table 7.2. Textural properties of the supports and calcined catalysts determined by N_2 adsorption-desorption.

Sample	S_{BET} ($m^2 \cdot g^{-1}$)	Total pore volume ($cm^3 \cdot g^{-1}$)	Average pore diameter* (nm)
MSA	723.1	0.45	4.7
Ni1Mo6/MSA	580.0	0.15	4.7
Al_2O_3	341.2	1.21	12.0
Ni1Mo6/Al_2O_3	282.2	0.60	11.5

*BJH model applied to the adsorption branch of the isotherms.

Figure 7.1 shows the changes in the isotherms for the supports, Al_2O_3 and MSA, as well as the NiMo catalysts. The Al_2O_3 exhibited a Type IV isotherm with a hysteresis loop H3 which matches materials formed by plate-like particles assembled in parallel. In contrast, the MSA support also had a Type IV isotherm but with a hysteresis loop H2, which has been reported for materials with “ink bottle” pores (126). The isotherms of both materials matched the ones reported in the literature that describes their respective synthesis (160,222). The area of the hysteresis loop for Ni1Mo6/MSA increased when compared to the area of the MSA. This indicates a reduction in the pore mouth size (88), which could be caused by interaction of the Ni and Mo compounds with the MSA, although a structural change of the support cannot be ruled

out. The isotherm for Ni1Mo6/MSA decreased in the relative N_2 uptake from the MSA although the pattern of the curve did not change. This can be correlated to a loss of surface area, possibly due to NiMo loadings, while the porous nature of the material remained unchanged. A full description of Ni1Mo6/Al_2O_3 is available in Section 5.2.2. It was observed in the PSD profiles (Figure 7.1 inset) of the materials that the pore size of this alumina is greater than others reported in the literature (146) whereas the MSA has pore sizes similar to other reported MSA supports (148). The pore volume was reduced for the PSD curves of the catalysts as metals partially covered the supports.

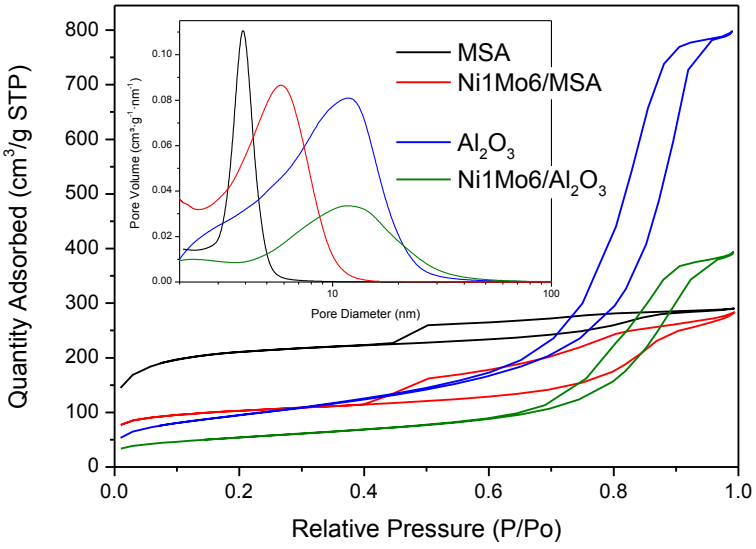

Figure 7.1. N_2 adsorption-desorption isotherms and pore size distribution curves for the calcined MSA, Ni1Mo6/MSA, Al_2O_3 and Ni1Mo6/Al_2O_3.

Results for acidity studies performed using ammonia temperature programmed desorption are presented in Figure 7.2. It was observed that both the Al_2O_3 support and Ni1Mo6/Al_2O_3 had higher acidities than the MSA across several temperature ranges. Since the cracking function of MSA was low, a low metal loading was chosen for the catalyst. Also, since hydroprocessing catalysts deactivate rapidly when upgrading heavy feeds low metal loadings can be used (88).

All catalysts presented some strong acidity (above 400 °C). The Ni1Mo6/MSA catalyst presented very low acidity, which could result in reduced cracking activity. It would be expected that the more acidic catalysts would have a stronger cracking function, which could lead to higher coking rates (191).

XRD diffraction patterns (Figure 7.3) of the catalysts showed no Mo or Ni metal oxide crystallite reflections. The diffraction patterns corresponded only to the Al_2O_3, which

was similar to γ-Al_2O_3, or MSA microcrystalline materials, suggesting that the Mo and Ni metal oxide crystallites were highly dispersed in the supports and had a size of less than 4 nm (149,180,188,223).

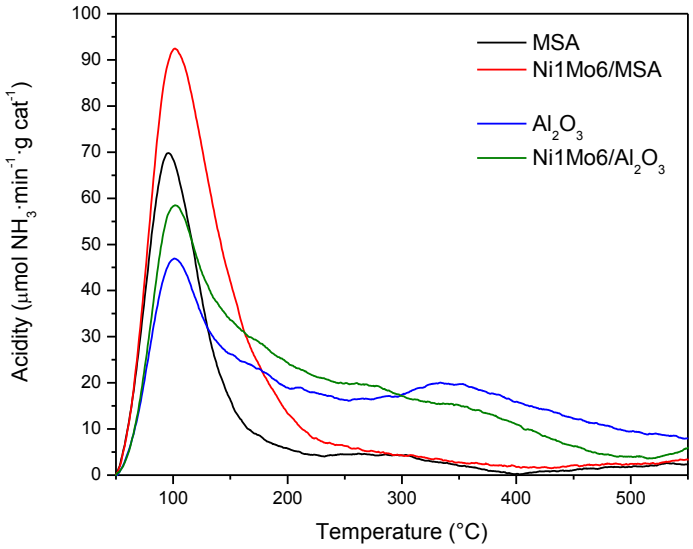

Figure 7.2. NH_3-TPD profiles for the calcined MSA, Ni1Mo6/MSA, Al_2O_3 and Ni1Mo6/Al_2O_3.

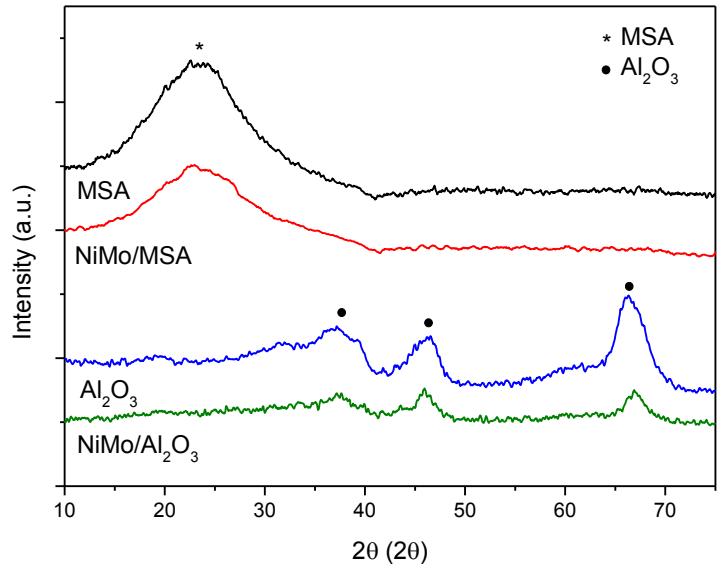

Figure 7.3. Powder XRD patterns of calcined MSA, Ni1Mo6/MSA, Al_2O_3 and Ni1Mo6/Al_2O_3.

Figure 7.4 shows that the TPR profiles of the Ni1Mo6/Al_2O_3 and Ni1Mo6/MSA contained two main peaks, a broad peak from 300 °C to 700 °C and another one at higher temperatures (800 °C). Qu et al. (174) presented separate TPR profiles for Ni, Mo, and

NiMo catalysts on Al_2O_3 and a silica support. The authors showed that Mo oxides have two main peak regions, the first one around 370 °C and 400 °C, and the second peak at 830 °C and 800 °C for Al_2O_3 and silica supports, respectively. The two regions that contained reduced Mo also matched other literature data (173,175). The first Mo peak was assigned to the partial reduction of Mo (Mo^{6+} → Mo^{4+}) and the peak at higher temperature was identified as occurring from the deep reduction of all Mo species. In the TPR profiles shown in Figure 7.4 the first Mo peak occurred at a similar temperature for both supports. In the low temperature range, the signals corresponding to the reduction of the Ni and Mo merged, creating a broad and large signal, although the main Ni peak can be distinguished at 500 °C and 550 °C for Al_2O_3 and MSA, respectively. The high temperature peak can be associated to the reduction of Mo species strongly bound to the support, for example highly dispersed tetrahedral Mo (174). The H_2 consumption for Ni1Mo6/Al_2O_3 was higher than for Ni1Mo6/MSA, thus the metals were easier to reduce for the former catalyst.

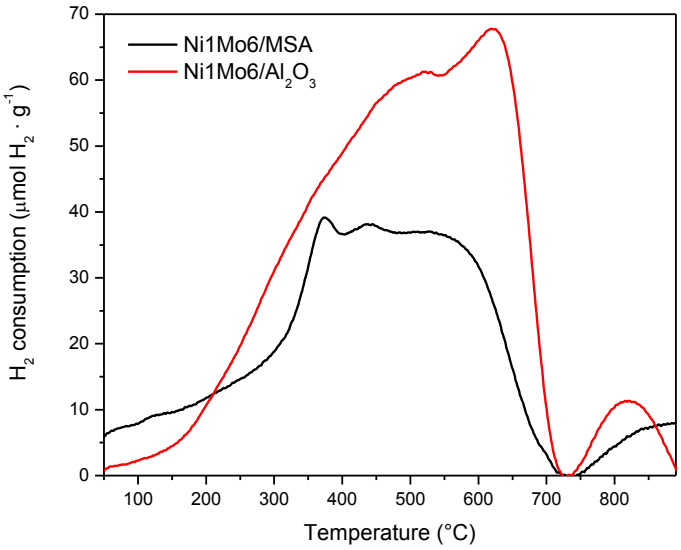

Figure 7.4. TPR spectra of calcined MSA, Ni1Mo6/MSA, Al_2O_3 and Ni1Mo6/Al_2O_3.

7.3. RESULTS AND DISCUSSION

The results are divided into two parts as follows: Section 7.3.1 which focuses on VR conversion, asphaltene upgrading and the corresponding product distribution and Section 7.3.2 which deals with changes in the spent catalysts.

7.3.1. Reaction products

7.3.1.1. Conversion

VR was hydrocracked at 400 and 450 °C and the performance of the catalysts and supports was evaluated at both temperatures. The conversion of the fraction of VR boiling above 450 °C ($C_{>450°C}$) obtained from the first and subsequent reutilisation reactions using catalysts and supports is reported in Figure 7.5a and b for MSA and Al_2O_3 materials, respectively. Supports were included to evaluate the hydrogenating activity of the metals. Numerical values for these figures are available in Table 10.1, 10.7 and 10.12 (Appendix 1). Coke deposits were taken into account as unconverted feed thereby affecting conversion negatively. Their stabilisation contributed to an increase in conversion for most materials during the reutilisation reactions, in line with observations reported in other hydrocracking studies (54).

It was observed that VR conversions ranged from: a) 0.15 to 0.35 for the 400 °C reactions; and b) 0.55 to 0.80 for the 450 °C reactions. In the 400 °C reused catalyst experiments, the conversions for Ni1Mo6/Al_2O_3 and Al_2O_3 were similar to those of the initial run, while at 450 °C an increase in conversion was observed in the run with catalyst reutilisation. Values for the reutilisation of MSA were higher than for the initial reaction at both temperatures. Ni1Mo6/MSA did not maintain its activity during the second run at 450 °C when the catalyst was reused. This is likely the result of pore blockage, given that pores of Ni1Mo6/MSA were smaller than those of Ni1Mo6/Al_2O_3 as observed in Figure 7.1. Most of the coke was deposited on the catalysts in the first run, as will be described in Section 7.3.1.2. When reusing the catalysts only marginal coke formation occurred, resulting in stabilisation or even a decrease in the amount of carbonaceous deposits. These trends are in agreement with the literature (54,108,134) where the same approach of catalyst reutilisation was employed.

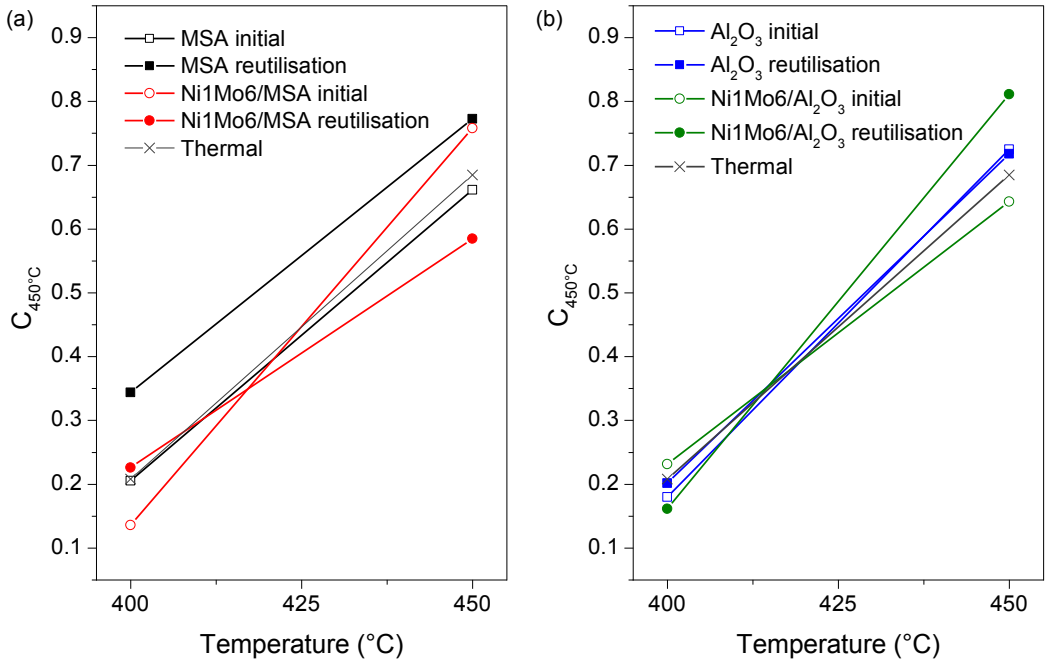

Figure 7.5. $C_{>450°C}$ for (a) MSA, Ni1Mo6/MSA, (b) Al_2O_3 and Ni1Mo6/Al_2O_3 catalysts for initial and reutilisation reactions. Reactions were at 185 bar H_2 pressure for 60 minutes.

A significant extent of thermal cracking was observed in the hydrocracking runs without catalyst, with conversion increasing at the higher temperature. For catalysts and supports, the increase in reaction temperature from 400 to 450 °C caused VR conversions to double or even triple. Conversion values are in agreement with others obtained for Maya vacuum residue (224,225), highlighting the predominant role of thermal over catalytic conversion. Catalysts containing Ni and Mo did not necessarily outperform their respective supports in terms of $C_{>450ºC}$, although as discussed below, there were marked differences in terms of asphaltene conversion. The MSA led to a slightly higher conversion than the Ni1Mo6/MSA, likely due to its higher surface area, with the exception of the initial reaction at 450 °C, in which the large carbon deposition on MSA led to lower conversions.

The conversions of asphaltenes ($C_{Asphaltenes}$) for the initial and reutilisation catalyst experiments for MSA and Al_2O_3 materials are shown in Figure 7.6a and b, respectively. Ni1Mo6/Al_2O_3 had a higher $C_{Asphaltenes}$ in its reutilisation reaction, contrary to the behaviour of the other materials. The use of Al_2O_3 and MSA led to negligible, or negative, $C_{Asphaltenes}$, as could be expected since they lacked a hydrogenation function. This might have caused cracking and subsequent polymerisation and coke formation, resulting in a small reduction in the asphaltenic content. Negative $C_{Asphaltenes}$ values were obtained because of the polymerisation of asphaltenes into coke and of high

boiling point maltenes into asphaltenes. It was observed that the reutilisation reactions produced a higher $C_{Asphaltenes}$ because most coke deposits reached a steady state during the first reactions. Therefore asphaltenes were transformed into lighter products rather than coke, although this included formation of gases as well as desirable products.

$C_{Asphaltenes}$ was heavily influenced by reaction temperature although very low asphaltene upgrading was observed in the thermal experiments. MSA had a low performance in the initial reactions because a significant amount of coke was deposited on it. In the subsequent catalyst reutilisation reaction $C_{Asphaltenes}$ was higher as coke deposits had possibly stabilised. In addition, deposition may generate a reduction in the acidity of the catalysts or supports, which then would be better balanced with the hydrogenation activity.

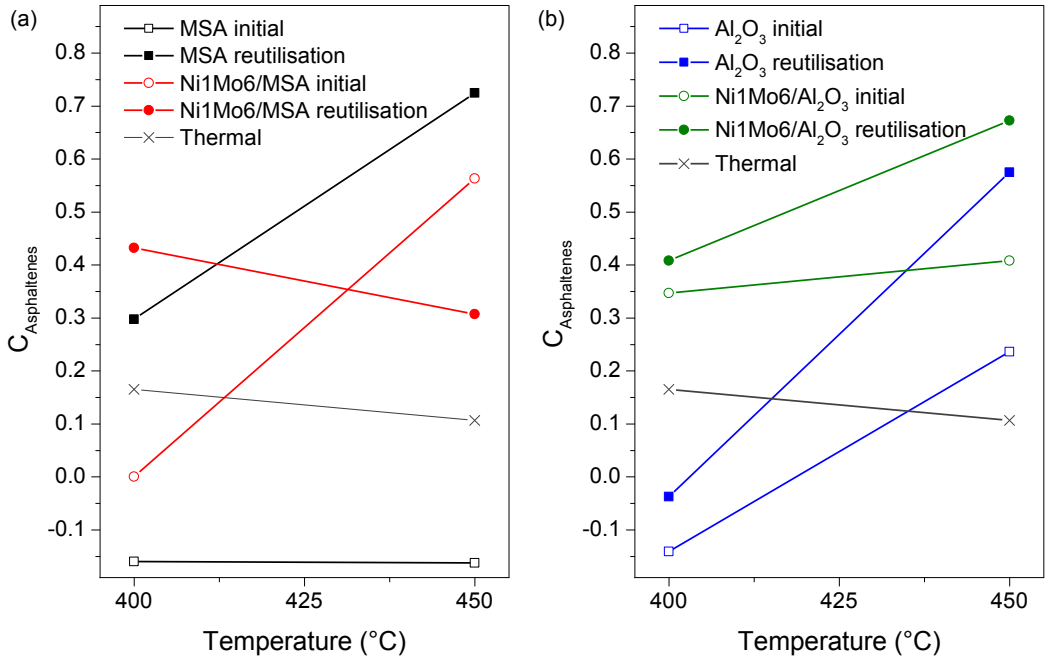

Figure 7.6. $C_{Asphaltenes}$ for (a) MSA, Ni1Mo6/MSA, (b) Al_2O_3 and Ni1Mo6/Al_2O_3 catalysts for initial and reutilisation reactions. Reactions were at 185 bar H_2 pressure for 60 minutes.

These results are consistent with the reports in the literature showing a significant increase in conversion of asphaltenes in hydrocracking above 425 °C for Middle East VR (194), hydroprocessing above 430 °C for heavy feeds (98), and hydrotreating of Maya crude over 440 °C (193). The latter feed only contained 13 wt % of asphaltenes compared to the 33 wt % content of the Maya VR used in these studies. The former crude was less viscous, thereby facilitating H_2 transfer into the feed as well as diffusion of the VR into the catalyst pores. Asphaltene conversion values compared well with

hydrocracking of Maya crude oil at high temperatures using CoMo supported on zeolite and alumina (196).

7.3.1.2. Yields

The product distributions for the initial and reutilisation reactions are reported in Table 7.3 and 7.4 respectively. Products were divided into the following: Gas, Maltenes boiling below 450 °C ($Maltenes_{<450°C}$), Maltenes boiling above 450 °C ($Maltenes_{>450°C}$), Asphaltenes and Solids. When comparing the initial and reutilisation runs, it can be observed that the main changes in the products occurred in the solid yields because most of the coke deposits were formed in the first reaction as discussed above. The Al_2O_3 and MSA, since they did not present hydrogenation activity, had a small increase in Solid yield in their reutilisation, with higher coke deposits in the Al_2O_3, which were promoted by its higher acidity. The significant amount of coke deposited on MSA at the initial 450 °C reaction resulted in the smallest conversion value for this set of reactions.

Reaction temperature affected gas production in a substantial manner, indicating that a significant amount of thermal cracking took place at 450 °C. This was confirmed by the large amount of gas products (44 wt %) observed in the thermal run, without catalytic material, which led to a small reduction in asphaltene content. This increase in gas production with reaction temperature is well documented in the literature, for example during hydrocracking of Maya crude oil on CoMo supported on a mixture of zeolite and alumina (196).

Gas production (calculated using Equation 5) was lower in experiments with $Ni1Mo6/Al_2O_3$ than in those with the Al_2O_3 itself. The Al_2O_3 support had the highest acidity among all these catalysts and it was not balanced by a hydrogenating function. The support showed a slight increase in coke formation when compared to the $Ni1Mo6/Al_2O_3$, as the presence of the hydrogenation function in the latter stabilised reactive cracking products in an intermediate boiling point range, leading to a reduction in gas yield and asphaltene content accompanied by an increase in $Maltenes_{<450°C}$. On the other hand, the MSA support produced lower gas yield at 450 °C than the Ni1Mo6/MSA and a higher coke formation than any other material tested. The high surface area and relatively small pore volume of MSA suggest that it was prone to coke deposition and reduced hydrogenating activity resulting in PAHs conversion into coke. Its lack of hydrogenation function was also observed in the minimal yield of the $Maltenes_{<450°C}$ fraction for the reutilisation reaction at 450 °C. Even though the use of Ni1Mo6/MSA led to lower conversions than MSA at 400 °C, its coke deposition was lower in the initial reactions possibly because the metal sites in the Ni1Mo6/MSA

provided hydrogenation activity. The reduced acidity of the material did not trigger cracking reactions. Increasing the temperature also favoured a decrease in the $Maltenes_{>450°C}$ materials. In the case of MSA, even though there was a reduction in the asphaltene content, all the high boiling point hydrocarbon materials were converted into coke. Comparing the performance of MSA and Al_2O_3 supports, it was observed that the Al_2O_3 materials showed higher Solids yield than the MSA materials in the catalyst reutilisation reactions. The high values $C_{>450°C}$ and $C_{Asphaltenes}$ observed previously for the MSA reutilisation at 450 °C reaction did not show that conversion into $Maltenes_{<450°C}$ was very low. MSA and Ni1Mo6/MSA underperformed when compared to Al_2O_3 and Ni1Mo6/Al_2O_3. Ni1Mo6/MSA had considerably higher Asphaltene yields than Ni1Mo6/Al_2O_3 at the 400 °C initial reaction and at the 450 °C reutilisation reaction. At these conditions the Asphaltene yields of Ni1Mo6/MSA were closer to the thermal reactions. Another difference that was observed was for the 450 °C initial reaction, where the Gas and $Maltenes_{<450°C}$ yields were unfavourable for Ni1Mo6/MSA.

Table 7.3. Product yields for initial reactions of MSA, Ni1Mo6/MSA, Al_2O_3 and Ni1Mo6/Al_2O_3; 60 min reactions with an initial 185 bar H_2 pressure.

Sample	T (°C)	Gas (wt %)	$Maltenes_{<450°C}$ (wt %)	$Maltenes_{>450°C}$ (wt %)	Asphaltenes (wt %)	Solids (wt %)
Thermal	400	10.2	0.0	61.7	26.4	1.7
	450	43.5	0.0	26.4	21.2	8.9
MSA	400	1.0	12.6	47.4	31.1	7.9
	450	36.2	17.5	7.2	12.6	26.5
Ni1Mo6/MSA	400	0.0	11.6	43.2	42.4	2.2
	450	46.5	8.9	30.1	11.1	3.6
Al_2O_3	400	0.0	10.1	51.5	28.5	9.9
	450	37.3	18.8	18.2	18.2	7.5
Ni1Mo6/Al_2O_3	400	0	16.3	61.7	12.9	9.1
	450	28.0	20.6	31.5	11.5	8.4

Table 7.4. Product yields for reutilisation reactions of NixMox/Al_2O_3 catalysts; 60 min reactions with an initial 185 bar H_2 pressure.

Sample	T (°C)	Gas (wt %)	$Maltenes_{<450°C}$ (wt %)	$Maltenes_{>450°C}$ (wt %)	Asphaltenes (wt %)	Solids (wt %)
MSA	400	0.0	33.9	42.5	22.9	0.7
	450	52.1	0.3	38.3	9.3	0.0
Ni1Mo6/MSA	400	3.4	16.5	61.0	19.1	0.0
	450	31.9	7.1	37.7	23.3	0.0
Al_2O_3	400	0.4	16.1	48.6	30.8	4.1
	450	41.6	9.9	34.2	12.2	2.1
Ni1Mo6/Al_2O_3	400	2.5	11.4	66.2	19.9	0.0
	450	32.0	40.2	16.7	11.0	0.1

The difference between catalytic hydrocracking and thermal cracking lies in the quantity of coke generated; thermal cracking produces a higher weight yield of coke than liquid products, and a high gas yield (226). In this work the catalytic effect can be observed from the reduction in coke deposits along with higher conversion into material boiling below 450 °C and less gas formation.

7.3.1.3. Product chemical characterisation

Figure 7.7 presents the SEC chromatograms for VR and reaction products of Ni1Mo6/Al_2O_3 and Al_2O_3. Maltenes plus asphaltenes, the maltene fraction and the asphaltene fraction are shown separately in Figure 7.7a, b and c, respectively. The SEC chromatograms of the VR showed a bimodal distribution, where the earlier-eluting peak ("excluded peak") corresponds to higher apparent mass material that does not enter the column porosity and therefore elutes faster. However, it has been proposed that molecular conformation rather than molecular weight (129) may play a predominant role in these molecules being excluded from the column porosity. The second peak, referred here as "retained", corresponds to material able to penetrate into the column pores. This peak in the VR SEC chromatogram (Figure 7.7a) presented a maximum at around 20 minutes, corresponding to 435 u according to the polystyrene calibration, and a range expanding into several thousand u. The VR asphaltenes and maltenes showed elution times shifted towards higher and lower molecular weight distributions respectively.

It is observed in Figure 7.7a that the retained peaks for all reaction products shifted to longer elution times than VR with increasing reaction temperature. Slight differences between elution times for Ni1Mo6/Al_2O_3 and Al_2O_3 were observed; therefore the molecular sizes of the products were very similar. The chromatograms for Al_2O_3 reaction products were broader than for Ni1Mo6/Al_2O_3, thus the molecular size distribution would be broader as well. The intensity of the excluded peaks decreased with increasing reaction temperature. Figure 7.7b shows the maltene fractions of the products and compares them to the maltenes from the VR. Longer elution times were also observed for the retained peaks with increasing reaction temperature. The chromatograms for maltenes from Ni1Mo6/Al_2O_3 and Al_2O_3 reaction products were very similar at 450 °C, possibly because thermal cracking dominated. On the other hand, smaller molecular sizes were observed for maltenes from Ni1Mo6/Al_2O_3 than for Al_2O_3 at 400 °C, indicating the effect of catalytic activity. Therefore maltenes that still remained in the $Maltenes_{>450°C}$ fraction, discussed in the previous section, underwent

molecular size reduction. The intensity of the excluded peaks also decreased with increasing reaction temperature.

The same trend is observed in Figure 7.7c, where it was identified that asphaltenes which did not convert into a different fraction underwent molecular size reduction by shifting to longer elution times. The shift in elution times was greater for the 450 °C sample, indicating that the severity of the process impacted the size of the asphaltenes. Asphaltenes from Ni1Mo6/Al_2O_3 and Al_2O_3 reaction products were very similar.

UV-F spectroscopy provided information on extents of aromatic conjugation, showing a signal at higher wavelengths for samples containing molecules with larger fused-ring aromatics. The UV-F spectra shown in Figure 7.8 are displayed peak normalised; the spectra of the products are presented and compared to the spectra of the VR. Maltenes plus asphaltenes, the maltene fraction and the asphaltene fraction are shown separately in Figure 7.8a, b and c, respectively. A shift to shorter wavelengths was observed for reaction products for wavelengths below 500 nm (Figure 7.8a). For wavelengths above 500 nm the normalised intensity of the signal of the products was lower than the one for VR. This indicates a reduction in aromatic group sizes. When reaction temperature was increased from 400 to 450 °C a shift to even shorter wavelengths was observed. The spectra for Ni1Mo6/Al_2O_3 products had lower wavelengths than the one for Al_2O_3 reaction products even though molecular sizes were very similar, as determined by SEC analysis (Figure 7.7). The same trend was observed for the product maltene fractions (Figure 7.8b) with higher shifts to shorter wavelengths with increasing reaction temperature. The spectra for products from experiments using Ni1Mo6/Al_2O_3 and Al_2O_3 were very similar, even though the products from the 400 °C reactions had lower molecular size (Figure 7.7).

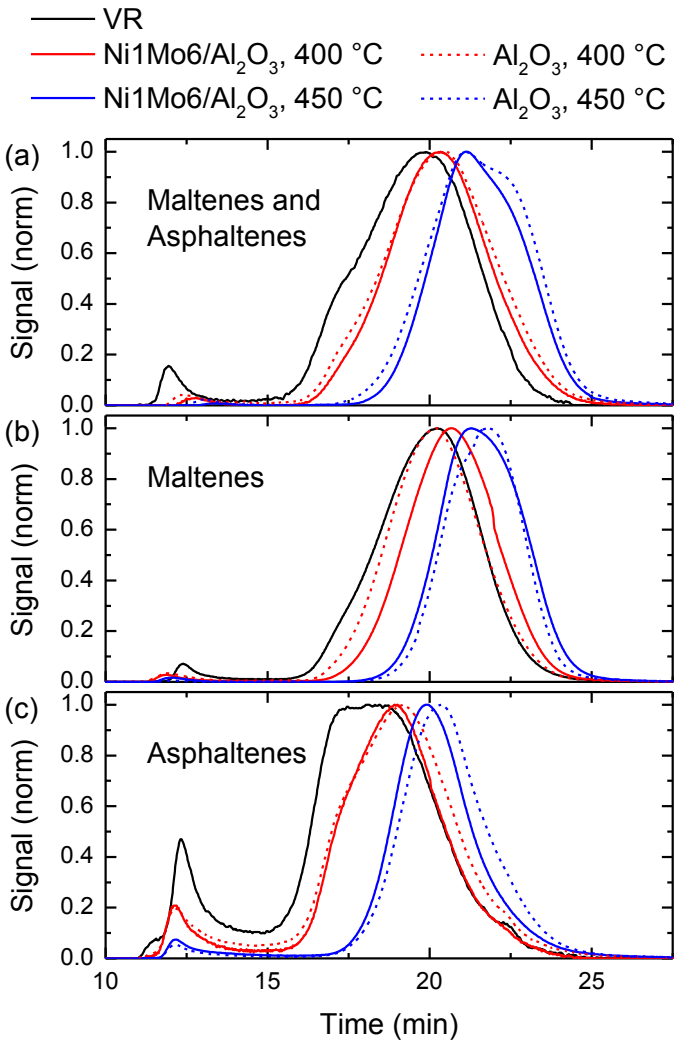

Figure 7.7. SEC on (a) whole fraction, (b) maltene fraction and (c) asphaltene fraction for VR and initial reaction products with Al_2O_3 and Ni1Mo6/Al_2O_3 using NMP/$CHCl_3$ (6:1) and detection at 300 nm UV absorbance. Reactions were at 185 bar H_2 pressure for 60 minutes.

For the asphaltene fraction, shown in Figure 7.8c, the reaction product spectra were very similar to the VR asphaltenes, although shifted to shorter wavelengths, which indicates certain reduction in aromatic group sizes in the asphaltenic fraction. It was expected that the asphaltenes would be represented by larger polyaromatic ring systems compared to the maltenes based on previous studies (131). It is likely that this shift is at least partly due to removal of the larger asphaltenic structures as coke, which was produced in large amounts in runs with these catalysts. The spectra of the Ni1Mo6/Al_2O_3 reaction products appeared at slightly longer wavelengths than the VR asphaltenes. Overall, the UV-F spectra were not very different between feed and products, showing that hydrocracking reactions did not greatly affect chromophore sizes even though significant changes in the size of the product molecules were observed by SEC. This could be attributed to breakage of side chains or chains between aromatic

ring clusters without significantly affecting the size of the fused-ring clusters themselves. This could also explain the large production of gases, which could be generated from cleaving aliphatic side chains.

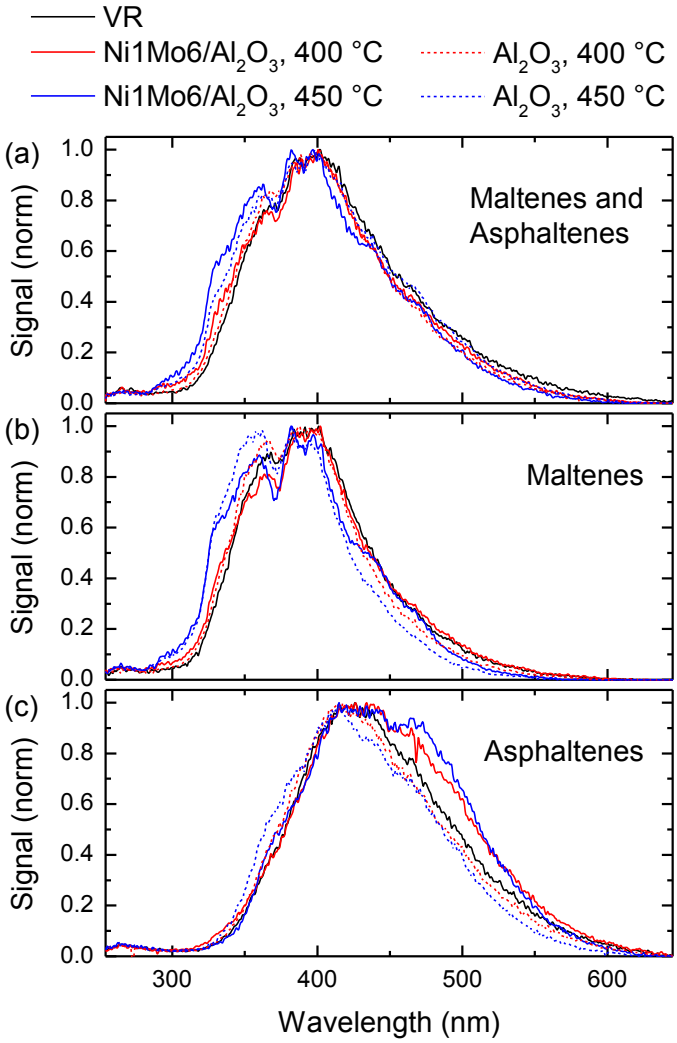

Figure 7.8. Synchronous UV-fluorescence spectra of (a) whole fraction, (b) maltene fraction and (c) asphaltene fraction for VR and initial reaction products with Al_2O_3 and Ni1Mo6/Al_2O_3 in $CHCl_3$. Reactions were at 185 bar H_2 pressure for 60 minutes.

7.3.2. Spent catalysts

7.3.2.1. Coke on catalyst

Coke deposits on Ni1Mo6/MSA, Ni1Mo6/Al_2O_3, MSA and Al_2O_3 are shown in Table 7.5, expressed as gram of coke per gram of catalyst. These data correspond to the solids yield discussed previously and are discussed in greater detail in this section in association to changes in the catalysts textural properties. It was observed that MSA had less coke deposits than Al_2O_3 for the 400 °C reactions, although at 450 °C significantly higher deposits occurred on MSA. A reduction in coke deposits took place

for MSA in the reutilisation at 450 °C. Coke deposits were very high in the first reaction at 450 °C and possibly redissolved in the reutilisation reaction, thus yielding lower coke deposits. Soft coke, which adsorbs initially on the catalyst, can react because it consists of aromatics and asphaltenes (200). The same reduction in coke deposits took place for Ni1Mo6/MSA for the 400 °C reutilisation. Coke deposits for this catalyst were very similar at 400 and 450 °C, contrary to what was observed for Ni1Mo6/Al_2O_3 which showed lower deposits at higher temperatures. This is typically observed for a batch system, as discussed in Section 5.3.2.1.

Table 7.5. Coke on catalyst for MSA, Ni3Mo14/MSA, Al_2O_3 and Ni3Mo14/Al_2O_3 determined by TGA analysis. All reactions lasted 60 minutes with an initial 185 bar H_2 pressure.

Sample	g coke per g catalyst at different reaction temperatures* (°C)			
	400 (i)	400 (r)	450 (i)	450 (r)
MSA	0.32	0.36	1.06	0.89
Ni1Mo6/MSA	0.15	0.11	0.14	0.14
Al_2O_3	0.41	0.59	0.31	0.39
Ni1Mo6/Al_2O_3	0.41	0.41	0.35	0.35

* (i) for initial and (r) for reutilisation reactions.

7.3.2.2. Textural properties

After each reaction spent catalysts were characterised by N_2 adsorption to evaluate changes in their textural properties. The textural properties for the fresh materials from Table 7.2 are listed as well. Changes in textural properties for Ni1Mo6/Al_2O_3 and Al_2O_3 have been described in detail in Sections 5.3.2.2 and 6.3.2.3, respectively, and are included here for comparison purposes. It was observed that the textural properties of MSA and Ni1Mo6/MSA suffered significant changes after reaction. MSA and Ni1Mo6/MSA were comprised of ink-bottle pores, as observed in the N_2 adsorption-desorption isotherm (Figure 7.1) and the significant reduction in S_{BET} and pore volume were due to pore mouth plugging.

Almost all S_{BET} and pore volume were lost and an increase in average pore diameter was observed after reactions because only the larger pores remained available (107,111). Even though the coke deposits on MSA were significantly larger than on Ni1Mo6/MSA, both materials presented pore mouth plugging, which suggested that ink bottle pores are not suitable for heavy oil upgrading. The textural properties of the Al_2O_3 support and catalyst were reduced after reaction as well. Nevertheless, these materials retained a significant S_{BET} and total pore volume. The plate-like particles showed significant advantage over ink-bottle pores that greatly reduce the S_{BET} and have steric hindrance issues when processing heavy fractions (87).

Table 7.6. Textural properties of the spent supports and catalysts determined by N_2 adsorption. All reactions lasted 60 minutes with an initial 185 bar H_2 pressure.

Sample	T* (°C)	S_{BET} ($m^2 \cdot g^{-1}$)	Total pore volume ($cm^3 \cdot g^{-1}$)	Average pore diameter** (nm)
MSA	Fresh	723.1	0.45	4.7
	400 (i)	3.39	0.01	12.79
	400 (r)	2.52	0.01	14.39
	450 (i)	3.85	0.01	15.68
	450 (r)	1.85	0.00	16.68
Ni1Mo6/MSA	Fresh	580.0	0.15	4.7
	400 (i)	6.9	0.02	12.2
	400 (r)	6.9	0.02	10.9
	450 (i)	2.7	0.01	20.1
	450 (r)	2.3	0.01	15.1
Al_2O_3	Fresh	341.2	1.21	12.0
	400 (i)	164.8	0.68	14.1
	400 (r)	200.5	0.74	12.9
	450 (i)	203.9	0.79	13.2
	450 (r)	252.4	0.95	13.1
Ni1Mo6/Al_2O_3	Fresh	282.2	0.60	11.5
	400 (i)	57.8	0.09	6.7
	400 (r)	92.5	0.15	6.1
	450 (i)	73.7	0.12	6.0
	450 (r)	107.6	0.18	6.4

*(i) for initial and (r) for reutilisation reactions.

**BJH model applied to the adsorption branch of the isotherms

The N_2 adsorption-desorption isotherms for spent Ni1Mo6/MSA, MSA, Ni1Mo6/Al_2O_3 and Al_2O_3 are represented in Figure 7.9. The description for Ni1Mo6/Al_2O_3 and Al_2O_3 are provided in Sections 5.3.2.2 and 6.3.2.3, respectively. It was observed that significant pore mouth plugging occurred for Ni1Mo6/MSA and MSA since the hysteresis loops increased and the N_2 uptake capacity at low P/Po values was higher for the desorption than for the adsorption curves (46). Changes in relative P/Po values for the hysteresis cycles indicated that the pore size of the materials changes, as previously observed in Table 7.6. A significant decrease in N_2 uptake capacity was observed for the spent materials in the whole P/Po range, demonstrating that coke deposits affected pores of all sizes. The isotherms for the reutilised catalysts at 450 °C presented lower N_2 adsorption capacity than the isotherms for the catalysts used at 400 °C. For MSA, this was induced by higher coke deposits at 450 °C. Even though Ni1Mo6/MSA had similar coke deposits at both reaction temperatures, its textural properties were more affected at higher reaction temperatures. This behaviour was the opposite of the one observed for Ni1Mo6/Al_2O_3 and Al_2O_3.

It has been published that isotherms can drastically change shape when materials are covered with coke deposits, specifically for ink-bottle types (70,87). In those reports the N_2 uptake capacity was reported as a relative value, i.e. with the maximum uptake capacity given a value of 1. Thus it was not possible to elucidate if the same significant loss of area as the one which took place for Ni1Mo6/MSA and MSA was also observed in those works.

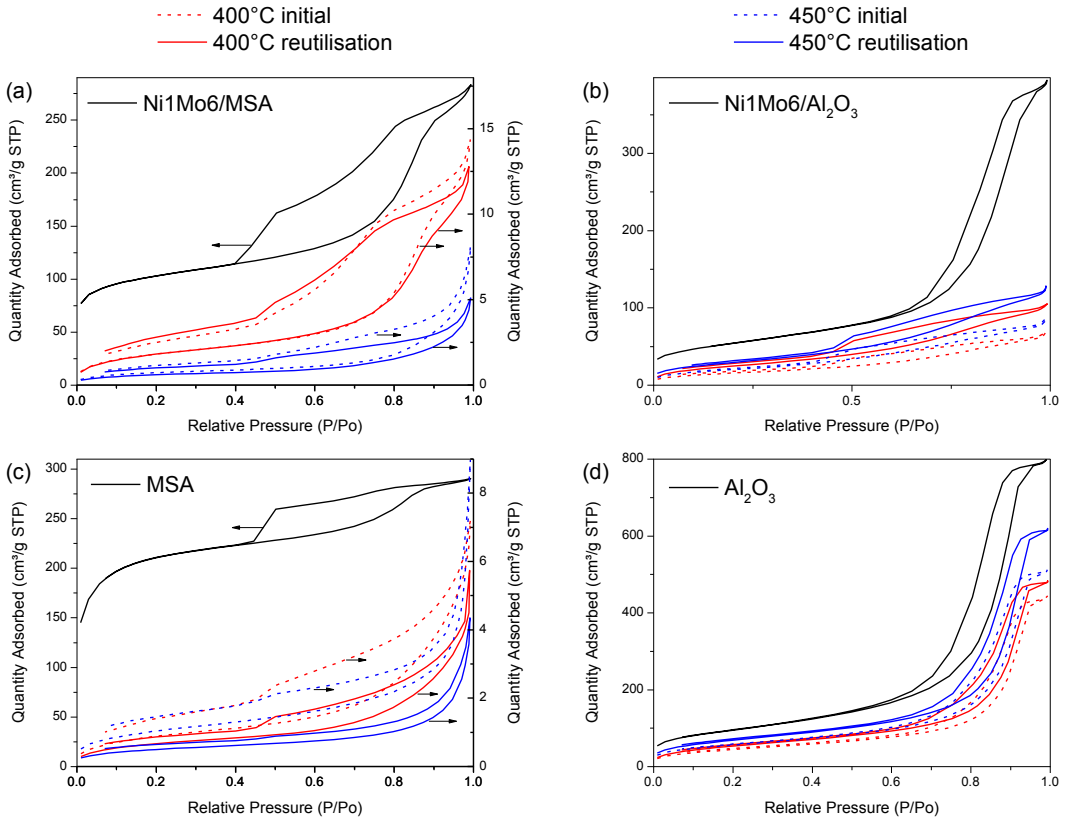

Figure 7.9. N_2 adsorption-desorption isotherms of fresh and spent (a) Ni1Mo6/MSA, (b) Ni1Mo6/Al_2O_3, (c) MSA and (d) Al_2O_3. All reactions lasted 60 minutes with an initial 185 bar H_2 pressure.

Changes in pore size distribution curves for spent Ni1Mo6/MSA, MSA, Ni1Mo6/Al_2O_3 and Al_2O_3 are shown in Figure 7.10. Ni1Mo6/Al_2O_3 and Al_2O_3 are included for comparison purposes; the description of the PSD profiles of the materials are available in Sections 5.3.2.2 and 6.3.2.3, respectively. It was observed that an important blockage of pores occurred for Ni1Mo6/MSA and MSA. The pore volume significantly decreased and was almost completely lost after reaction.

The loss of textural properties for Ni1Mo6/MSA and MSA were reflected in the product yields observed in Section 7.3.1.2. When MSA was reutilised at 450 °C the $Maltenes_{<450°C}$ yield was 0.3 wt %, compared to 9.9 wt % for Al_2O_3. For Ni1Mo6/MSA the $Maltenes_{<450°C}$ yield for the initial reaction at 450 °C was 8.9 wt %, compared to

20.6 wt % for Ni1Mo6/Al_2O_3; for the reutilisation at the same temperature 7.1 wt % of $Maltenes_{<450°C}$ were obtained contrasted to 40.0 wt % for Ni1Mo6/Al_2O_3. At the latter conditions a 23.3 wt % of Asphaltenes were observed which were double the yield than for Ni1Mo6/Al_2O_3 (11.0 wt %). Therefore the loss of textural properties accounted for a reduction in the catalytic activity of MSA materials.

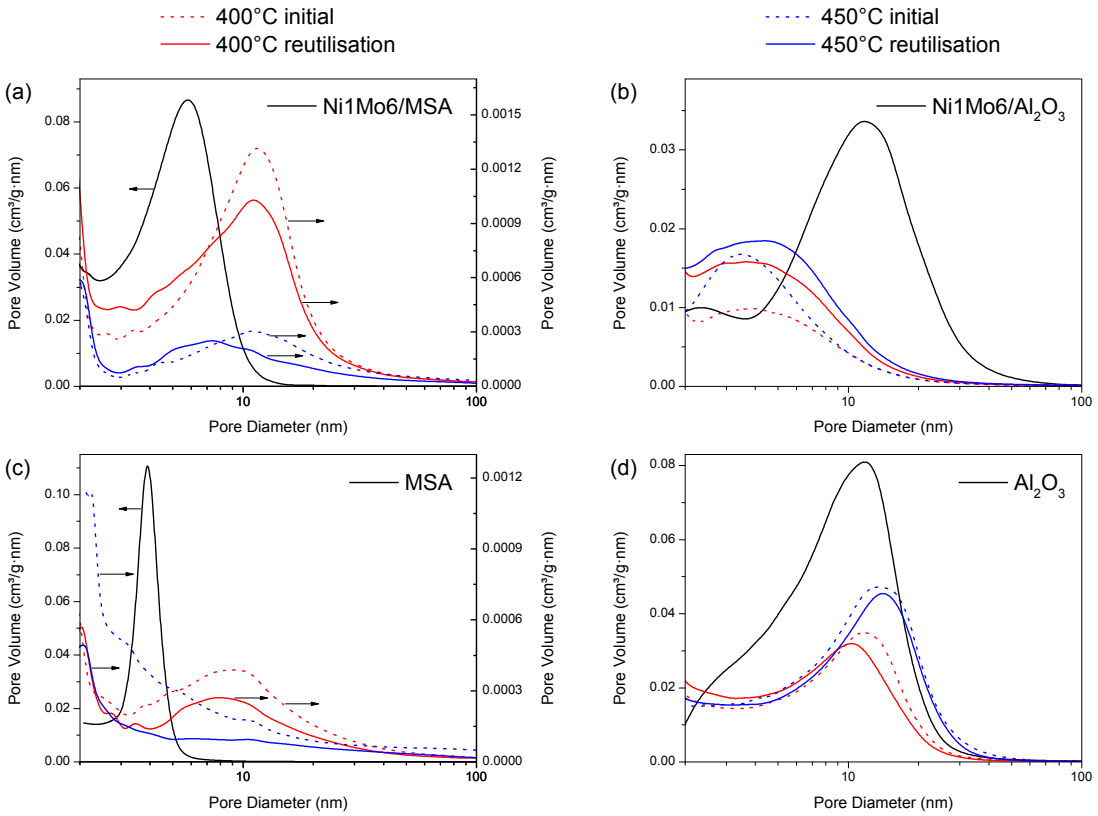

Figure 7.10. Pore size distribution profiles for spent (a) Ni1Mo6/MSA, (b) Ni1Mo6/Al_2O_3, (c) MSA and (d) Al_2O_3. All reactions lasted 60 minutes with an initial 185 bar H_2 pressure.

7.4. CONCLUSIONS

Novel mesoporous NiMo catalysts were prepared with Al_2O_3 and silica alumina as supports and tested in hydrocracking reactions at temperatures between 400 and 450 °C and 185 bar H_2 pressure. A heavy and viscous VR from Maya crude oil was used for hydrocracking reactions, evaluating the conversion of the VR itself along with the conversion of asphaltenes with the novel materials. The catalysts were reutilised to observe their coking propensity and longer term stability. When the catalysts and supports were utilised in a first reaction with VR, an important amount of carbonaceous deposits was formed. Afterwards, when the coked catalysts and supports were reutilised with fresh VR, the Ni1Mo6/Al_2O_3 and the Ni1Mo6/MSA had negligible increase in coke content whereas the supports still showed some additional coke deposition.

Both VR and asphaltene conversions were highly driven by reaction temperature. Significant asphaltene conversions were maintained in the reutilisation reaction for the metal catalysts, with the Ni1Mo6/Al_2O_3 performing better, due to its larger pores. Since the supports alone did not have a hydrogenation capability, the cracked hydrocarbons suffered condensation reactions into asphaltenes, PAH, and coke instead of lighter compounds. This was reflected in the higher asphaltene conversions of the Ni1Mo6/Al_2O_3 and Ni1Mo6/MSA when compared to the Al_2O_3 and MSA. SEC chromatograms identified that asphaltenes underwent molecular size reduction during the reactions, with further decrease in size with an increase in reaction temperature. However, the size of the aromatic ring systems did not appear to change considerably. This indicates that cracking mostly took place by cleaving of side chains in the structure being responsible for size reduction. A fraction of the products with boiling point below 450 °C and reduced asphaltene content was obtained.

The textural properties of MSA and Ni1Mo6/MSA were greatly affected by coke deposits, almost all S_{BET} and pore volume were lost in the first reactions. This shows that the architecture of the Al_2O_3 mesopores, plate-like particles, presented a significant advantage over ink-bottle type pores for heavy oil processing.

Chapter 8: NiMo catalysts supported on carbon nanofibres for VR hydroprocessing

Catalysts supported on functionalised carbon nanofibres were synthesised and characterised. Results from hydroprocessing reactions using VR as feed (conversions for the fraction boiling above 450 °C and asphaltenes, as well as sulfur and metals removal) were correlated to the properties of the fresh catalysts. An emphasis was placed on the creation of active metal sites as a function of the synthesis conditions of the CNF, functionalisation treatment and tempering temperature. Results using Ni3Mo14/Al_2O_3 from Chapter 5 were included for comparison purposes. The materials preparation was performed at CSIC-ICB in Zaragoza, Spain, as part of the joint project "Nanostructured Carbon-Supported Catalysts for Hydroprocessing of Heavy Oils".

8.1. INTRODUCTION

Carbon materials have been studied extensively as catalytic support because of their textural properties and chemical nature. Graphitic carbon has been used as catalytic support since the 1980's (227). The discovery of carbon nanotubes (CNT) in 1991 by Ijima (228) heightened the interest in carbonaceous materials composed of graphene arrangements. Different chemical structures of CNT and carbon nanofibres (CNF) are available in the form of CNT, platelet CNF, fishbone CNF, ribbon CNF, stacked-cup CNF and thickened CNF. A full description of the structures is available in the literature (229). Most CNT are produced from catalytic chemical vapour decomposition (CVD) of a carbon feedstock, such as light hydrocarbons, using a reduced catalyst. The CNF morphology depends on variables such as metallic catalyst, like Fe, Ni and Co, metal crystal size, carbon gas source as well as the synthesis conditions (230). The use of CNT and CNF as catalytic support has high potential, although research in the field is in early stages (231).

This chapter will focus on the use of catalysts supported on fishbone CNF, which are constructed with graphene layers that grow onto the catalyst particle in an inclined axis, creating a hollow or solid core as shown in Figure 8.1. The formation of fishbone CNF on a Ni catalyst is described in the literature as a decomposition of the carbon in the gas feed on the metal surface of the catalyst followed by the dissolution and diffusion of the carbon into the metal. Finally the carbon precipitates in the form of a CNF, with each precipitation step forming a new CNF layer (232).

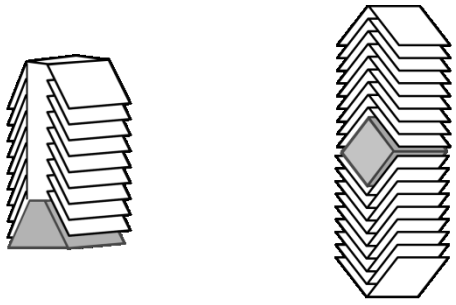

Figure 8.1. Schematic pathway for organised mesoporous alumina synthesis.

CNF can be used as catalytic support because the materials possess: a) high surface area, b) large pore volume and c) limited microporosity with a mesoporous nature (230). Their structure is a negative copy of a conventional support, with the spaces between the CNF serving as pores and the metal sites anchoring to the CNF walls, as shown in Figure 8.2. Other characteristics that make them promising supports are a low tendency for sintering, high mechanical strength, and that they are inert. On the other hand, CNF are reactive in an oxygen or hydrogen environment.

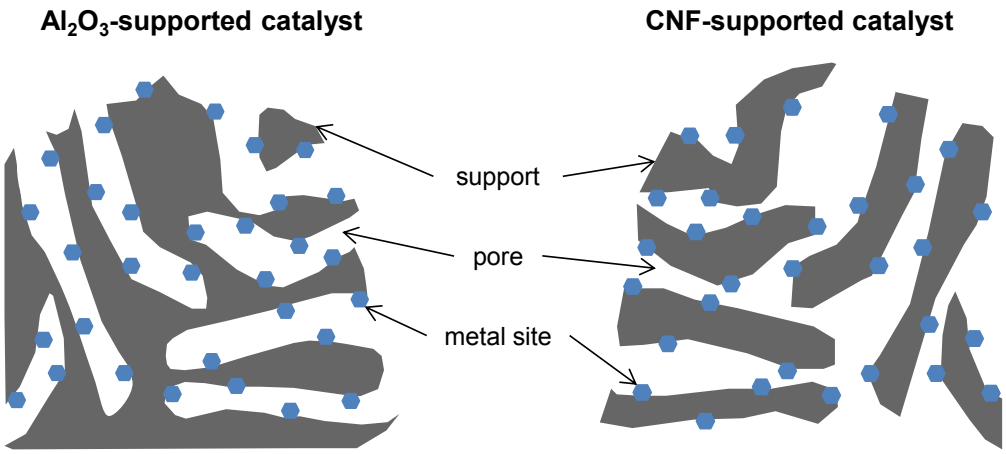

Figure 8.2. Differences in architecture for conventional catalysts and CNF-supported catalysts.

The surface of CNF is hydrophobic, generally without heteroatoms or functional groups. Thus, metal catalyst particles have no anchoring points. Catalysts are commonly prepared by incipient wetness using aqueous solutions, so the wettability of the CNF is also important. A treatment needs to be performed to modify the surface of the CNF first, to remove the catalyst particles used to synthesise the CNF and also to allow metals to anchor with adequate dispersion (233). These treatments are classified as covalent and non-covalent (234). The former can be performed in gas phase or liquid phase, usually in air, CO_2 or H_2O, whereas the latter using acids such as HNO_3 and/or H_2SO_4. These treatments create oxygen groups on the CNF surface, such as carboxylic, carboxyl anhydrides, lactonic, phenolic, carbonylic, and quinonic groups, among others. Furthermore, acid treatments can increase the surface wettability of the materials by polar solvents, which allow better impregnation during catalyst synthesis (235). Additionally, the surface area of treated CNF can be slightly higher than that of the untreated material, with larger total pore volume and APD. A review of the different surface treatments and methods for catalyst deposition is available in the literature (236). Effective treatments were reported with HNO_3 and H_2SO_4, although the wettability of the CNF was only increased when both acids were used simultaneously. Different approaches have been considered, ranging from long term contact of CNF with dilute acid at room temperature to short term contact with boiling concentrated acid.

Carbonaceous materials such as activated carbon, carbon black and, to less extent, CNT and CNF have been used as catalytic support. Carbons have been used as catalytic support in hydroprocessing reactions, obtaining higher HDM activity than alumina-supported catalysts, nevertheless with lower HDS and HDA activity. This was expected since the carbon support did not contain the required acidity for cracking reactions. Therefore it was determined that pretreatments were needed for the carbonaceous support to generate acidity. A review of the use of these catalysts is available (9). Advantages of carbon supports over alumina include lower coke formation propensity and lower support-metal interactions, which enables more activity in the metal sites (237). Catalysts supported on CNF have been used for fuel cell applications as well as in chemical synthesis areas such as hydrogenation and Fischer-Tropsch reactions (236,238–240). The use of nanostructured carbon-supported catalysts for hydroprocessing reactions has recently attracted attention of the scientific community. Studies focus on HDS, hydrogenation (HYD) and HDN, mostly with model compounds, for example HDS of thiophene with multi-walled CNT or fishbone and platelet CNF (241,242) or HDS of dibenzothiophene (243). Higher HDS conversions

were observed when using CNF supports than when using conventional alumina supports. Increases in activity have been linked to better metal dispersion achieved with carbonaceous supports. This was explained because of lower interactions between metals and the carbon support, which allows an easier sulfidation of the metal active sites and better metal dispersion (244–246). Studies with real feeds have been performed as well, focusing on hydrotreating reactions. Multi-wall CNT were treated with HCl and HNO_3 and then Ni and Mo were added by incipient wetness (247). Experiments were performed in a continuous reactor with light gas oil (LGO) derived from Athabasca bitumen at temperatures above 345 °C and 88 bar of H_2 pressure, with higher hydrotreating activity observed for NiMo supported on CNT than on conventional alumina. Additionally CNT were impregnated with Co and Mo and used as catalyst for vacuum residue hydrocracking (248). Reactions took place at 430 °C with 80 bar H_2 pressure for 1.5 hr in a batch reactor. The Co/Mo ratio was analysed; different optimal ratios were found for CNF than for conventional γ-Al_2O_3. Lower coke yields and higher HDS activity were found when a conventional alumina support was used.

Mo catalysts supported on CNF and CNT have been synthesised using different procedures. An overview of these is provided given than they differ from the novel synthesis method employed in this work. Ammonium thiomolybdates were mixed in aqueous/ethanol solutions with functionalised CNT and afterward HCl was added to precipitate MoO_3 on the CNT (249). Amorphous MoO_3 nanoparticles formed on the CNT at low loadings whereas a layer was formed with 69 wt % MoS_3; no XRD peaks were observed for MoS_3. The catalysts were evaluated for their electrochemical properties. In another study, incipient wetness was used to impregnate aqueous solutions of $(NH_4)_6Mo_7O_{24}{\cdot}4H_2O$ on CNT after which the catalysts were dried and tempered in Ar flow at 450 °C (250). The size of the crystallites were obtained with XRD and varied from 10 to 27 nm. The smaller Mo particles deposited inside the CNT structure whereas the larger ones on the surface (ca. 20%). The catalysts were afterward sulfided and then used to produce alcohols from syngas. Incipient wetness was also used to deposit $(NH_4)_6Mo_7O_{24}{\cdot}4H_2O$ with cobalt nitrate on CNT (243). The materials were tempered at 500 °C in N_2 flow and afterward sulfided and used for thiophene HDS.

The objective of this chapter was the synthesis and functionalisation of CNF for use as catalytic support for NiMo hydroprocessing catalysts. These catalysts were tested for hydrotreating of Maya VR at 425 °C and compared to results from a $NiMo/Al_2O_3$ catalyst.

8.2. MATERIALS

8.2.1. Preparation

8.2.1.1. Carbon nanofibres synthesis

The CNF were prepared by catalytic decomposition of a hydrocarbon gaseous mix. A Ni/Al catalyst synthesised by a fusion method using a Ni:Al molar ratio of 2:1 (251) was used to grow the CNF. Approximately 5 g of catalyst, sieved to 100-200 μm, were introduced into a rotary bed reactor fully described elsewhere (252). Briefly, the reactor consisted of a cylindrical drum that rotated on its horizontal axis. The Ni/Al catalyst was reduced in H_2 atmosphere at 550 °C and afterward a gas mixture with a CH_4:CO_2 ratio of 1:1, used as the carbon source, was fed into the reactor. The CNF were synthesised at 600 °C, using a gas flow of 150 $L_N \cdot h^{-1}$.

8.2.1.2. Carbon nanofibres functionalisation

The CNF were functionalised with acid treatment with two main objectives: a) removing the Ni catalyst from which the CNF were grown and b) generating functionalities on the surface to allow metal particles to anchor to the CNF. Three different acid treatments were performed, summarised in Table 8.1 along the weight loss ratio when compared to the initial CNF. For each treatment, ca. 10 g of CNF were placed in a flask with 250 mL of acid. The flask was rapidly heated to 125 °C and kept under reflux conditions for a specific time. Afterward the mixture was filtered (GF 52 glass microfiber filter without binder, 1 μm, Hahnemühle FineArt). The functionalised CNF were washed with DI water until the pH of the filtrate was above 6. Finally the materials were dried overnight at 80 °C. The mass of the recovered materials was lower than the initial CNF, thus weight loss was incurred. HNO_3 at 65% and H_2SO_4 at 96% were sourced from Panreac (Spain) and used as received. Given that strong acids at boiling temperature were used, extreme care was taken in the procedures with appropriate PPE and work was performed inside a fume cupboard. The functionalised CNF were named CNF_X where X was the acid treatment used.

Table 8.1. Acid treatments for CNF.

Sample	Acid treatment			Weight loss (wt %)
	Acid		Time (min)	
CNF_{N30}	HNO_3		30	12
CNF_{N120}	HNO_3		120	16
CNF_{NS30}	HNO_3/H_2SO_4	(1:1 vol/vol)	30	11

8.2.1.3. Catalyst synthesis

The functionalised CNF were afterward impregnated by incipient wetness to prepare catalysts. Nominal NiO loadings of 3 wt % and MoO_3 loadings of 14 wt % were used, as in Chapters 5 and 6. An aqueous solution was used to impregnate ammonium tetrathiomolybdate after which the materials were dried overnight at 80 °C. The impregnation was carried out in two stages to ensure the Mo salt was completely in solution. Then an aqueous solution containing $Ni(NO_3)_2.6H_2O$ was impregnated. The catalysts were dried overnight at 80 °C. Afterward approximately 1 g of catalyst was placed in a quartz tube inside a tubular furnace. A tempering treatment aimed to decompose the metal precursor salt was carried out by flowing N_2 at 50 $mL \cdot min^{-1}$ for 4 hr at 450 or 600 °C after which the materials were recovered. The catalysts are named as $Ni3Mo14/CNF_{X-T}$, where X is the type of acid treatment and T the tempering temperature.

8.2.2. Characterisation

8.2.2.1. Support

The surface of CNF has to be modified to be used as catalytic support (236). In this section the textural, surface and morphological properties of CNF are compared to the properties of the functionalised CNF.

The XRD patterns for CNF and the functionalised materials are shown in Figure 8.3, where peaks for graphite and Ni are observed for CNF. A prominent reflection at ca. 26° and a weak peak at ca. 43° were assigned to graphitic carbon (planes 002 and 100, respectively). The as-produced CNF revealed the presence of metallic nickel with reflections at 44.6°, 52° and 76.6° corresponding to the active phase in the Ni/Al_2O_3 catalyst used to grow the carbonaceous structures. No significant changes in reflections assigned to C were observed after the functionalisation treatments. Ni reflections, on the other hand, were no longer present after the functionalisation treatments. This revealed that the acid treatment was effective in the removal of the catalyst particles from the original CNF.

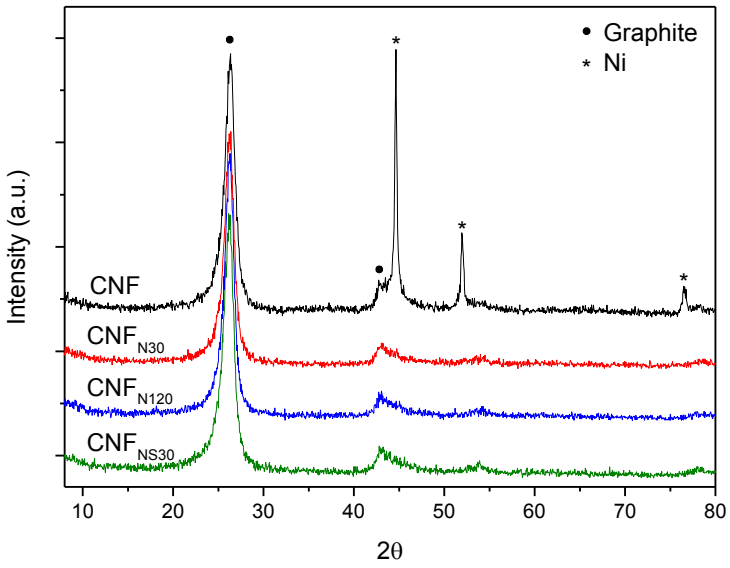

Figure 8.3. Powder XRD patterns of CNF, CNF$_{N30}$, CNF$_{N120}$ and CNF$_{NS30}$.

The temperature programmed oxidation weight loss profiles for the original CNF and the functionalised materials are shown in Figure 8.4. This analysis was performed to evaluate the degree of ordering in carbon materials. Graphitic carbons (highly ordered) combust at higher temperatures than amorphous ones. It was observed that weight loss of the functionalised materials occurred at lower temperatures than the original CNF, with increasing oxidation temperatures in the following order: CNF$_{NS30}$ (553 °C) < CNF$_{N120}$ (618 °C) < CNF$_{N30}$ (628 °C) < CNF (670 °C).

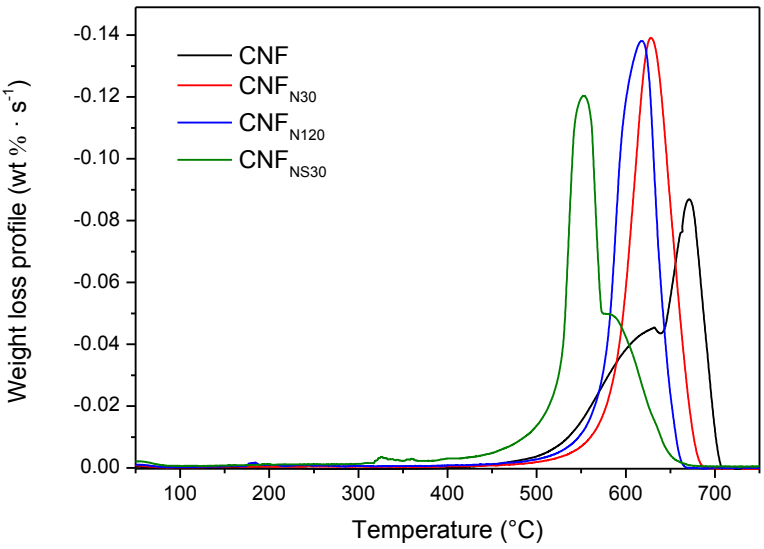

Figure 8.4. TPO weight loss profile of CNF$_{N30}$, CNF$_{N120}$ and CNF$_{NS30}$.

TPO values were in the range reported for CNF combustion (236). The reduction in oxidation temperature for functionalised materials is caused by the formation of functional groups on the edges of the CNF (253). It was observed that when using H_2SO_4 in the acid treatment the CNF oxidised at lower temperatures. TPO also corroborated the removal of the Ni catalyst from the functionalised CNF. Ni content was reduced from 11.2 wt % in the original CNF to values around 1.6 wt % for the functionalised CNF.

Temperature programmed desorption permits the evaluation of surface oxygenated groups. These groups work as anchoring points for the metal sites and decompose into CO or CO_2 at different temperatures (254). Results for CNF and functionalised materials are shown in Figure 8.5. It was observed that all acid treatments generated surface groups that were not present in the original CNF. Compounds that desorb as CO_2, such as carboxylic acids, were present in similar amounts for CNF_{N120} and CNF_{NS30}. Desorption into CO usually takes place for phenols, esters and carbonyls, of which CNF_{N120} had greater amounts. The areas for the different oxygenated groups decreased in the following order for CO_2 and CO: CNF_{NS30} > CNF_{N120} > CNF_{N30}.

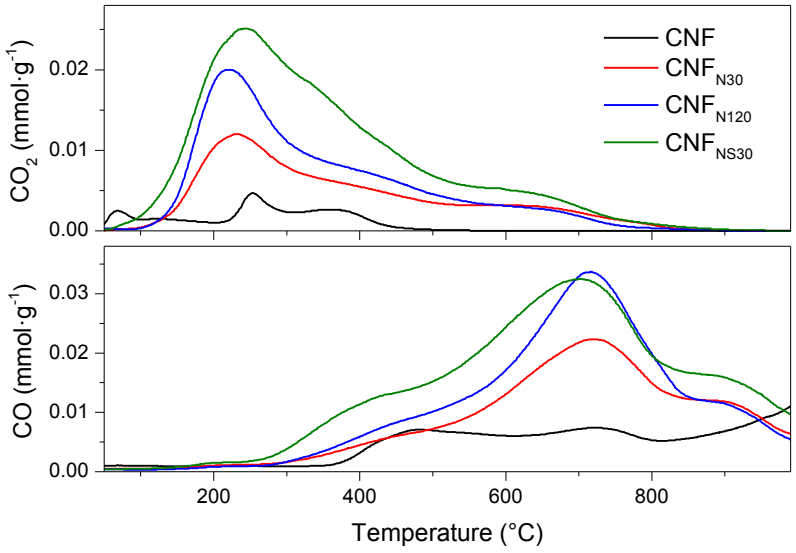

Figure 8.5. TPD profiles for CNF, CNF_{N30}, CNF_{N120} and CNF_{NS30}.

The acidity of the functionalised CNF increased after the acid treatments when compared to the original CNF. Ammonia TPD profiles are shown in Figure 8.6.

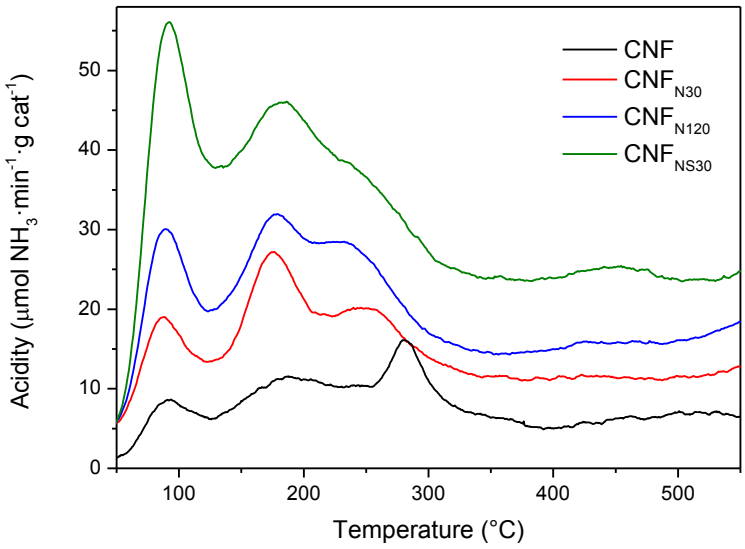

Figure 8.6. NH_3-TPD profiles for CNF_{N30}, CNF_{N120} and CNF_{NS30}.

The textural properties determined by N_2 adsorption-desorption of the CNF and functionalised CNF are listed in Table 8.2. Overall, the acid treatments increased the S_{BET} total pore volume and APD of the original CNF. No significant differences were observed between the different acid treatments. Figure 8.7 shows the N_2 adsorption-desorption isotherms and pore size distribution (inset) for CNF and the functionalised materials. The isotherms were Type IV with hysteresis loop H3, typically assigned to mesoporous materials, which correspond to condensation taking place in mesopores and plate-like particles in parallel (126). The shape of the isotherms did not change after the acid treatments, although slight increases in N_2 uptake capacity were reflected in an increase in pore volume for pores above 10 nm.

Table 8.2. Textural properties of CNF and functionalised CNF determined by N_2 adsorption.

Sample	S_{BET} ($m^2 \cdot g^{-1}$)	Total pore volume ($cm^3 \cdot g^{-1}$)	Average pore diameter* (nm)
CNF	92.0	0.23	13.2
CNF_{N30}	98.8	0.26	14.4
CNF_{N120}	106.9	0.28	13.9
CNF_{NS30}	95.8	0.27	15.0

*BJH model applied to the adsorption branch of the isotherms.

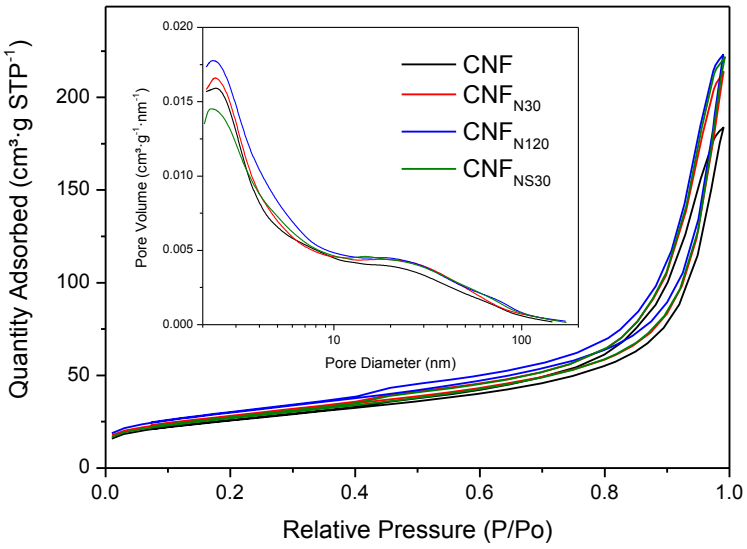

Figure 8.7. N_2 adsorption-desorption isotherms and pore size distribution curves (inset) for CNF, CNF_{N30}, CNF_{N120} and CNF_{NS30}.

TEM micrographs were performed to obtain a better understanding of the morphology of the CNF materials. TEM micrographs at 10,000X, 60,000X, 150,000X and 250,000X magnifications are shown in Figure 8.8a to d. It was observed that the shape of the Ni catalyst particles guided the growth of the CNF (255). The diamond shape of the Ni particles led to the formation of solid fishbone CNF, which were formed by inclined graphene planes (highlighted).

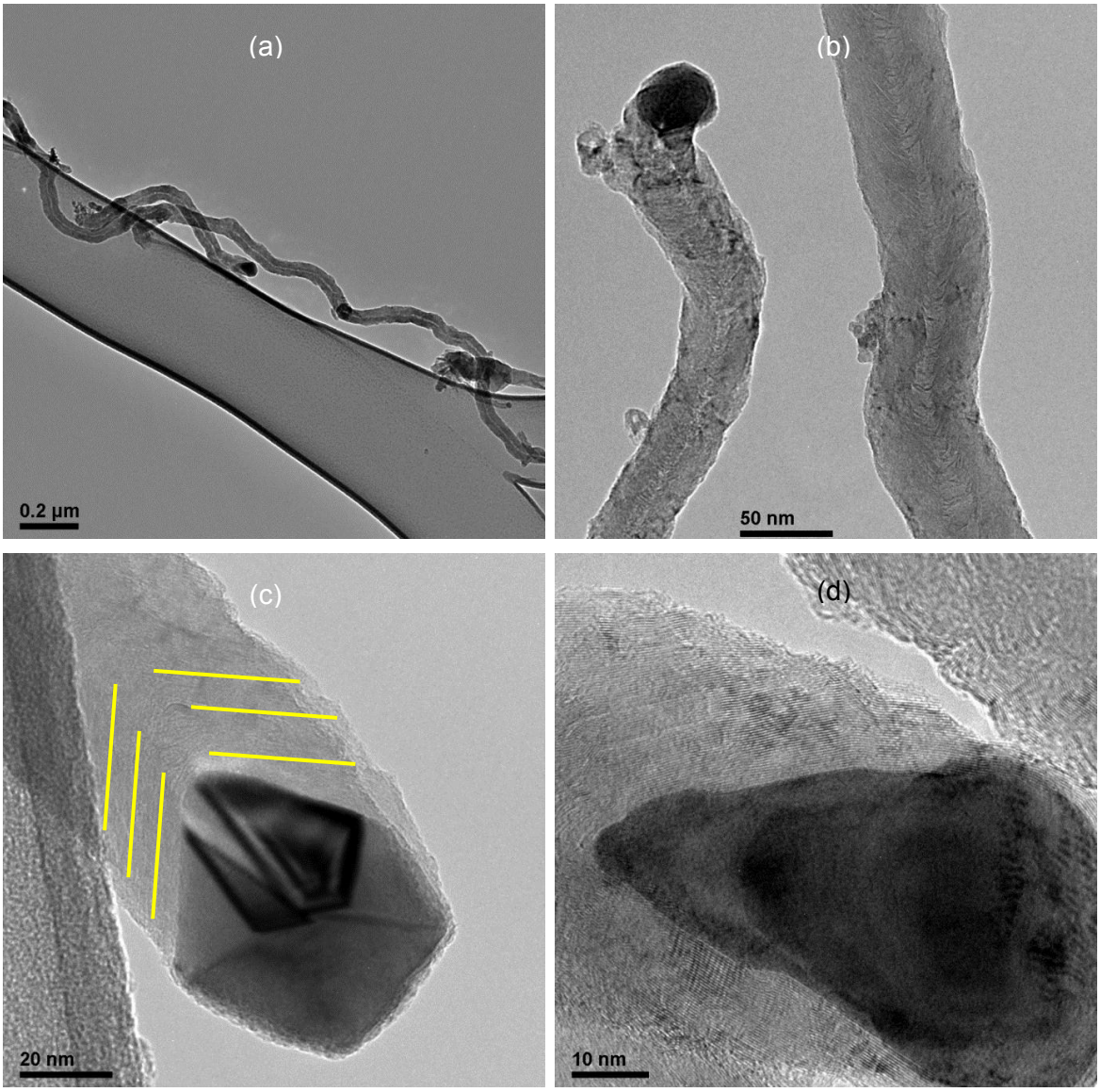

Figure 8.8. TEM images of CNF at different magnifications: (a) 10,000X, (b) 60,000X, (c) 150,000X and (d) 250,000X.

The removal of the Ni metal particles after the acid treatment was observed in TEM micrographs for CNF_{N120} (Figure 8.9a to d). The removal of the metal particles from the tip of the carbon filaments can account for the slight increment in surface area reported previously. Micrographs for CNF_{N30} and CNF_{NS30} are not shown because they displayed the same morphology as CNF_{N120}. Representative TEM micrographs showed that the Ni particles at the head of the CNF were successfully removed without modifying or destroying the graphene arrangement. The hollow spaces left after removal of the catalysts are circled in Figure 8.9a and can be clearly observed in Figure 8.9b and c. Finally, an example of how a CNF finished growing is shown in Figure 8.9d, in which the two inclined graphene layers were joined.

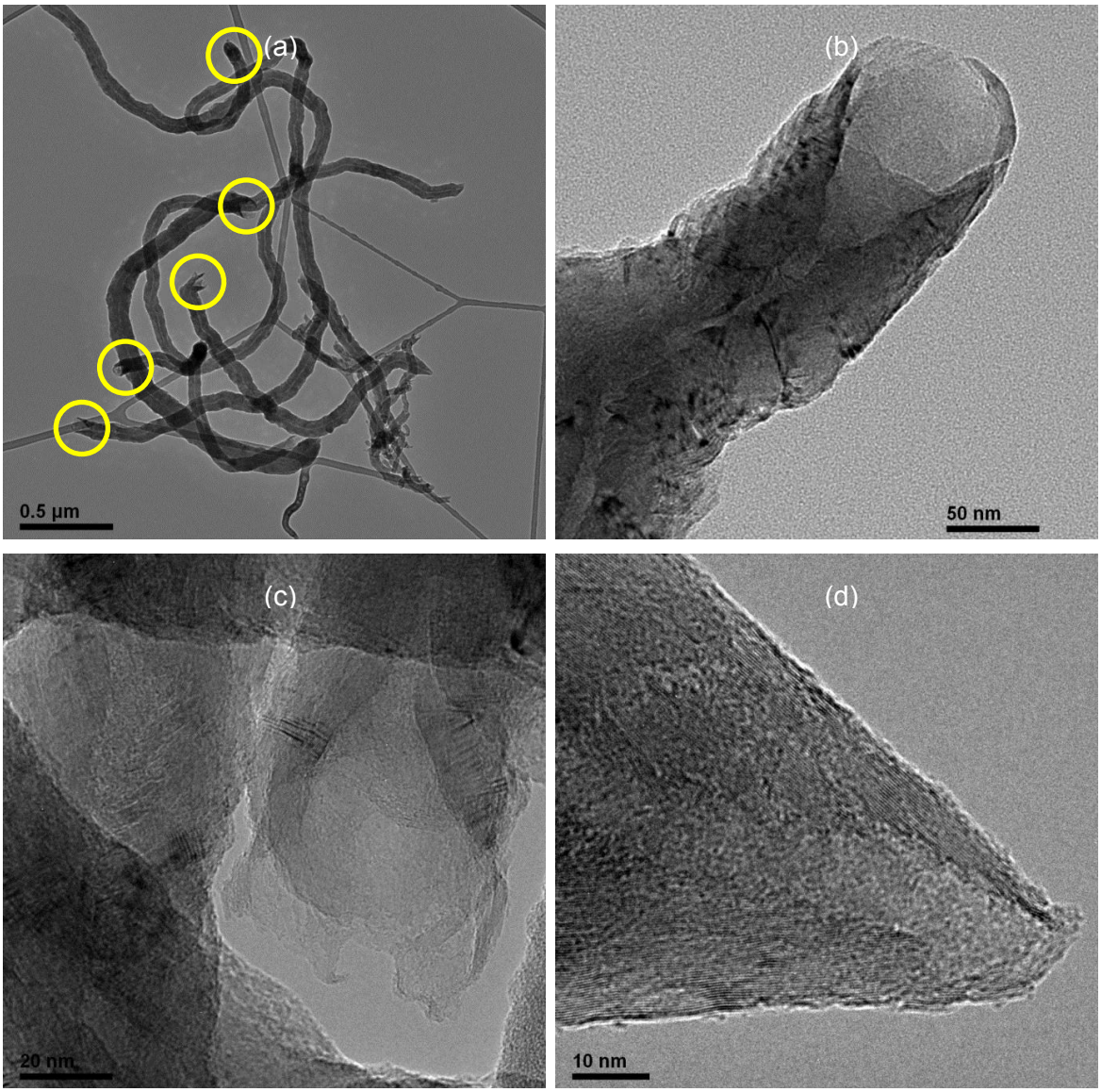

Figure 8.9. TEM images of CNF_{N120} at different magnifications: (a) 6,000X, (b) 60,000X, (c) 150,000X and (d) 250,000X.

8.2.2.2. Catalysts

TEM micrographs were obtained after impregnating Ni and Mo on the functionalised CNF and tempering the catalysts. These are shown in Figures 8.11 to 8.14 for Ni3Mo14/$CNF_{N30-450}$, Ni3Mo14/$CNF_{N30-600}$, Ni3Mo14/$CNF_{N120-450}$ and Ni3Mo14/$CNF_{NS30-450}$, respectively. At high magnifications (10,000X) no discernible differences between the catalysts were observed. In all samples the carbon nanofilaments were covered by stacks; their chemical nature was confirmed to be MoS_2 with EDX analysis. TEM-EDX profiles of the stack areas for selected catalysts are shown in Figure 8.10. For all materials, Mo and S peaks were observed along the support elements (C and O). The Cu peak corresponds to the grid used to support the samples for analysis.

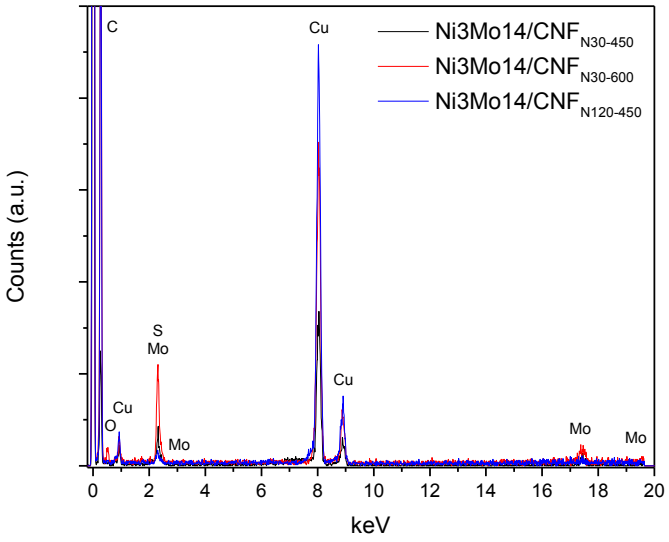

Figure 8.10. EDX analysis on TEM micrograph areas for Ni3Mo14/$CNF_{N30-450}$, Ni3Mo14/$CNF_{N30-600}$ and Ni3Mo14/$CNF_{N120-450}$ (at 250,000X, 400,000X and 400,000X magnification, respectively).

The morphology of the MoS_2 structures varied between the catalysts. The functionalisation treatment and the tempering temperature affected the stacking degree and length of the MoS_2 stacks. Ni3Mo14/$CNF_{N30-450}$ (Figure 8.11b to d) was homogenously covered by slabs of MoS_2. The stacking degree ranged from 2 to 5 and the length of the stacks varied from 10-20 nm, as observed in TEM images.

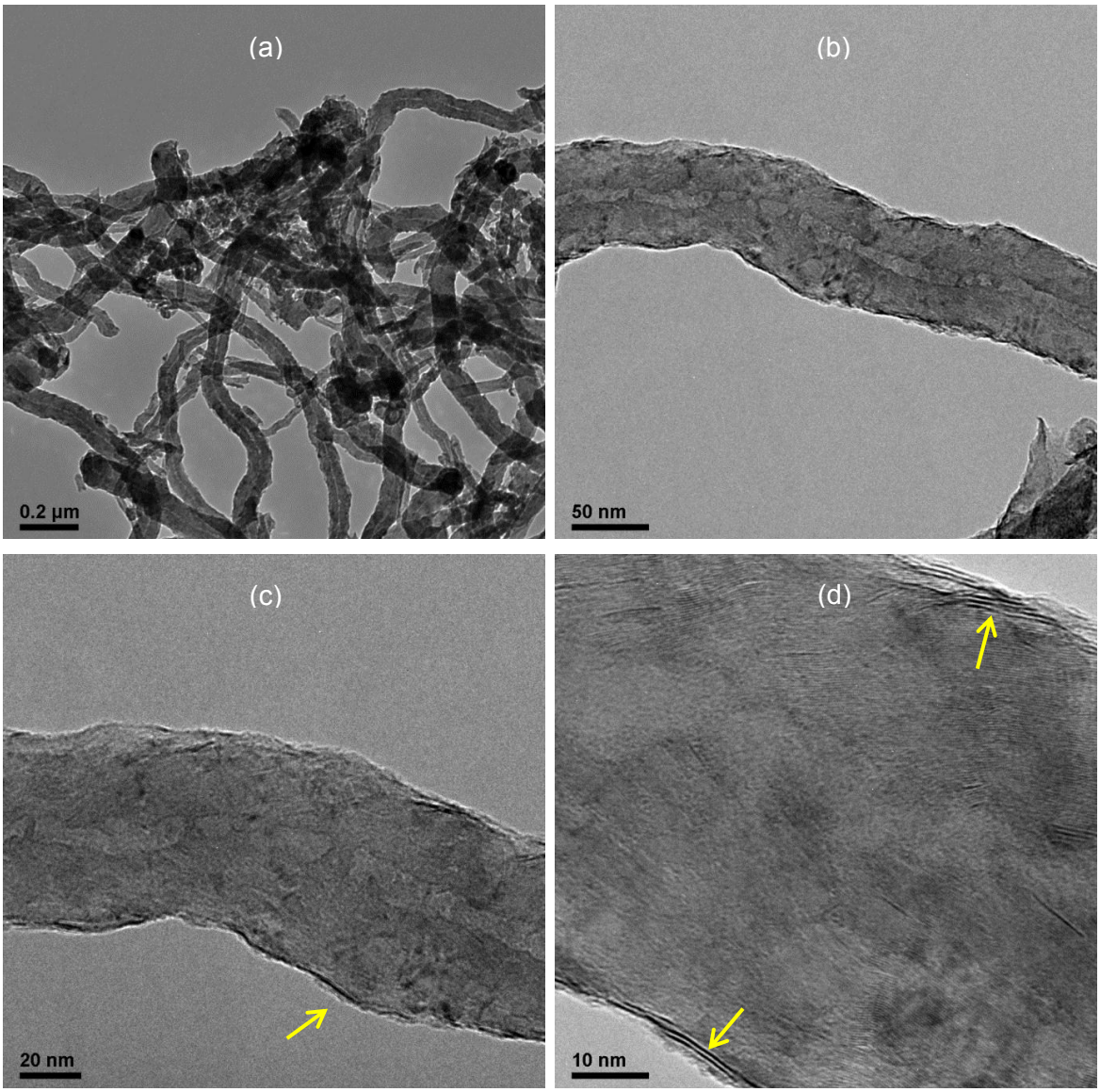

Figure 8.11. TEM images of Ni3Mo14/$CNF_{N30-450}$ at different magnifications: (a) 10,000X, (b) 50,000X, (c) 150,000X and (d) 250,000X.

The effect of the tempering temperature was observed when comparing Ni3Mo14/$CNF_{N30-450}$ with Ni3Mo14/$CNF_{N30-600}$ (Figure 8.12). The latter presented a less homogeneous covering of the CNF with some coated nanofilaments coexisting with uncovered CNF. Small round-shaped metal particles (ca. 20 nm) in Figure 8.12c inserted into the tubular structures were observed; these particles were not present in Ni3Mo14/$CNF_{N30-450}$. The stacking degree for the catalyst was 2-3 slabs, as observed in Figure 8.12d.

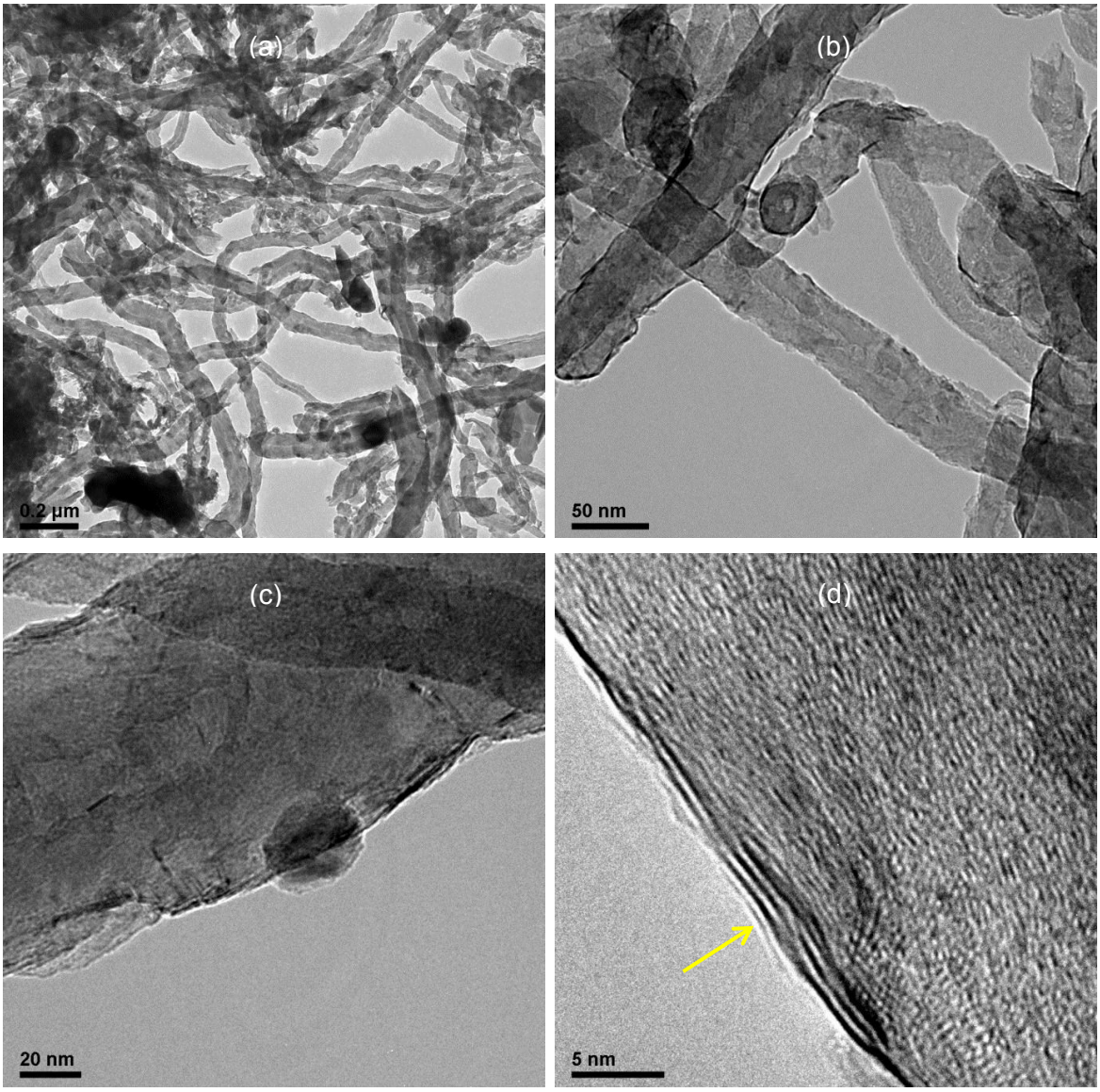

Figure 8.12. TEM images of Ni3Mo14/$CNF_{N30-600}$ at different magnifications: (a) 10,000X, (b) 50,000X, (c) 150,000X and (d) 500,000X.

Differences with the functionalisation treatment were observed in Figure 8.13, which shows TEM micrographs for Ni3Mo14/$CNF_{N120-450}$, supported on the CNF with the harsher acid treatment. A higher MoS_2 stacking degree was observed than in Ni3Mo14/$CNF_{N30-450}$. Figure 8.13b showed that the edges of CNF_{N120} were covered by the metal stacks although sections without metals were present. Greater detail is provided in Figure 8.13c and d, with four to eight layers forming a MoS_2 stack of approximately 20 nm in length. Stacks next to each other were not homogeneous and had different stacking degrees.

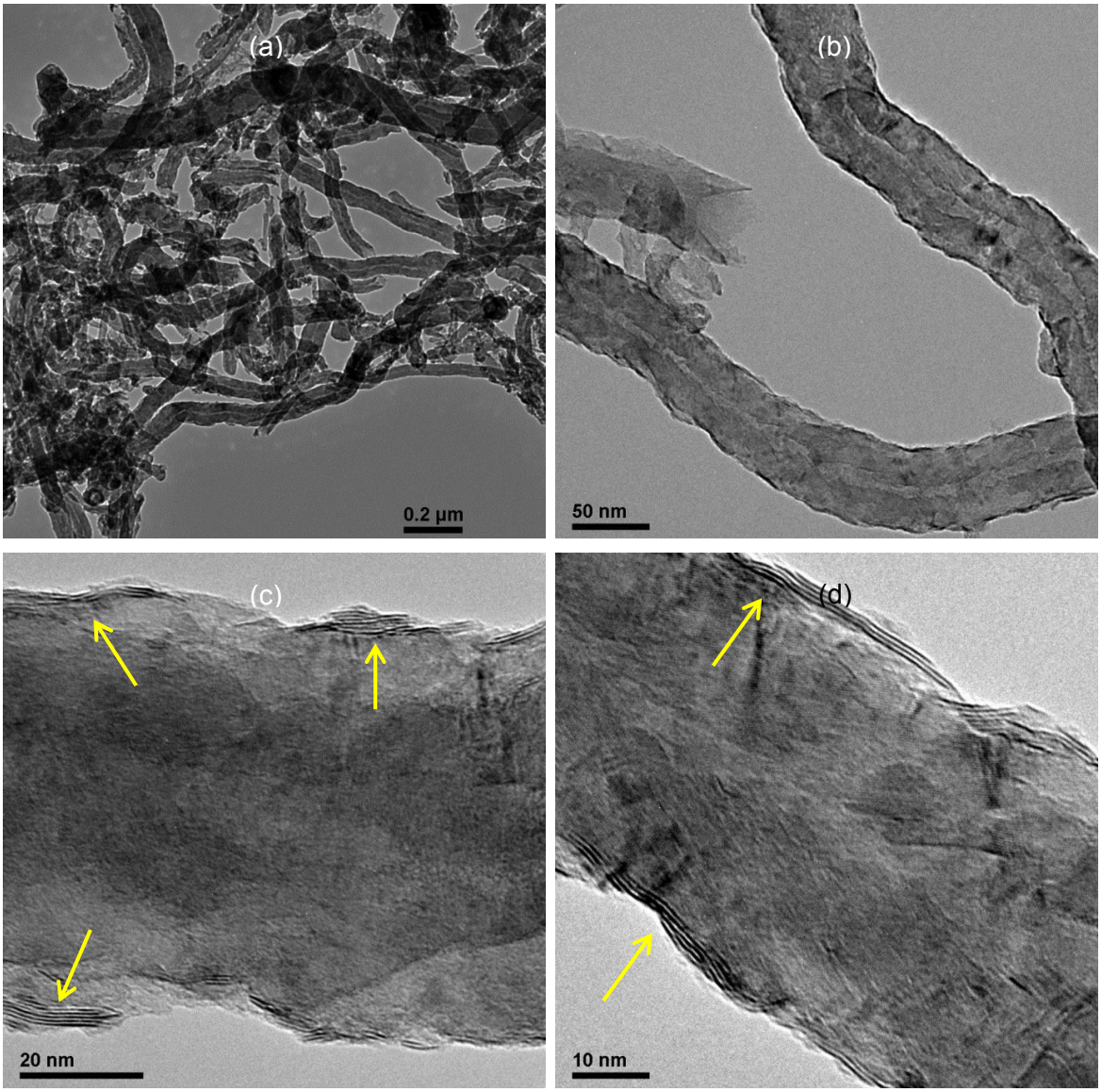

Figure 8.13. TEM images of Ni3Mo14/$CNF_{N120-450}$ at different magnifications: (a) 10,000X, (b) 50,000X, (c) 150,000X and (d) 250,000X.

TEM micrographs for Ni3Mo14/$CNF_{NS30-450}$ are shown in Figure 8.14. Up to 10 layers of MoS_2 formed a stack. Also, the stacks were considerably longer (>60 nm) than the ones shown for the previous catalysts. Nevertheless, in Figure 8.14c it was observed that the covering of the CNF with MoS_2 was not homogeneous.

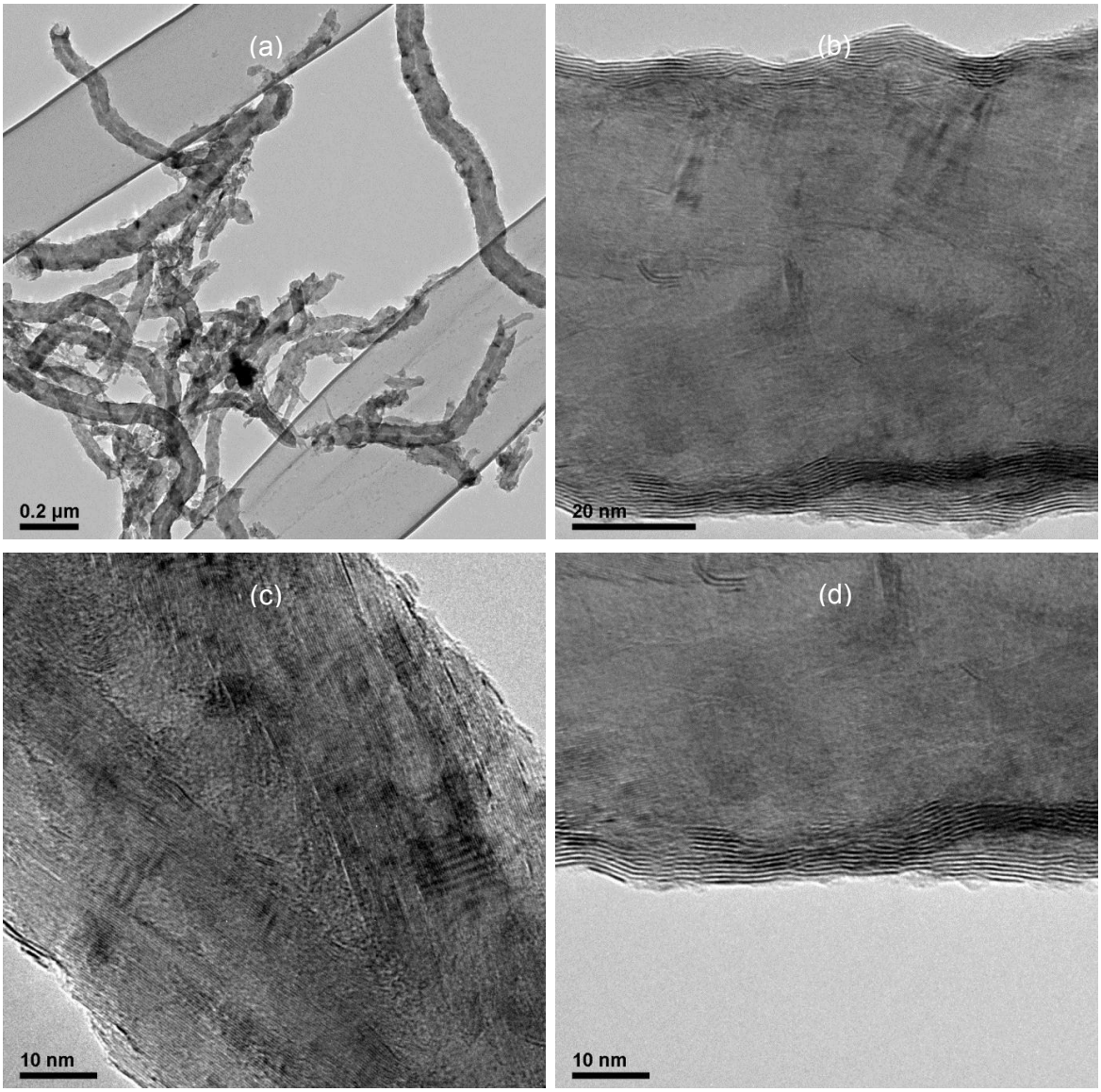

Figure 8.14. TEM images of Ni3Mo14/$CNF_{NS30-450}$ at different magnifications: (a) 10,000X, (b) 150,000X and (c, d) 250,000X.

It was discussed previously that the type of the acid treatment had an important effect in the creation of functionalities on the CNF surface (Figure 8.5 and 8.4). Functional groups on the surface of the CNF created anchoring points for the catalyst metals to attach to. The TEM micrographs from this section confirmed that these functionalities in turn influenced the ability of metals to attach to the surface by observing different structures of MoS_2 stacks. The stacking degree and the length of the stacks increased

when more functionalities were available on the surface of the CNF. Stacks were less defective when HNO_3/H_2SO_4 was used instead of only HNO_3 during a 30 min acid treatment.

After observing the morphology of the materials, XRD analysis was performed to determine the chemical nature of the MoS_2 layers. Figure 8.15 shows the XRD patterns for CNF_{N30} and CNF_{N30}-supported catalysts. The XRD patterns for the catalysts supported on CNF_{N120} and CNF_{NS30} are not reported as the type of acid treatment did not show any effect on them. Ni3Mo14/$CNF_{N30-450}$ and Ni3Mo14/$CNF_{N30-600}$ presented the same reflections assigned to graphitic carbon as the support. Additionally, the appearance of diffraction peaks at 2θ: 14.1°, characteristic of the (0 0 2) basal plane of crystalline MoS_2, were observed. The intensity of the peak was higher for the sample tempered at 600 °C. ATM is known to decompose under inert atmosphere into MoS_3 at 260 °C and into amorphous MoS_2 at higher temperatures (300-500 °C) (256). The formation of crystalline MoS_2 by a re-stacking of the sulfide at temperatures above 500 °C was reported (257). This sample also shows MoS_2 diffraction peaks at 33.1º, which correspond to the (1 0 0) plane. Weak reflections that can be assigned to MoO_2 and NiO were observed in the Ni3Mo14/$CNF_{N30-600}$ diffractogram. MoO_2 peaks could appear because of partial oxidation of the catalyst when in contact with air. No evidence of nickel sulfide crystalline phases was observed by XRD.

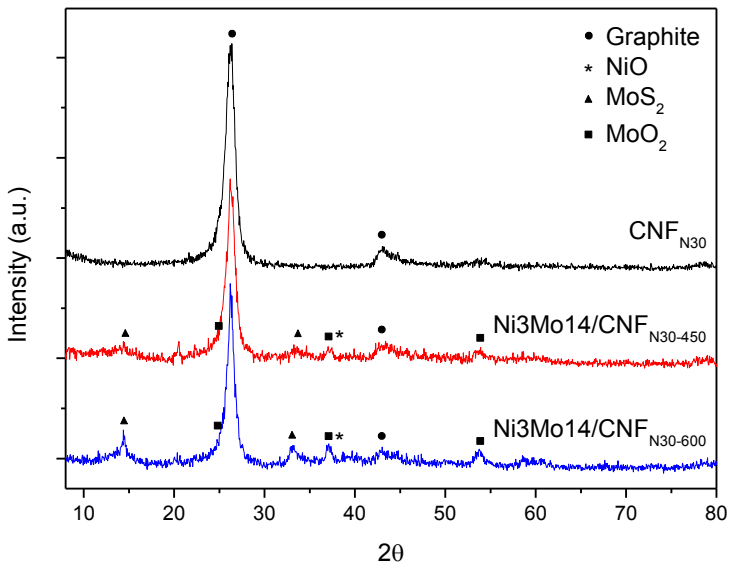

Figure 8.15. Powder XRD patterns of CNF_{N30} and NiMo catalysts supported on CNF_{N30}.

The textural properties of the catalysts are observed in Table 8.3. The catalysts had lower S_{BET} and total pore volume than their respective supports, albeit higher APD. This

was expected since the metals can block the smaller pores and therefore their removal increased the APD, as observed with the TEM images for the catalysts (Figures 8.11 to 8.14). No conclusive differences were observed linked to the tempering temperatures of the catalysts and the textural properties.

Table 8.3. Textural properties of functionalised CNF and tempered NiMo/CNF_X catalysts determined by N_2 adsorption.

Sample	S_{BET} ($m^2 \cdot g^{-1}$)	Total pore volume ($cm^3 \cdot g^{-1}$)	Average pore diameter* (nm)
CNF_{N30}	98.8	0.26	14.4
Ni3Mo14/$CNF_{N30-450}$	65.2	0.20	15.6
Ni3Mo14/$CNF_{N30-600}$	73.8	0.20	14.4
CNF_{N120}	106.9	0.28	13.9
Ni3Mo14/$CNF_{N120-450}$	69.0	0.20	15.1
Ni3Mo14/$CNF_{N120-600}$	58.0	0.20	17.0
CNF_{NS30}	95.8	0.27	15.0
Ni3Mo14/$CNF_{NS30-450}$	74.3	0.22	15.8
Ni3Mo14/$CNF_{NS30-600}$	67.9	0.22	15.6

*BJH model applied to the adsorption branch of the isotherms.

Figure 8.16 shows the N_2 adsorption-desorption isotherms and PSD curves for CNF_{N30} and the respective catalysts. The isotherms of the catalysts retained the same shape as the support (Type IV, hysteresis loop H3) with lower N_2 uptake capacity throughout the whole P/Po range which was observed in lower S_{BET} and pore volume for the catalysts (Table 8.3). Variations between the catalysts tempered at different temperatures mostly occurred at P/Po below 0.8, and were thereby reflected on similar PSD for pores above 10 nm. Ni3Mo14/$CNF_{N30-450}$ retained less pore volume than Ni3Mo14/$CNF_{N30-600}$ for pores smaller than 10 nm. Thus, the APD of the catalysts increased slightly when compared to the support.

Figure 8.17 shows the N_2 adsorption-desorption isotherms and PSD curves for CNF_{N120} and the respective catalysts. The same behaviour as with catalysts supported on CNF_{N30} was observed, with lower N_2 uptake capacity throughout the whole P/Po range for the catalysts than the support, as a consequence of lower S_{BET} and total pore volume (Table 8.3). In this case, Ni3Mo14/$CNF_{N120-450}$ had higher N_2 adsorption capacity than Ni3Mo14/$CNF_{N120-600}$ for pores below 10 nm.

The adsorption-desorption isotherms and PSD curves for CNF_{NS30} and the respective catalysts are shown in Figure 8.18. As with the previous two figures, lower N_2 uptake capacity was observed throughout the whole P/Po range for the catalysts when compared to the support, along with lower S_{BET} and total pore volume (Table 8.3). Smaller differences in the isotherms and PSD curves were observed for the catalysts

tempered at different temperatures supported on the CNF with the stronger functionalisation. The adsorption capacity of the two catalysts was very similar, along with the pore volume for pores below 10 nm.

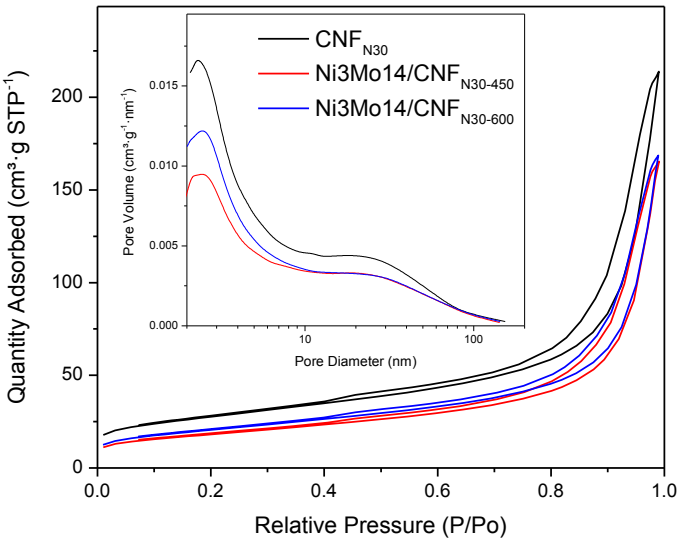

Figure 8.16. N_2 adsorption-desorption isotherms and pore size distribution curves (inset) for CNF_{N30} and catalysts.

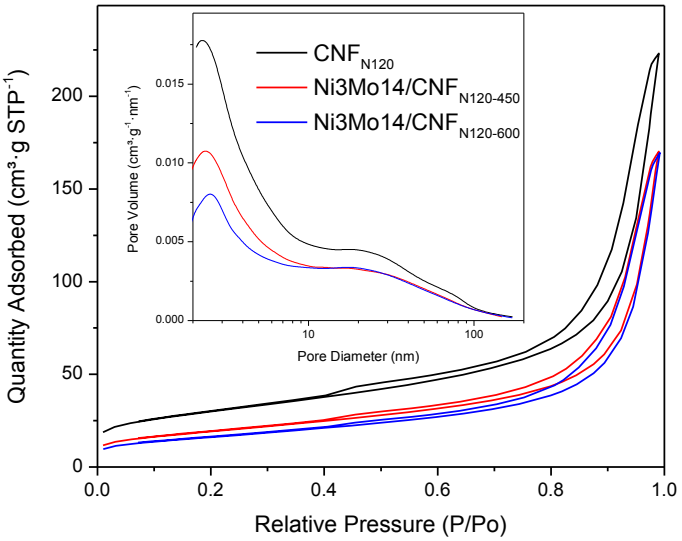

Figure 8.17. N_2 adsorption-desorption isotherms and pore size distribution curves (inset) for CNF_{N120} and catalysts.

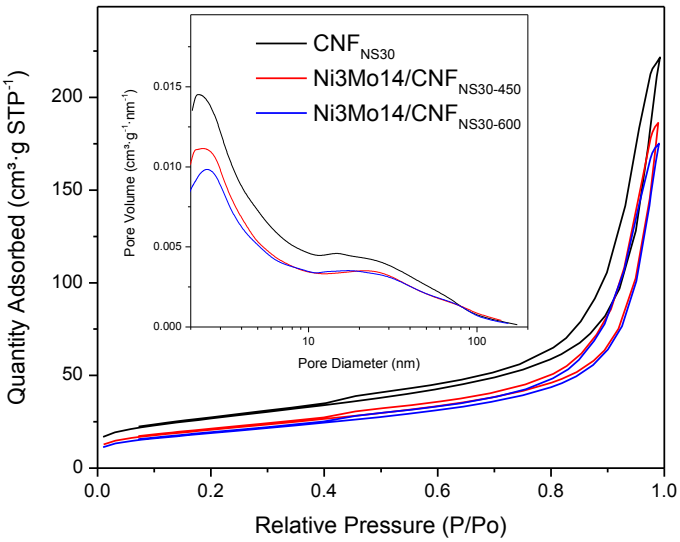

Figure 8.18. N_2 adsorption-desorption isotherms and pore size distribution curves (inset) for CNF_{NS30} and catalysts.

NH_3-TPD was used to observe that after Ni and Mo were deposited on the supports, no acidity remained (results not shown).

The catalysts were subjected to TPR studies, which differ from the TPR reported in other chapters because in this case the catalysts were in the sulfided form. Thus, TPR was denoted as TPR-S. This technique has been used previously for sulfided NiMo catalysts and it provides a measure of chemical reactivity (258). The consumption of H_2 is related to the formation of surface anion vacancies in the surface metal species which can be correlated to a catalytic active site, or CUS (259). TPR-S profiles for all catalysts are shown in Figure 8.19. A peak centred at ca. 300 °C was observed for all catalysts, as previously reported for AC supported NiMo catalysts (260). The chemical nature of the reactant sulfur in this region can be probably assigned to different contributions: (i) non-stoichiometric sulfur atoms (S_x) weakly adsorbed on coordinated unsaturated edge/corner sites (204,261) and (ii) recombination of –SH groups and/or reaction of –SH groups with H_2 (262). Additionally, a shoulder at temperatures between 350 and 500 °C was also observed, assigned to the hydrogenation of S species more labile than stoichiometric sulfide sulfur, probably consisting of surface anions located at the edges of the crystallites (263). The reduction of MoS_2-like species in supported catalysts occurs at high temperatures (700-900 °C) (204,258) and could not be determined with these samples due to the carbonaceous nature of the support, which would lead to its hydrogasification.

Effect of functionalisation. The TPR-S peaks at 300 °C for catalysts supported on the different carbon nanofibres (CNF_{N30}, CNF_{N120} and CNF_{NS30}) tempered at 450 °C had different intensity. Thus the type of acid treatment had an effect on creating CUS. $Ni3Mo14/CNF_{N120-450}$, supported on the CNF with the stronger acid treatment, had the higher total H_2 consumption. Nevertheless, the TPR-S peaks of each catalyst were deconvoluted to evaluate the contribution of the peak at 300 °C, related to CUS as mentioned previously (Figure 10.4, Appendix 1). The areas had values in the following decreasing order: $Ni3Mo14/CNF_{N30}$ > $Ni3Mo14/CNF_{N120}$ > $Ni3Mo14/CNF_{NS30}$. The influence of the type of the acid treatment in relation to the stacking degree of the metals deposited on CNF has not been reported previously. This novel result can provide insight into the development of carbonaceous catalytic supports, given that the degree of stacking can be tailored to the specific end reaction.

Effect of tempering temperature. The effect of tempering temperature was clearly independent of acid treatment. The amount of H_2 consumed in the low temperature region was much higher for $Ni3Mo14/CNF_{X-450}$ compared to $Ni3Mo14/CNF_{X-600}$. This fact is indicative of different amount of weakly bonded sulfur species in the catalyst surface, implying that the sample tempered at low temperature had a larger number of CUS. It was thus decided that $Ni3Mo14/CNF_{N120-600}$ and $Ni3Mo14/CNF_{NS30-600}$ would not be tested for their catalytic activity since the materials presented very low H_2 consumption in the TPR-S study.

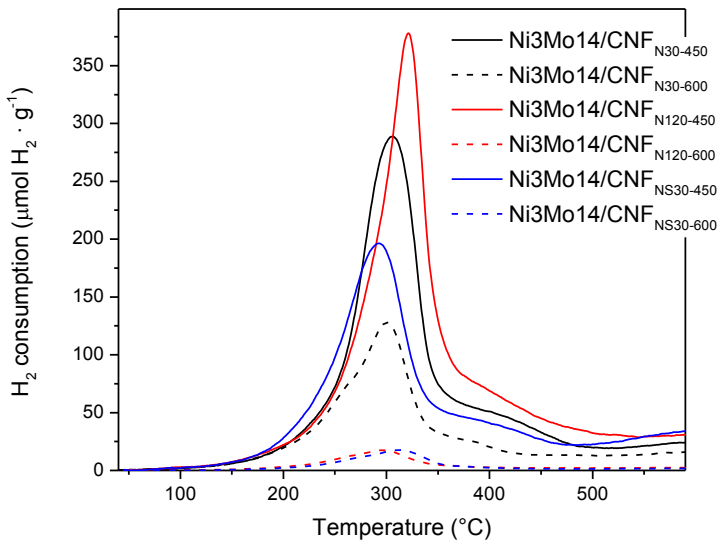

Figure 8.19. TPR-S spectra of tempered NiMo catalysts supported on CNF_{N30}, CNF_{N120} and CNF_{NS30}.

8.3. HYDROPROCESSESING RESULTS AND DISCUSSION

The catalysts supported on functionalised CNF were used for hydroprocessing of VR. To assess catalytic performance, several aspects were considered. Section 8.3.1 focuses on VR conversion, asphaltene upgrading, product distribution and HDS and HDM conversions and Section 8.3.2 deals with changes in the spent catalysts. All experiments were performed at 425 °C for 60 minutes. The discussions include results of Ni3Mo14/Al_2O_3 from Chapter 5 for comparison purposes.

8.3.1. Feed and products

8.3.1.1. Conversion

The conversion values of the >450 °C fraction ($C_{>450°C}$) and asphaltenes ($C_{Asphaltenes}$) are shown in Table 8.4. As previously mentioned in Chapter 3, both conversion definitions take coke formation into account as unconverted products (Equations 1 and 2), so an increase in coke production affects the resulting values negatively. Values for $C_{>450°C}$ were very similar for all CNF-supported catalysts as well as the non-catalytic run. The upgrading of molecules with a boiling point higher than 450 °C in VR studied can be mainly considered as a thermal driven process, thus explaining the small differences observed. On the other hand, a strong catalytic influence was observed in $C_{Asphaltenes}$. The Al_2O_3 supported catalyst underperformed in terms of asphaltene conversion to the Ni3Mo14/$CNF_{N30-450}$ catalyst and yielded similar conversion to the Ni3Mo14/$CNF_{N30-600}$ catalyst.

Effect of functionalisation treatment. Ni3Mo14/$CNF_{N30-450}$ presented the best asphaltene conversion of all catalysts. Similar conversions as Ni3Mo14/Al_2O_3 were achieved with Ni3Mo14/$CNF_{N30-450}$. The catalysts supported on CNF_{N120} and CNF_{NS30} presented lower $C_{Asphaltenes}$, which can be correlated with the lower amount of CUS determined by TPR-S (Figure 8.19). The creation of differently sized MoS_2 stacks affected the amount of CUS on the catalysts and thus $C_{Asphaltenes}$.

Effect of tempering temperature. Ni3Mo14/$CNF_{N30-450}$ had a higher $C_{Asphaltenes}$ than Ni3Mo14/$CNF_{N30-600}$, thus it was observed that the tempering temperature had a strong effect on the catalyst performance. This can be attributed to the large amount of CUS available in the catalyst subjected to decomposition at low temperature, as deduced from the TPR-S study shown in Figure 8.19. This fact can also be the reason for the better performance of the Ni3Mo14/$CNF_{N30-450}$ catalyst than Ni3Mo14/Al_2O_3, since the latter catalyst presents a much higher support-metal interaction that may prevent the

complete sulfidation of the active phase. However, better hydrogen transfer of the carbon based catalyst cannot be ruled out.

Asphaltene upgrading activity of catalysts supported on CNF has not been previously reported, thus it proved difficult to compare against other results. Active carbons (AC) have been used successfully as catalytic support during hydroprocessing of heavy feeds. A mesoporous AC support was used for hydrocracking reactions with a VR with 7 wt % asphaltenes at temperatures above 415 °C in a semi-batch reactor. It was found that the AC limited the condensation reactions of asphaltenes that led to coke formation by providing adsorption sites to the free radicals, thus avoiding polymerisation reactions (264). An asphaltene conversion of 0.58 was obtained. Similar results were obtained by hydrocracking VR in continuous reactors with the same AC (265). The Ni3Mo14/$CNF_{N30-450}$ catalyst used in this study led to $C_{Asphaltenes}$ in the same range as the ones reported in the literature using AC, using a VR with significantly higher asphaltene content (33 vs. 7 wt %).

Table 8.4. Conversion values for the >450 °C fraction ($C_{>450°C}$) and asphaltenes ($C_{Asphaltenes}$) for Ni3Mo14/CNF_{X-T} and Ni3Mo14/Al_2O_3. All reactions lasted 60 minutes at 425 °C with an initial 185 bar H_2 pressure.

Sample	$C_{>450°C}$	$C_{Asphaltenes}$
Ni3Mo14/$CNF_{N30-450}$	0.51	0.73
Ni3Mo14/$CNF_{N30-600}$	0.49	0.57
Ni3Mo14/$CNF_{N120-450}$	0.47	0.64
Ni3Mo14/$CNF_{NS30-450}$	0.49	0.64
Ni3Mo14/Al_2O_3	0.55	0.59
Thermal	0.54	0.12

8.3.1.2. Yields

The product distributions obtained in the above reactions are shown in Table 8.5. Solids were determined by thermogravimetric analysis and were considered as the materials which combusted between 300-500 °C. It was observed that gas production was very similar for all catalysts. It has been mentioned previously that it is mostly thermally driven. The yields of $Maltenes_{<450°C}$ were lower for the CNF-supported catalysts than for Ni3Mo14/Al_2O_3, hence the lower $C_{>450°C}$ obtained for these materials. $Maltenes_{>450°C}$ and Asphaltene yields were higher for the CNF-supported catalysts than for Ni3Mo14/Al_2O_3. Since solids were significantly lower for all Ni3Mo14/CNF_{X-T} than for Ni3Mo14/Al_2O_3, $C_{Asphaltenes}$ described in the previous section was higher for Ni3Mo14/CNF_{X-450}. Higher Solids yields can be clearly associated to the higher acidity

of Al_2O_3 supported catalysts, as compared to the CNF supported catalysts and may also help explain the better performance of the CNF based catalysts.

It is known that the amount of coke deposited in the hydrotreating catalysts is predominant at the early stages of the reaction, and it is followed by a steady state in which coke does not affect catalyst stability (103). In this work, 1 h reaction tests were performed in a batch reactor, thus the amount of coke deposited on Ni3Mo14/Al_2O_3 can be considered relatively large. Longer reaction times or reaction tests in a continuous flow reactor would be necessary in order to evaluate the long term activity of the CNF supported catalysts.

Effect of functionalisation treatment. Differences for the catalysts were mainly observed in the Asphaltenes yields. It showed that Ni3Mo14/$CNF_{N30-450}$ had better asphaltene conversion activity, as expected from the higher number of CUS determined by TPR-S. The higher stacking degree of Ni3Mo14/$CNF_{N120-450}$ and Ni3Mo14/$CNF_{NS30-450}$, observed by TEM (Figure 8.13 and 8.14), could present some steric hindrance issues for large molecules, as well. Access of larger molecules to the MoS_2 layers that are closer to the support could be more difficult. It was reported that a large molecule such as dibenzothiophene preferentially access corner sites (28). Nevertheless, an even larger molecule than DBT (4,6-dimethyldibenzothiophene) adsorbed flat on top of the MoS_2 cluster and not preferentially on the corner sites. Therefore, steric hindrance issues could prevent large molecules from accessing the CUS in the bottom stacks.

Effect of tempering temperature. Ni3Mo14/$CNF_{N30-600}$ led to higher Asphaltenes yield, as expected, since it had less active sites which would thus hydrogenate the cracked molecules (determined by TPR study, Figure 8.19).

Table 8.5. Product yields for reactions of for Ni3Mo14/CNF_{X-T} and Ni3Mo14/Al_2O_3. All reactions lasted 60 minutes at 425 °C with an initial 185 bar H_2 pressure.

Sample	Gas (wt %)	$Maltenes_{<450°C}$ (wt %)	$Maltenes_{>450°C}$ (wt %)	Asphaltenes (wt %)	Solids (wt %)
Ni3Mo14/$CNF_{N30-450}$	19.8	18.4	52.6	8.0	1.2
Ni3Mo14/$CNF_{N30-600}$	19.1	16.5	50.1	12.3	2.0
Ni3Mo14/$CNF_{N120-450}$	18.5	16.1	53.4	10.8	1.2
Ni3Mo14/$CNF_{NS30-450}$	18.3	18.3	51.3	10.0	2.1
Ni3Mo14/Al_2O_3	18.1	23.7	44.5	6.5	7.2
Thermal	30.4	0	40.0	24.3	5.3

8.3.1.3. Selectivity

The maltene to asphaltene ratio along the coke and gas production for the catalytic and thermal reactions are shown in Table 8.6. A higher maltene to asphaltene ratio was obtained with Ni3Mo14/Al_2O_3, though Ni3Mo14/$CNF_{N30-450}$ had good performance as well.

Effect of functionalisation treatment. Ni3Mo14/$CNF_{N120-450}$ and Ni3Mo14/$CNF_{NS30-450}$ had lower maltene to asphaltene ratios than Ni3Mo14/$CNF_{N30-450}$. This was possibly a consequence of the defects observed on the MoS_2 slabs and CUS availability. The coke and gas production for all Ni3Mo14/CNF_{X-T} catalysts were slightly lower to Ni3Mo14/Al_2O_3.

Effect of tempering temperature. As expected, Ni3Mo14/$CNF_{N30-600}$ had the lowest maltene to asphaltene ratio of all catalysts due to the lower amount of CUS available.

Table 8.6. Maltene to asphaltene ratio in products and coke and gas production for Ni3Mo14/CNF_{X-T} and Ni3Mo14/Al_2O_3. All reactions lasted 60 minutes at 425 °C with an initial 185 bar H_2 pressure.

Sample	Maltene to asphaltene ratio in products	Coke and gas production (wt % of feed)
Ni3Mo14/$CNF_{N30-450}$	8.9	21.0
Ni3Mo14/$CNF_{N30-600}$	5.4	21.1
Ni3Mo14/$CNF_{N120-450}$	6.5	19.7
Ni3Mo14/$CNF_{NS30-450}$	6.9	20.4
Ni3Mo14/Al_2O_3	10.5	25.3
Thermal	1.7	32.2

8.3.1.4. HDS and HDM

Hydrodesulfurisation and hydrodemetallisation conversions for Ni3Mo14/CNF_{X-T} and Ni3Mo14/Al_2O_3 are presented in Table 8.7, calculated from Equations 9 to 12 taking into account the concentration of the heteroatoms in the VR feed. HDM and HDS conversions were lower for the CNF-supported catalysts than the ones obtained with Ni3Mo14/Al_2O_3. On the other hand, the higher HDM and HDS for Ni3Mo14/Al_2O_3 can be related to its also higher coke deposition, which would allow for removal of a larger fraction of heteroatoms present in PAH in the VR as coke.

Effect of functionalisation treatment. No significant effect of the functionalisation treatment was observed on the HDS and HDM rates for the Ni3Mo14/CNF_{X-450} catalysts. These catalysts showed better selectivity towards V than Ni in HDM reactions.

Effect of tempering temperature. The comparison between the two CNF supported catalysts revealed the same trend observed for VR upgrading in terms of $C_{>450°C}$ and $C_{Asphaltenes}$. The catalyst tempered at 450 °C performed better that the one tempered at 600 °C in terms of HDS and HDM. For instance, HDM was 0.86 and 0.74 for the Ni3Mo14/$CNF_{N30-450}$ and Ni3Mo14/$CNF_{N30-600}$, respectively.

Table 8.7. S, Ni and V content in reaction products; HDS and HDM conversions for Ni3Mo14/CNF_{X-T} and Ni3Mo14/Al_2O_3. All reactions lasted 60 minutes at 425 °C with an initial 185 bar H_2 pressure.

Catalyst	S (wt %)	HDS conversion	Ni (ppm)	V (ppm)	C_{Ni}	C_V	HDM conversion
Ni3Mo14/$CNF_{N30-450}$	1.5	0.83	38.5	17.3	0.67	0.94	0.86
Ni3Mo14/$CNF_{N30-600}$	2.0	0.78	63.1	43.6	0.46	0.85	0.74
Ni3Mo14/$CNF_{N120-450}$	1.4	0.84	37.4	19.1	0.68	0.93	0.86
Ni3Mo14/$CNF_{NS30-450}$	1.5	0.82	35.6	16.3	0.69	0.94	0.87
Ni3Mo14/Al_2O_3	0.7	0.90	6.0	5.3	0.95	0.98	0.97

The hydrotreating performance of CNT with real feeds has been reported. LGO was hydrotreated at 375 °C and 88 bar of H_2 pressure in a continuous reactor, with very similar HDS activity observed for NiMo supported on conventional alumina as on CNT (247). The authors attribute the high activity for NiMo/CNT to the pore size uniformity and absence of strong acid sites. Sulfur conversion was ca. 90%, in the same range as the one obtained for this work, even though the VR feed used in this study had 4.4 times more sulfur than the LGO. Another study used a heavier feed, VR, with 2 wt % asphaltenes and 2.3 wt % S for hydroprocessing at 430 °C with 80 bar H_2 pressure for 1.5 hr in a batch reactor (248). CoMo/CNT and CoMo/Al_2O_3 catalysts were used, obtaining slightly higher HDS with the latter. Values for HDS conversion ranged from 0.43 to 0.56, lower than the ones obtained in this work despite the higher S content in the feed. Nevertheless, product S content was similar for both studies (1-2 wt %), which could indicate that the removed sulfur was easier to process.

No studies on HDM properties of catalysts supported on CNF or CNT were found to compare against. CoMo catalysts supported on alumina and carbon were evaluated for their HDM and HDS properties using Maya crude oil as feed at 380 °C (266). The type of carbon used was not specified, but given its high surface area it was likely an AC. HDM and HDS were significantly lower for the CoMo catalyst supported on carbon than the one supported on alumina. The HDM and HDS values for the former catalysts were ca. 0.4 and 0.3, respectively. It is worth mentioning that the conversion values reported in the aforementioned work using the Al_2O_3 based catalysts were lower than the ones obtained in this work using CNF. This shows that CNF can have high HDM values similar to other alumina-supported catalysts.

8.3.2. Spent catalysts

Coke deposits on the catalysts are shown in Table 8.8, expressed as gram of coke per gram of catalyst. These data are discussed in greater detail in this section in association to changes in the catalysts textural properties. It was observed that five times the amount of coke was deposited on Ni3Mo14/Al_2O_3 than in Ni3Mo14/$CNF_{N30-450}$. Less acid supports have lower cracking function and thus lower coke formation (9,231). Coke values for Ni3Mo14/$CNF_{NS30-450}$ were higher, possibly due to the lower amount of CUS available to upgrade coke precursors.

Table 8.8. Coke on catalyst for Ni3Mo14/CNF_{X-T} and Ni3Mo14/Al_2O_3. All reactions lasted 60 minutes at 425 °C with an initial 185 bar H_2 pressure.

Sample	g coke per g catalyst
Ni3Mo14/$CNF_{N30-450}$	0.05
Ni3Mo14/$CNF_{N30-600}$	0.08
Ni3Mo14/$CNF_{N120-450}$	0.05
Ni3Mo14/$CNF_{NS30-450}$	0.09
Ni3Mo14/Al_2O_3	0.28

8.3.2.1. Textural properties

After each reaction spent catalysts were characterised with N_2 adsorption to evaluate changes in their textural properties, reported in Table 8.9. A reduction of the S_{BET} and total pore volume occurred for all the materials, due to coke deposition. Since coke blocked the smaller pores, an increase in the average pore diameter was observed for all materials. Even though the carbon materials had lower S_{BET} than the alumina support, some surface area was still available after reaction. Total pore volume was reduced proportionally for CNF and alumina catalysts. The APD was significantly increased for the CNF-supported catalysts when compared to Ni3Mo14/Al_2O_3. Thus, the spent Ni3Mo14/CNF_{X-T} catalysts had an APD four times higher than spent Ni3Mo14/Al_2O_3. No correlation was found between the functionalisation or tempering temperature with the loss of textural properties for the spent materials.

The adsorption-desorption isotherms and pore size distribution profiles are shown in Figure 8.20a and b, respectively, for the fresh and spent CNF-supported catalysts. The adsorption-desorption isotherms and pore size distribution for Ni3Mo14/Al_2O_3 were discussed in Section 5.3.2.2. It was observed that the shape of the isotherms and position of the hysteresis loops did not change for the spent materials, thus pore mouth plugging was minimal. N_2 uptake decreased for all spent catalysts in low relative pressures, as a consequence of a decrease in microporosity and small mesopores as observed in Figure 8.20b. The volumes for pores with a diameter smaller than 10 nm

were greatly impacted by coke deposits whereas larger pores maintained most of the volume, hence the large increase in APD of the materials. Thus coke deposits covered mainly the internal surface of the CNF. Since pores above 10 nm were not affected, the external surface of the materials which contained CUS would still be accessible for VR. No considerable differences were observed between the catalysts.

Table 8.9. Textural properties of spent Ni3Mo14/CNF_{X-T} and Ni3Mo14/Al_2O_3. All reactions lasted 60 minutes at 425 °C with an initial 185 bar H_2 pressure. The percentage of the corresponding textural property of the fresh catalysts which was retained is noted in parenthesis.

Sample	S_{BET} ($m^2 \cdot g^{-1}$)		Total pore volume ($cm^3 \cdot g^{-1}$)		Average pore diameter* (nm)	
Ni3Mo14/$CNF_{N30-450}$	26.5	(41%)	0.13	(65%)	22.8	(147%)
Ni3Mo14/$CNF_{N30-600}$	26.3	(36%)	0.13	(65%)	23.3	(162%)
Ni3Mo14/$CNF_{N120-450}$	31.6	(46%)	0.16	(82%)	23.8	(158%)
Ni3Mo14/$CNF_{NS30-450}$	32.8	(44%)	0.17	(75%)	24.1	(153%)
Ni3Mo14/Al_2O_3	229.4	(67%)	0.40	(60%)	5.8	(56%)

*BJH model applied to the adsorption branch of the isotherms

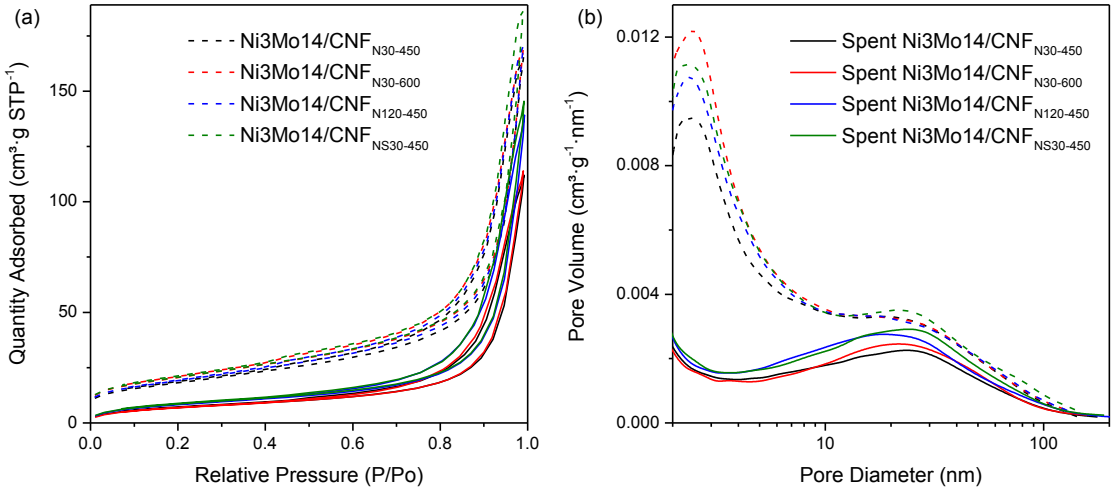

Figure 8.20. (a) N_2 adsorption-desorption isotherms and (b) Pore diameter distribution curves of fresh and spent Ni3Mo14/CNF_{X-T}. All reactions lasted 60 minutes at 425 °C with an initial 185 bar H_2 pressure.

8.4. CONCLUSIONS

CNF were synthesised from CH_4:CO_2 using a Ni/Al catalyst. Three acid treatments were performed to remove the Ni catalyst and to generate functionalities on the surface to allow metal particles to anchor to the CNF: HNO_3 treatment for 30 minute (CNF_{N30}), for 120 min (CNF_{N120}) and also a 30 min treatment with HNO_3 and H_2SO_4 (50:50 vol/vol) (CNF_{NS30}). All acid treatments increased the S_{BET} and total pore volume of the original CNF. Materials with a bimodal pore size distribution were obtained; S_{BET} were around

100 $m^2 \cdot g^{-1}$ and APDs of ca. 14.5 nm. XRD patterns showed that the Ni catalysts that were used to synthesise the CNF were successfully removed by the acid treatments. Furthermore, TEM micrographs showed that the Ni particles at the head of the CNF were successfully removed without modifying or destroying the graphene arrangement. Different functionalities were created on the CNF depending on the acid treatment, observed by TPD. Compounds such as carboxylic acids, were present in similar amounts for CNF_{N120} and CNF_{NS30}. Phenols, esters and carbonyls were present in greater amounts for CNF_{N120}. Strong acidity for the functionalised CNF occurred in the following increasing order: $CNF_{N30} < CNF_{N120} < CNF_{NS30}$. The same order was observed for TPO weight loss, thus when H_2SO_4 was used functional groups that oxidised at lower temperatures were created.

Ni and Mo were impregnated using ATM and nickel nitrate on the functionalised CNF and tempered at two temperatures, 450 and 600 °C. The novel synthesis method allowed for the direct formation of MoS_2 on the carbon support. Electron microscopy studies showed that the structural arrangement of deposited Ni and Mo varied depending on the functionalised CNF support. All catalysts presented MoS_2 stacks (confirmed by TEM-EDX), since the Mo precursor used in this study decomposed directly into MoS_2 allowing the direct formation of the sulfide form of the catalyst. The functionalities in the supports influenced the ability of metals to attach to the surface and create MoS_2 stacks. It was observed that the stacking degree and the length of the stacks increased when more functionalities were available on the surface of the CNF. Stacks were less defective when HNO_3/H_2SO_4 was used instead of only HNO_3 during the acid treatment. Mo reflections were observed in XRD patterns, although these were not large enough to enable crystallite sizes to be measured, which showed that the metals were well dispersed. TPR-S spectra showed that when the catalysts were tempered at 600 °C, very low H_2 consumption was observed when compared to the catalysts tempered at 450 °C. Thus, the tempering temperature had an important effect on the creation of CUS. Since these results have not been reported before, this work helps in understanding the influence of the acid treatment in relation to the stacking degree of the metals deposited on CNF supports.

The catalysts supported on functionalised CNF were used for hydroprocessing of VR where conversion, asphaltene upgrading, product distribution and HDS and HDM conversions were analysed. Conversion of the fraction boiling above 450 °C, $C_{>450°C}$, was very similar for all CNF-supported catalysts. This conversion was mostly thermally driven; nonetheless the CNF-supported catalysts had lower conversions than $Ni3Mo14/Al_2O_3$ or the thermal reaction. The catalyst with lower stacking degree,

Ni3Mo14/$CNF_{N30-450}$, presented better asphaltene conversion than Ni3Mo14/Al_2O_3. These results are novel since the asphaltene upgrading activity of catalysts supported on CNF has not been previously reported. Solids yields (coke deposition) were significantly lower for CNF-supported catalysts than for Ni3Mo14/Al_2O_3. This was probably due to higher adsorption of asphaltene free radicals on carbonaceous supports, which helped avoid polymerisation reactions. Higher coke content was observed for Ni3Mo14/$CNF_{NS30-450}$, which had the least defective MoS_2 stacks. All CNF catalysts yielded lower maltene to asphaltene ratios than Ni3Mo14/Al_2O_3. When more defects were observed on the MoS_2 slabs, a higher maltene to asphaltene ratio was measured. Encouraging HDS and HDM conversions were obtained, albeit slightly lower than for Ni3Mo14/Al_2O_3. HDS values compared well to values reported in the literature. HDM on CNF-supported catalysts has not been reported before. These novel results show that CNF can have high HDM values similar to an alumina support.

A reduction of the S_{BET} and total pore volume occurred for all the spent catalysts, due to coke deposition. Since coke blocked the smaller pores, an increase in the average pore diameter was observed. No considerable differences in textural properties were observed between the spent catalysts. The shape of N_2 adsorption-desorption isotherms and the position of the hysteresis loops did not change for the spent materials, thus pore mouth plugging was minimal. The volumes for pores with a diameter smaller than 10 nm were greatly impacted by coke deposits whereas larger pores maintained most of the volume, hence the increase in APD of the materials.

In summary, NiMo catalysts were synthesised on functionalised CNF, which proved effective for asphaltene upgrading, HDS and HDM. Depending on the catalyst synthesis conditions, functionalities were created which allowed for different MoS_2 stacking. Asphaltene conversion was higher than for a reported NiMo/Al_2O_3 catalyst. HDS and HDM rates were slightly lower than for the alumina-supported catalyst. Results were encouraging and thus further research into the development of CNF as catalytic support for heavy oil upgrading is deemed interesting.

Chapter 9: Conclusions and recommendations for future work

This study was set out to explore the development of mesoporous materials that would serve as catalysts in hydrocracking reactions using a heavy hydrocarbon feed. Since the use of heavy oils is expected to increase steadily, the development of new catalysts that can withstand deactivation by PAH and coke can be readily applied in industry.

Novel materials for which limited information has been published were developed and tested in hydrocracking reactions. In Chapter 4 the synthesis of mesoporous aluminas was described. In Chapter 5 catalysts with different metal loadings, supported on a selected mesoporous alumina from Chapter 4, were used to determine the influence of metal loading in hydrocracking reactions. Chapter 6 showed that a catalyst supported on alumina doped with Cr can achieve higher metal and coke dispersion than a catalyst supported on a mesoporous alumina from Chapter 5. Chapter 7 addressed the use of mesoporous silica alumina as catalytic support, albeit with discouraging results. Finally in Chapter 8 the use of carbon nanofibres as catalytic support was explored, obtaining notable results. This chapter provides concluding remarks on the achievements of the study and ends with recommendations for future work.

9.1. CONCLUSIONS

Materials were developed and tested in a batch system for hydrocracking of VR. An experimental methodology for batch reactions using VR was developed. Four classes of materials were prepared and characterised: mesoporous aluminas, mesoporous aluminas doped with Cr, mesoporous silica alumina and carbon nanofibres. These materials were used as supports of NiMo catalysts. The catalysts were tested in short time hydrocracking reactions after which the reaction products were analysed in terms of catalyst deactivation and reaction conditions. A comparison was performed between the different materials and the mesoporous alumina.

Mesoporous aluminas were synthesised via two routes: surfactant templating and nanocasting. The synthesis conditions had significant effects on the textural properties of resulting aluminas as well as in their TEM images. The H_2O:Al ratio was the most important variable that determined pore size for aluminas synthesised via surfactant templating. A higher H_2O:Al ratio yielded an alumina with larger average pore diameter. The H_2O:Al ratio was determinant for the materials surface area, total pore volume as well as average pore diameter because the surfactant micelles would swell and increase in diameter depending on the amount of water used. The effects of ageing temperature and calcination rate were dependent on the H_2O:Al ratio. For aluminas prepared by nanocasting the selection of Al precursor influenced the textural properties of the resulting materials. Higher surface area and pore volume were obtained when aluminium isopropoxide was used instead of aluminium nitrate with a slower calcination rate.

Catalysts supported on Al_2O_3, Al_2O_3-Cr, MSA and CNF were tested in VR hydrocracking reactions at different temperatures: 400, 425 and/or 450 °C. They were reutilised in most of the cases in a second reaction with fresh feed. Catalysts were characterised before and after the reactions to evaluate coke deposition and changes in textural properties. Reaction products were analysed to observe asphaltene conversion in the reactions. The strategy of reutilising the catalysts allowed the assessment of their activity when coated with carbon deposits, which were mainly formed during the initial reactions. Reaction temperature had an important impact on conversions and product distributions, thus thermal cracking was important. Higher reaction temperatures accounted for higher VR and asphaltene conversions at the expense of a large increase in gas yields. In general, conversions for the fraction boiling above 450 °C were found to be in the range of literature results. For the best performing catalysts, asphaltene conversion values were high given the VR feed used.

Three catalysts with different metal loadings supported on Al_2O_3 were evaluated in Chapter 5. It was found that metal loading did not influence conversion of the >450 °C fraction because it was dominated by thermal cracking. Nevertheless, metal loading on the catalysts was determinant for asphaltene upgrading; higher asphaltene conversions were obtained with higher metal loading. The catalysts presented large amounts of coke deposits, but higher metal loadings reduced coke deposition in the first run. No evidence of pore mouth plugging was observed, indicating that the catalysts could accommodate coke while retaining most of their textural properties. Coke deposits behaved in a dynamic form and changed structurally in the reutilisation reactions. The higher Ni and Mo composition achieved higher asphaltene conversion as well as

maintained the textural properties of the spent catalyst. This higher metal loading served as benchmark for catalysts supported on Al_2O_3-Cr and CNF.

A Cr-doped Al_2O_3 was successfully synthesised using a similar procedure to the aluminas obtained by surfactant templating. It was observed that when Cr was introduced into the alumina matrix, the mesoporosity of the material was not affected. An isotherm for plate-like particles assembled in parallel was obtained, just as for mesoporous Al_2O_3. The catalyst supported on Al_2O_3-Cr maintained the support pore size distribution relatively unaffected, showing that Cr helped disperse the NiMo metals. This was confirmed with XRD by the absence of Ni or Mo peaks. The reducibility of metal sites by TPR indicated that more active sites were available for Ni3Mo14/Al_2O_3-Cr than for Ni3Mo14/Al_2O_3.

Catalysts supported on Al_2O_3 and Al_2O_3-Cr were compared in their hydrocracking reactivity and in their ability to maintain the textural properties. It was found that the spent Ni3Mo14/Al_2O_3-Cr catalysts retained their textural properties despite higher coke deposition than Ni3Mo14/Al_2O_3. The Cr dopant aided in dispersing not only the Ni and Mo metal sites but possibly also coke in the spent catalysts. Conversions for asphaltenes were higher for NiMo/Al_2O_3-Cr than for NiMo/Al_2O_3, mainly at high reaction temperatures. The plate-like particles present in Al_2O_3 and Al_2O_3-Cr show an advantage over other types of alumina reported in the literature because they do not present pore mouth plugging.

A catalyst supported on MSA was compared to the catalyst with equivalent metal loading supported on Al_2O_3. VR conversions were similar for the two materials, reinforcing what was previously observed with Al_2O_3 materials: thermal cracking dominated this conversion. In contrast, asphaltene conversion was higher and coke deposits were lower for Ni1Mo6/Al_2O_3 than for Ni1Mo6/MSA. The effectiveness of the Al_2O_3 supported catalyst over the MSA was explained mainly by its larger pores that can allow better diffusion of asphaltene molecules. The textural properties of MSA and Ni1Mo6/MSA were greatly affected by coke deposits. This showed that the architecture of the Al_2O_3 mesopores, plate-like particles, presented a significant advantage over the ink-bottle type pores of the MSA.

Results from catalysts supported on CNF showed that the conditions of the functionalisation of CNF as well as the tempering of the catalysts had an important effect on the resulting materials. The functionalisation of the CNF successfully removed the catalyst particles used to grow the CNF without modifying or destroying the graphene arrangement and also created functionalities. These functionalities

influenced the ability of the catalyst metals, Ni and Mo, to attach to the surface and create MoS_2 stacks. It was observed that the stacking degree and the length of the stacks decreased when less functionalities were available in the surface of the CNF. When stacks had more defects, additional edges and active sites acting as CUS were available. The effect of tempering conditions was also important. When a temperature of 450 °C was employed, higher content of active sites were obtained. On the other hand, when a tempering temperature of 600 °C was used the number of sulfided metal species of the resulting materials were significantly lower, thus lower CUS formed. The catalyst with less stacking presented better asphaltene conversion and similar HDS and HDM conversions when compared to the catalyst supported on mesoporous Al_2O_3. This showed that catalysts supported on CNF can potentially be as active as catalysts supported on conventional alumina supports.

In summary, materials were designed and tested in heavy oil hydrocracking reactions, contributing to novel results in the field. NiMo catalysts supported on mesoporous alumina, mesoporous alumina doped with Cr and carbon nanofibres could obtain considerable asphaltene conversions without suffering significant deactivation. On the other hand, results indicated that the MSA supported catalyst was active mainly due to thermal reactions and its pores were almost completely blocked by coke deposits by the second hour of reaction. The pore configuration of Al_2O_3 or Al_2O_3-Cr could allow high coke deposition without having pore mouth plugging, contrary to the configuration of MSA. The development of catalysts on CNF has significant potential, although further investigation is needed to optimise the synthesis conditions of the materials.

9.2. RECOMMENDATIONS FOR FUTURE WORK

There are intrinsic limitations to the work performed for this thesis, including time constraints as well as materials and equipment availability. The two aims of this work included catalyst synthesis and VR characterisation so work was divided between material design and testing. The analytical techniques that were used were chosen according to their accessibility and also to allow for the timely input of results into the next cycle of catalyst development or experiment planning. The microbomb reactor is a versatile equipment since it permits the testing of a large number of materials. However, since it is a batch reactor, reaction times were kept short. The selection of VR as feed proved challenging, particularly in product characterisation.

This section describes future work that can be performed on the development of experiments that can help understand to a greater extent the catalysts that were used, the mechanism of hydrocracking of heavy oils, as well as new ideas that can be tested.

Some of the techniques that are proposed in this section imply that an expertise in the method itself would need to be acquired. Therefore the advantage of producing more information on the materials would need to be balanced with the added value of the information itself.

9.2.1. Catalysts

9.2.1.1. Research on existing catalysts

Test catalysts from Chapter 4. Due to unpredicted circumstances, the catalysts with different porosity reported in Chapter 4 were not tested in hydrocracking reactions. Different studies are available on the effects of support pore size on hydroprocessing reactions (44,61,150). On the other hand, the testing of a catalyst supported on an alumina synthesised by nanocasting with carbon nanofibres has not been reported, so priority would be given to the Ni3Mo14/NC3 catalyst.

Perform more reutilisation cycles for the catalysts. Catalysts were employed for a maximum of two hours of reaction in this study. The reaction-catalyst collection cycle could be extended for one or two more cycles to evaluate in greater detail the initial catalyst deactivation.

Study the effect of sulfidation. The formation of MoS_2 and CUS depends on the sulfidation conditions (267). The catalysts employed in this work were not analysed after sulfidation because this was performed in-situ prior to reaction. Thus, it would be interesting to perform characterisation studies on the sulfided materials before they come in contact with the hydrocarbon feed. In order to do this, a catalyst would be placed in the microbomb reactor with the sulfidation agent (CS_2 or DMDS) and pressurised with H_2. The reactor would be immersed in the sand bath with different temperature intervals maintaining the temperature for a certain time (196). Afterwards the reactor would be cooled down and pressure would be decreased by purging the gases into a fume hood; pressure would be maintained above atmospheric. Then the system would be pressurised above 10 bar with a gas mix of O_2 diluted in N_2 of He to allow for passivation of the material. The system could be depressurised and pressurised with the aforementioned gas mix in several cycles to achieve passivation. Afterwards the catalyst could be removed from the microbomb reactor for further analysis. Sulfidation conditions would need to be optimised. Several characterisation methods could be employed on the sulfided materials: a) XRD could add information on the crystallinity and size of the MoS_2 stacks; b) N_2 adsorption-desorption would determine if changes on textural properties occurred after sulfidation, although small

changes have been observed in other studies (268); c) NH_3-TPD would determine if the acidity of the materials changed; d) sulfur TPR would help determine the amount of active MoS_2 species and NiMoS moieties present; and e) TEM-EDX analysis would help visualise the formation of MoS_2 stacks.

Perform sulfidation ex-situ. Building on the previous recommendation, ex-situ sulfidation of the catalysts could be performed with easier recovery of the catalysts and better control of the sulfidation conditions. Catalysts with higher activity can be obtained by ex-situ sulfidation (9). A similar system to the one set up to temper the CNF-supported catalysts (Chapter 8) could be used. A tubular furnace would be set up using a quartz tube to contain the catalyst between quartz wool or wire mesh. A controlled flow of H_2S/H_2 would be passed through the tube while heating the catalyst to a determined temperature at conditions employed in the literature (267). Afterwards the furnace would be cooled down to room temperature and a flow of O_2 diluted in N_2 or He would be used to passivate the catalyst. Sulfidation conditions would need to be optimised. The characterisation studies mentioned in the previous section would also be applicable.

Regenerate the catalysts. Even though the catalysts were used for short reaction times in this study, they could be regenerated in air flow to observe if the properties of the fresh catalyst were maintained after coke removal. Studies such as N_2 adsorption-desorption and XRD could be performed on the regenerated catalysts.

Further characterise the catalysts. Catalyst characterisation can be performed by a myriad of techniques. The ones used in this work were chosen because they were fundamental to understand the catalysts. Nevertheless, further characterisation techniques can be used which would add information on the fresh as well as the spent catalysts. Therefore the following techniques are recommended: a) Raman spectroscopy, to provide details on the oxide surface species, which would allow for the identification of MoO_3, MoO_2, $NiMoO_4$ (269) and would thus help understand the interactions with the support; and b) X-ray photoelectron spectroscopy (XPS) to help identify the elements that are present in the outermost layer of the samples, along their chemical state. XPS would help in determining if Mo is available as Mo^0, MoS_2 or MoO_3 as well as the chemical state of Cr in the Al_2O_3-Cr supported catalysts. XPS can be performed on catalysts in an oxidic or sulfided state as well as on spent catalysts (40,270).

Study the accumulation of metals on spent catalysts. High HDM rates were achieved with Ni3Mo14/Al_2O_3, Ni3Mo14/Al_2O_3-Cr and for the catalysts supported on CNF. Thus it

would be helpful to evaluate Ni and V deposition on the catalysts. Even though metal deposition occurs throughout the reaction cycle and metals accumulate with time, it would be interesting to observe the evolution of metal deposits on the catalysts because the VR employed contains a large content of Ni and V. ICP could be used for this purpose because it requires low amounts of sample. A distinction between the Ni available on the catalyst before and after reaction would need to be made. This study would also be useful when the supports were tested (Al_2O_3, Al_2O_3-Cr and MSA) because the hydrogenation that was observed could be due to the formation of "auto-catalysts" from the deposition of Ni and V sulfides from the feed (88).

9.2.1.2. New materials

Study the influence of calcination conditions. The catalysts synthesised with chelating agent (DETA) supported on Al_2O_3, Al_2O_3-Cr and MSA were calcined in this work. The advantages of calcination are not clear (63) so studies on the effects of calcination could be performed. Catalysts could be synthesised in the same manner but foregoing the calcination step. The tempering process used for CNF supported materials could be employed.

Test one-pot synthesis of catalysts. The method to synthesise Al_2O_3-Cr described in Chapter 6 can prove interesting for synthesis of NiMo catalysts supported on Al_2O_3. Even though it has the risk of creating very strong interactions between the metals and the Al_2O_3 and as a consequence reducing the content of active sites, perhaps very high dispersion of the metals can be achieved. Also, catalysts with higher surface area, pore size and pore volume could be obtained.

Synthesise unsupported catalysts. The use of unsupported catalysts show that high conversions can be obtained when processing heavy feeds (39). Thus, NiMo complexes prepared with chelating agents could be synthesised and tested in hydrocracking reactions (67,68).

Test direct synthesis of MoS_2. Results from Chapter 8 showed that direct synthesis of MoS_2 can be achieved. Thus the same synthesis procedure could be used to develop catalysts supported on Al_2O_3 and Al_2O_3-Cr.

Vary concentration of Cr dopant in Al_2O_3-Cr. The synthesis of Cr-doped alumina (Chapter 6) was only performed with a concentration of Cr of 6 wt %. The effect of the concentration of Cr could be studied by varying its concentration and observing the changes in Ni and Mo reducibility by TPR.

Synthesise monometallic catalysts supported on Al_2O_3-Cr. The effect of Ni has been studied elsewhere for NiMo catalysts supported on Al_2O_3 materials. On the other hand, the promotion of Ni in the Ni3Mo14/Al_2O_3-Cr catalyst shown in Chapter 6 could be evaluated. Monometallic Mo14/Al_2O_3-Cr catalysts could be synthesised, characterised and tested in VR hydrocracking reactions. TPR tests would indicate if the reducibility of Mo was affected by Ni or by the combined effect of Cr in the support and Ni.

Vary MoS_2 stacking in CNF. Catalysts supported on CNF reported in Chapter 8 show that synthesis conditions heavily influence the formation of MoS_2 stacks of different length. Ni is known to introduce defects in the MoS_2 structure (27). Catalysts with higher Ni loadings could be developed and the simultaneous deposition of Ni and Mo can be explored to form shorter MoS_2 stacks on the CNF support.

Evaluate different doping agents. In this work Cr was explored as a doping agent for Al_2O_3. Nevertheless, as it was summarised in Section 6.1, other elements can be utilised. A study of other elements, such as Fe and Cu, can be performed by using the same synthesis procedure used for Al_2O_3-Cr. The use of Fe and Cu was reported to increase the pore size of alumina (203).

9.2.2. Hydrocarbon feed and products

Further characterise products. To develop a deeper understanding of the hydrocracking reactions, further analysis on the VR and reaction products could be performed. Several techniques could be employed, for example: a) elemental analysis (C, H, N, S) to determine the C/H ratio of the feed and products and thus evaluate how much hydrogenation is taking place, also to observe HDN rates; b) TPO of spent catalysts performed in a TGA equipped a mass detector to determine if soft or hard coke deposits are forming (109,110); c) ^{13}C and ^{1}H NMR on the products, specially of the asphaltene fraction, to determine reductions in the aromaticity; d) FTIR on the feed and product samples to evaluate if changes in functional groups are observed; and e) the GC ASTM D5443 method could be implemented to determine the paraffinic, naphthenic, and aromatic hydrocarbon content in the samples, nevertheless this method is limited to samples with a boiling point below 270 °C.

Modify asphaltene content. It would be interesting to evaluate the influence of asphaltenes in the hydrocracking reactivity of VR. To do this, maltenes could be separated from asphaltenes from VR following the ASTM methods D3279 or D2007-80. Then different dilutions of maltenes and asphaltenes would be performed –paying attention to the redissolution of the mixture– thus rendering synthetic VRs with varying asphaltene content. These feeds would be tested in hydrocracking reactions.

Study the influence of solvent. It was observed in this work that VR has low reactivity and that thermal cracking reactions need to take place to obtain higher upgrading of the feed. Solvents have been used extensively because they can serve as hydrogen carriers (87,88,101,108). Solubility tests of VR in different solvents could be performed to then test the solvents in hydrocracking reactions. Solvents that could be used include toluene, n-methyl naphthalene, diesel and gas oils.

Use of model compounds. A better understanding of the catalysts could be gained by studying simpler feeds such as model compounds. PAH with different molecular size such as naphthalene, anthracene and pyrene could be used to evaluate how the pore size of the catalyst influences the conversion of molecules of different size.

Study sludge formation. Studies on toluene insoluble "sludge" compounds formed during reaction have been performed (271). In this work, low sludge formation was observed in some reactions, particularly when high reaction temperatures were employed, accounting to up to 5 wt % of the recovered products. Due to time restrictions these materials were not analysed. It would be interesting to observe the nature of these compounds with SEC.

9.2.3. Reaction engineering

Increase mixing of materials. The microbomb reactor could be modified with a wire mesh to allow stainless steel ball bearings to be added into the reaction T. This would permit better mixing of H_2 with the hydrocarbon feed (192).

Modify reactor into semi-batch process. Semi-batch reactors with continuous H_2 feed have been employed in hydrocracking reactions (139,141,190). The microbomb reactor used in this study could be modified into a semi-batch reactor with the process diagram available in Figure 9.1. The H_2 feed would be regulated by a mass flow controller (MFC) and would feed into the reaction T via a perforated tube. Wire mesh would hold the catalyst inside the reactor. The production of gases would be controlled with a back pressure regulator (BPR). The advantage of this reactor over the present configuration would allow for the removal of gas products and provide better mixing of H_2 with the feed. VR has a high S content, nevertheless the use of a H_2/H_2S feed would need to be evaluated in order to maintain the catalyst in a sulfided state. Special attention would need to be provided in the safety specifications because constant H_2 feed would be employed.

Test catalysts in continuous reactor. The microbomb reactor has limitations because the reactivity of the feed decreases with time. If longer reactions were carried out,

asphaltene conversion would not necessarily increase since the largest molecules which were unreactive would possibly undergo thermal cracking and yield higher coke deposits. Additionally, if longer reaction times were used, the solubility of asphaltenes in the system could decrease and thus form further deposits. The method of reutilising the catalyst is practical when short reaction times are employed but continuous testing of the materials would prove helpful to evaluate if the materials have advantages over commercial catalysts, focusing on long term deactivation. This would add the complication of a VR continuous feeding system because, as mentioned previously, VR is solid at room temperature and extremely viscous. Solvents could be used to allow a continuous VR feed or a high temperature feeding system could be employed. Catalysts could be pelletised in order to load them into the reactor to allow better mixing with the feed and avoid large pressure drops in the system.

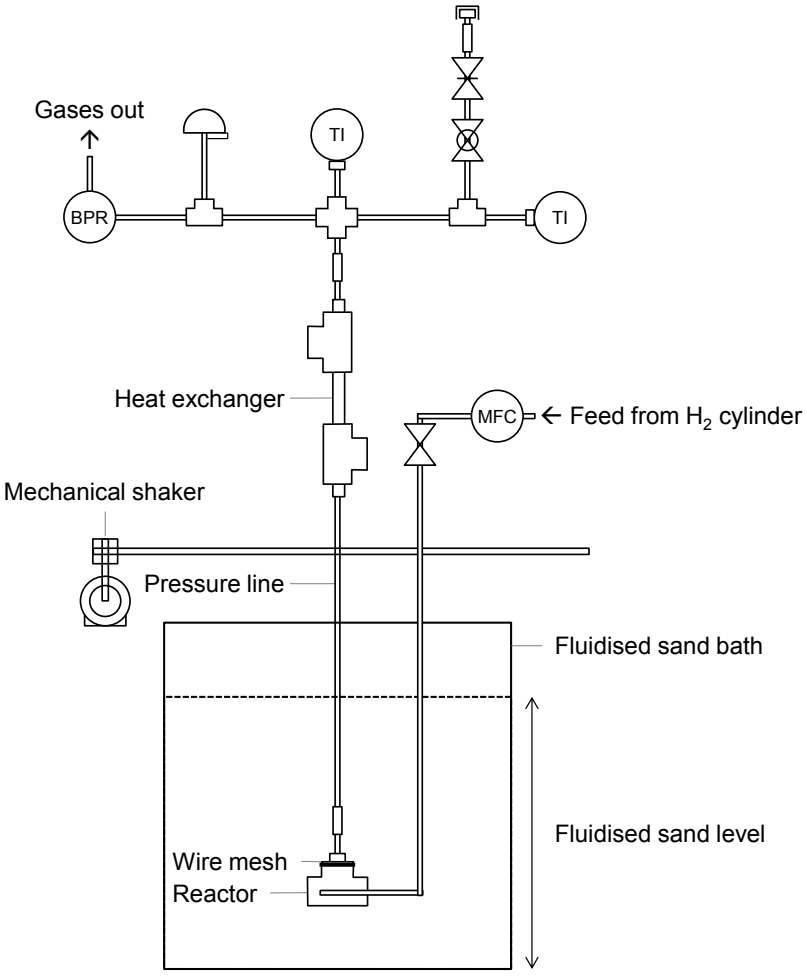

Figure 9.1. Proposed diagram for semi-batch microbomb reactor.

This thesis attempts to increase the understanding of heavy oil hydrocracking catalysts. The suggestions described in this section indicate that different paths can be explored to continue work in this field. The use of heavy oils will continue growing, thus research in the topic will probably yield valuable results.

References

1. Key World Energy Statistics 2009. International Energy Agency; 2009.

2. Heavy Crude Oil: A Global Analysis & Outlook to 2035. Hart Energy Research Group; 2011.

3. Speight JG. The chemistry and technology of petroleum. Marcel Dekker; 1999.

4. Leliveld RG, Eijsbouts SE. How a 70-year-old catalytic refinery process is still ever dependent on innovation. Catalysis Today. 2008 Jan 15;130(1):183–9.

5. Parlevliet F, Eijsbouts S. Research on sulfidic catalysts: Match between academia and industry. Catalysis Today. 2008;130(1):254–64.

6. Ancheyta J, Speight JG. Hydroprocessing of heavy oils and residua. 2007.

7. Gray MR. Upgrading petroleum residues and heavy oils. M. Dekker; 1994.

8. Wiehe IA, Liang KS. Asphaltenes, resins, and other petroleum macromolecules. Fluid Phase Equilibria. 1996;117(1–2):201–10.

9. Furimsky E. Catalysts for upgrading heavy petroleum feeds. Studies in Surface Science and Catalysis. 2007; 169.

10. Takeuchi C, Shiroto Y, Nakamura M, Fukui Y. RTD 4 (1) Upgrading through Asphaltenic Bottom Conversion. 11th World Petroleum Congress. 1983.

11. Ancheyta J, Trejo F, Rana MS. Asphaltenes: Chemical Transformation during Hydroprocessing of Heavy Oils. CRC Press; 2010.

12. Rana MS, Ancheyta J, Maity SK, Rayo P. Hydrotreating of Maya Crude Oil: II. Generalized Relationship between Hydrogenolysis and HDAs. Petroleum Science and Technology. 2007;25(1-2):201–13.

13. Millan M, Behrouzi M, Karaca F, Morgan TJ, Herod AA, Kandiyoti R. Characterising high mass materials in heavy oil fractions by size exclusion chromatography and MALDI-mass spectrometry. Catalysis Today. 2005;109(1-4):154–61.

14. Rodgers RP, Marshall AG. Petroleomics: Advanced Characterization of Petroleum-Derived Materials by Fourier Transform Ion Cyclotron Resonance Mass Spectrometry (FT-ICR MS). In: Mullins OC, Sheu EY, Hammami A, Marshall AG, editors. Asphaltenes, Heavy Oils, and Petroleomics. Springer New York; 2007.

15. Sanford EC. Molecular approach to understanding residuum conversion. Industrial & Engineering Chemistry Research. 1994;33(1):109–17.

16. Gosselink JW, Stork WHJ. Coping with Catalyst Deactivation in Hydrocracking: Catalyst and Process Development. Ind Eng Chem Res. 1997;36(8):3354–9.

17. From OSHA Technical Manual, Section IV, Chapter 2, Petroleum Refining Processes.

18. Minderhoud JK, van Veen JAR. First-stage hydrocracking: process and catalytic aspects. Fuel Processing Technology. 1993;35(1–2):87–110.

19. Ali MA, Tatsumi T, Masuda T. Development of heavy oil hydrocracking catalysts using amorphous silica-alumina and zeolites as catalyst supports. Applied Catalysis A, General. 2002;233(1-2):77–90.

20. Furimsky E. Selection of catalysts and reactors for hydroprocessing. Applied Catalysis A, General. 1998;171(2):177–206.

21. Scherzer J, Gruia AJ. Hydrocracking science and technology. CRC; 1996.

22. Egorova M, Prins R. The role of Ni and Co promoters in the simultaneous HDS of dibenzothiophene and HDN of amines over Mo/γ-Al2O3 catalysts. Journal of Catalysis. 2006;241(1):162–72.

23. Topsøe N-Y, Topsøe H. Characterization of the structures and active sites in sulfided CoMo/Al2O3 and NiMo/Al2O3 catalysts by NO chemisorption. Journal of Catalysis. 1983;84(2):386–401.

24. Topsoee H, Clausen BS, Topsoee NY, Pedersen E. Recent basic research in hydrodesulfurization catalysis. Ind Eng Chem Fund. 1986;25(1):25–36.

25. Topsøe H, Clausen BS. Active sites and support effects in hydrodesulfurization catalysts. Applied Catalysis. 1986;25(1–2):273–93.

26. Van Doorn J, Moulijn JA, Djéga-Mariadassou G. High-resolution Electron Microscopy of Spent Ni-Mo/Al203 Hydrotreating Catalysts. Applied Catalysis. 1990;63(1):77–90.

27. Eijsbouts S, Mayo SW, Fujita K. Unsupported transition metal sulfide catalysts: From fundamentals to industrial application. Applied Catalysis A: General. 2007;322:58–66.

28. Tuxen AK, Füchtbauer HG, Temel B, Hinnemann B, Topsøe H, Knudsen KG, et al. Atomic-scale insight into adsorption of sterically hindered dibenzothiophenes on MoS2 and Co–Mo–S hydrotreating catalysts. Journal of Catalysis. 2012;295:146–54.

29. Qabazard H, Abu-Seedo F, Stanislaus A, Andari M, Absi-Halabi M. Comparison Between The Performance Of Conventional And High Metal CoMo And NiMo Catalysts In Deep Desulfurization Of Kuwait Atmospheric Gas Oil. Fuel Science and Technology International. 1995;13(9):1135–51.

30. Hu H, Wachs IE, Bare SR. Surface Structures of Supported Molybdenum Oxide Catalysts: Characterization by Raman and Mo L3-Edge XANES. J Phys Chem. 1995;99(27):10897–910.

31. Ahuja SP, Derrien ML, Le Page JF. Activity and selectivity of hydrotreating catalysts. Industrial & Engineering Chemistry Product Research and Development. 1970;9(3):272–81.

32. Grange P. Catalytic Hydrodesulfurization. Catalysis Reviews. 1980;21(1):135–81.

33. Kasztelan S, Toulhoat H, Grimblot J, Bonnelle JP. A geometrical model of the active phase of hydrotreating catalysts. Applied Catalysis. 1984;13(1):127–59.

34. Houssenbay S, Kasztelan S, Toulhoat H, Bonnelle JP, Grimblot J. Nature of the different nickel species in sulfided bulk and alumina-supported nickel-molybdenum hydrotreating catalysts. J Phys Chem. 1989;93(20):7176–80.

35. Lemberton JL, Touzeyidio M, Guisnet M. Catalytic hydroconversion of simulated coal tars: III. Activity of sulphided NiMo on alumina-zeolite catalysts for the hydroconversion of model compounds. Applied Catalysis A: General. 1991;79(1):115–26.

36. Genuit D, Afanasiev P, Vrinat M. Solution syntheses of unsupported Co(Ni)–Mo–S hydrotreating catalysts. Journal of Catalysis. 2005;235(2):302–17.

37. Kaluža L, Gulková D, Šolcová O, Žilková N, Čejka J. Hydrotreating catalysts supported on organized mesoporous alumina: Optimization of Mo deposition and promotional effects of Co and Ni. Applied Catalysis A: General. 2008;351(1):93–101.

38. Gao Q, Ofosu TNK, Ma S-G, Komvokis VG, Williams CT, Segawa K. Catalyst development for ultra-deep hydrodesulfurization (HDS) of dibenzothiophenes. I: Effects of Ni promotion in molybdenum-based catalysts. Catalysis Today. 2011;164(1):538–43.

39. Galarraga CE, Pereira-Almao P. Hydrocracking of Athabasca Bitumen Using Submicronic Multimetallic Catalysts at Near In-Reservoir Conditions. Energy Fuels. 2010;24(4):2383–9.

40. Eijsbouts S, Van Gestel JNM, Van Veen JAR, De Beer VHJ, Prins R. The effect of phosphate on the hydrodenitrogenation activity and selectivity of alumina-supported sulfided Mo, Ni, and Ni□Mo catalysts. Journal of Catalysis. 1991;131(2):412–32.

41. Isabel Vazquez M, Escardino A, Corma A. Activity and selectivity of nickel-molybdenum/HY ultrastable zeolites for hydroisomerization and hydrocracking of alkanes. Ind Eng Chem Res. 1987;26(8):1495–500.

42. Swangphol TT, McCauley M, Hu M, Adarme R. A Bold Move in Hydrocracking Catalyst Selection Resulted in a Significant Boost in Hydrocracker Margins. NPRA; 2008.

43. Thakur DS, Thomas MG. Catalyst deactivation in heavy petroleum and synthetic crude processing: a review. Applied Catalysis. 1985;15(2):197–225.

44. Song C, Hanaoka K, Nomura M. Influence of pore structure and chemical properties of supported Mo catalysts on their performance in upgrading heavy coal liquids. Energy & Fuels. 1992;6:619–28.

45. Adams CT, del Paggio AA, Schaper H, Stork WHJ, Shiflett WK. Hydroprocess catalyst selection. Hydrocarbon Processing. 1989;68(9)57-61.

46. Ancheyta J, Rana MS, Furimsky E. Hydroprocessing of heavy petroleum feeds: Tutorial. Catalysis Today. 2005;109(1-4):3–15.

47. Thomas CL. Chemistry of Cracking Catalysts. Industrial & Engineering Chemistry. 1949;41(11):2564–73.

48. Thomas JM, Thomas WJ. Principles and practice of heterogeneous catalysis. Wiley VCH, 1997.

49. Maxwell IE. Zeolite catalysis in hydroprocessing technology. Catalysis Today. 1987;1(4):385–413.

50. Vaughan DEW. Pillared clays -- a historical perspective. Catalysis today. 1988;2(2-3):187–98.

51. Sychev M, Shubina T, Rozwadowski M, Sommen APB, De Beer VHJ, van Santen RA. Characterization of the microporosity of chromia-and titania-pillared montmorillonites differing in pillar density. I. Adsorption of nitrogen. Microporous and Mesoporous Materials. 2000;37(1-2):187–200.

52. Corma A. From Microporous to Mesoporous Molecular Sieve Materials and Their Use in Catalysis. Chemical Reviews. 1997;97(6):2373–420.

53. Skoularikis ND, Coughlin RW, Kostapapas A, Carrado K, Suib SL. Catalytic performance of iron (III) and chromium (III) exchanged pillared clays. Applied catalysis. 1988;39(1-2):61–76.

54. Millan M, Adell C, Hinojosa C, Herod AA, Kandiyoti R. Mechanisms of catalytic activity in heavily coated hydrocracking catalysts. Oil & Gas Science and Technology-Revue de l'IFP. 2008;63(1):69–78.

55. Jia M, Afanasiev P, Vrinat M. The influence of preparation method on the properties of NiMo sulfide catalysts supported on ZrO2. Applied Catalysis A, General. 2005;278(2):213–21.

56. Perego C, Villa P. Catalyst preparation methods. Catalysis Today. 1997;34(3–4):281–305.

57. Bowker M. The basis and applications of heterogeneous catalysis. Oxford University Press; 1998.

58. Rase HF. Handbook of commercial catalysts. CRC Press; 2000.

59. Tilley RD, Jefferson DA. The preparation of chromium, nickel and chromium–nickel alloy nanoparticles on supports. Journal of Materials Chemistry. 2002;12(12):3809–13.

60. Roggenbuck J, Waitz T, Tiemann M. Synthesis of mesoporous metal oxides by structure replication: Strategies of impregnating porous matrices with metal salts. Microporous and Mesoporous Materials. 2008;113(1–3):575–82.

61. Song C, Nihonmatsu T, Nomura M. Effect of pore structure of nickel-molybdenum/alumina catalysts in hydrocracking of coal-derived and oil sand derived asphaltenes. Industrial & Engineering Chemistry Research. 1991;30(8):1726–34.

62. Medici L, Prins R. The Influence of Chelating Ligands on the Sulfidation of Ni and Mo in NiMo/SiO2Hydrotreating Catalysts. Journal of Catalysis. 1996;163(1):38–49.

63. Trejo F, Rana MS, Ancheyta J. CoMo/MgO–Al2O3 supported catalysts: An alternative approach to prepare HDS catalysts. Catalysis Today. 2008;130(2–4):327–36.

64. Sun M, Nicosia D, Prins R. The effects of fluorine, phosphate and chelating agents on hydrotreating catalysts and catalysis. Catalysis Today. 2003;86(1–4):173–89.

65. Rana MS, Ramírez J, Gutiérrez-Alejandre A, Ancheyta J, Cedeño L, Maity SK. Support effects in CoMo hydrodesulfurization catalysts prepared with EDTA as a chelating agent. Journal of Catalysis. 2007;246(1):100–8.

66. Coulier L, de Beer VH., van Veen JA., Niemantsverdriet J. Correlation between Hydrodesulfurization Activity and Order of Ni and Mo Sulfidation in Planar Silica-Supported NiMo Catalysts: The Influence of Chelating Agents. Journal of Catalysis. 2001;197(1):26–33.

67. Ho TC, Young, II AR, Chianelli RR, Jacobson AJ. United States Patent: 4591429 - Hydrotreating process employing catalysts comprising a supported mixture of a sulfide of a promoter metal, trivalent chromium and molybdenum or tungsten, 1986.

68. Chianelli RR, Ho TC, Jacobson AJ, Young AR. United States Patent: 4626339 - Supported chromium-molybdenum and tungsten sulfide catalysts, 1986.

69. Sanchez S, Rodriguez MA, Ancheyta J. Kinetic model for moderate hydrocracking of heavy oils. Industrial and Engineering Chemistry Research. 2005;44(25):9409–13.

70. Rana MS, Ancheyta J, Rayo P. A comparative study for heavy oil hydroprocessing catalysts at micro-flow and bench-scale reactors. Catalysis Today. 2005;109(1-4):24–32.

71. Greensfelder BS, Voge HH, Good GM. Catalytic and Thermal Cracking of Pure Hydrocarbons: Mechanisms of Reaction. Industrial & Engineering Chemistry. 1949;41(11):2573–84.

72. Frankenburg WG. Advances in catalysis and related subjects. Academic Press; 1962.

73. Coonradt HL, Garwood WE. Mechanism of Hydrocracking. Reactions of Paraffins and Olefins. Industrial & Engineering Chemistry Process Design and Development. 1964;3(1):38–45.

74. Degnan TF, Kennedy CR. Impact of catalyst acid/metal balance in hydroisomerization of normal paraffins. AIChE J. 1993;39(4):607–14.

75. Khorasheh F, Rangwala HA, Gray MR, Dalla Lana IG. Interactions between thermal and catalytic reactions in mild hydrocracking of gas oil. Energy & Fuels. 1989;3(6):716–22.

76. Yang SH, Satterfield CN. Catalytic hydrodenitrogenation of quinoline in a trickle-bed reactor. Effect of hydrogen sulfide. Ind Eng Chem Proc Des Dev. 1984;23(1):20–5.

77. Martens JA, Jacobs PA, Weitkamp J. Attempts to rationalize the distribution of hydrocracked products. II. Relative rates of primary hydrocracking modes of long chain paraffins in open zeolites. Applied Catalysis. 1986;20(1-2):283–303.

78. Martens JA, Jacobs PA, Weitkamp J. Attempts to rationalize the distribution of hydrocracked products. I qualitative description of the primary hydrocracking modes of long chain paraffins in open zeolites. Applied Catalysis. 1986;20(1-2):239–81.

79. Martens JA, Tielen M, Jacobs PA. Attempts to rationalize the distribution of hydrocracked products. III. mechanistic aspects of isomerization and hydrocracking of branched alkanes on ideal bifunctional large-pore zeolite catalysts. Catalysis Today. 1987;1(4):435–53.

80. Sanford EC. Conradson Carbon Residue Conversion during Hydrocracking of Athabasca Bitumen: Catalyst Mechanism and Deactivation. Energy & Fuels. 1995;9(3):549–59.

81. De Jong KP. Effects of Vapor-Liquid Equilibria on Coke Deposition in Trickle-Bed Reactors during Heavy Oil Processing. 1. Experimental Results. Ind Eng Chem Res. 1994;33(4):821–4.

82. Gray MR, McCaffrey WC. Role of Chain Reactions and Olefin Formation in Cracking, Hydroconversion, and Coking of Petroleum and Bitumen Fractions. Energy Fuels. 2002;16(3):756–66.

83. Leyva C, Rana MS, Trejo F, Ancheyta J. On the Use of Acid-Base-Supported Catalysts for Hydroprocessing of Heavy Petroleum. Ind Eng Chem Res. 2007;46(23):7448–66.

84. Yang M-G, Nakamura I, Fujimoto K. Hydro-thermal cracking of heavy oils and its model compound. Catalysis Today. 1998;43(3–4):273–80.

85. Gray MR, Khorasheh F, Wanke SE, Achia U, Krzywicki A, Sanford EC, et al. Role of catalyst in hydrocracking of residues from Alberta bitumens. Energy & fuels. 1992;6(4):478–85.

86. Rana MS, Sámano V, Ancheyta J, Diaz JAI. A review of recent advances on process technologies for upgrading of heavy oils and residua. Fuel. 2007;86(9):1216–31.

87. Rana MS, Ancheyta J, Maity SK, Rayo P. Hydrotreating of Maya Crude Oil: I. Effect of Support Composition and Its Pore-diameter on Asphaltene Conversion. Petroleum Science and Technology. 2007;25(1-2):187–99.

88. Rana MS, Ancheyta J, Maity SK, Rayo P. Characteristics of Maya crude hydrodemetallization and hydrodesulfurization catalysts. Catalysis Today. 2005;104(1):86–93.

89. Rana MS, Sámano V, Ancheyta J, Diaz JAI. A review of recent advances on process technologies for upgrading of heavy oils and residua. Fuel. 2007;86(9):1216–31.

90. Ancheyta J, Sánchez S, Rodríguez MA. Kinetic modeling of hydrocracking of heavy oil fractions: A review. Catalysis Today. 2005;109(1-4):76–92.

91. Fukuyama H, Terai S. Kinetic Study on the Hydrocracking Reaction of Vacuum Residue Using a Lumping Model. Petroleum Science and Technology. 2007;25(1-2):277–87.

92. Martínez J, Ancheyta J. Kinetic model for hydrocracking of heavy oil in a CSTR involving short term catalyst deactivation. Fuel. 2012;100:193–9.

93. Galarraga CE, Scott C, Loria H, Pereira-Almao P. Kinetic Models for Upgrading Athabasca Bitumen Using Unsupported NiWMo Catalysts at Low Severity Conditions. Ind Eng Chem Res. 2012;51(1):140–6.

94. Mohanty S, Saraf DN, Kunzru D. Modeling of a hydrocracking reactor. Fuel Processing Technology. 1991;29(1–2):1–17.

95. Ayasse AR, Nagaishi H, Chan EW, Gray MR. Lumped kinetics of hydrocracking of bitumen. Fuel. 1997;76(11):1025–33.

96. Reddy KM, Wei B, Song C. Mesoporous molecular sieve MCM-41 supported Co–Mo catalyst for hydrodesulfurization of petroleum resids. Catalysis Today. 1998;43(3–4):261–72.

97. Stanislaus A, Absi-Halabi M, Khan Z. Influence of catalyst pore size on asphaltenes conversion and coke-like sediments formation during catalytic hydrocracking of kuwait vacuum residues. Catalysts in Petroleum Refining and Petrochemical Industries 1995, Proceedings of the 2nd International Conference on Catalysts in Petroleum Refining and Petrochemical Industries.

98. Absi-Halabi M, Stanislaus A, Trimm DL. Coke formation on catalysts during the hydroprocessing of heavy oils. Applied Catalysis. 1991;72(2):193–215.

99. Callejas MA, Martínez MT. Hydrocracking of a Maya Residue. Kinetics and Product Yield Distributions. Ind Eng Chem Res. 1999;38(9):3285–9.

100. Ancheyta-Juarez J, Betancourt-Rivera G, Marroquin-Sanchez G, Perez-Arellano AM, Maity SK, Cortez MT, et al. An exploratory study for obtaining synthetic crudes from heavy crude oils via hydrotreating. Energy Fuels. 2001;15(1):120–7.

101. Gray MR, Zhao Y, McKnight CM, Komar DA, Carruthers JD. Coking of Hydroprocessing Catalyst by Residue Fractions of Bitumen. Energy & Fuels. 1999;13(5):1037–45.

102. Ancheyta J, Betancourt G, Centeno G, Marroquin G. Catalyst deactivation during hydroprocessing of Maya heavy crude oil.(II) Effect of temperature during time-on-stream. Energy Fuels. 2003;17(2):462–7.

103. Oelderik JM, Sie ST, Bode D. Progress in the catalysis of the upgrading of petroleum residue: A review of 25 years of R&D on Shell's residue hydroconversion technology. Applied Catalysis. 1989;47(1):1–24.

104. Ancheyta J, Betancourt G, Centeno G, Marroquin G, Alonso F, Garciafigueroa E. Catalyst deactivation during hydroprocessing of Maya heavy crude oil. 1. Evaluation at constant operating conditions. Energy Fuels. 2002;16(6):1438–43.

105. Furimsky E, Massoth FE. Deactivation of hydroprocessing catalysts. Catalysis Today. 1999;52(4):381–495.

106. Maity SK, Ancheyta J, Soberanis L, Alonso F. Catalysts for hydroprocessing of Maya heavy crude. Applied Catalysis A, General. 2003;253(1):125–34.

107. Ancheyta-Juárez J, Maity SK, Betancourt-Rivera G, Centeno-Nolasco G, Rayo-Mayoral P, Gómez-Pérez MT. Comparison of different Ni-Mo/alumina catalysts on hydrodemetallization of Maya crude oil. Applied Catalysis A: General. 2001;216(1-2):195–208.

108. Richardson SM, Nagaishi H, Gray MR. Initial Coke Deposition on a NiMo/[gamma]-Al2O3 Bitumen Hydroprocessing Catalyst. Ind Eng Chem Res. 1996;35(11):3940–50.

109. Matsushita K, Hauser A, Marafi A, Koide R, Stanislaus A. Initial coke deposition on hydrotreating catalysts. Part 1. Changes in coke properties as a function of time on stream. Fuel. 2004;83(7–8):1031–8.

110. Hauser A, Stanislaus A, Marafi A, Al-Adwani A. Initial coke deposition on hydrotreating catalysts. Part II. Structure elucidation of initial coke on hydrodematallation catalysts. Fuel. 2005;84(2–3):259–69.

111. Beuther H, Larson OA, Perrotta AJ. The Mechanism of Coke Formation on Catalysts. B. Delmon and G.F. Froment, editor. Studies in Surface Science and Catalysis. 1980;Volume 6:271–82.

112. Marafi A, Hauser A, Stanislaus A. Deactivation patterns of Mo/Al2O3, Ni–Mo/Al2O3 and Ni–MoP/Al2O3 catalysts in atmospheric residue hydrodesulphurization. Catalysis Today. 2007;125(3–4):192–202.

113. Marafi M, Stanislaus A. Influence of Catalyst Acidity and Feedstock Quality on Hydrotreating Catalyst Deactivation by Coke Deposition. Petroleum Science and Technology. 2001;19(5-6):697–710.

114. Stanislaus A, Hauser A, Marafi M. Investigation of the mechanism of sediment formation in residual oil hydrocracking process through characterization of sediment deposits. Catalysis Today. 2005;109(1–4):167–77.

115. Bartholomew CH. Mechanisms of catalyst deactivation. Applied Catalysis A: General. 2001;212(1–2):17–60.

116. Gualda G, Kasztelan S. Initial deactivation of residue hydrodemetallization catalysts. Journal of Catalysis. 1996;161(1):319–37.

117. Marafi A, Stainslaus A, Hauser A, Matsushita K. An Investigation of the Deactivation Behavior of Industrial Mo/Al2O3 and Ni-Mo/Al2O3 Catalysts in Hydrotreating Kuwait Atmospheric Residue. Petroleum Science and Technology. 2005;23(3-4):385–408.

118. Weitkamp J, Puppe L. Catalysis and zeolites: fundamentals and applications. Springer; 1999.

119. Thakur DS, Thomas MG. Catalyst deactivation during direct coal liquefaction: a review. Ind Eng Chem Prod Res Dev. 1984;23(3):349–60.

120. Callejas MA, Martínez MT, Blasco T, Sastre E. Coke characterisation in aged residue hydrotreating catalysts by solid-state 13C-NMR spectroscopy and temperature-programmed oxidation. Applied Catalysis A: General. 2001;218(1–2):181–8.

121. Hauser A, Marafi A, Stanislaus A, Al-Adwani A. Relation between Feed Quality and Coke Formation in a Three-Stage Atmospheric Residue Desulfurization (ARDS) Process. Energy Fuels. 2005;19(2):544–53.

122. Eijsbouts S, Battiston AA, van Leerdam GC. Life cycle of hydroprocessing catalysts and total catalyst management. Catalysis Today. 2008;130(2–4):361–73.

123. Rahimi PM, Gentzis T. Thermal hydrocracking of Cold Lake vacuum bottoms asphaltenes and their subcomponents. Fuel Processing Technology. 2003;80(1):69–79.

124. Vogelaar BM, Eijsbouts S, Bergwerff JA, Heiszwolf JJ. Hydroprocessing catalyst deactivation in commercial practice. Catalysis Today. 2010;154(3–4):256–63.

125. Bogdanor JM, Rase HF. Characteristics of a commercially aged nickel-molybdenum-alumina hydrotreating catalyst: component distribution, coke characteristics, and effects of regeneration. Industrial & Engineering Chemistry Product Research and Development. 1986;25(2):220–30.

126. Sing KSW, Everett DH, Haul RAW, Moscou L, Pierotti RA, Rouquerol J, et al. Reporting physisorption data for gas/solid systems. Pure Appl Chem. 1985;57(4):603–19.

127. Everett DH. IUPAC manual of symbols and terminology. J Pure Appl Chem. 1972;31:578.

128. Maciver DS, Tobin HH, Barth RT. Catalytic aluminas I. Surface chemistry of eta and gamma alumina. Journal of Catalysis. 1963;2(6):485–97.

129. Berrueco C, Venditti S, Morgan TJ, Álvarez P, Millan M, Herod AA, et al. Calibration of Size-Exclusion Chromatography Columns with 1-Methyl-2-pyrrolidinone (NMP)/Chloroform Mixtures as Eluent: Applications to Petroleum-Derived Samples. Energy & Fuels. 2008;22(5):3265–74.

130. Karaca F, Islas CA, Millan M, Behrouzi M, Morgan TJ, Herod AA, et al. The calibration of size exclusion chromatography columns: molecular mass distributions of heavy hydrocarbon liquids. Energy Fuels. 2004;18(3):778–88.

131. Suelves I, Islas C., Millan M, Galmes C, Carter J., Herod A., et al. Chromatographic separations enabling the structural characterisation of heavy petroleum residues. Fuel. 2003;82(1):1–14.

132. Ward JW. Hydrocracking processes and catalysts. Fuel Processing Technology. 1993;35(1–2):55–85.

133. Zhang SF, Xu B, Moore SA, Herod AA, Kandiyoti R. Comparison of hydrocracking reactivities of coal extracts from a flowing-solvent reactor, a mini-bomb and a pilot plant. Fuel. 1996;75(5):597–605.

134. Millan M, Adell C, Hinojosa C, Herod AA, Dugwell D, Kandiyoti R. Effect of catalyst deactivation and reaction time on hydrocracking heavy hydrocarbon liquids. Energy and Fuels. 2007;21(3):1370–8.

135. Venditti S. Characterization of Petroleum Fouling with Respect to Operational Parameters. PhD Thesis, Imperial College London; 2010.

136. Del Bianco A, Panariti N, Di Carlo S, Beltrame PL, Carniti P. New Developments in Deep Hydroconversion of Heavy Oil Residues with Dispersed Catalysts. 2. Kinetic Aspects of Reaction. Energy Fuels. 1994;8(3):593–7.

137. Nielsen LP, Christensen SV, Topsøe H, Clausen BS. Changes in metal–sulfur bond energy in promoted and unpromoted molybdenum catalysts. Catalysis letters. 2000;67(2):81–5.

138. Morawski I, Mosio-Mosiewski J. Effects of parameters in Ni-Mo catalysed hydrocracking of vacuum residue on composition and quality of obtained products. Fuel Processing Technology. 2006;87(7):659–69.

139. Heck RH, Rankel LA, DiGuiseppi FT. Conversion of petroleum resid from Maya crude: Effects of H-donors, hydrogen pressure and catalyst. Fuel Processing Technology. 1992;30(1):69–81.

140. Sánchez S, Ancheyta J. Effect of Pressure on the Kinetics of Moderate Hydrocracking of Maya Crude Oil. Energy Fuels. 2007;21(2):653–61.

141. Heck RH, DiGuiseppi FT. Kinetic and Mechanistic Effects in Resid Hydrocracking. Energy & Fuels. 1994;8(3):557–60.

142. Mochida I, Zhao XZ, Sakanishi K. Catalytic two-stage hydrocracking of Arabian vacuum residue at a high conversion level without sludge formation. Ind Eng Chem Res. 2011;29(3):334–7.

143. Van Doorn J, Moulijn JA. A model of coke on hydrotreating catalysts under reaction conditions. Fuel Processing Technology. 1993;35(3):275–87.

144. Trimm DL, Stanislaus A. The control of pore size in alumina catalyst supports: A review. Applied Catalysis. 1986;21(2):215–38.

145. Cejka J, Illkova N, Kaluza L, Zdrazil M. Mesoporous alumina as a support for hydrodesulfurization catalysts. Nanoporous Materials III, Proceedings of the 3rd International Symposium on Nanoporous Materials. 2002;Volume 141:243–50.

146. Čejka J. Organized mesoporous alumina: synthesis, structure and potential in catalysis. Applied Catalysis A: General. 2003;254(2):327–38.

147. Kaluža L, Zdražil M, Žilková N, Čejka J. High activity of highly loaded MoS2 hydrodesulfurization catalysts supported on organised mesoporous alumina. Catalysis Communications. 2002;3(4):151–7.

148. Corma A, Martinez A, Martinezsoria V, Monton JB. Hydrocracking of Vacuum Gasoil on the Novel Mesoporous MCM-41 Aluminosilicate Catalyst. Journal of Catalysis. 1995;153(1):25–31.

149. Maity SK, Ancheyta J, Rana MS. Support Effects on Hydroprocessing of Maya Heavy Crude. Energy Fuels. 2005;19(2):343–7.

150. Looi PY, Mohamed AR, Tye CT. Hydrocracking of residual oil using molybdenum supported over mesoporous alumina as a catalyst. Chemical Engineering Journal. 2012;181–182:717–24.

151. Pinnavaia TJ, Zhang Z, Hicks RW. An overview of mesostructured forms of alumina with crystalline framework walls. Abdelhamid Sayari and Mietek Jaroniec, editor. Studies in Surface Science and Catalysis. 2005;Volume 156:1–10.

152. Ray JC, You K-S, Ahn J-W, Ahn W-S. Mesoporous alumina (I): Comparison of synthesis schemes using anionic, cationic, and non-ionic surfactants. Microporous and Mesoporous Materials. 2007;100(1–3):183–90.

153. Márquez-Alvarez C, Žilková N, Pérez-Pariente J, Čejka J. Synthesis, Characterization and Catalytic Applications of Organized Mesoporous Aluminas. Catalysis Reviews: Science and Engineering. 2008;50(2):222.

154. Bagshaw SA, Prouzet E, Pinnavaia TJ. Templating of Mesoporous Molecular Sieves by Nonionic Polyethylene Oxide Surfactants. Science. 1995;269(5228):1242–4.

155. Bagshaw SA, Pinnavaia TJ. Mesoporous Alumina Molecular Sieves. Angewandte Chemie International Edition in English. 1996;35(10):1102–5.

156. Tzou MS, Pinnavaia TJ. Chromia pillared clays. Catalysis today. 1988;2(2-3):243–59.

157. Zhang Z, Pinnavaia TJ. Mesostructured γ-Al2O3 with a Lathlike Framework Morphology. J Am Chem Soc. 2002;124(41):12294–301.

158. Zhang Z, Hicks RW, Pauly TR, Pinnavaia TJ. Mesostructured Forms of γ-Al2O3. J Am Chem Soc. 2002;124(8):1592–3.

159. Shan Z, Jansen JC, Zhou W, Maschmeyer T. Al-TUD-1, stable mesoporous aluminas with high surface areas. Applied Catalysis A: General. 2003;254(2):339–43.

160. Lesaint C, Glomm WR, Borg Ø, Eri S, Rytter E, Øye G. Synthesis and characterization of mesoporous alumina with large pore size and their performance in Fischer-Tropsch synthesis. Applied Catalysis A: General. 2008;351(1):131–5.

161. Yuan Q, Yin A-X, Luo C, Sun L-D, Zhang Y-W, Duan W-T, et al. Facile Synthesis for Ordered Mesoporous γ-Aluminas with High Thermal Stability. J Am Chem Soc. 2008;130(11):3465–72.

162. Lesaint C, Kleppa G, Arla D, Glomm WR, Øye G. Synthesis and characterization of mesoporous alumina materials with large pore size prepared by a double hydrolysis route. Microporous and Mesoporous Materials. 2009;119(1-3):245–51.

163. Yang P, Zhao D, Margolese DI, Chmelka BF, Stucky GD. Generalized syntheses of large-pore mesoporous metal oxides with semicrystalline frameworks. Nature. 1998;396(6707):152–5.

164. Niesz K, Yang P, Somorjai GA. Sol-gel synthesis of ordered mesoporous alumina. Chemical Communications. 2005;(15):1986.

165. Li W-C, Lu A-H, Schmidt W, Schüth F. High Surface Area, Mesoporous, Glassy Alumina with a Controllable Pore Size by Nanocasting from Carbon Aerogels. Chemistry – A European Journal. 2005;11(5):1658–64.

166. Qu L, He C, Yang Y, He Y, Liu Z. Hydrothermal synthesis of alumina nanotubes templated by anionic surfactant. Materials Letters. 2005;59(29–30):4034–7.

167. Kuang D, Fang Y, Liu H, Frommen C, Fenske D. Fabrication of boehmite AlOOH and γ-Al2O3 nanotubes via a soft solution route. Journal of Materials Chemistry. 2003;13(4):660–2.

168. Lee HC, Kim HJ, Rhee CH, Lee KH, Lee JS, Chung SH. Synthesis of nanostructured γ-alumina with a cationic surfactant and controlled amounts of water. Microporous and Mesoporous Materials. 2005;79(1–3):61–8.

169. Wu Z, Li Q, Feng D, Webley PA, Zhao D. Ordered Mesoporous Crystalline γ-Al2O3 with Variable Architecture and Porosity from a Single Hard Template. J Am Chem Soc. 2010;132(34):12042–50.

170. Malmsten M, Lindman B. Self-assembly in aqueous block copolymer solutions. Macromolecules. 1992;25(20):5440–5.

171. De Llobet S, Puron H, Pinilla JL, Moliner R, Millán M, Suelves I. Tailored synthesis of organised mesoporous aluminas prepared by non-ionic surfactant templating using a Box-Wilson CCF design. Microporous and Mesoporous Materials. 2013;179:69–77.

172. González-Peña V, Díaz I, Márquez-Alvarez C, Sastre E, Pérez-Pariente J. Thermally stable mesoporous alumina synthesized with non-ionic surfactants in the presence of amines. Microporous and Mesoporous Materials. 2001;44-45:203–10.

173. López Cordero R, Gil Llambias FJ, López Agudo A. Temperature-programmed reduction and zeta potential studies of the structure ofMo/O3Al2O3 andMo/O3SiO2 catalysts effect of the impregnation pH and molybdenum loading. Applied Catalysis. 1991;74(1):125–36.

174. Qu L, Zhang W, Kooyman PJ, Prins R. MAS NMR, TPR, and TEM studies of the interaction of NiMo with alumina and silica–alumina supports. Journal of Catalysis. 2003;215(1):7–13.

175. Alibouri M, Ghoreishi SM, Aghabozorg HR. Hydrodesulfurization Activity of NiMo/Al-HMS Nanocatalyst Synthesized by Supercritical Impregnation. Industrial & Engineering Chemistry Research. 2009;48(9):4283–92.

176. Li C, Chen Y-W. Temperature-programmed-reduction studies of nickel oxide/alumina catalysts: effects of the preparation method. Thermochimica Acta. 1995;256(2):457–65.

177. Borowiecki T, Gac W, Denis A. Effects of small MoO3 additions on the properties of nickel catalysts for the steam reforming of hydrocarbons: III. Reduction of Ni-Mo/Al2O3 catalysts. Applied Catalysis A: General. 2004;270(1–2):27–36.

178. Leyva C, Ancheyta J, Rana MS, Marroquín G. A comparative study on the effect of promoter content of hydrodesulfurization catalysts at different evaluation scales. Fuel. 2007;86(9):1232–9.

179. Ferraz SGA, Zotin FMZ, Araujo LRR, Zotin JL. Influence of support acidity of NiMoS catalysts in the activity for hydrogenation and hydrocracking of tetralin. Applied Catalysis A: General. 2010;384(1-2):51–7.

180. Kaluza L, Zdrazil M, Zilková N, Cejka J. High activity of highly loaded MoS2 hydrodesulfurization catalysts supported on organised mesoporous alumina. Catalysis Communications. 2002;3(4):151–7.

181. Lemberton JL, Touzeyidio M, Guisnet M. Catalytic hydroconversion of simulated coal tars: III. Activity of sulphided NiMo on alumina-zeolite catalysts for the hydroconversion of model compounds. Applied Catalysis A: General. 1991;79(1):115–26.

182. Kagami N, Vogelaar BM, Langeveld AD van, Moulijn JA. Reaction pathways on NiMo/Al2O3 catalysts for hydrodesulfurization of diesel fuel. Applied Catalysis A: General. 2005;293:11–23.

183. Gutiérrez OY, Pérez F, Fuentes GA, Bokhimi X, Klimova T. Deep HDS over NiMo/Zr-SBA-15 catalysts with varying MoO3 loading. Catalysis Today. 2008;130(2–4):292–301.

184. Núñez M, Villamizar M. Optimization of the design of catalysts for the hydrodemetallation of deasphalted vacuum bottoms. Applied Catalysis A: General. 2003;252(1):51–6.

185. Ancheyta J, Betancourt G, Marroqu n G, Centeno G, Castañeda LC, Alonso F, et al. Hydroprocessing of Maya heavy crude oil in two reaction stages. Applied Catalysis A, General. 2002;233(1-2):159–70.

186. Rana MS, Srinivas BN, Maity SK, Murali Dhar G, Prasada Rao TSR. Origin of Cracking Functionality of Sulfided (Ni) CoMo/SiO2–ZrO2 Catalysts. Journal of Catalysis. 2000;195(1):31–7.

187. Dhar GM, Srinivas B., Rana M., Kumar M, Maity S. Mixed oxide supported hydrodesulfurization catalysts—a review. Catalysis Today. 2003;86(1–4):45–60.

188. Kim P, Kim Y, Kim H, Song IK, Yi J. Synthesis and characterization of mesoporous alumina with nickel incorporated for use in the partial oxidation of methane into synthesis gas. Applied Catalysis A: General. 2004;272(1-2):157–66.

189. Pedraza F, Fuentes S, Vrinat M, Lacroix M. Deactivation of MoS 2 catalysts during the HDS of thiophene. Catalysis letters. 1999;62(2):121–6.

190. Miki Y, Yamadaya S, Oba M, Sugimoto Y. Role of catalyst in hydrocracking of heavy oil. Journal of Catalysis. 1983;83(2):371–83.

191. Absi-Halabi M, Stanislaus A, Trimm DL. Coke formation on catalysts during the hydroprocessing of heavy oils. Applied Catalysis. 1991;72(2):193–215.

192. Savage PE, Klein MT, Kukes SG. Asphaltene reaction pathways. 3. Effect of reaction environment. Energy Fuels. 1988;2(5):619–28.

193. Ancheyta J, Centeno G, Trejo F, Marroquín G. Changes in Asphaltene Properties during Hydrotreating of Heavy Crudes. Energy & Fuels. 2003; 17(5):1233–8.

194. Gauthier T, Danial-Fortain P, Merdrignac I, Guibard I, Quoineaud A-A. Studies on the evolution of asphaltene structure during hydroconversion of petroleum residues. Catalysis Today. 2008;130(2-4):429–38.

195. Dehkissia S, Larachi F, Chornet E. Catalytic (Mo) upgrading of Athabasca bitumen vacuum bottoms via two-step hydrocracking and enhancement of Mo–heavy oil interaction. Fuel. 2004;83(10):1323–31.

196. Rana MS, Ancheyta J, Maity SK, Rayo P. Heavy crude oil hydroprocessing: A zeolite-based CoMo catalyst and its spent catalyst characterization. Catalysis Today. 2008;130(2-4):411–20.

197. Panariti N, Del Bianco A, Del Piero G, Marchionna M, Carniti P. Petroleum residue upgrading with dispersed catalysts: Part 2. Effect of operating conditions. Applied Catalysis A: General. 200;204(2):215–22.

198. Oelderik JM, Sie ST, Bode D. Progress in the catalysis of the upgrading of petroleum residue: A review of 25 years of R&D on Shell's residue hydroconversion technology. Applied Catalysis. 1989;47(1):1–24.

199. Wood J, Gladden L. Effect of coke deposition upon pore structure and self-diffusion in deactivated industrial hydroprocessing catalysts. Applied Catalysis A: General. 2003;249(2):241–53.

200. Van Doorn J, Moulijn JA. Extraction of spent hydrotreating catalysts studied by fourier transform infra-red spectroscopy. Fuel Processing Technology. 1990;26(1):39–51.

201. Richardson SM, Gray MR. Enhancement of residue hydroprocessing catalysts by doping with alkali metals. Energy Fuels. 1997;11(6):1119–26.

202. Stanislaus A, Absi-Halabi M, Al-Doloma K. Effect of phosphorus on the acidity of γ-alumina and on the thermal stability of γ-alumina supported nickel—molybdenum hydrotreating catalysts. Applied Catalysis. 1988;39:239–53.

203. Kumar K-N, Tranto J, Kumar J, Engell JE. Pore-structure stability and phase transformation in pure and M-doped (M= La, Ce, Nd, Gd, Cu, Fe) alumina membranes and catalyst supports. Journal of materials science letters. 1996; 15(3):266–70.

204. Mangnus PJ, Riezebos A, Vanlangeveld AD, Moulijn JA. Temperature-Programmed Reduction and HDS Activity of Sulfided Transition Metal Catalysts: Formation of Nonstoichiometric Sulfur. Journal of Catalysis. 1995;151(1):178–91.

205. Sarbak Z. NiMo Catalysts supported on chromium modified zeolites of type X and Y—their structure and HDS activity. Applied Catalysis A, General. 2001;207(1-2):309–14.

206. Thiollier A, Afanasiev P, Cattenot M, Vrinat M. Preparation and properties of chromium-containing hydrotreating catalysts (NiMo)/ZrO2Cr2O3. Catalysis Letters. 1998;55(1):39–45.

207. Liu YM, Feng WL, Wang LC, Cao Y, Dai WL, He HY, et al. Chromium supported on mesocellular silica foam (MCF) for oxidative dehydrogenation of propane. Catalysis Letters. 2006;106(3):145–52.

208. Khashagul'gova NS, Freiman LL, Zelentsov YN, Nefedov BK, Gorbatkina IE. Increasing the hydrogenation activity of commercial catalysts for selective hydrocracking. Chemistry and Technology of Fuels and Oils. 1993;29(11):533–7.

209. Gomez-Cazalilla M, Infantes-Molina A, Merida-Robles J, Rodriguez-Castellon E, Jimenez-Lo pez A. Chromium Species as Captors of Sulfur Molecules on Nickel-Based Hydrotreating Catalysts. Energy & Fuels. 2008;23(1):101–10.

210. Vuurman MA, Hardcastle FD, Wachs IE. Characterization of CrO3/Al2O3 catalysts under ambient conditions: Influence of coverage and calcination temperature. Journal of Molecular Catalysis. 1993;84(2):193–205.

211. Shee D, Sayari A. Light alkane dehydrogenation over mesoporous Cr2O3/Al2O3 catalysts. Applied Catalysis A: General. 2010;389(1–2):155–64.

212. Rao TVM, Yang Y, Sayari A. Ethane dehydrogenation over pore-expanded mesoporous silica supported chromium oxide: 1. Catalysts preparation and characterization. Journal of Molecular Catalysis A: Chemical. 2009;301(1–2):152–8.

213. Gil A, Gandia LM, Vicente MA. Recent Advances in the Synthesis and Catalytic Applications of Pillared Clays. Catalysis Reviews. 2000;42(1-2):145–212.

214. Han YS, Yamanaka S, Choy JH. A new thermally stable SiO2–Cr2O3 sol pillared montmorillonite with high surface area. Applied Catalysis A, General. 1998;174(1-2):83–90.

215. Bodman SD, McWhinnie WR, Begon V, Suelves I, Lazaro MJ, Morgan TJ, et al. Metal-ion pillared clays as hydrocracking catalysts (I): Catalyst preparation and assessment of performance at short contact times. Fuel. 2002;81(4):449–59.

216. Bodman SD, McWhinnie WR, Begon V, Millan M, Suelves I, Lazaro MJ, et al. Metal-ion pillared clays as hydrocracking catalysts (II): effect of contact time on products from coal extracts and petroleum distillation residues. Fuel. 2003;82(18):2309–21.

217. Gyftopoulou ME, Millan M, Bridgwater AV, Dugwell D, Kandiyoti R, Hriljac JA. Pillared clays as catalysts for hydrocracking of heavy liquid fuels. Applied Catalysis A, General. 2005;282(1-2):205–14.

218. Abello MC, Gomez MF, Ferretti O. Oxidative Conversion of Propane over Al 2 O 3-Supported Molybdenum and Chromium Oxides. Catalysis letters. 2003;87(1):43–9.

219. Zhang L, Deng J, Dai H, Au CT. Binary Cr–Mo oxide catalysts supported on MgO-coated polyhedral three-dimensional mesoporous SBA-16 for the oxidative dehydrogenation of iso-butane. Applied Catalysis A: General. 2009;354(1–2):72–81.

220. Yokoyama T, Fujita N. Hydrogenation of aliphatic carboxylic acids to corresponding aldehydes over Cr2O3-based catalysts. Applied Catalysis A: General. 2004;276(1–2):179–85.

221. Babich I., Moulijn J. Science and technology of novel processes for deep desulfurization of oil refinery streams: a review. Fuel. 2003 Apr;82(6):607–31.

222. Perego C, Amarilli S, Carati A, Flego C, Pazzuconi G, Rizzo C, et al. Mesoporous silica-aluminas as catalysts for the alkylation of aromatic hydrocarbons with olefins. Microporous and Mesoporous Materials. 1999;27(2-3):345–54.

223. García MF. Supported metals in catalysis. Imperial College Press; 2005.

224. Niemann K, Wenzel F. The VEBA-COMBI-CRACKING-Technology: An update. Fuel Processing Technology. 1993;35(1-2):1–20.

225. Wenzel F. VEBA-COMBI-Cracking—A commercial route for bottom-of-the-barrel upgrading. Proceedings of the International Symposium on Heavy Oil and Residue Upgrading and Utilization Fushun, China. 1992;185–201.

226. Gray MR. Extraction and Upgrading of Oil Sands Bitumen: Intensive short course. Edmonton; 2001.

227. Ehrburger P. Dispersion of small particles on carbon surfaces. Advances in Colloid and Interface Science. 1984;21(3–4):275–302.

228. Iijima S. Helical microtubules of graphitic carbon. nature. 1991;354(6348):56–8.

229. Martin-Gullon I, Vera J, Conesa JA, González JL, Merino C. Differences between carbon nanofibers produced using Fe and Ni catalysts in a floating catalyst reactor. Carbon. 2006;44(8):1572–80.

230. Chinthaginjala JK, Seshan K, Lefferts L. Preparation and Application of Carbon-Nanofiber Based Microstructured Materials as Catalyst Supports. Ind Eng Chem Res. 2007;46(12):3968–78.

231. Furimsky E. Carbons and Carbon-supported Catalysts in Hydroprocessing. Royal Society of Chemistry; 2008.

232. Toebes ML, Bitter JH, van Dillen AJ, de Jong KP. Impact of the structure and reactivity of nickel particles on the catalytic growth of carbon nanofibers. Catalysis Today. 2002;76(1):33–42.

233. Ros TG, van Dillen AJ, Geus JW, Koningsberger DC. Surface Oxidation of Carbon Nanofibres. Chemistry – A European Journal. 2002;8(5):1151–62.

234. Husny Pahmy R, Mohamed AR. Utilization of Carbon Nanotubes as a Support Material in Metal-Based Catalyst Systems: Applications in Catalysis. Recent Patents on Engineering. 2012;6(1):31–47.

235. Rodríguez-reinoso F. The role of carbon materials in heterogeneous catalysis. Carbon. 1998;36(3):159–75.

236. Serp P, Corrias M, Kalck P. Carbon nanotubes and nanofibers in catalysis. Applied Catalysis A: General. 2003;253(2):337–58.

237. Abotsi GMK, Scaroni AW. A review of carbon-supported hydrodesulfurization catalysts. Fuel Processing Technology. 1989;22(2):107–33.

238. De Jong KP, Geus JW. Carbon Nanofibers: Catalytic Synthesis and Applications. Catalysis Reviews. 2000;42(4):481–510.

239. Bezemer GL, Bitter JH, Kuipers HPCE, Oosterbeek H, Holewijn JE, Xu X, et al. Cobalt Particle Size Effects in the Fischer−Tropsch Reaction Studied with Carbon Nanofiber Supported Catalysts. J Am Chem Soc. 2006;128(12):3956–64.

240. Su DS, Perathoner S, Centi G. Catalysis on nano-carbon materials: Going where to? Catalysis Today. 2012;186(1):1–6.

241. Dong K, Ma X, Zhang H, Lin G. Novel MWCNT-Support for Co-Mo Sulfide Catalyst in HDS of Thiophene and HDN of Pyrrole. Journal of Natural Gas Chemistry. 2006;15(1):28–37.

242. Yu Z, Fareid LE, Moljord K, Blekkan EA, Walmsley JC, Chen D. Hydrodesulfurization of thiophene on carbon nanofiber supported Co/Ni/Mo catalysts. Applied Catalysis B: Environmental. 2008;84(3–4):482–9.

243. Shang H, Liu C, Xu Y, Qiu J, Wei F. States of carbon nanotube supported Mo-based HDS catalysts. Fuel Processing Technology. 2007;88(2):117–23.

244. Candia R, Sørensen O, Villadsen Jør, Topsøe N-Y, Clausen BS, Topsøe H. Effect of Sulfiding Temperature on Activity and Structures of CO-MO/AL2O3 Catalysts. ii. Bulletin des Sociétés Chimiques Belges. 1984;93(8-9):763–74.

245. Farag H, Whitehurst D., Sakanishi K, Mochida I. Carbon versus alumina as a support for Co–Mo catalysts reactivity towards HDS of dibenzothiophenes and diesel fuel. Catalysis Today. 1999;50(1):9–17.

246. Prabhu N, Dalai AK, Adjaye J. Hydrodesulphurization and hydrodenitrogenation of light gas oil using NiMo catalyst supported on functionalized mesoporous carbon. Applied Catalysis A: General. 2011;401(1–2):1–11.

247. Eswaramoorthi I, Sundaramurthy V, Das N, Dalai AK, Adjaye J. Application of multi-walled carbon nanotubes as efficient support to NiMo hydrotreating catalyst. Applied Catalysis A: General. 2008;339(2):187–95.

248. Li C, Shi B, Cui M, Shang H, Que G. Application of Co-Mo/CNT catalyst in hydro-cracking of Gudao vacuum residue. Journal of Fuel Chemistry and Technology. 2007;35(4):407–11.

249. Lin T-W, Liu C-J, Lin J-Y. Facile synthesis of MoS3/carbon nanotube nanocomposite with high catalytic activity toward hydrogen evolution reaction. Applied Catalysis B: Environmental. 2013;134–135:75–82.

250. Surisetty VR, Tavasoli A, Dalai AK. Synthesis of higher alcohols from syngas over alkali promoted MoS2 catalysts supported on multi-walled carbon nanotubes. Applied Catalysis A: General. 2009;365(2):243–51.

251. Pinilla JL, de Llobet S, Suelves I, Utrilla R, Lázaro MJ, Moliner R. Catalytic decomposition of methane and methane/CO2 mixtures to produce synthesis gas and nanostructured carbonaceous material. Fuel. 2011;90(6):2245–53.

252. Pinilla JL, Utrilla R, Lázaro MJ, Suelves I, Moliner R, Palacios JM. A novel rotary reactor configuration for simultaneous production of hydrogen and carbon nanofibers. International Journal of Hydrogen Energy. 2009;34(19):8016–22.

253. Cuervo MR, Asedegbega-Nieto E, Díaz E, Vega A, Ordóñez S, Castillejos-López E, et al. Effect of carbon nanofiber functionalization on the adsorption properties of volatile organic compounds. Journal of Chromatography A. 2008; 1188(2):264–73.

254. Zhou J-H, Sui Z-J, Zhu J, Li P, Chen D, Dai Y-C, et al. Characterization of surface oxygen complexes on carbon nanofibers by TPD, XPS and FT-IR. Carbon. 2007;45(4):785–96.

255. De Llobet S, Pinilla JL, Lázaro MJ, Moliner R, Suelves I. Catalytic decomposition of biogas to produce H2-rich fuel gas and carbon nanofibers. Parametric study and characterization. International Journal of Hydrogen Energy. 2012;37(8):7067–76.

256. Brito JL, Ilija M, Hernández P. Thermal and reductive decomposition of ammonium thiomolybdates. Thermochimica Acta. 1995;256(2):325–38.

257. Alonso G, Valle MD, Cruz J, Licea-Claverie A, Petranovskii V, Fuentes S. Preparation of MoS2 and WS2 catalysts by in situ decomposition of ammonium thiosalts. Catalysis Letters. 1998;52(1-2):55–61.

258. Scheffer B, Dekker NJJ, Mangnus PJ, Moulijn JA. A temperature-programmed reduction study of sulfided CoMo/Al2O3 hydrodesulfurization catalysts. Journal of Catalysis. 1990;121(1):31–46.

259. Afanasiev P. On the interpretation of temperature programmed reduction patterns of transition metals sulphides. Applied Catalysis A: General. 2006; 303(1):110–5.

260. Matos J, Brito JL, Laine J. Activated carbon supported NiMo: effects of pretreatment and composition on catalyst reducibility and on ethylene conversion. Applied Catalysis A: General. 1997;152(1):27–42.

261. Liu B, Chai Y, Wang Y, Zhang T, Liu Y, Liu C. A simple technique for preparation of presulfided eggshell MoS2/Al2O3 catalysts and kinetics approach for highly selective hydrodesulfurization of FCC gasoline. Applied Catalysis A: General. 2010;388(1–2):248–55.

262. Puello-Polo E, Gutiérrez-Alejandre A, González G, Brito JL. Relationship Between Sulfidation and HDS Catalytic Activity of Activated Carbon Supported Mo, Fe–Mo, Co–Mo and Ni–Mo Carbides. Catal Lett. 2010;135(3-4):212–8.

263. Calais C, Matsubayashi N, Geantet C, Yoshimura Y, Shimada H, Nishijima A, et al. Crystallite Size Determination of Highly Dispersed Unsupported MoS2Catalysts. Journal of Catalysis. 1998;174(2):130–41.

264. Fukuyama H, Terai S. An Active Carbon Catalyst Prevents Coke Formation from Asphaltenes during the Hydrocracking of Vacuum Residue. Petroleum Science and Technology. 2007;25(1-2):231–40.

265. Fukuyama H, Terai S, Uchida M, Cano JL, Ancheyta J. Active carbon catalyst for heavy oil upgrading. Catalysis Today. 2004;98(1–2):207–15.

266. Maity SK, Blanco E, Ancheyta J, Alonso F, Fukuyama H. Early stage deactivation of heavy crude oil hydroprocessing catalysts. Fuel. 2012;100:17–23.

267. Eijsbouts S, van den Oetelaar LCA, van Puijenbroek RR. MoS2 morphology and promoter segregation in commercial Type 2 Ni–Mo/Al2O3 and Co–Mo/Al2O3 hydroprocessing catalysts. Journal of Catalysis. 2005;229(2):352–64.

268. De Jong KP, van den Oetelaar LCA, Vogt ETC, Eijsbouts S, Koster AJ, Friedrich H, et al. High-Resolution Electron Tomography Study of an Industrial Ni−Mo/γ-Al2O3 Hydrotreating Catalyst. J Phys Chem B. 2006;110(21):10209–12.

269. Leyva C, Rana MS, Ancheyta J. Surface characterization of Al2O3–SiO2 supported NiMo catalysts: An effect of support composition. Catalysis Today. 2008; 130(2–4):345–53.

270. Vogelaar BM, Steiner P, van der Zijden TF, van Langeveld AD, Eijsbouts S, Moulijn JA. Catalyst deactivation during thiophene HDS: The role of structural sulfur. Applied Catalysis A: General. 2007;318:28–36.

271. Mochida I, Zhao X, Sakanishi K, Yamamoto S, Takashima H, Uemura S. Structure and properties of sludges produced in the catalytic hydrocracking of vacuum residue. Industrial & Engineering Chemistry Research. 1989;28(4):418–21.

Appendix 1: Experimental data

Table 10.1. Conversions and product distribution for thermal reactions (without catalyst).

Conversions and product distribution	Thermal reaction temperature		
	400 °C	425 °C	450 °C
$C_{>450°C}$	0.21	0.54	0.68
$C_{Asphaltenes}$	0.17	0.12	0.11
Gas (wt %)	10.3	30.2	43.5
$Maltenes_{<450°C}$ (wt %)	0	0	0
$Maltenes_{>450°C}$ (wt %)	61.7	40.0	26.4
Asphaltenes (wt %)	26.4	24.3	21.2
Solids (wt %)	1.7	5.5	8.9

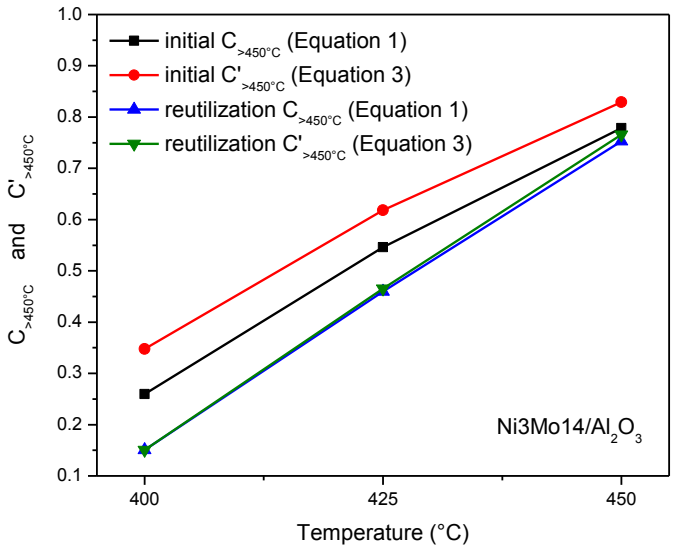

Figure 10.1. Conversion values for the >450 °C fraction using $Ni3Mo14/Al_2O_3$ with Equation 1 ($C_{>450°C}$) and Equation 3 ($C'_{>450°C}$).

Equation 1 includes coke as >450 °C material whereas Equation 3 does not consider coke formation.

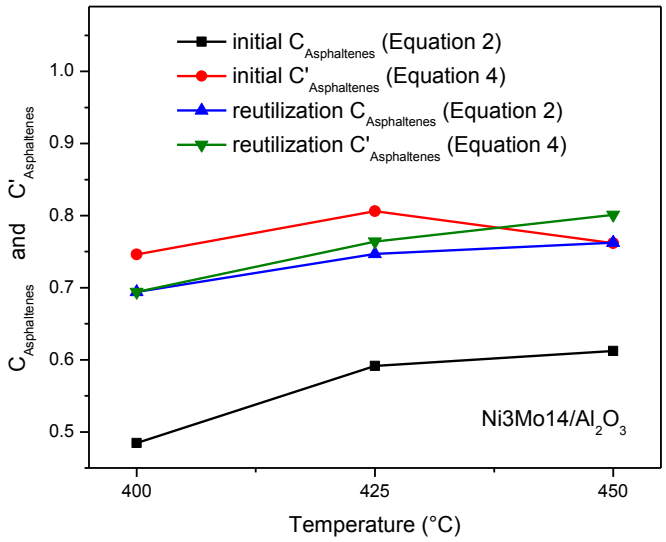

Figure 10.2. Conversion values for asphaltenes using $Ni3Mo14/Al_2O_3$ with Equation 2 ($C_{Asphaltenes}$) and Equation 4 ($C'_{Asphaltenes}$).

Equation 2 includes coke as unconverted asphaltenes whereas Equation 4 does not consider coke formation.

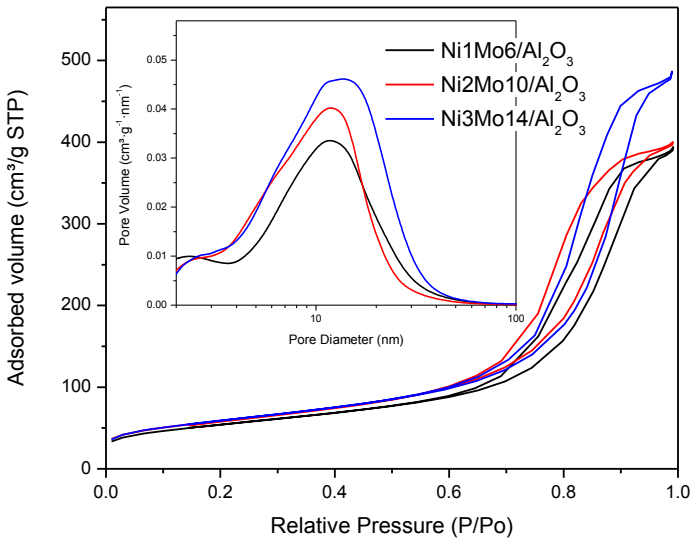

Figure 10.3. N_2 adsorption-desorption isotherms of the calcined catalysts $NixMox/Al_2O_3$ and pore size distribution (inset).

Table 10.2. Conversion values using $Ni1Mo6/Al_2O_3$, $Ni2Mo10/Al_2O_3$ and $Ni3Mo14/Al_2O_3$ for initial and reutilisation reactions. All reactions lasted 60 minutes with an initial 185 bar H_2 pressure.

Sample	T (°C)	$C_{>450°C}$		$C_{Asphaltenes}$	
		initial	reutilisation	initial	reutilisation
$Ni1Mo6/Al_2O_3$	400	0.23	0.16	0.35	0.41
	425	0.48	0.47	0.34	0.55
	450	0.64	0.81	0.41	0.67
$Ni2Mo10/Al_2O_3$	400	0.18	0.12	0.25	0.36
	425	0.46	0.46	0.42	0.70
	450	0.77	0.78	0.52	0.84
$Ni3Mo14/Al_2O_3$	400	0.26	0.17	0.48	0.69
	425	0.55	0.46	0.59	0.75
	450	0.78	0.75	0.61	0.76

Table 10.3. Product yields for initial reactions using $Ni1Mo6/Al_2O_3$, $Ni2Mo10/Al_2O_3$ and $Ni3Mo14/Al_2O_3$ catalysts; 60 min reactions with an initial 185 bar H_2 pressure.

Sample	T (°C)	Gas (wt %)	$Maltenes_{<450°C}$ (wt %)	$Maltenes_{>450°C}$ (wt %)	Asphaltenes (wt %)	Solids (wt %)
$Ni1Mo6/Al_2O_3$	400	0	16.4	61.7	12.9	9.1
	425	16.9	16.1	44.8	12.7	9.4
	450	28.0	20.6	31.5	11.5	8.4
$Ni2Mo10/Al_2O_3$	400	0.2	10.8	63.9	16.5	8.6
	425	15.2	17.5	47.8	11.3	8.2
	450	41.9	20.0	21.9	8.6	7.7
$Ni3Mo14/Al_2O_3$	400	2.7	14.8	65.1	8.5	8.8
	425	18.0	23.7	44.5	6.5	7.2
	450	39.8	24.1	23.0	8.0	5.0

Table 10.4. Product yields for reutilisation reactions using $Ni1Mo6/Al_2O_3$, $Ni2Mo10/Al_2O_3$ and $Ni3Mo14/Al_2O_3$ catalysts; 60 min reactions with an initial 185 bar H_2 pressure.

Sample	T (°C)	Gas (wt %)	$Maltenes_{<450°C}$ (wt %)	$Maltenes_{>450°C}$ (wt %)	Asphaltenes (wt %)	Solids (wt %)
$Ni1Mo6/Al_2O_3$	400	2.5	11.4	66.2	19.9	0
	425	18.3	16.3	50.4	14.7	0.3
	450	32.0	40.2	16.8	11.0	0.1
$Ni2Mo10/Al_2O_3$	400	0	10.9	67.6	19.8	1.6
	425	17.8	16.4	55.7	9.4	0.8
	450	42.7	18.7	33.1	5.2	0.2
$Ni3Mo14/Al_2O_3$	400	0	14.7	72.8	10.0	2.5
	425	16.3	18.9	56.3	7.9	0.6
	450	35.6	26.0	30.4	6.7	1.3

Table 10.5. Product yields for Maltenes$_{>450°C}$ fraction for reutilisation reactions using Ni1Mo6/Al_2O_3, Ni2Mo10/Al_2O_3 and Ni3Mo14/Al_2O_3 catalysts; 60 min reactions with an initial 185 bar H_2 pressure.

Sample	T (°C)	Heavy naphtha (wt %)	Kerosene (wt %)	Diesel (wt %)	Gas Oils (wt %)	Residue (wt %)
Ni1Mo6/Al_2O_3	400	0.9	1.7	16.6	27.8	53.0
	425	0.6	1.6	20.5	29.7	47.7
	450	0.3	4.3	33.4	34.0	27.9
Ni2Mo10/Al_2O_3	400	1.0	1.1	16.4	25.7	55.8
	425	0.5	2.0	21.1	30.0	46.4
	450	0.3	2.6	30.7	34.3	32.2
Ni3Mo14/Al_2O_3	400	1.0	1.1	16.0	27.2	54.6
	425	0.5	2.2	21.4	29.8	46.1
	450	0.2	3.4	31.7	34.9	29.8

Table 10.6. Reutilisation reaction products maltene and asphaltene content using Ni1Mo6/Al_2O_3, Ni2Mo10/Al_2O_3 and Ni3Mo14/Al_2O_3. All reactions lasted 60 minutes with an initial 185 bar H_2 pressure.

Sample	T (°C)	Liquid products (wt %)	
		Maltenes	Asphaltenes
Ni1Mo6/Al_2O_3	400	79.6	20.4
	425	81.9	18.1
	450	83.9	16.1
Ni2Mo10/Al_2O_3	400	79.8	20.2
	425	88.5	11.5
	450	90.9	9.1
Ni3Mo14/Al_2O_3	400	89.7	10.3
	425	90.5	9.5
	450	89.4	10.6

Table 10.7. Conversion values using Ni3Mo14/Al_2O_3-Cr, Al_2O_3-Cr and Al_2O_3 for initial and reutilisation reactions. All reactions lasted 60 minutes with an initial 185 bar H_2 pressure.

Sample	T (°C)	$C_{>450°C}$		$C_{Asphaltenes}$	
		initial	reutilisation	initial	reutilisation
Ni3Mo14/Al_2O_3-Cr	400	0.24	0.14	0.52	0.58
	425	0.48	0.52	0.62	0.82
	450	0.75	0.81	0.52	0.88
Al_2O_3-Cr	400	0.20	0.23	0	0.15
	450	0.72	0.76	0.27	0.52
Al_2O_3	400	0.18	0.20	-0.14	-.04
	450	0.72	0.72	0.24	0.57

Table 10.8. Product yields for initial and reutilisation reactions using Ni3Mo14/Al_2O_3-Cr; 60 min reactions with an initial 185 bar H_2 pressure.

Sample	T (°C)	Gas (wt %)	Maltenes$_{<450°C}$ (wt %)	Maltenes$_{>450°C}$ (wt %)	Asphaltenes (wt %)	Solids (wt %)
Initial reactions	400	2.2	11.9	69.7	5.4	10.8
	425	15.8	17.4	53.9	3.3	9.6
	450	40.6	19.3	24.1	5.1	10.9
Reutilisation reactions	400	0.0	10.9	75.0	11.0	3.1
	425	18.1	21.8	53.9	4.3	1.9
	450	44.5	20.7	30.9	3.9	0.0

Table 10.9. Product yields for initial and reutilisation reactions using Al_2O_3-Cr; 60 min reactions with an initial 185 bar H_2 pressure.

Sample	T (°C)	Gas (wt %)	Maltenes$_{<450°C}$ (wt %)	Maltenes$_{>450°C}$ (wt %)	Asphaltenes (wt %)	Solids (wt %)
Initial reactions	400	0	13.3	53.1	25.0	8.6
	450	4.6	13.4	53.3	27.3	1.4
Reutilisation reactions	400	41.9	9.5	24.1	18.1	6.4
	450	45.7	9.5	28.7	15.1	1.0

Table 10.10. Product yields for initial and reutilisation reactions using Al_2O_3; 60 min reactions with an initial 185 bar H_2 pressure.

Sample	T (°C)	Gas (wt %)	Maltenes$_{<450°C}$ (wt %)	Maltenes$_{>450°C}$ (wt %)	Asphaltenes (wt %)	Solids (wt %)
Initial reactions	400	0	10.1	51.5	28.5	9.9
	450	0.4	16.2	48.5	30.8	4.1
Reutilisation reactions	400	37.4	18.8	18.1	18.2	7.5
	450	41.6	9.9	34.2	12.2	2.1

Table 10.11. Reutilisation reaction products maltene and asphaltene content using Ni3Mo14/Al_2O_3-Cr. All reactions lasted 60 minutes with an initial 185 bar H_2 pressure.

Sample	T (°C)	Liquid products (wt %)		Gas and Solids (wt %)
		Maltenes	Asphaltenes	
Ni3Mo14/Al_2O_3-Cr	400	88.6	11.4	3.1
	425	94.6	5.4	20.0
	450	92.9	7.1	44.5

Table 10.12. Conversion values for initial and reutilisation reactions using MSA and Ni1Mo6/MSA. All reactions lasted 60 minutes with an initial 185 bar H_2 pressure.

Sample	T (°C)	$C_{>450°C}$		$C_{Asphaltenes}$	
		initial	reutilisation	initial	reutilisation
MSA	400	0.21	0.34	-0.16	0.30
	450	0.66	0.77	-0.16	0.72
Ni1Mo6/MSA	400	0.14	0.23	-0.33	0.43
	450	0.76	0.58	0.56	0.31

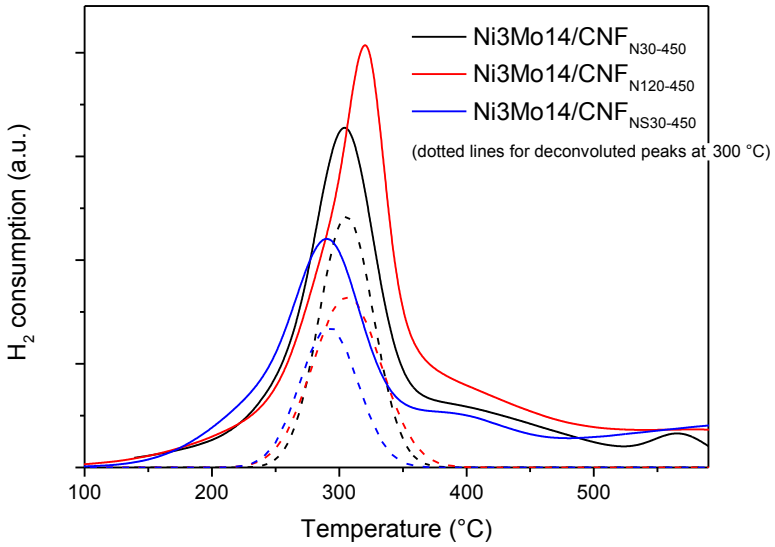

Figure 10.4. Deconvoluted TPR-S spectra of NiMo catalysts supported on $CNF_{N30-450}$, $CNF_{N120-450}$ and $CNF_{NS30-450}$.

Appendix 2: Publications related to the present work

Accepted:

i. José Luis Pinilla, Holda Purón, Daniel Torres, Saúl de Llobet, Rafael Moliner, Isabel Suelves, Marcos Millán. Carbon nanofibres coated with Ni decorated MoS_2 nanosheets as catalyst for Vacuum Residue hydroprocessing. Accepted for publication in Applied Catalysis B: Environmental, 2013.
ii. Holda Purón, Pedro Arcelus-Arrillaga, Kee Kee Chin, José Luis Pinilla, Beatriz Fidalgo, Marcos Millán. Kinetic Analysis of Vacuum Residue Hydrocracking in Early Reaction Stages. Fuel. 2014; 117: 408–414.
iii. Holda Purón, José Luis Pinilla, César Berrueco, J.A. Montoya de la Fuente, Marcos Millán. Hydrocracking of Maya vacuum residue with NiMo catalysts supported on mesoporous alumina and silica alumina. Energ. Fuel. 2013; 27 (7): 3952-3960.
iv. Saúl de Llobet, Holda Purón, José Luis Pinilla, Rafael Moliner, Marcos Millán, Isabel Suelves. Tailored synthesis of organised mesoporous aluminas prepared by non-ionic surfactant templating using a Box-Wilson CCF design. Micropor. Mesopor. Mat. 2013; 179: 69-77.
v. José Luis Pinilla, Pedro Arcelus-Arrillaga, Holda Purón, Marcos Millán. Reaction pathways of anthracene selective catalytic steam cracking using a NiK/Al_2O_3 catalyst. Fuel. 2013;109: 303-308.
vi. José Luis Pinilla, Pedro Arcelus-Arrillaga, Holda Purón, Marcos Millán. Selective Catalytic Steam Cracking of anthracene using mesoporous Al_2O_3 supported Ni-based catalysts doped with Na, Ca or K. Appl. Catal. Gen. 2013;459:17-25.

In preparation:

i. Holda Purón, José Luis Pinilla, Marcos Millán. Vacuum residue hydroprocessing using a NiMo catalyst supported on Cr doped alumina. Submitted to Applied Catalysis A.
ii. Holda Purón, José Luis Pinilla, J.A. Montoya de la Fuente, Marcos Millán. Effect of metal loading in $NiMo/Al_2O_3$ catalysts on Maya vacuum residue hydrocracking.
iii. Holda Purón, José Luis Pinilla, Daniel Torres, Rafael Moliner, Isabel Suelves, Marcos Millán. Carbon nanofibres functionalised by different acid treatments used as hydroprocessing catalyst support.